UNIVERSITÀ DEGLI STUDI FIRENZE

DOTTORATO DI RICERCA IN
SCIENZE CHIMICHE

CICLO XXXIV

COORDINATORE Prof. Piero Baglioni

Neurotransmitters-derived biopolymers for future diagnostics and bioanalysis

Settore Scientifico Disciplinare CHIM/01

Dottorando
Dott. Francesca Torrini

Tutore
Prof. Maria Minunni

Co-Tutore
Prof. Simona Scarano

Coordinatore
Prof. Piero Baglioni

Anni 2018/2021

UNIVERSITÀ
DEGLI STUDI
FIRENZE

DOTTORATO DI RICERCA IN SCIENZE CHIMICHE

CICLO XXXIV

COORDINATORE Prof. Piero Baglioni

Neurotransmitters-derived biopolymers for diagnostics and bioanalysis

Settore Scientifico Disciplinare CHIM/01

Dottorando
Dott. Francesca Torrini

Tutore
Prof. Maria Minunni

Co-Tutore
Prof. Simona Scarano

Coordinatore
Prof. Piero Baglioni

Anni 2018/2021

Preface

Before beginning the introduction of this dissertation …

… I would like to say that these three years in the research world have been incredible, like a roller coaster. During my second PhD year, a global pandemic, never faced before, has broken out and has claimed millions of lives while changing the ways in which we relate with each other and how we travel. We got stuck in the lockdown and our research work was interrupted for a few months. After being "locked-up", we were more motivated and more aware of how essential research is, in all fields. Today, I am very glad to have been able to learn about the research world, with its daily successes and failures, and to have been part of it for these three years. I am thankful to my supervisors for their excellent guidance, constant encouragement, and support during this PhD journey. More in general, I would like to thank all those who have walked beside me, with two or four legs. Thank you for coloring my journey with fun, love and care, teamwork, and support (…yes, also a lot of patience)!

I hope you enjoy reading.

Francesca Torrini

Florence, October 30th, 2021

TABLE OF CONTENTS

List of abbreviations

Abbreviations	Meaning
A	
Ab/s	Antibody/ies
ABC	Athlete biological passport
AC	Analytical chemistry
	Aminochrome (Chapter 5)
ACN	Acetonitrile
B	
bb	Building block
BELISA	Biomimetic enzyme-linked
	immunosorbent assay
BG	Biotinylated gonadorelin
BSA	Bovine serum albumin
C	
CAD	Collision gas
CE	Collision energy
cTnI	Cardiac Troponin I
CUR	Curtain gas
CXP	Collision exit potential
D	
DA	Dopamine
DAQ(DQ)	Dopamine-quinone
DB	Dilution buffer
DHBA-NE	3,4-dihydroxybenzaldehyde
	norepinephrine
DHI	5,6-dihydroxyindole
DLS	Dynamic light scattering
DP	Declustering potential

E	
ELISA	Enzyme-linked immunosorbent assay
ELONA	Enzyme-linked oligonucleotide assay
ELPs	Elastin-like polypeptides
EMA	European Medicines Agency
EP	Entrance potential
F	
FA	Formic acid
FIP	Fingerprint imprinting
FSH	Follicle-stimulating hormone
G	
G	Gonadorelin (synthetic peptide)
G-mAb	Anti-G antibody
G-250	Coomassie brilliant blue G-250
GAP	GnRH-associated peptide
GMR	Guided mode resonance
GnRH	Gonadorelin (endogenous peptide)
GnRH-R	GnRH receptors
GPCRs	G-protein coupled receptors
GS	Gas source
H	
hCG	Human chorionic gonadotropin
HPG	Hypothalamic-pituitary-gonadal
HRP	Horseradish peroxidase
I	
IBPs	Imprinted biopolymers
IQ	Indole-5,6-quinone
ISTD	Internal standard
ISV	Ion spray voltage

K	
K_D	Equilibrium dissociation constant
KLH	Keyhole limpet hemocyanin
L	
LC	Leukoaminochrome
LEU	Leuprolide
LFA	Lateral flow assays
LH	Luteinizing hormone
M	
MELISA	Mobile-phone based ELISA
MIP	Molecularly imprinted polymer
MIT	Molecular imprinting technology
MRPL	Minimum Required Performance Levels
N	
NE	Norepinephrine
NIP	Non imprinted polymer
NPs	Nanoparticles
O	
OVA	Ovalbumin
P	
PAEK	Polyaryletherketone
PBT	Polybutylene terephthalate
PC	Polycarbonate
pCA/s	Poly(catecholamine/s)
PDA	Polydopamine
PDI	Polydispersity index
PD-1	Programmed cell death 1 receptor
PD-L1	Programmed cell death ligand 1
PEP	Polyepinephrine
PET	Polyethylene terephthalate

pLD	Polylevodopa
PNE	Polynorepinephrine
POA	Polyoctapamine
POC	Point-of-care
PPC	Poly(propylene carbonate)
PSA	Potentiometric stripping analysis
PSE	Poyserotonin
PVC	Poly(vinyl chloride)
Q	
Q	Quantifier
q	Qualifiers
R	
rHuEPO	Recombinant human erythropoietin
RIA	Radioimmunoassay
S	
S	Streptavidin
SEM	Scanning electron microscopy
SERS	Surface-enhanced Raman scattering
SPE	Solid-phase extraction
SPW	Surface plasma wave
SPR	Surface plasmon resonance
SRM	Selected reaction monitoring
T	
TEM	Source temperature
TIR	Total internal reflection
TMB	Tetramethylbenzidine
V	
VCM	Vinyl chloride monomer
W	
WB	Washing buffer

CHAPTER 1

Introduction and context

We need alternatives to antibodies for diagnostics and bioanalysis!

A near future, in which mimetic entities will be able to replace the use of antibodies (Abs) in diagnostics, is upcoming. Abs production has relied for decades on animal immunization, but today this approach is no longer acceptable. During the last years, it has been flanked by new technologies based on mimetics, affinity elements obtained without impacting on animal welfare. Besides, it is crucial not only to have a sustainable vision of the mimetic receptors of the future, but also to move in the direction of low-cost, high-impact technologies, speed of implementation, and versatility.

1.1 Content and structure of the dissertation

This dissertation primarily focuses on biomimicry, the term coming from the Greek words *bios* meaning life in Greek and *mimesis* meaning *to* imitate [1], a field that seeks to mimic natural mechanisms, structures, and functions to exploit them into several scientific applications. We have been exploring nature-inspired catecholamine-based biopolymers to straightforwardly develop molecularly imprinted polymers (MIPs), mimetic receptors, for bioanalytical and diagnostics applications. From a more comprehensive standpoint, this dissertation addressed the broad need for simple, cost-effective, and accurate catecholamine-based assays, using animal-free reagents. The general structure of this dissertation is explained herein along with an overview of the research goals.

Chapter 1 is devoted to the description of MIPs design and to how they are synthesized. The Chapter gives a brief outline of molecular imprinting technology (MIT) along with recent MIPs synthesis progresses, focusing on the selection of the template molecule, a critical factor to assemble efficient receptor mimics.

Chapter 2 deals with catechol-derived biopolymers, chiefly focusing on polydopamine (PDA) and polynorepinephrine (PNE), which are becoming increasingly appreciated as soft, sustainable, versatile, and biocompatible materials able to address challenging tasks.

Chapter 3 reports on the use of MIPs for the detection of the small peptide, namely gonadorelin, in biological specimens, i.e., human urines. This is the main purpose of the PhD research study which is part of a larger project entitled "New analytical approaches aimed at tackling doping in sports: development of optical biosensors for the analysis of peptide hormones through molecularly imprinted polymers" funded by the Italian Ministry of Health. First, an optical, label-free, and real time sensing strategy was developed for the detection of gonadorelin using Surface Plasmon Resonance (SPR) transduction. In addition, a portable test was settled, motivated by the lack of decentralized rapid gonadorelin assays for quick decision-making and

extensive athlete monitoring before and during competitions. More in detail, a biomimetic enzyme-linked immunosorbent assay (BELISA) was developed onto disposable microplates aiming to cut testing costs and time that are usually required for gonadorelin detection (e.g., mass spectrometry). The detection of gonadorelin through a MIP-based bioanalytical approach has been a very ambitious goal, as no point-of-care devices and only a few monoclonal antibodies are commercialized targeting this analyte. The MIP based approach is able to cheaply measure the drug levels directly from human urine specimens by using a small sample volume (in order of microliters). More specifically, a polynorepinephrine (PNE) based MIP was first designed for targeting gonadorelin, and then it was employed as a receptor element in an SPR-based optical sensing platform. A competitive bioanalytical label-free assay has been built over the MIP for gonadorelin quantification in urine samples. After this, the second task of the project involved the scaling down of the competitive assay, i.e., BELISA, into a portable and simple platform to analyze human urine. The strategy developed was validated by mass spectrometric analysis. Urine samples and LC-MS/MS equipment were available at Pisa University Hospital's Clinical Pathology Lab, partner of the project.

Very soon, the journey across MIPs will continue in the direction of nano-MIPs, which we foresee could be further used as advantageous alternatives to antibodies, both in *vitro* diagnostics and in *vivo* therapeutic applications.

Chapter 4 is, thus, about the preliminary development of catecholamine-based nanoparticles which will be implemented in the MIPs nanotechnological applications.

Chapter 5 describes how catecholamines may be exploited in colorimetric microplate-based bioassays to screen different analytes, in addition to their use as functional monomers in mimetics (MIPs) synthesis. In this case, the redox PDA properties, and the capability to build up coating, non-imprinted material, were exploited for analytical purposes. Two colorimetric tests for molecular diagnostics were developed and applied respectively to analyze serum albumin, a biomarker for kidney function, in human fluids (urine) and

to preliminarily screen hypochlorous acid, a key determinant for neurodegenerative disorders.

Chapter 6 summarizes the pithiest points of the PhD research studies, discussed in the preceding chapters, and introduces considerations for future work on the topic.

1.2 Imprinting technology (IT) for molecular recognition: beyond natural antibodies

Biomimetic receptors including affibodies, aptamers (nucleic acids), polypeptides (engineered binding proteins), oligopeptides, and molecularly imprinted polymers (MIPs, inorganic or organic matrices) have recently gained a lot of attention for specific recognition of biomolecules [2]. They are an attractive alternative affinity tool to antibodies for both diagnostic and therapeutic approaches. Antibodies are routinely used in affinity technology (immunoassays, immunoaffinity separation, biosensors, bioimaging, etc.,) and biomedicine for their ability to specifically recognize an antigen, the target molecule, which perfectly fits the antibody's binding sites [3].

Antibodies are proteins and come with a few drawbacks which limit their production on a large-scale and hamper their integration into standard processes. The latter limitations are mainly related to the high costs associated with *in vivo* animal immunization and processing, biochemical instability at high temperature with the consequence that most antibodies are stored at low temperature to prevent degradation and microbial infection, and "limited" availability for certain targets.

In this context, biomimetic affinity tools should be designed and synthesized mimicking the functions of the natural receptor entities, while going beyond their limits. As a result, the research in the area of mimetic (artificial) receptors has been expanded markedly in recent decades. Their chief advantages over protein receptors, to be emphasized, are the high stability under harsh conditions as well as the extended lifetimes in biological fluids

[4-5]. Biomimetics' production is relatively simple, cost-effective, and does not require animals [3].

Besides, mimetic receptors can be synthesized to recognize different target molecules, including likewise small non-immunogenic compounds and toxic molecules to animals [6].

In this dissertation, our attention largely centered on the design and "*household"* synthesis of PNE-based MIPs. In this section, we provide a general introduction about MIPs and the existing strategies to build them.

1.3 A long molecular imprinting history: background

Molecular imprinting is a technique to create biomimetic recognition sites within polymeric materials that mimic biological receptors. The polymeric architecture consists of a "skeleton" built *via* a template-assisted synthesis [5,7-9]. In detail, the functional monomers are co-polymerized in the presence of a template, that can be the whole target molecule or a portion of it, and of possible crosslinkers and initiators [3-9].

After the polymerization reaction occurs, the template molecule is extracted by leaving binding cavities in the polymer network which retains complementarity in shape, structure, and functional groups assembly to the template molecule. The functioning mechanism resembles a "lock and key" process [4] to selectively re-bind the target molecule by mimicking the biological antibody-antigen affinity [10]. Currently MIPs, thanks to the relentless research on material science, appear as rivaling their natural counterparts in molecular recognition assays. Specifically, MIPs low-cost and ease of production, their chemical and thermal stability (e.g., tolerance to solvents and extreme pH, the possibility of undergoing sterilization), firmness during storage under non-controlled environmental conditions, and the morphological freedom (films or nanostructures) as well as the electronics integrability, are gainful features which have entailed an outstanding interest during the years [5,11]. Moreover, MIPs retain numerous biomimetic functions beyond the molecular recognition ability, including catalytic activity and stimuli-responsive functions [9]. The concept of MIPs arose most notably

around 1940 following the L. Pauling theory about the *in vitro* antibodies' manufacture using template molecules [9-12]. Nevertheless, the beginnings of MIPs prosperity have indisputably occurred since 1970 with two seminal works pioneered by Wulff and by Mosbach [3]. They proposed two different approaches in molecular imprinting, on one side Wulff reported a covalent imprinting method to obtain MIPs, on the other side, Mosbach described a non-covalent imprinting approach. The number of research articles concerning MIPs has rapidly increased since 2013 and to date, through a bibliometric analysis over time (1999-2022) by using the Scopus database, more than 10,000 papers have been published.

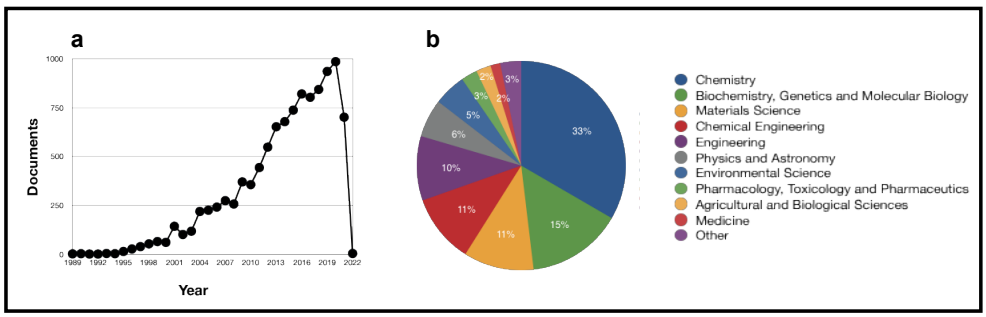

Fig. 1 (**a**) The annual (black dots) and cumulative (black line) numbers of research articles about molecularly imprinted polymers indexed in Scopus from 1989 until 2022; (**b**) cumulative numbers of research articles divided per subject area

As can be seen from Fig. 1, the molecular imprinting technique has attracted the attention of many scientists and has greatly diversified in terms of materials, templates' type used, and area of application.

As a whole, MIPs are excellent versatile tools in different research fields, including biosensing [14-21], separation science [22-23], biomedical diagnostics [24], environmental monitoring [25-28], pharmaceutical screening [29], drug delivery [30-31], and tissue engineering [32-35].

Regarding the healthcare field, MIPs are exploited to address both diagnostic and therapeutic challenges. The use of MIPs for *in vitro* diagnosis is based on

the detection and quantification of a certain measurable biomarker associated with biological state or (patho-) physiological condition. In this area, MIPs are ideal to set-up diagnostic assays onto solid-support or in solution or for pre-analytical uses, i.e., proteins enrichment or interferences removal, for example from complex biological samples (blood, plasma, serum). In addition, further efforts have been undertaken to design MIPs with *in vivo* therapeutic properties. This is one of the main tasks pursued in the field of nanomedicine which is an emerging and fast-growing area of application for MIPs. These antibody mimetics, usually in the form of spherical nanoparticles (namely nano-MIPs), are used as immune checkpoint inhibitors or as a drug delivery system [31] to a specific pathological site. In general, nano-MIPs act as a "dart" towards a pre-determined target, e.g., cancer cells [36].

The combination of diagnostic and therapeutic properties, namely theranostic, within a single MIP formulation, has recently started to be drawn [37]. In this regard, only a few examples are presented in the scientific literature, and it has not been the subject of interest of this experimental dissertation. A general synthetic receptor-analyte recognition mechanism is expressed by a reversible affinity reaction: [MIP] + [A] ↔ [MIPA], where [MIP] is the concentration/density of the surface MIP binding sites, [A] is the concentration of free analyte (g mol^{-1}) while [MIPA] is the complex concentration, so the concentration analyte which is bounded to the mimetic receptor, MIP. To evaluate the effectiveness of the mimetic receptors in the analyte recognition analyte event and to evaluate their performances, three main parameters can be assessed [3]:

1) Binding affinity, which is expressed as dissociation equilibrium constant, K_D (mol L^{-1}) = [MIP][A]/[MIPA]. In this case, stronger binding corresponds to lower K_D;
2) Specificity, which is defined as the MIP's ability to bind only the analyte, without interferences due to other molecules;
3) Imprinting factor (IF), which is expressed as the ratio of the analyte-MIP vs. analyte-NIP (non-imprinted polymers) average binding response (IF = MIP/NIP) under identical conditions.

The NIP's surface is synthesized as a MIP receptor in absence of the template molecule [38-39].

The following paragraphs will briefly describe the rationale behind the MIPs, and the diverse imprinting strategies that have been employed for their preparation intended for *in vitro* and *in vivo* applications.

1.4 Fundamentals of designing molecularly imprinted polymers (MIPs)

Biomimetic thin films are frequently exploited in the field of diagnostics where different planar solid supports are involved, both in benchtop and in point of care diagnostic systems. Recent years have witnessed a significant progress in molecular imprinting technology which led to the expansion of the MIPs use to the burgeoning *in vivo* therapeutic areas. This technology-driven shift from film layer into nanostructures domain. In particular, spherical MIP nanoparticles (or nano-MIPs) have gained great attention because of their high surface-area-to volume ratio and handling ability [40]. Beyond the mimetics' format we are going to develop, the key issue in designing these types of mimetic receptors is the rational choice of template molecules. In the following sections, we deal with this issue by briefly describing the main imprinting strategies in relation to the chosen template.

1.5 An excursion into various molecular imprinting strategies

Relatively to the choice of the appropriate template to be involved in the imprinting process, a distinction must be made between biomolecules that differ greatly in size (across angstrom-to-micrometer length scales). The choice of the template from a small molecule is relatively a simple task due to the fact that, usually, it matches with the target itself (including toxins, antibiotics, molecular markers as peptides constituted by few amino acids, metal ions, etc. scheme 1); in other words, the whole target molecule is imprinted. Unlikely, the imprinting of large molecules (proteins,

glycoproteins, nucleic acids, cells, bacteria, viruses, etc.) is an intriguing and challenging task due to their large size, complexity, flexibility, and poor solubility in organic solvents [41].

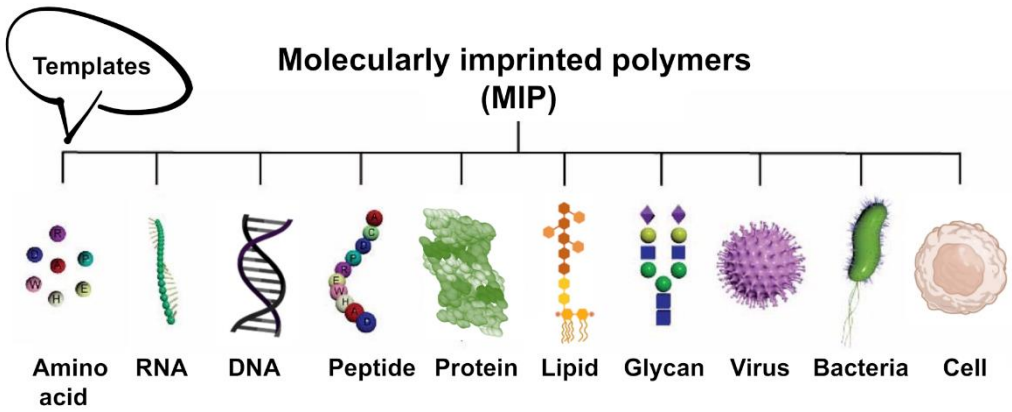

Scheme 1 Schematic depiction of the templates' panel, with a very different dimensions, that may be involved in the imprinting process

In this scenario, the following paragraphs are dedicated to providing an overview of the main existing molecular imprinting techniques including bulk imprinting, epitope imprinting, micro-contact imprinting, and oriented-surface/site-directed imprinting.

1.5.1 Bulk imprinting

By this type of approach, namely bulk imprinting (scheme 1.1), the target molecule is imprinted as a whole in the polymer matrix.

Bulk imprinting, at first glance, appears as the simplest approach to create template-shaped sites in the polymer network which can bind and release the target molecule. In a general process, the monomer and the template, possibly cross-linkers and initiators, if required in the type of polymerization pursued, are let to react to form a polymer matrix [42]. The functional groups of the monomers can non-covalently assemble (by involving weak interactions like hydrogen-bonds, ion pair interactions, Van der Waals forces, and dipole-dipole bonds) with the template molecule allowing its incorporation in the polymeric matrix during the synthesis. The template

molecules involved in the interaction are held in position by the highly crosslinked polymeric network formed around. The number of non-covalent interactions must be sufficient to allow the *stochastic* organization of the binding pockets during the polymerization reaction. This approach is extremely useful to imprint small molecules (molecular weight, MW, less than 1000-1300 Da), both inorganic and/or organic, while it is still challenging with biomacromolecules due to their huge dimension, complex spatial structure, unstable (variable) conformation of the template [43], and environmental depended conformation. Accordingly, recently, significant progress has been reached in this direction in order to solve difficulties associated with large biomolecules imprinting, in particular, their poor compatibility with the organic environment, template leakage (loss of conformational epitope) upon unfolding of the tertiary and quaternary structure [41], high cost of template molecules, and scarce removal efficacy of the template entrapped in the polymer network.

So, are the biomolecules too large to fit in polymer networks?

To troubleshoot this challenging issue, other approaches have been established such as epitope-mediated imprinting, oriented surface imprinting, and micro-contact imprinting.

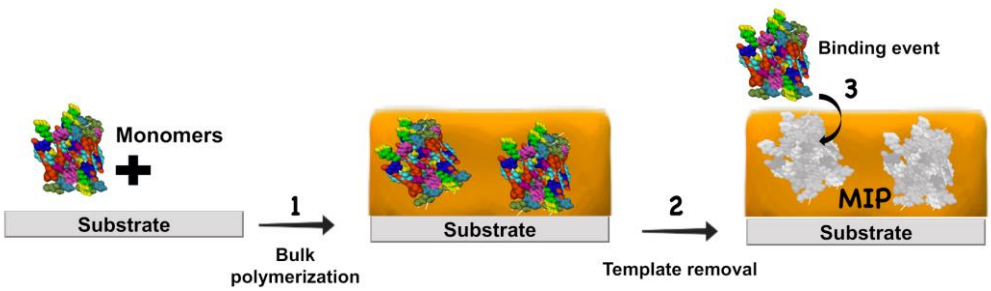

Scheme 1.1 Schematic illustration of bulk imprinting

1.5.2 Epitope-mediated imprinting

The epitope approach (or fingerprint imprinting (FIP, scheme 1.2)) [44-49] is one of the most promising imprinting techniques for MIPs production which was firstly introduced by Rachkov and Minoura [50]. It is based on the use of a short "fingerprint" synthetic peptide (few amino acids 10-15 are rationally selected), as a template, that constitutes only a small portion of the large macromolecule to which belongs, and that, in turn, may be recognized by the MIP. This technique allows to achieve unexpected advancements in the recognition of large biomolecules, by mimicking the efficacy of the natural binding of antibodies. In detail, it mimics the natural antibody-antigen recognition, in which the paratope on the antibody, *i.e.*, the antigen-binding site, recognizes and interacts with the antigen determinant (the epitope) through affinity binding to trigger an immune response. The same epitope, if known, can be eventually exploited for diagnostic purposes i.e., detecting the presence/absence of the analyte by affinity-based assays. In Nature, epitopes of few amino acid residues (less than ten) are able, alone, to evoke highly specific recognition by antibodies.

To translate the 'epitope approach' to MIPs production, the first phase is to perform a modelling of the target biomolecule structure by using bioinformatic tools. Free computational approaches are employed to bridge the gap between the known analyte sequence and the 3D structure, even if this approach is limited to sequences available as X-ray structures and deposited in the Protein Data Bank (PDB) [51]. In this way, it is possible to evaluate potential peptide templates for polymer imprinting by selecting well-exposed and flexible portions. For example, the external portion of a loop region, in the 3D biomolecule structure, likewise to the specific portion/s of the antigen (epitope) to which an antibody paratope may bind (known structural epitopes from the literature), define possible portions (peptides) to be selected. Bioinformatics software may be also worthwhile to perform multiple sequence alignment, in order to identify unique epitopes over a protein family and/or isoforms (e.g., mutation involving the SARS-CoV-2 spike variants, glycoprotein hormones, IgG subclasses, etc.,). Similarly, also

the portion of amino acid sequences, which are preserved among the families, may be selected if the receptor is designed to bind a whole family/class of molecules. Moreover, a multiple template approach may be used in two different modalities. In the first case, more than one epitope can be selected from the same macromolecule, and in this scenario arose the concept of cooperative binding. The epitopes cooperation may be advantageous to better anchor the target biomolecule to be determined, but also it can help to bind the target with a certain structural orientation, eventually increasing the binding affinity (expressed as equilibrium dissociation constant). In the second case, two or more epitopes may also belong to different molecules or close molecule analogues and this selection may be very interesting for a multi-analyte determination on the MIPs cavities.

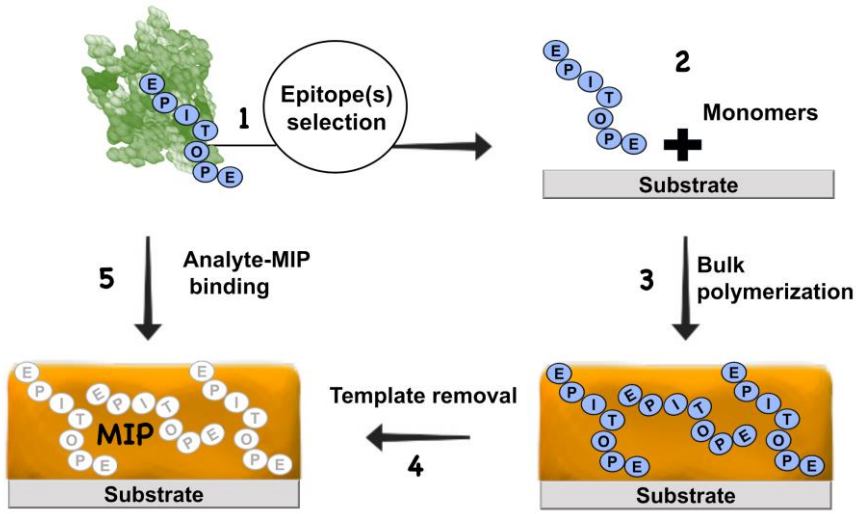

Scheme 1.2 Schematic illustration of epitope-mediated imprinting

1.5.3 Oriented-surface imprinting

An alternative strategy to bulk and epitope polymerization provides the chemical orientation of the template molecule over a functionalized substrate to build the mimetic receptor. In this case, also whole molecules can be successfully imprinted via the creation of reversible strong non-covalent or covalent interactions between key functional groups of the template/target and solid support, modified with appropriate chemistry [41]. Then, the polymerization was carried out around the template, as in the previous cases, but here the attention must be paid to the growth of the polymeric film, not above the diameter of the immobilized biomolecule. If the film grows above the diameter, the extraction of the templates from the polymer matrix is complicated, as already faced in bulk polymerization. After the polymerization, the bonds between the template and the substrate are cleaved. The functional groups are renewed to allow them to make the same covalent interactions with the target molecule in the obtained binding cavities of the polymer. Wulff et al. [52] introduced the first covalent imprinting by using boronic acid which is well known for its ability to reversibly interact with the diol groups found in sugars, glycoproteins, and catecholamines [53-54] (scheme 1.3). Besides boronic acid, the most common functionalities involved in this process are aldehyde, diols, or amine groups. This approach requires a deep *a priori* knowledge about the dimension and the functional groups of the template and the polymer film thickness. For this reason, it is not an approach that can be easily pursued for the imprinting of all molecules.

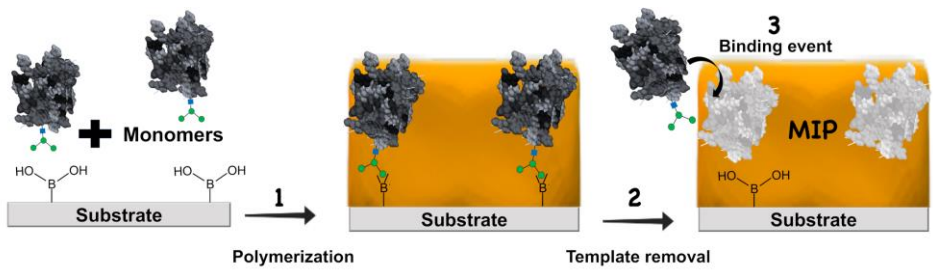

Scheme 1.3 Schematic illustration of oriented-surface imprinting

1.5.4 Micro-contact imprinting

Finally, the last imprinting technique onto a solid substrate, namely micro-contact imprinting (scheme 1.4), is described here. This is an encouraging technique, which shares some similarities with soft phototypography, also because a variety of substrate materials, both hydrophilic and hydrophobic, can be printed [55]. It is successfully adopted to create MIPs for biomolecules; actually, it overcomes some challenges associated with the bulk imprinting (e.g., solubility, conformational stability, and aggregation during the polymerization reaction) [41]. In a typical procedure, a template or a pattern of template molecules for inking, are primarily immobilized or absorbed onto a solid support (such as glass or PDMS slabs), that act/s as an imprinting mask to create the MIP cavities. Then, the mask is placed in micro-contact and softly pressed, for a certain period of time, over the functional monomer solution, undergoing polymerization [55-56]. The imprinted receptor is ready for use after detaching off the mask, to extract the template molecules.

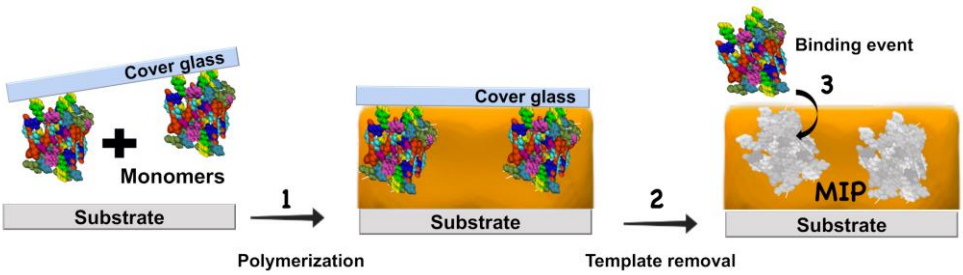

Scheme 1.4 Schematic representation of micro-contact imprinting

1.6 Building blocks that make up polymers: from *hard* to *soft*

Many examples of scaffolds may be used to create polymeric mimetic receptors, MIPs. There are multiple synthetic building blocks to develop classic polymers, like polyester or nylon, polyethylene, and polyvinylchloride, and can be assembled by different polymerization reactions. For example, polyesters may be assembled using a step-growth condensation reaction that takes place between the monomers and forms linking ester groups [57]. Among these, there are polyethylene terephthalate (PET) [58] produced by ethylene glycol and terephthalic acid, as building blocks, polybutylene terephthalate (PBT) produced by polybutylene pipe, and polycarbonate (PC) produced by bisphenol A reacting with phosgene. Other synthetic polymers, such as polypropylene are produced by polymerization catalysts and among these, we can report the example of poly(propylene carbonate) (PPC) which is made from polypropylene oxide, as a building block, that reacts with carbon dioxide in a catalytic process.

Poly(vinyl chloride)-based polymers (PVC) are another class widely produced by employing vinyl chloride monomer (VCM), while polyaryletherketone-based (PAEK) ones are composed of bis(phenolate) salts as functional monomers [59]. Nowadays, the research for new materials is increasingly moving toward greener, soft, and sustainable polymer syntheses involving building blocks coming from Nature. In the following chapter (Chapter 2) the state-of-the-art on biopolymers is briefly reviewed and, among them, a special focus primarily on the poly(catecholamines) is reported. Besides, an interesting and still poorly explored field is the use of natural ingredients as building blocks for MIPs creation, which can be assembled by living organisms to build mimetic receptors.

References

1. Lurie-Luke E. Product and technology innovation: What can biomimicry inspire? Biotechnol Adv. 2014; https://doi.org/10.1016/j.biotechadv.2014.10.002
2. Moreno-Bondi MC, Benito-Peña E. Analytical applications of biomimetic recognition elements — an update. Anal Bioanal Chem. 2021; https://doi.org/10.1007/s00216-021-03534-x
3. Haupt K, Rangel PXM, Bui. BTS. Molecularly Imprinted Polymers: Antibody Mimics for Bioimaging and Therapy. Chem Rev. 2020; https://dx.doi.org/10.1021/acs.chemrev.0c00428
4. Bonatti AF, De Maria C, Vozzi G. Molecular imprinting strategies for tissue engineering applications: A review. Polymers 2021; https://doi.org/ 10.3390/polym13040548
5. Pasquardini L, Bossi AM. Molecularly imprinted polymers by epitope imprinting: a journey from molecular interactions to the available bioinformatics resources to scout for epitope templates. Anal Bioanal Chem. 2021; https://doi.org/10.1007/s00216-021-03409-1
6. Laustsen AH, María Gutiérrez J, Knudsen C, Johansen KH, Bermúdez-Méndez E, Cerni FA, Jürgensen JA, Ledsgaard L, Martos-Esteban A, Øhlenschlæger M, Pus U, Andersen MR, Lomonte B, Engmark M, Pucca MB. Pros and cons of different therapeutic antibody formats for recombinant antivenom development. Toxicon 2018; https://doi.org/https://doi.org/10.1016/j.toxicon.2018.03.004
7. Chen L, Wang X, Lu W, Wu X, Li J. Molecular imprinting: perspectives and applications. Chem Soc Rev. 2016; https://doi.org/10.1039/C6CS00061D
8. Belbruno JJ. Molecularly Imprinted Polymers. Chem Rev. 2019; https://doi.org/10.1021/acs.chemrev.8b00171
9. Takeuchi T, Sunayama H. Beyond natural antibodies – a new generation of synthetic antibodies created by post-imprinting modification of molecularly imprinted polymers. Chem Commun. 2018; https://doi.org/10.1039/C8CC02923G
10. Lamaoui A, Palacios-Santander JM, Amine A, Cubillana-Aguilera L. Molecularly imprinted polymers based on polydopamine: Assessment of non-specific adsorption. Microchem J. 2021; https://doi.org/10.1016/j.microc
11. Cui B, Liu P, Liu X, Liu S, Zhang Z. Molecularly imprinted polymers for electrochemical detection and analysis: progress and perspectives. J Mater res technol. 2020; https://doi.org/10.1016/j.jmrt.2020.08.052

12. Pauling L, Campbell DH. The manufacture of antibodies in vitro. J Exp Med. 1942; https://doi.org/10.1084/jem.76.2.211
13. Takeuchi T, Sunayama H. Molecularly imprinted polymers. Encyclopedia of Polymeric Nanomaterials 2014; https://doi.org/10.1007/978-3-642-36199-9_126-1
14. Baldoneschi V, Palladino P, Banchini M, Minunni M, Scarano S. Norepinephrine as new functional monomer for molecular imprinting: an applicative study for the optical sensing of cardiac biomarkers. Biosens. Bioelectron. 2020; https://doi.org/10.1016/j.bios.2020.112161
15. Chen B, Zhang Y, Lin L, Chen H, Zhao M. Au nanoparticles @metal organic framework/polythionine loaded with molecularly imprinted polymer sensor: Preparation, characterization, and electrochemical detection of tyrosine. J. Electroanal. Chem. 2021; https://doi.org/10.1016/j.jelechem.2020.114052
16. Cui F, Zhou Z, Zhou HS. Molecularly imprinted polymers and surface imprinted polymers based electrochemical biosensor for infectious diseases. Sensors 2020; https://doi.org/10.3390/s20040996
17. Lee M-H, Thomas JL, Su Z-L, Zhang Z-X, Lin C-Y, Huang Y-S, Yang C-H, Lin H-Y. Doping of transition metal dichalcogenides in molecularly imprinted conductive polymers for the ultrasensitive determination of 17β-estradiol in eel serum. Biosens. Bioelectron. 2020; https://doi.org/10.1016/j.bios.2019.111901
18. Liu J, Wang T, Liu X, Yuan Q, Zhang Y, Li Y. Novel molecularly imprinted polymer [MIP] multiple sensors for endogenous redox couples determination and their applications in lung cancer diagnosis. Talanta 2019; https://doi.org/10.1016/j.talanta.2019.03.018
19. Palladino P, Minunni M, Scarano S. Cardiac Troponin T capture and detection in real-time via epitope-imprinted polymer and optical biosensing. Biosens. Bioelectron. 2018; https://doi.org/10.1016/j.bios.2018.01.068
20. Turco A. Preparation and characterization of molecularly imprinted mussel inspired film as antifouling and selective layer for electrochemical detection of sulfamethoxazole, Sensor Actuat. B-Chem. 2018; https://doi.org/10.1016/j.snb.2017.09.164
21. Zhao W, Yang H, Xu S, Cai J, Luo J, Wei W, Liu X, Zhu Y. Preparation of molecularly imprinted polymer/Au nanohybrids as an effective biosensing material, Colloids Surf. A. 2018; https://doi.org/10.1016/j.colsurfa.2018.06.054

22. Baimani N, Azar PA, Husain SW, Panahi HA, Mehramizi A. Ultrasensitive separation of methylprednisolone acetate using a photoresponsive molecularly imprinted polymer incorporated polyester dendrimer based on magnetic nanoparticles. J. Sep. Sci. 2019; https://doi.org//10.1002/jssc.201801093
23. Middeleer GD, Dubruel P, Saeger SD. Molecularly imprinted polymers immobilized on 3D printed scaffolds as novel solid phase extraction sorbent for metergoline. Anal. Chim. Acta 2017; https://doi.org/10.1016/j.aca.2017.07.059
24. Lieberzeit PA, Chunta S, Navakul K, Sangma C, Jungmann C. Molecularly imprinted polymers for diagnostics: sensing high density lipoprotein and dengue virus. Procedia 2016; https://doi.org/10.1016/j.proeng.2016.11.157
25. Altintas Z, Gittens M, Guerreiro A, Thompson K-A, Walker J, Piletsky S, Tothill IE. Detection of waterborne viruses using high affinity molecularly Imprinted polymers, Anal. Chem. 2015; https://doi.org/10.1021/acs.analchem.5b00989
26. Azizi A, Bottaro CS. A critical review of molecularly imprinted polymers for the analysis of organic pollutants in environmental water samples. J. Chromatogr. 2020; https://doi.org/10.1016/j.chroma.2019.460603
27. Fan Y, Zeng G, Ma X. Multi-templates surface molecularly imprinted polymer for rapid separation and analysis of quinolones in water. Environ. Sci. Pollut. Res. Int. 2020; https://doi.org/10.1007/s11356-019-07437-4
28. Yin J, Meng Z, Du M, Liu C, Song M, Wang H. Pseudo-template molecularly imprinted polymer for selective screening of trace β-lactam antibiotics in river and tap water. J. Chromatogr. A 2010; https://doi.org/10.1016/j.chroma.2010.06.044
29. Xiao D, Jiang Y, Bi Y. Molecularly imprinted polymers for the detection of illegal drugs and additives: a review, Microchim. Acta 2018; https://doi.org/10.1007/s00604-018-2735-4
30. Bodoki AE, Iacob B-C, Bodoki E. Perspectives of molecularly imprinted polymer-based drug delivery systems in cancer therapy, Polymers 2019; https://doi.org/10.3390/polym11122085
31. Zaidi SA. Molecular imprinting: A useful approach for drug delivery. Mater. Sci. Technol. 2020; https://doi.org/10.1016/j.mset.2019.10.012
32. Boysen RI, Advances in the development of molecularly imprinted polymers for the separation and analysis of proteins with liquid chromatography. J. Sep. Sci. 2018; https://doi.org/10.1002/jssc.201800945

33. Haupt K, Molecularly Imprinted Polymers: The Next Generation, Anal. Chem. 2003; https://doi.org/10.1021/ac031385h
34. Liu J, Deng Q, Tao D, Yang K, Zahng L, Liang Z, Zhang Y. Preparation of protein imprinted materials by hierarchical imprinting techniques and application in selective depletion of albumin from human serum. Sci. Rep. 2014; https://doi.org/10.1038/srep05487
35. Neves MI, Wechsler ME, Gomes ME, Reis RL, Granja PL, Peppas NA. Molecularly imprinted intelligent scaffolds for tissue engineering applications. Tissue Eng. Part B Rev. 2017; https://doi.org/10.1089/ten.TEB.2016.0202
36. Bossi AM. Plastic antibodies for cancer therapy? Nat Chem. 2020; https://doi.org/10.1038/s41557-019-0415-6
37. Parisi OI, Ruffo M, Malivindi R, Vattimo AF, Pezzi V, Puoci F. Molecularly Imprinted Polymers (MIPs) as Theranostic Systems for Sunitinib Controlled Release and Self-Monitoring in Cancer Therapy. Pharmaceutics. 2020; https://doi.org/10.3390/pharmaceutics12010041
38. Curk Tine, Dobnikar Jure, Frenkel D. Rational design of molecularly imprinted polymers. Soft Matter 2016; https://doi.org/10.1039/C5SM02144H
39. Pardeshi S, Patrikar R, Dhodapkar R, Kumar A. Validation of computational approach to study monomer selectivity toward the template gallic acid for rational molecularly imprinted polymer design. J Mol Model. 2012; https://doi.org/10.1007/s00894-012-1481-5
40. Zhang H, Molecularly Imprinted Nanoparticles for Biomedical Applications. Adv Mater 32. 2020. https://doi.org/10.1002/adma.201806328
41. Refaat D, Aggour MG, Farghali AA, Mahajan R.; Wiklander JG.; Nicholls IA.; Piletsky SA. Strategies for Molecular Imprinting and the Evolution of MIP Nanoparticles as Plastic Antibodies—Synthesis and Applications. Int. J. Mol. Sci. 2019; https://doi.org/10.3390/ijms20246304
42. Dong C, Shi H, Han Y, Yang Y, Wang R, Men J. Molecularly imprinted polymers by the surface imprinting technique. 2021; https://doi.org/10.1016/j.eurpolymj.2020.110231
43. Chen W, Fu M, Zhu X, Liu Q. Protein recognition by polydopamine-based molecularly imprinted hollow spheres. Biosens Bioelectron. 2019; https://doi.org/10.1016/j.bios.2019.111492
44. Bossi AM, Sharma PS, Montana L, Zoccatelli G, Laub O. Fingerprint-imprinted polymer: rational selection of peptide epitope templates for the determination of

proteins by molecularly imprinted polymers, Anal. Chem. 2012; https://doi.org/10.1021/ac203422r

45. Chen L, Wang X, Lu W, Wu X, Li J. Molecular imprinting: perspectives and applications. Chem. Soc. Rev. 2016; https://doi.org/10.1039/C6CS00061D
46. Li D-H, Zhang X-M, Yan Y-J, He X-W, Li W-Y. Thermo-sensitive imprinted polymer embedded carbon dots using epitope approach. Biosens. Bioelectron. 2016; httpss://doi.org/10.1016/j.bios.2015.12.016
47. Nishino H, Huang C-S, Shea KJ. Selective protein capture by epitope imprinting. Angew. Chem. 2006; https://doi.org/10.1002/anie.200503760
48. Vaneckova T, Bezdekova J, Hanc G, Adama V, Vaculovicova M. Application of molecularly imprinted polymers as artificial receptors for imaging. Acta. Biomater. 2020; https://doi.org/10.1016/j.actbio.2019.11.007
49. Whitcombe MJ, Chianella I, Larcombe L, Piletsky SA, Noble J, Porter R, Horgan A, The rational development of molecularly imprinted polymer-based sensors for protein detection. Chem. Soc. Rev. 2011; https://doi.org/10.1039/C0CS00049C
50. Rachkov A, Minoura N. Towards molecularly imprinted polymers selective to peptides and proteins. The epitope approach. Biochim Biophys Acta. 2001 https://doi.org/10.1016/s0167-4838(00)00226-0
51. Fiser A. Template-Based Protein Structure Modeling. In: Fenyö D. (eds) Computational Biology. Methods in Molecular Biology (Methods and Protocols), 2010. Humana Press, Totowa, NJ. https://doi.org/10.1007/978-1-60761-842-3_6
52. Ulubayram K. Molecularly Imprinted Polymers. In: Hasirci N., Hasirci V. (eds) Biomaterials. Advances in Experimental Medicine and Biology, 2004. Springer, Boston, MA. https://doi.org/10.1007/978-0-306-48584-8_10
53. Ptak T, Młynarz P, Dobosz A, Rydzewska A, Prokopowicz M. Potentiometric and NMR complexation studies of phenylboronic acid PBA and its aminophosphonate analog with selected catecholamines. J Mol Struct 2013; https://doi.org/10.1016/j.molstruc.2013.02.013
54. Hongyi Liu, Wanwan Shen, Bonan Li, Tianfu Li, Hong Chang, and Yiyun Cheng. Natural Polyphenols Augment Cytosolic Protein Delivery by a Functional Polymer. Chemistry of Materials 2019; https://doi.org/10.1021/acs.chemmater.8b04672
55. Pan J, Chen W, Mab Y, Pan G. Molecularly imprinted polymers as receptor mimics for selective cell recognition. Chem Soc Rev. 2018; https://doi.org/10.1039/C7CS00854F

56. Prasad BB, Singh R. A new micro-contact imprinted l-cysteine sensor based on sol–gel decorated graphite/multiwalled carbon nanotubes/gold nanoparticles composite modified sandpaper electrode. Sens Actuators B Chem. 2015; https://doi.org/10.1016/j.snb.2015.01.119
57. Chandru K, Mamajanov I, James CH, Jia TZ. Polyesters as a Model System for Building Primitive Biologies from Non-Biological Prebiotic Chemistry. 2020; https://doi.org/10.3390/life10010006
58. Yang W, Liu R, Li C, Song Y, Hu C. Hydrolysis of waste polyethylene terephthalate catalyzed by easily recyclable terephthalic acid. Waste Manag. 2021; https://doi.org/10.1016/j.wasman.2021.09.009
59. Ishikawa J, Fujiyama S, Inoue K, Omi T, Tamai S. Highly sulfonated poly(aryl ether ketone) block coplymers having a cross-linking structure. J Memb Sci 2007; https://doi.org/10.1016/j.memsci.2007.03.057

CHAPTER 2

Catechol-derived imprinted biopolymers: recent advances and challenges for diagnostic and therapeutic applications

Nowadays green (environmentally friendly) and biocompatible materials which also possess bioactive potentialities, are desirable for all *in vitro* diagnostic and *in vivo* biomedical applications. For this purpose, the relentless research, throughout history, for new materials has pushed in the direction of naturally bio-inspired polymers [1] which not only challenged the traditional materials but also contributed to extend the range of their applicability. In the past decades, the research on biomaterials (biopolymers, scheme 2.1) expressing useful chemical/physical/biological properties extensively blossomed, gaining inspiration from the biological architectures of living organisms. Thus, looking at the surrounding natural resources, by mimicking their architecture and/or their building blocks by re-using some of the discarded sources, several functional biomaterials can be identified and implemented [2].

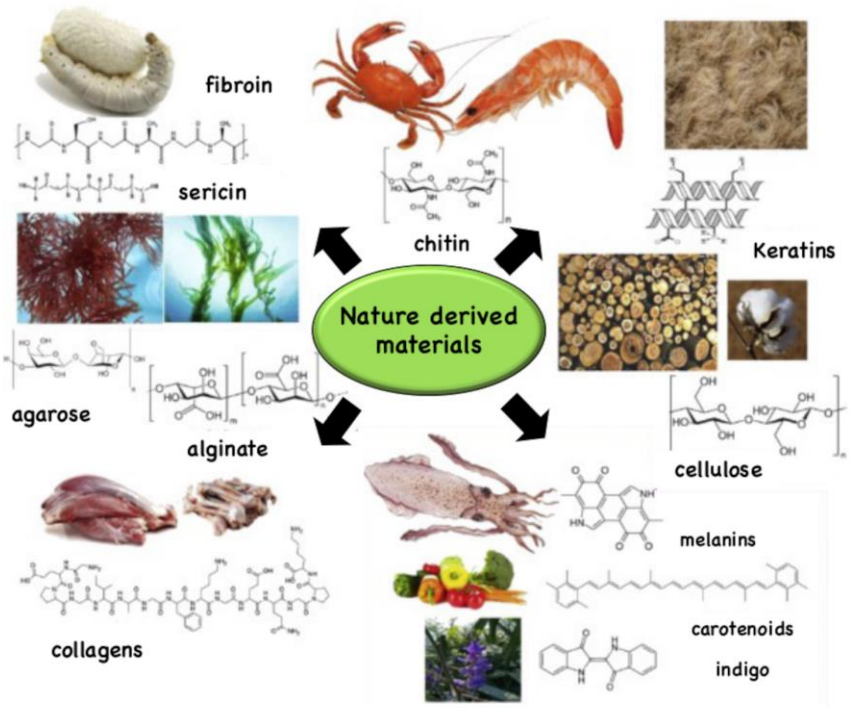

Scheme 2.1 Overview of few nature-derived materials (reproduced from ref. [5])

Additionally, green, and straightforward production strategies have been employed to design tailored biomaterials with finely tuned unique properties. Natural polyphenols, relevant to numerous compounds derived from plants (e.g., tea polyphenols, tannin and lignans, melanin-related phenolic polymers [3-4]), protein-based polymers (elastin-like polypeptides (ELPs), collagen, gelatin) and polysaccharide derivatives, etc. (alginates, dextrin, gelatin, casein, starches [6] and chitosan) [1,5] are examples of sustainable biopolymers present in the literature. All of these materials retain peculiar and tunable properties that may be exploited for a multitude of applications (bioanalysis, biomedicine, bioengineering, etc.). A new biopolymer inspired by mussels was presented by PB. Messersmith et al. in 2007 [7] and in a short time it turned one of the most promising biomaterials, opening the way to modifying various substrates and much more. In this scenario, the

following sections provide a comprehensive overview of poly(catecholamines) (pCA) family starting from polydopamine (PDA), considered the leading material, up to analogues, e.g., poly-norepinephrine (PNE), -epinephrine (PEP), -levodopa (pLD) [8]. From a structural point of view, all of these molecules derive from phenylalanine and/or tyrosine [8–9]. In detail, the pertaining functional monomers are formed by a benzene ring with two ortho-hydroxyl groups, amine moieties, and a few distinct functional groups which provide biopolymers with their own features. Dopamine (DA), as well as norepinephrine (NE) are endogenous neurotransmitters that have an important role in the central nervous system's functions affecting motor control, cognition, emotion, memory processing, and endocrine modulation [10]. Among the pCA series, there are also polyserotonin (PSE) [11] and poly-octopamine (POA) which are very similar to the neurotransmitters (monomeric structures) listed above but differ from them due to the loss of a hydroxyl group from the catecholic functionality.

The following paragraph introduces the foremost physico-chemical and biological properties of PDA and PNE, which have been exploited for analytical chemical purposes aiming to design novel, sensitive, selective, and specific diagnostic strategies as well as to develop modern detection devices. We would like to underline that analytical chemistry (AC) has played a vital role in life sciences and has provided important support also for the development of material/energy/environmental/space sciences [12]. In addition, AC has increasingly addressed exciting challenges, currently boosting multidisciplinary investigations to implement frontier research from its very beginning. Following this path, Chapter 4 introduces some insights on the chemical physical characterization of biopolymers, dealing with recent advances and future perspectives.

2.1 Poly-dopamine (PDA) as "class leading" bio-inspired material – an overview

The discovery of PDA, currently one of the most widely employed bio-inspired soft materials for surface coating and functionalization, was presented by Messersmith and coworkers in 2007, replying to the following question: How can mussels, in wet conditions, cling to surfaces? [7] The secret lies in the mussels' plaque, composed by an abundance of adhesive mussel foot proteins (mfps) constituted, in turn, by a high percentage of 3,4-dihydroxyphenylalanine (L-DOPA), lysine and histidine residues (primary and secondary amines) [7,13-16]. The second route of PDA inspiration is related to the natural melanin (eumelanin), which is found in mammals' pigments of hair and skin, or in the substantia nigra (SN) of the midbrain [16-17]. In relation to this, the Messersmith group discovered that PDA can be used as a cheap and versatile alternative to dopa-enriched peptides [18-19]. From these sources of inspiration, dopamine (DA, 3,4-dihydroxyphenylethylamine), structurally close to L-DOPA [14], has been the first small-molecule catecholamine extensively exploited to modify countless solid substrates. This is a consequence of the excellent ability of PDA to strongly stick to all types of solid surfaces even in wet conditions, thanks to the catechol moieties assisted by amino groups [18, 20]. DA is easily oxidized to self-polymerize under alkaline aerobic conditions (pH > 7.5), which simulate the natural environment of mussels. For all of these features mentioned, PDA has been explored for an impressive plethora of applications (energy harvest, storage, separations, environmental remediation, healthcare, and biosensing) [16]. Further, despite the exciting properties of PDA and the numerous attempts to characterize it (through solid NMR, high-performance liquid chromatography (HPLC) mass spectrometry (MS), X-ray crystallography, FTIR spectroscopy, AFM, etc.), the exact mechanism of DA polymerization is still uncleared and debated. The pathway(s) of PDA formation start(s) by auto-oxidation of the catechol ring of DA leading to the production of dopamine-quinone (DAQ) followed by intramolecular cyclization

via 1,4 Michael-type addition to yield leuco-dopamine chrome (Fig. 2.2). Further oxidation and rearrangement formed the indole quinone units, 5,6-dihydroxyindole (DHI), which is easily oxidized to form 5,6-indolequinone (Fig. 3.1). The dihydroxyindole structure can form several tautomers [14,18,20-21]. All of these intermediates can be involved in the formation of a single C-C bond, the PDA central scaffold, in a random manner. Nonetheless, the latter reactions and the nature of such couplings remain unclear as well as the chemical structure of PDA.

A never-ending story? Liebscher *et al*. posed this question [22].

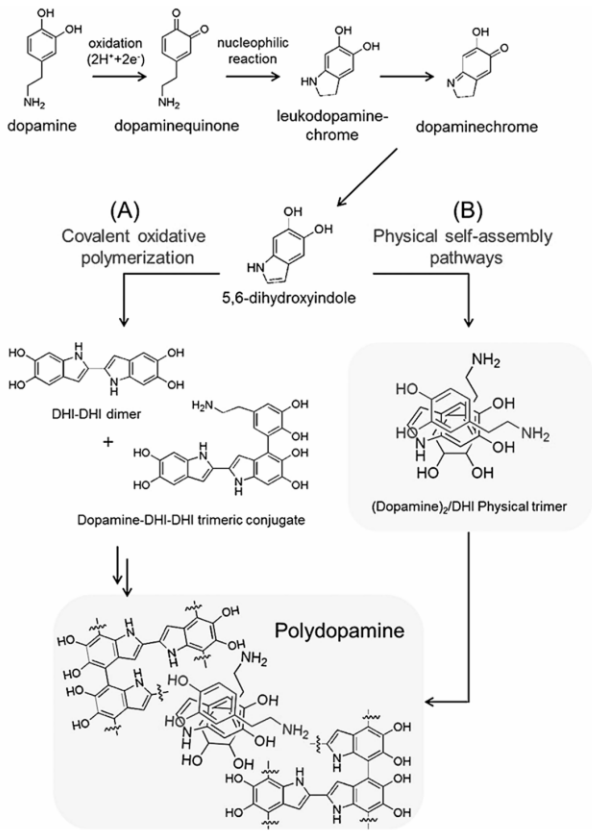

Fig. 2.2 Pathways process for the formation of PDA through (A) covalent bonds and *via* (B) physical self-assembly of dopamine and DHI. Adapted with permission from ref. [14] Copyright {2014} American Chemical Society

The most common hypothesis is that PDA is a supramolecular aggregate/mixture of monomeric and/or oligomeric species differing in chain length (composed of dihydroxyindoline, indolinedione, and dopamine units in diverse oxidative states [22]) that are held together through weak interactions (hydrogen bonding, charge transfer, π-π stacking interaction, π-cation assembly and/or quinhydrone-like interactions) [18]. The $(dopamine)^2$/DHI physical trimers, that can be formed, lead to the formation of a brown-black polydopamine precipitate. Delparastan et al. recently provided insights into the understanding of PDA polymeric nature [16] proposing an alternative pathway of reaction (covalent binding). Based on the results acquired via single-molecule force spectroscopy (SMFS) characterization, they provided structural information about PDA films constituted by high-molecular-weight polymer chains units whose subunits are covalently linked. As a whole, PDA is a dark-black solid polymer insoluble in most solvents, with an isoelectric point (pI) about 4 ± 0.2 [23]. When the pH < pI PDA possesses a total positive surface charge (protonated amino groups), whilst when pH > pI it has a negatively charged surface (deprotonated hydroxyl groups). It is optically characterized by a wide UV/Vis absorption extending from visible to near-infrared region (210-325 nm). In addition, under excitation with UV light, polydopamine exhibits a weak fluorescence, unlike DA, at 400-550 nm [24-25].

Concerning the PDA chemical reactivity, among the strong adhesion reactivity, due to the presence of various functional groups (amino imine and carboxylic groups, catechol or quinone functions, planar indole units, etc.) in the chemical structure. All of these groups are reactive starting points to trigger covalent or non-covalent modifications with different molecules. The reactivity is mainly related to the catechol/quinone chemical equilibrium; under basic conditions the catechol groups can be oxidized into the corresponding quinones, acting as electron acceptor sites, by transferring two electrons ($2e^-$) [18]. The cross-linking reaction of PDA with nucleophilic molecules, possessing amine and/or thiol groups, occurred via Michael-type addition and/or Schiff base reaction, as depicted in Fig. 2.3 [26-27].

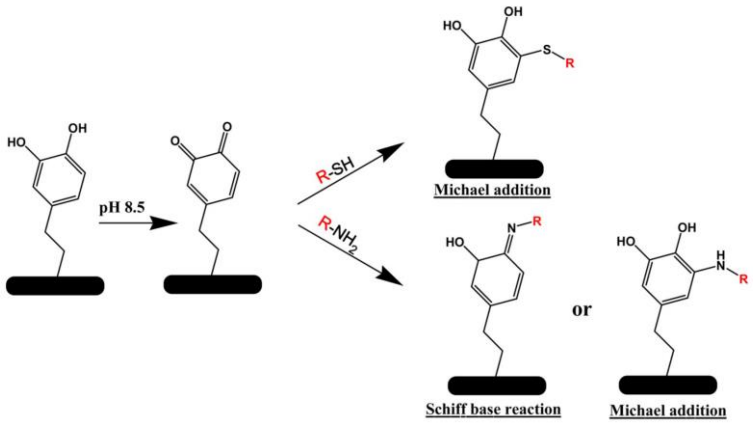

Fig. 2.3 Schematic illustration of Michael addition and Schiff base reactions, respectively, between amine- and/or thiol functional groups with reactive functionalities of PDA. Adapted with permission from ref. [16] Copyright {2016} American Chemical Society

Moreover, PDA can be also functionalized via the Aza-Michael addition reaction, occurring between nucleophilic amine groups and $\alpha,\beta-$ unsaturated carbonyl compounds [28], or exploiting the pH sensitive reactivity to form catechol-boronate esters [29-30]. Among these covalent reactions, other types of organic molecules can modify PDA surface also by establishing non-covalent interactions, for example, metal chelations, charge-transfer interactions, π−π stacking, and electrostatic interactions.

These reactivity features are extremely important to perform a multitude of secondary modifications with specific functionalities on PDA, including the anchoring of molecules or cells, etc., intensifying its application. Additionally, another valuable feature of PDA lies in the outstanding redox-activity, since catechol/o-quinone functional groups can be oxidized and reduced, respectively (redox potential = -530 mV) [31]. The PDA redox capability is mainly exploited toward the direct reduction of metal ions into nanoparticles in the fabrication of original organic-inorganic hybrid materials.

The formation of PDA films, on an endless surface type (organic and inorganic), with a thickness in the nanometer range, typically 1-50 nm [14], requires a variable period of time from minutes to hours. The monomer concentrations, type, and pH of the buffer (e.g. Tris, phosphate saline, sodium hydrogen carbonate, piperidine, etc. buffers), temperature or microwave irradiation, and nature of oxidants used (oxygen, NaOH, NH_3, H_2O_2, NaClO, metal ions, etc. [32-33]) are all key factors that affect the speed/time of polymerization and in particular the thickness of the deposited film that can be tuned to the specific desires/synthetic route. Complementarily to the classical synthesis method, it is also possible to produce PDA by means of an enzymatic oxidation process or through direct electropolymerization of DA [34-35]. In addition, it is important to note that the PDA anchoring process is effective at an early stage of the polymeric formation when aminoethyl groups are not cyclized yet. This is because when the indoles are formed, these are more reluctant to join supports [18]. Additionally, the multi-use of PDA is not restricted to surface coatings, but it is capable also to self-assemble into nanostructures or different architectures. For this reason, also considering the excellent biocompatibility, PDA is efficiently incorporated into a wide range of applications across the chemical, biological, medical, and materials sciences, as well as in applied science engineering.

In the analytical field, the main benefit gained from the employment of PDA comes from its exceptionally straightforward and versatile synthesis [36]. PDA has earned a prominent place in the scientific literature to easily modify bioactive surfaces and to develop bio-mimetic receptors, without the need for expensive equipment. The awesome growing broad applications of PDA, as attested by the enormous number of publications (more than 20,000 by Scopus search results), recorded from its first report, is not going to stop. This trend clearly reveals the global significance and the interest in PDA [14]. Concerning mimetics receptors (MIPs), more than 200 studies about the development of PDA-based MIPs selective for inorganic and organic molecules, are reported [36-41]. This universal interfacial bio-glue paved a

new way for the functionalization of biomaterials, significantly expanding its applicability to a plethora of support materials for (bio)analytical purposes, i.e. metals, semi-metals, glass, and silicon for biosensing; soft (e.g. polydimethylsiloxane, PDMS) and hard polymers used for disposable UV-Vis and fluorescent detection, included ELISA plates; cellulose paper for lateral flow assays (LFA) [42] and more. In light of the physicochemical properties described, our research group started working with PDA and developed several smart optical-based assays [43–46] and MIPs-based mimetic receptors for biosensing [18,47-49]. More recently, also polynorepinephrine (PNE), a close analogue of PDA, displayed very good analytical performances when exploited for MIPs synthesis, giving interesting and promising results [50–52]. In general, catecholamines-based MIPs, in this dissertation focusing mainly on PNE, are very attractive since their polymerization is obtained spontaneously and under mild aqueous conditions starting from the corresponding low-cost monomer, i.e., norepinephrine (NE), and can be performed in any laboratory as they do not require specific technology (being easy to operate) or expensive devices.

2.2 Poly-norepinephrine (PNE): challenge and opportunities

Norepinephrine (NE) is a close chemical analogue molecule of dopamine (DA) slightly differing for a supplementary aliphatic hydroxyl group from DA. Besides the physiological role as neurotransmitter, NE shares with DA the same capacity to self-polymerize, by inducing electrons transfer (2e-), and to stick to different surfaces [52-54]. Compared to PDA, which drew impressive researchers' attention, PNE currently has been neglected as underlined by the incidence of scarce studies in the literature that lacks insight into this analogue catecholamine, as pointed out by Baldoneschi et al. [52-53].

Prompted by this, besides DA studies [55,36,43-46], our research group recently started to explore the potential of this close homologue monomer in

the analytical field, mainly for mimetics receptors building for further application in bioassays.

In this section, we provide an overview about the unique key features (properties and polymerization mechanism process) proper of PNE, mainly related to the incorporation of an additional anchoring site -OH, as the other chemical-physical features remain basically similar to PDA (described in paragraph 2.1). We focus mainly on its potential development in bioanalysis and biomedicine, including the most recent studies. From the structural point of view, NE and DA, both being endogenous molecules, differ only for a supplementary hydroxyl group in NE. These catecholamine functional monomers share the impressive capability to self-polymerize in "green" mild alkaline environment, without the use of hazardous solvents, leading to highly adhesive pCA nanolayers or nanoparticles [9,57-64].

On the other hand, PNE displays a markedly more hydrophilic trait as well as more homogenous and smoother surfaces [63-64], by shrinking surfaces' roughness typical of PDA, which represent one of the drawbacking features for its use in MIP-based diagnostic assays. The formation of a smoother and more homogenous PNE surface is related to the presence of a reaction intermediate 3,4-dihydroxybenzaldehyde norepinephrine (DHBA-NE), not present in the PDA formation mechanism (Fig. 2.4).

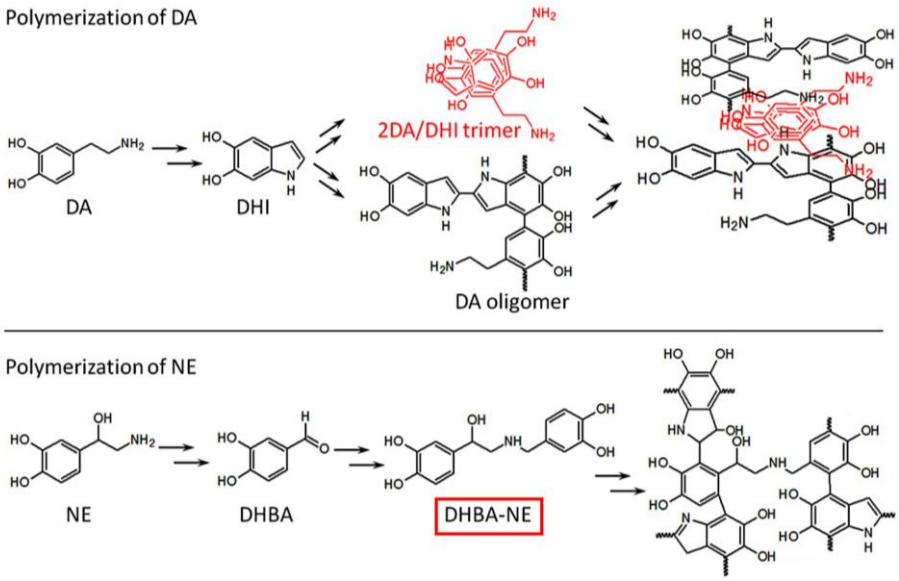

Fig. 2.4 Schematic PDA and PNE polymerization mechanisms. Adapted with permission from ref. [9] Copyright {2018} American Chemical Society

Among a few examples of PNE applications in materials science, PNE has been revealed as a powerful tool in medicine and (bio)-analytical field, although currently, research studies reported are limited. The interest for PNE in the (bio)analytical field is mainly centered on separation science for the elution of molecules [53]; in turn, the applications in bioanalysis/biosensing are limited to a few examples.

Considering the urgent need for alternatives to antibodies production and use for diagnostics, we believe that PNE deserves much more attention, as it could be an innovative and performing functional monomer alternative to DA to build improved natural mimetic receptors. As previously demonstrated for PDA, PNE can be exploited in affinity sensing as well as in bioanalytical assays (e.g., ELISA-like), thanks to the extremely low-cost of the starting monomer and the long-term stability features. In the analytical panorama, the first examples of PNE-based receptors were employed in separation science to wrap capillary columns or microchips for electrophoresis and electrochromatography to separate chiral molecules, amino acids and

proteins, or to extract a specific class of pharmaceuticals [58,63,65-68]. Differently, here we present the innovative exploitation of PNE for mimetic receptors production, an appealing alternative beyond antibodies for diagnostics. In this context, we used the advantages of PNE, compared to the leading PDA, in terms of superior hydrophilicity, which drastically contributes to the reduction of non-specific adsorption of molecules on the polymeric surface, increasing the selectivity of the imprinted biopolymers (IBPs), as demonstrated by our group in the first examples [50-51,69].

The first studies performed by Baldoneschi [51] et al., and Battaglia et al. [69], as well as those here presented and further detailed [50], involved the use of pioneering PNE-based mimetic receptors, integrated into an optical biosensor based on a surface plasmon resonance (SPR) transduction, to address different diagnostic issues (see paragraph 3.5.3.1).

The first example introduced a PNE-based epitope imprinting approach (EIA) (detailed in paragraph 1.5.2) in which a small portion of cardiac Troponin I (cTnI) was rationally selected as an epitope for acute myocardial infarction diagnosis [51]. Conversely, the second study successfully involved the whole canine/equine procalcitonin imprinting, as sepsis biomarker [69]. These first mimetic receptors showed high recognition ability, high stability, good repeatability, and sensitivity in real untreated matrices. Due to the successful outcomes recorded so far, now our work is moving beyond bench to prove that, in addition, to being effective when coupled to the SPR biosensor, these new generations of IBPs are suitable for replacing antibodies even on widely used platforms i.e., 96-well plates for ELISA readers. In this context, it appears a fundamental task to take a leap forward, as an outlook on the future investigation, in a deeper understanding of the actual potential of the imprinting technology. Accordingly, we propose two major research paths to track for the expansion of PNE and pCA analogues (i.e., PSE, POA, etc.). On one hand, one of the issues to address is which type of template, generally one or more peptides, must be chosen to succeed in having specific and high affinity IPBs. We observed that PNE (but also other pCAs) shows a marked predilection to efficiently incorporate some peptide templates into the

polymeric network to generate recognition cavities. Contrarily, other peptides failed in being included into the polymeric matrix thus being able to be excluded *a priori* as imprinting epitopes. On the other hand, it is important to establish new insights into the chemical/physical characterization of polymer matrix-template interaction and the surface density distribution of recognition cavities on the surface of the IBP. This latter task is extremely challenging due to the dimension of peptides which require a sub-ångström (Å) resolution.

References

1. Perera AS, Coppens M-O. Re-designing materials for biomedical applications: from biomimicry to nature-inspired chemical engineering. Philos Trans A. 2018; https://doi.org/10.1098/rsta.2018.0268
2. Suarato G, Bertorelli R, Athanassiou A. Borrowing from nature: biopolymers and biocomposites as smart wound care materials. Front Bioeng Biotechnol. 2018; https://doi.org/10.3389/fbioe.2018.00137
3. Solano F. Melanin and melanin-related polymers as materials with biomedical and biotechnological applications—cuttlefish ink and mussel foot. Int J Mol Sci. 2017; https://10.3390/ijms18071561è
4. Yang P, Zhou X, Zhang J, Zhong J, Zhu F, Liu X, Gu Z, Li Y. Natural polyphenol fluorescent polymer dots. Green Chem. 2021; https://doi.org/10.1039/d0gc02824
5. Pradhan S, Brooks AK, Yadavalli VK. Nature-derived materials for the fabrication of functional biodevices. Mater Today Bio. 2020; https://doi.org/10.1016/j.mtbio.2020.10
6. Maiti B, Abramov A, Finn MG, Díaz DD. Biopolymers as sustainable metal bio-adhesives. J Appl Polym Sci. 2021; https://doi.org/10.1002/app.49783
7. Lee H, Dellatore SM, Miller WM, Messersmith PB. Mussel-inspired surface chemistry for multifunctional coatings. Science 2007; https://doi.org/ 10.1126/science.1147241
8. Tan X, Gao P, Li Y, Qi P, Liu J, Shen R, Wang L, Huang N, Xiong K, Tian W, Tu Q. Poly-dopamine, poly-levodopa, and poly-norepinephrine coatings: Comparison of physico-chemical and biological properties with focus on the application for blood-

contacting devices. Bioact Mater. 2021; https://doi.org/10.1016/j.bioactmat.2020.06.024

9. Iwasaki T, Tamai Y, Yamamoto M, Taniguchi T, Kishikawa K, Kohri M. Melanin Precursor Influence on Structural Colors from Artificial Melanin Particles: PolyDOPA, Polydopamine, and Polynorepinephrine. Langmuir 2018; https://doi.org/10.1021/acs.langmuir.8b02444
10. Kobayashi K, Role of catecholamine signaling in brain and nervous system functions: new insights from mouse olecular genetic gtudy. J Investig Dermatol Symp. 2001; https://doi.org/10.1046/j.0022-202x.2001.00011.x
11. Nakatsuka N, Hasani-Sadrabadi MM, Cheung KM, Young TD, Bahlakeh G, Moshaverinia A, Weiss PS, Andrews AM. Polyserotonin Nanoparticles as Multifunctional Materials for Biomedical Applications. ACS Nano 2018; https://doi.org/10.1021/acsnano.8b01470
12. Ju H. Grand challenges in analytical chemistry: towards more bright eyes for scientific research, social events and human health. Front Chem. 2013 ; https://doi.org/10.3389/fchem.2013.00005
13. Lee H, Scherer NF, Messersmith PB. Single-molecule mechanics of mussel adhesion. Proc Natl Acad Sci U S A. 2006; https://doi.org/ 10.1073/pnas.0605552103
14. Liu Y, Ai K, Lu L. Polydopamine and its derivative materials: Synthesis and promising applications in energy, environmental, and biomedical fields. Chem Rev. 2014; https://doi.org/10.1021/cr400407a
15. Batul R, Tamanna T, Khaliqb A, Yu A. Recent progress in the biomedical applications of polydopamine nanostructures, Biomater Sci. 2017; https://doi.org/10.1039/C7BM00187H
16. Delparastan P, Malollari KG, Lee H, Messersmith PB. Direct Evidence for the Polymeric Nature of Polydopamine. Angew Chemie. 2019; https://doi.org/10.1002/ange.201811763
17. Zecca L, Tampellini D, Gerlach M, Riederer P, Fariello RG, Sulzer D. Substantia nigra neuromelanin: structure, synthesis, and molecular behaviour. Mol Pathol. 2001; PMC1187132
18. Liebscher J. Chemistry of polydopamine – scope, variation, and limitation. Eur J Org Chem. 2019; https://doi.org/10.1002/ejoc.201900445

19. Zhang C, B Wu B, Zhou Y, Zhou F, Liu W and Wang Z. Mussel-inspired hydrogels: from design principles to promising applications. Chem. Soc. Rev. 2020; https:/doi.org/10.1039/C9CS00849G
20. Ryu JH, Messersmith PB, Lee H. Polydopamine Surface Chemistry: A Decade of Discovery. ACS Appl Mater Interfaces. 2018; https://doi.org/10.1021/acsami.7b19865
21. Hong S, Na YS, Choi S, Song IT, Youn Kim W, Lee H. Non-Covalent Self-Assembly and Covalent Polymerization Co-Contribute to Polydopamine Formation. Adv Funct Mater. 2012; https://doi.org/10.1002/adfm.201201156
22. Liebscher J, Mrówczyński R, Scheidt HA, Filip C, Hădade ND, Turcu R, Bende A, Beck S. Structure of polydopamine: a never-ending story? Langmuir 2013; https://doi.org/10.1021/la4020288
23. Klosterman L, Bettinger CJ. Calcium-Mediated Control of Polydopamine Film Oxidation and Iron Chelation. Int. J. Mol. Sci. 2017; https://doi.org/10.3390/ijms18010014
24. Nageswara Rao R, Shinde DD, Kumar Talluri MVN. Development and validation of a reversed phase liquid chromatographic method for separation and determination of related substances of modafinil in bulk drugs. Talanta 2007; https://doi.org/10.1016/j.talanta.2007.03.057
25. Lin J-H, Yu C-J, Yang Y-C, Tseng W-L. Formation of fluorescent polydopamine dots from hydroxyl radical-induced degradation of polydopamine nanoparticles. Phys Chem Chem Phys. 2015; https:// 10.1039/C5CP00932D
26. Liu CY, Huang CJ. Functionalization of Polydopamine via the Aza-Michael Reaction for Antimicrobial Interfaces. Langmuir 2016; https://doi.org/10.1021/acs.langmuir.6b00990
27. Yu QH, Zhang CM, Jiang ZW, Qin SY, Zhang AQ. Mussel-Inspired Adhesive Polydopamine-Functionalized Hyaluronic Acid Hydrogel with Potential Bacterial Inhibition. Glob Chall. 2019; https://doi.org/10.1002/gch2.201900068
28. H. Ruan, J. Liao, R. Tan, J. Pan, A. Sotto, C. Gao. Dual functional layers modified anion exchange membranes with improved fouling resistant for electrodialysis. Adv Mater Interfaces. 2018; https://doi.org/10.1002/admi.201800909
29. Liu C, Shen W, Li B, Li T, Chang H, Cheng Y. Natural Polyphenols Augment Cytosolic Protein Delivery by a Functional Polymer. Chem Mater; 2019; https://doi.org/10.1021/acs.chemmater.8b04672

30. Ptak T, Młynarz P, Dobosz A, Rydzewska A, Prokopowicz M: Potentiometric and NMR complexation studies of phenylboronic acid PBA and its aminophosphonate analog with selected catecholamines. J Mol Struct. 2013; https://doi.org/10.1016/j.molstruc.2013.02.013
31. Bernsmann F, Ball V, Addiego F, Ponche A, Michel M, Gracio JJ, Toniazzo V, Ruch D. Dopamine-melanin film deposition depends on the used oxidant and buffer solution. Langmuir 2011; https://doi.org/10.1021/la104981s
32. Zmerli I, Michel JP, Makky A. Bioinspired polydopamine nanoparticles: synthesis, nanomechanical properties, and efficient PEGylation strategy. J Mater Chem B. 2020; https://doi.org/10.1039/c9tb02769f
33. Wang X, Wang N , Yang Y , Wang X , Liang J , Tian X , Zhang H , Leng X. Polydopamine nanoparticles carrying tumor cell lysate as a potential vaccine for colorectal cancer immunotherapy. Biomater Sci. 2019; https://doi.org/10.1039/c9bm00010k
34. Li N, Wang HB, Thia L, Wang JY, Wang X. Enzymatic reaction induced production of polydopamine nanoparticles for sensitive and visual sensing of urea. Analyst 2015; https://doi.org/10.1039/c4an01900h
35. Cai J, Huang J, Ge M, Iocozzia J, Lin Z, Zhang KQ, Lai Y. Immobilization of Pt Nanoparticles via Rapid and Reusable Electropolymerization of Dopamine on TiO2 Nanotube Arrays for Reversible SERS Substrates and Nonenzymatic Glucose Sensors Small, 2017; https://doi.org/10.1002/smll.201604240
36. Palladino P, Bettazzi F, Scarano S. Polydopamine: surface coating, molecular imprinting, and electrochemistry-successful applications and future perspectives in (bio)analysis. Anal Bioanal Chem. 2019; https://doi.org/10.1007/s00216-019-01665-w
37. Turco A. Preparation and characterization of molecularly imprinted mussel inspired film as antifouling and selective layer for electrochemical detection of sulfamethoxazole, Sensor Actuat B-Chem. 2018; https://doi.org/10.1016/j.snb.2017.09.164
38. Chen W, Fu M, Zhu X, Liu Q. Protein recognition by polydopamine-based molecularly imprinted hollow spheres. Biosens Bioelectron. 2019; https://doi.org/10.1016/j.bios.2019.111492
39. Li W, Zhang Q, Wang Y, Ma Y, Guo Z, Liu Z. Controllably Prepared Aptamer-Molecularly Imprinted Polymer Hybrid for High-Specificity and High-Affinity

Recognition of Target Proteins. Anal Chem. 2019; https://doi.org/10.1021/acs.analchem.9b00465

40. Lin Z, Wang J, Tan X, Sun L, Yu R, Yang H, Chen G. Preparation of boronate-functionalized molecularly imprinted monolithic column with polydopamine coating for glycoprotein recognition and enrichment. J Chromatogr A. 2013; https://doi.org/10.1016/j.chroma.2013.10.059
41. Tretjakov, A., Syritski, V., Reut, J. et al. Surface molecularly imprinted polydopamine films for recognition of immunoglobulin G. Microchim Acta 2013; https://doi.org/10.1007/s00604-013-1039-y
42. He Y, Hong S, Wang M, Wang J, Abd El-Aty AM, Hacimuftuoglu A, Khan M, She Y. Development of fluorescent lateral flow test strips based on an electrospun molecularly imprinted membrane for detection of triazophos residues in tap water. New J Chem. 2020; https://doi.org/10.1039/d0nj00269k
43. Scarano S, Pascale E, Palladino P, Fratini E, Minunni M. Determination of fermentable sugars in beer wort by gold nanoparticles@polydopamine: a layer-by-layer approach for localized surface plasmon resonance measurements at fixed wavelength. Talanta 2018; https://doi.org/10.1016/j.talanta.2018.02.044
44. Torrini F, Scarano S, Palladino P, Minunni M. Polydopamine-based quantitation of albuminuria for the assessment of kidney damage. Anal Bioanal Chem. 2021; https://doi.org/10.1007/s00216-021-03192-z
45. Scarano S, Palladino P, Pascale E, Brittoli A, Minunni M. Colorimetric determination of p-nitrophenol by using ELISA microwells modified with an adhesive polydopamine nanofilm containing catalytically active gold nanoparticles. Microchim Acta 2019; https://doi.org/10.1007/s00604-019-3259-2
46. Palladino P, Brittoli A, Pascale E, Minunni M, Scarano S. Colorimetric determination of total protein content in serum based on the polydopamine/protein adsorption competition on microplates. Talanta 2019; https://doi.org/10.1016/j.talanta.2019.01.095
47. Chianella I, Guerreiro A, Moczko E, Caygill JS, Piletska E V, De Vargas Sansalvador IMP, Whitcombe MJ, Piletsky SA. Direct replacement of antibodies with molecularly imprinted polymer nanoparticles in ELISA - development of a novel assay for vancomycin. Anal Chem. 2013; https://doi.org/10.1021/ac402102j
48. Chen S, Gan N, Zhang H, Hu F, Li T, Cui H, Cao Y, Jiang Q. A portable and antibody-free sandwich assay for determination of chloramphenicol in food based

on a personal glucose meter. Anal Bioanal Chem. 2015; https://doi.org/10.1007/s00216-015-8478-8

49. Xie C, Wang X, He H, Ding Y, Lu X. Mussel-inspired hydrogels for self-adhesive bioelectronics. Adv Funct Mater. 2020; https://doi.org/10.1002/adfm.201909954
50. Torrini F, Palladino P, Baldoneschi V, Scarano S, Minunni M. Sensitive 'two-steps' competitive assay for gonadotropin-releasing hormone detection via SPR biosensing and polynorepinephrine-based molecularly imprinted polymer. Anal Chim Acta 2021; https://doi.org/10.1016/j.aca.2021.338481
51. Baldoneschi V, Palladino P, Banchini M, Minunni M, Scarano S. Norepinephrine as new functional monomer for molecular imprinting: An applicative study for the optical sensing of cardiac biomarkers. Biosens Bioelectron. 2020; https://doi.org/10.1016/j.bios.2020.112161
52. Battaglia F, Baldoneschi V, Meucci V, Intorre L, Minunni M, Scarano S. Detection of canine and equine procalcitonin for sepsis diagnosis in veterinary clinic by the development of novel MIP-based SPR biosensors. Talanta 2021; https://doi.org/10.1016/j.talanta.2021.122347
53. Baldoneschi B, Palladino P, S. Scarano, M. Minunni, Polynorepinephrine: state-of-the-art and perspective applications in biosensing and molecular recognition. Anal Bioanal Chem. 2020; https://doi.org/10.1007/s00216-020-02578-9
54. Hong S, Kim J, Na YS, Park J, Kim S, Singha K, Im GI, Han DK, Kim WJ, Lee H. Poly(norepinephrine): ultrasmooth material-independent surface chemistry and nanodepot for nitric oxide. Angew Chem Int Ed Engl. 2013; https/doi.org/10.1002/anie.201301646
55. Palladino P, Minunni M, Scarano S. Cardiac Troponin T capture and detection in real-time via epitope-imprinted polymer and optical biosensing. Biosens Bioelectron. 2018; https://doi.org/10.1016/j.bios.2018.01.068
56. Palladino P, Torrini F, Scarano S, Minunni M. Colorimetric analysis of the early oxidation of dopamine by hypochlorous acid as preliminary screening tool for chemical determinants of neuronal oxidative stress. J Pharm Biomed Anal. 2020; https://doi.org/10.1016/j.jpba.2019.113016
57. He Z, Su H, Zhen Y, Shi W, Liu X, Liu Y, Zhang F, Zhang Y, Sun Y, Ge D, Poly[norepinephrine]-coated FeOOH nanoparticles as carriers of artemisinin for cancer photothermal- chemical combination therapy, RSC Adv. 2019; https://doi.org/10.1039/C9RA01289C

58. Liang RP, Xiang CY, Wang JW, Qiu JD. Preparation of polynorepinephrine adhesive coating via one-step self-polymerization for enantioselective capillary electrochromatography coupled with electrogenerated chemiluminesense detection. J Chromatogr A. 2013; https//doi.org/10.1016/j.chroma.2013.02.007
59. Liu Y, Zhou G, Liu Z, Guo M, Jiang X, Taskin MB, Zhang Z, Liu J, Tang J, Bai R, Besenbacher F, Chen M, Chen C. Mussel Inspired Polynorepinephrine Functionalized Electrospun Polycaprolactone Microfibers for Muscle Regeneration. Sci Rep. 2017; https://doi.org/10.1038/s41598-017-08572-z
60. Liu X, Xie Z, Shi W, He Z, Liu Y, Su H, Sun Y, Ge D. Polynorepinephrine Nanoparticles: A Novel Photothermal Nanoagent for Chemo-Photothermal Cancer Therapy. ACS Appl Mater Interfaces. 2019; https://doi.org/10.1021/acsami.9b03458
61. Lu Z, Douek AM, Rozario AM, Tabor RF, Kaslin J, Follink B, Teo BM. Bioinspired polynorepinephrine nanoparticles as an efficient vehicle for enhanced drug delivery. J Mater Chem B. 2020; https//doi.org/10.1039/c9tb02375e
62. Taskin MB, Xu R, Zhao H, Wang X, Dong M, Besenbacher F, Chen M. Poly(norepinephrine) as a functional bio-interface for neuronal differentiation on electrospun fibers. Phys Chem Chem Phys. 2015; https://doi.org /10.1039/c5cp00413f
63. Xiao X, Zhang Y, Wu J, Jia L. Poly(norepinephrine)-coated open tubular column for the separation of proteins and recombination human erythropoietin by capillary electrochromatography. J Sep Sci. 2017; https//doi.org/10.1002/jssc.201700720
64. Hong S, Kim J, Na YS, Park J, Kim S, Singha K, Im GI, Han DK, Kim WJ, Lee H. Poly(norepinephrine): ultrasmooth material-independent surface chemistry and nanodepot for nitric oxide. Angew Chem Int Ed Engl. 2013; https://doi.org/10.1002/anie.201301646
65. Chen J, Liang RP, Wu LL, Qiu JD. One-step preparation and application of mussel-inspired poly(norepinephrine)-coated polydimethylsiloxane microchip for separation of chiral compounds. Electrophoresis. 2016; https://doi.org/10.1002/elps. 201600054.
66. Wu J, Xiao X, Li Z, Jia L. Enantioseparation of chiral β-blockers using polynorepinephrine-coated nanoparticles and chiral capillary electrophoresis. Anal Bioanal Chem. 2019; https://doi. org/10.1007/s00216-019-01641-4

67. Qiu J, Chen G, Liu S, Zhang T, Wu J, Wang F, et al. Bioinspired polyelectrolyte-assembled graphene-oxide-coated C18 composite solid-phase microextraction fibers for in vivo monitoring of acidic pharmaceuticals in fish. Anal Chem. 2016; https://doi. org/10.1021/acs.analchem.6b00417
68. Qiu J, Chen G, Zhu F, Ouyang G. Sulfonated nanoparticles doped electrospun fibers with bioinspired polynorepinephrine sheath for in vivo solid-phase microextraction of pharmaceuticals in fish and vegetable. J Chromatogr A. 2016; https://doi.org/10. 1016/j.chroma.2016.05.082
69. Battaglia F, Baldoneschi V, Meucci V, Intorre L, Minunni M, Scarano S. Detection of canine and equine procalcitonin for sepsis diagnosis in veterinary clinic by the development of novel MIP-based SPR biosensors. Talanta 2021; https://doi.org/10.1016/j.talanta.2021.122347

CHAPTER 3

A polynorepinephrine (PNE)-based mimetic against gonadorelin: from the design to bioanalysis

The main purpose of this dissertation deals with the design and integration of a novel PNE-based mimetic receptor in the development of an original bioanalytical assay in order to target a small peptide hormone, namely gonadorelin, for anti-doping control. The PNE-based mimetic receptor was synthesized, for the first time, by following a surface bulk imprinting polymerization (see paragraph 1.5.1). In this Chapter, we first introduce a general overview about the use of drug doping in sports and then narrow the field to the analyte's description; its physiological and pharmaceutical role, and the current state-of-the-art analytical methods (available in the research literature and on the market) used to detect it when misused illicitly in sports-setting. In addition, the motivation that prompted us to perform this experimental study, was explained, looking towards promising future

applications.

3.1 Doping in sports: an outline of prohibited substances in the S2 class

The word "doping" originates from the Dutch word 'dop' [1,2], a term that refers to a stimulant beverage used by African tribes during the eighteenth century. There is a long history of doping in the sports arena, but it grew remarkably during the 20th century with the introduction of amphetamine formulations [3]. The assumption of doping substances by athletes, attempting to enhance sports performance, has been attested since ancient Greece [4].

What is doping? *Doping* refers to - the use of forbidden substances/methods by athletes in order to increase either physical or psychological performance. The incessant desire to win, along with the vision of glory and money, prevails over sporting ethics and health [1]. Local level factors (e.g., team, school, home etc..) and their structural environment (e.g., education system, sport organizations etc..), the so called "dopogenic environment", are key issues that may influence the athlete's decision to violate anti-doping rules [5]. The recent debate encompasses the athletes' health risks associated with the use of doping substances and the role of anti-doping authorities in this regard [6]. Ongoing efforts by the authorities are dedicated to promoting social and structural actions that support athletes and their staff to behave responsibly [5]. Though-out time several unfair and harmful substances have been used in sport competitions. Since 2003, when the World Anti-Doping Agency (WADA) Code was adopted for the first time, documents containing the prohibited list of substances and methods have been regularly revisited and updated [7]. In detail, WADA's Prohibited List is formed by 11 classes of prohibited substances (S0-S9 plus P1 class) and by 3 categories of forbidden methods (M1-M3) [6,7]. Over the last few years, the use of doping agents and methods which are easily "masked" has grown along with the increase of athletes' monitoring. Blood manipulation, a practice to artificially boost the blood's ability to carry oxygen, and genetic engineering, which involves the

insertion of DNA into a person's body to enhance athletic performances [8-9], are recent technological doping practices which have been used (as in the first case) or that the prospect of being used is edging close (as in the second case). Athletes also misuse substances that are physiologically produced by our body such as peptide hormones of which synthetic analogues are also regularly employed to treat various diseases. Focusing on the main performance-enhancing drugs under the S2 class of the WADA Code, recombinant human erythropoietin (rHuEPO), as well as gonadotropins have been the most widespread peptide hormones. rHuEPO is a glycoprotein (MW ~ 34kDa) belonging to hematopoietic growth factors able to increase the number of circulating red blood cells by leading to enhance the body's blood-oxygen carrying capacity [9-10]. Among the gonadotropins, human chorionic gonadotropin (hGC) can be noticed. It is a heterodimeric glycoprotein hormone constituted by two subunits noncovalently linked (the α and β subunits), in which the β subunit is 85% closely homologous to luteinizing hormone (LH) [11]. hCG and LH are both used to stimulate testosterone production. A plethora of bioanalytical methods for detecting these macromolecules are currently present in the research literature. Vice versa, by moving the attention versus small molecule drugs such as small peptide hormones, constituted by a maximum of 10 amino acids (buserelin, deslorelin, gonadorelin, goserelin, leuprorelin, nafarelin and triptorelin), the bioassays available for their detection and measurement are impressively reduced. Thus, nowadays the necessity to widespread and improve analytical methods for targeting small peptide hormones, listed among the WADA's prohibited list, denote an important task for modern sports drug-testing programs [12].

3.2 Peptide hormones - definition

Peptide hormones are physiologically produced and denote one of the major classes of chemical signals, including polypeptide hormone, growth factors, neuropeptides, and glycoprotein hormones. They all consist of a few numbers of amino acids (10-100 aa) and are produced by specialized endocrine glands

[13,14]. Since the discovery of insulin in 1922, peptides have been recognized as chemical signals which regulate a broad spectrum of physiological processes [15]. The mature bioactive hormones were spawned in the rough endoplasmic reticulum and Golgi apparatus of the cells, where preprohormones are proteolytically cleaved by removing the N-terminal signal sequence (*signal sequence*, like a *flag*) to generate prohormones, and then further mature peptide hormones [14]. Once the peptide hormones are secreted and released into the bloodstream, they are directed to bind specific receptors situated on the plasma membrane of target cells. This event triggers multiple physiological regulating signaling pathways. Several peptide hormones were identified as potentially doping drugs for humans, in the course of history, and all of them are prohibited in sports and listed in the WADA code [7].

3.3 Gonadotropin-releasing hormone (GnRH) exploration

Gonadotropin-releasing hormone (GnRH) over decades has assumed multiple aliases name in the medical literature, some of these are: gonadotropin releasing hormone I (GnRH I), luteinizing hormone-releasing hormone (LHRH), gonadotropin-releasing factor (GnRF), gonadoliberin, luliberin and gonadorelin [16], widely used referring to the bioactive principle of a pharmaceutical drug [17]. Herein we use the following terminology, GnRH to indicate the tropic neuropeptide endogenously produced and gonadorelin (acronym G) to tag the same synthetic peptide. Gonadorelin (G), is a bioactive synthetic decapeptide (pGlu-His-Trp-Ser-Tyr-Gly-Leu-Arg-Pro-Gly-NH_2 MW = 1182.33 Da) with an isoelectric point (pI) in the alkaline pH range (pI around 9), that has the same chemical structure as the endogenous GnRH [18]. It possesses a pyroglutamic acid at the N-terminus and a C-terminal amidated. It is also possible that the amino acids residues -ProGly- at the C-terminus, from a 3D structure viewer, adopted a beta-turn motif [19] through hydrogen bonds (Fig. 3.1).

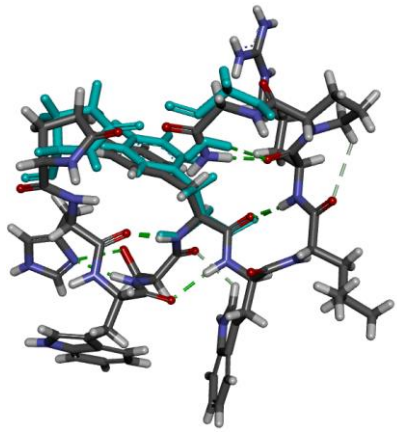

Fig. 3.1 The gonadorelin 3D chemical structure was generated from UniProt (protein data bank) – P01148 (GON1-HUMAN) and displayed in DS Biovia (San Diego: Dassault Systèmes, 2019)

In addition, the gonadorelin synthesis occurs on a solid phase in the N-to -C direction, as usual in the case of peptides. The UV peak of gonadorelin absorbance spectrum at 280 nm is associated with the presence of aromatic amino acids, tyrosine and tryptophan, in its sequence [20].

Physiologically, GnRH is a highly conserved decapeptide encoded by the *GnRH1* gene located on chromosome 8.p11.2-p21 [21]. It is the pivotal central regulator of the hypothalamic-pituitary-gonadal (HPG) axis and plays a significant role in the processes of mammalian reproduction [22-23]. The pulsatile secretion of GnRH, by a small number of neurons located in the medio basal hypothalamus, stimulates the synthesis and the release of pituitary gonadotropins, luteinizing hormone (LH) and follicle-stimulating hormone (FSH), both in adult males and females, by binding to the GnRH receptors (GnRH-R) which are mainly expressed in the anterior pituitary [22,24]. Detailing, the latter receptors belong to the G-protein coupled receptors (GPCRs, 328 amino acids (aa) [25]) family which are constituted by seven integral membrane proteins (IMPs) that are used by cells to transduce extracellular signals into intracellular signaling pathways for the regulation of the reproductive axis functions [26]. Besides, it is now well established that GnRH-R overexpression takes place in gonadal steroid-

dependent (responsive) tumors, such as prostate, breast, endometrial tumors, and ovarian adenocarcinomas [25,27].

The molecular pathway, triggered by pituitary GnRH-R, proceeds with the production of both steroid hormones (testosterone in males and progesterone in females) and gametes, triggered by the two gonadotropins which in turn act on the gonads, which regulate the endocrine functions [28].

From a structural point of view, GnRH is first synthesized and released by the hypothalamus as pre-prohormone, a large precursor protein named progonadoliberin-1 precursor (MW 10.380 Da, length 92 aa), which undergoes post-translational modifications carried out in multiple steps to obtain the mature form [29-30]. Firstly, the N-terminal signaling sequence of 23 amino acids (1-23 aa position) is removed and then the residual peptide (24-92 aa), the prohormone or pro-neuropeptide, is proteolytically cleaved by specific endopeptidases in two fragments: GnRH bioactive peptide (24-33 aa position - 10 aa length, MW 1182.33 Da) with amidation of the carboxy-terminal portion; GnRH-associated peptide (GAP 37-92 aa position – 45 aa, MW 1492 Da) [16]. Finally, the GnRH decapeptide is directly followed by a residual small polymer chain of three a.a. as dibasic cleavage site (Gly-Lys-Arg) [15,31-32]. To date, in addition to the hypothalamic GnRH form, other isoforms exist among vertebrates which have conserved the 10 amino acids length during the evolution. The isoforms can be classified in 3 different groups divided on the basis of development origin and physiologic analysis. GnRH I denoted the first GnRH structure identified in mammals and the amino acids of GnRH are completely conserved in most mammalian species [31]. Notwithstanding, other two GnRH forms were identified and the amino acids differing from the native form were highlighted in bold, as follows: GnRH II (pGlu-His-Trp-Ser-**His-**Gly-**Trp-Tyr**-Plo-Gly-NH_2) refers to the structure originally identified in the chicken brain but seems to be ubiquitous, found in fish as well as in humans; GnRH III is the form found in sea lamprey (pGlu-His-Trp-Ser-**His-Asp-Trp-Lys-**Pro-Gly-NH_2) [31]. The episodic production of GnRH from hypothalamus is controlled by the hypothalamic pulse generator identified by E. Knobil [33] approximately four decades ago even if the

genesis of GnRH pulse generation is still incompletely comprehended [34]. It is important to note that the frequency and the amplitude of pulsatile GnRH release plays an important role in controlling the loop-feedback mechanism of the HPG axis to avoid the downregulation of the GnRH-R in the pituitary [28]. Besides, differences in GnRH secretion were observed between females and males. In males, GnRH is pulsatile secreted at a constant frequency; otherwise, in females, the frequency of the pulses is more variable due to the reproductive cycle. The following paragraph describes the pharmaceutical role of gonadorelin.

3.4 Gonadorelin' use in sports: an introduction

Since 1971, when the GnRH (see paragraph 3.3) isolation and characterization has occurred from the hypothalamus of pigs and sheep [31 35], structural analogues of the endogenous GnRH have been developed. In some cases, L-peptides (e.g., native GnRH) are vulnerable to enzymatic degradation *in vivo* and can be replaced by analogues D-peptides which are more resistant towards proteolysis [36]. The GnRH synthetic analogues synthesized in the recent years, e.g., gonadorelin, buserelin, gonadorelin, goserelin, leuprorelin, nafarelin, and triptorelin [7], are used as pharmaceutical drugs to treat different pathophysiological states, e.g., hormonal dysfunctions, such as endometriosis, uterine fibroids, precocious puberty, infertility, and hormone-sensitive tumors whose cells overexpress the GnRH-R [37-40]. The reverse side is that these peptides with a wide spectrum of physiological activity, have been improperly misused by male athletes by triggering testosterone secretion to unnatural high levels [41], promoting muscle growth, with possible improvement in athletic performance. Continuous administration of gonadorelin and analogues drugs, available as intranasal "pulse-dose" spray (e.g., kryptocur), leads to the desensitization and down-regulation of GnRH-R pituitary gonadotrophs with impact on health, the so called "flare effect". Accordingly, to protect the athletes' health and ensure equal competitive opportunities, all these small peptides have been listed, since 2014, among the substances banned in sports in the S2 class of

the WADA code which is annually reviewed and updated [7,41-42].
It is important to note that gonadorelin is also included in veterinary medicine to treat animals with infertility secondary disorders, cystic ovarian disease, and to induce medical castration [43]. Thus, for pharmaceutical drugs, containing gonadorelin as active principle, are available on the market: Cystorelin® (gonadorelin diacetate tetrahydrate), Factrel® (gonadorelin hydrochloride), Fertagyl® (gonadorelin diacetate tetrahydrate), Gonabreed® (gonadorelin acetate). All of them are approved by the Food and Drug Administration since 2013 (except Cystorelin approved in 2018) for dairy and beef cows [44-45]. Unfortunately, in this case performance-enhancing drugs to animals' race, especially used in horses and greyhounds, are not involved in a Worldwide legislation but they are only prohibited, yet, at State level (e.g., Australia under the Rules of Racing) [46].

3.5 Analytical detection methods for gonadorelin: past, present and future

Peptide-derived drugs represent an emerging class of prohibited substances in modern doping controls as reported by Thevis et. al. [6].
Physiologically, GnRH (see paragraph 3.3) is not found in biological fluids, such as plasma and urine, because through various metabolic processes it is degraded to form metabolites. On the contrary, GnRH can be found in cerebrospinal fluid (basal CSF-GnRH 1.3 pg mL^{-1}) [47] and human milk (0.1-3 ng mL^{-1}) [48]. Nowadays, WADA labs lack unambiguous criteria regarding Gonadorelin (the so-called "pseudo-endogenous" peptide because it is endogenously produced and is prohibited if it is administered exogenously) to report adverse analytical findings. The ongoing development of an Endocrine Module of the athlete's biological passport (ABC) should further help to better detect the abuse of gonadorelin and other hormones. For this reason, gonadorelin is currently classified among the Non-Threshold Substances and for this, the Minimum Required Performance Levels (MRPL) = 2 ng ml^{-1} (1.69 nmol L^{-1}) was established to guarantee that all WADA-

accredited laboratories can report the presence of gonadorelin, in their routine daily analysis, in a uniform way [49-50].

In this section, we aim to provide an overview of the current detection methods used for gonadorelin (or the endogenous peptide analogue, GnRH) in biological fluids for sports medicine or related applications. Current research literature focuses primarily on clinical studies and drug delivery systems linked with GnRH pathophysiological conditions. First, we reviewed the analytical methods according to the research literature over the last 20 years and a tabulated comparison of the performances, in terms of detection limits, will be provided. Conventional immunoassays are also described covering strengths and limitations of those currently available. Moreover, the role of biosensors, with an emphasis on opto-biosensing platforms, and novel spectroscopic bioanalytical assays, will be addressed to introduce our recent breakthroughs on this topic (sections 3.5.3).

3.5.1 LC-MS/MS methods: an outline

The scientific literature dedicated to the synthetic peptide hormones detection is very limited, most of the studies reported in it allow the quantitative determination of these short peptides through high-performance liquid chromatography (HPLC) [51-52], tandem-MS techniques (LC-MS/MS) [53-56], or capillary zone electrophoresis [57-58]. The largest percentage of studies, related to the analytical field, involved the use of liquid chromatography coupled or not to mass spectrometry. Only a few studies involve conventional immunoassays and sensing platforms. WADA labs currently consider mass spectrometry as the gold standard analytical technique for the unambiguous detection of small molecules thanks to its high sensitivity. Furthermore, mass spectrometry is considered the only platform that ensures a timely analysis of all athletes' biological fluids from a technical, logistical, and cost-saving standpoint. This analytical technique addresses the need to analyze several hundreds of prohibited substances every day.

Chromatographic assets can be various, eventually coupled to detection approaches, i.e., optical, electrochemical, spectrometric etc. Among optical detection, fluorescence is suitable for sensitive peptides' detection [60] and the chemical derivatization is usually the pretreatment requested.

Conventional fluorogenic reagents used for the peptide's derivatization are o-phthalaldehyde, naphthalene-2,3-dicarboxaldehyde, fluorescamine, ninhydrin, and phenanthrenequinone [59-62] which react with primary or secondary amine groups. Benzoin or ninhydrin, newer derivatization reagents, can react with arginine present in the peptide, as gonadorelin. Arginine reacts with the guanidino group of the derivatization reagents under strongly basic conditions (pH 12) to generate a fluorescent product which is measured online. The excitation wavelengths for ninhydrin and benzoin are respectively 390 nm and 325 nm while the fluorescence emission was monitored with a 470 nm and 435 nm cut-off filters. In this way, arginine-containing peptides, as gonadorelin, may be detected [59-62].

Although a wide variety of detectors can be coupled to LC, in this context, the mass spectrometer has emerged as a selective, sensitive, and universal detector. A literature summary table about this task is reported (Table 3.1) to easily compare the analytical performance, mainly in terms of detection limits.

Table 3.1 Literature analytical chemistry methods for gonadorelin detection

Target company	Detection method*	LOD (ng mL^{-1})	Matrix	Ref.
LHRH ICN pharmaceuticals (Costa Mesa, CA)	HPLC UV detector (210 nm)	1	Not tested	[63]
GnRH Bachem (Bubendorf, Switzerland)	UPLC-MS/MS Ion source: electrospray positive ion mode Sample preparation method: SPE Targeted method	0.1	Urine samples spiked Recovery: 87 ± 10%	[42]
Gonadorelin Bachem Americas Inc. (Torrance, CA, USA)	HILIC-HRMS Ion source: electrospray positive ion mode Sample preparation method: SPE Untargeted method MS full-scan range m/z 200-2000	0.02 in plasma 0.04 in urine	Equine plasma and urine spiked with 44 peptides	[64]
LHRH Sigma-Aldrich (Saint Louis, MO, USA)	LC-HRMS/MS Ion source: ESI MS full-scan range m/z 300-1500 Online sample clean-up using a Dionex UltiMate 3000 Rapid Separation LC system	< 0.1	Human urine samples	[65]
GnRH Abbiotec, LLC (San Diego, CA, USA)	HPLC-MS (Q-TOF) Ion source: ESI MS full-scan range m/z 50-1350 Sample preparation method: SPE	0.1	Human urine samples spiked. Matrix effect: 59%	[66]
LH-RH Australian Sports Drug Testing Laboratory (Sydney, Australia)	LC-MS Ion source: ESI MS full-scan range m/z 50-1350 Sample preparation method: SPE	0.25	Human urine samples spiked	[67]

Kryptocur Sanofi-Aventis (Frankfurt, Germany)	LC-MS/MS (Orbitrap) Ion source: ESI MS full-scan range m/z 300-2000	0.005	Human urine samples	[60]
LHRH Bachem (Bubendorf, Switzerland)	UPLC-MS/MS (TSQ) Ion source: HESI Sample preparation method: SPE MS full-scan range m/z 300-2000	0.05	Human urine samples (diluted spiked Recovery%: 86	[68]
GnRH AusPep (Melbourne, Australia)	Nano LC-MS/MS (TSQ) Ion source: ESI	0.001	Equine urine spiked Matrix effect: 170 ± 8%	[69]
LHRH Sigma-Aldrich (Saint Louis, MO, USA)	ECD-Tandem FTICR MS Ion source: microESI	X	Not tested	[70]
LH-RH Sigma-Aldrich (Milan, Italy)	LC-MS/MS (TSQ) Ion source: ESI Sample preparation method: SPE	0.10	Artificial urine samples spiked Matrix effect: 35%	[61]
Gonadorelin. European Pharmacopoeia reference standards	Screening method: LC-MS/MS	50	Not tested	[71]
Kryptocur Sanofi-Aventis (Frankfurt, Germany) MW 1181.57 Da	nano-UHPLC-MS (Orbitrap) Ion source: nano-ESI Sample preparation method: SPE	0.002	Urine samples Recovery: 49%	[41]
LHRH	LC-MS (LTQ linear ion trap mass spectrometer)	59	Plasma samples spiked	[72]

Appropriate sample preparation represents a critical and long step for LC-MS techniques which therefore influence the high-throughput analysis. Solid-phase extraction (SPE) is a single-use low-resolution chromatographic process, and it is widely involved upstream of LC-MS allowing the extraction of the target from standard solutions or biological matrix. For example, Thomas et al. used an immunoaffinity purification in which biotinylated antibodies tethered to streptavidin magnetic beads are employed as stationary phase [60]. Conversely, Richards et al. [69] report the use of the first biomimetic receptor, a spiegelmer (NOX-1255, detailed in the next paragraph) for SPE, as an alternative to bioreagents by overcoming known limitations (extremely high costs for disposable use, etc.). The biomimetic receptor was immobilized on magnetic beads, through conventional biotin-streptavidin chemistry and employed in a pilot study to clean up gonadorelin from equine urine samples. The enrichment of peptide targets by biomimetic antibodies is an effective and outstanding alternative to the bioreagents.
The serial and long process required by LC-MS gonadorelin analysis, as well as the size/high cost of the instrumentation, the requirement of qualified operators, and long pre-treatment of the samples, limit high-throughput analysis in the case of a single specific target to quantify. This occurred nonetheless the current advancements of the analytical apparatus and the progress to reduce the pre-analytical sample processing.

3.5.2 Immunological techniques

Immunoassays denote a very powerful analytical techniques field. These are widely employed in clinical laboratories, as diagnostic tests for the analysis of multiple diverse analytes, or as immunoaffinity tools for pre-analytical samples' preparation due to its straightforwardness protocol and small samples' amounts required. Immunological techniques conventionally rely on antibody-antigen affinity reaction able to form a stable complex (Ab-Ag) that can be described according to the law of mass action: $Ag + Ab \underset{K_d}{\overset{K_a}{\rightleftharpoons}} Ag - Ab$; where Ag/Ab/Ag-Ab is the antigen/antibody/complex concentration,

respectively; k_a and k_d correspond to the kinetic constant respectively of association and dissociation [73]. The ratio of the two kinetic constants expresses the equilibrium constant. Besides, this technique allows the multiplexed screening of different biological samples (*e.g.,* blood, urine, saliva, etc.) or different analytes on disposable plastic microplates, offering many practical advantages. These microplates are usually constituted by several wells used singly as micro test tubes (till a maximum of 384 micro-test tubes for a single plate). In this scenario, enzyme-linked immunosorbent assay (ELISA) is the most established technology which integrates the specificity of antibodies and the sensitivity of a simple enzymatic signal amplification reporter. ELISA is considered one of the most widespread diagnostic tools in clinical routine measurements. It is used to detect and measure a wide variety of analytes belonging to peptides, proteins, viruses, cells, and other organic as well as inorganic molecules of interest in several bioanalytical and biomedical research areas. Moreover, it does not require expensive instrumentation and it is often readily available as commercial kits where the analytical signal is generally based on an optically active product [74]. There are different formats to design an ELISA detection strategy (direct, indirect, sandwich, and competitive format), and determining which one is appropriate for addressing the research question depends mainly on the analyte being detected and on the availability of the capturing agents (*i.e.*, specific antibodies). The ELISA assay has undergone numerous welcomed changes from the first one described by Engvall and Perlmann in 1971 [75]. As a result, the term ELISA now refers to a wide range of micro-welled plate assays, some of which do not involve enzymatic reactions [76-78] and/or immune complex formation [79-80]. The sensitivity and specificity of immunoassay have allowed the detection of analytes at very low concentrations not easily measured by other analytical techniques [73]. Nowadays, the smartphone technology, coupled with microplates-based assays enables rapid point-of-care (POC) diagnosis (or mHealth, mobile health) for in situ-analysis, namely mobile phone-based ELISA (MELISA) [81]. In this context, the bottleneck of immunoassays for the detection of small

molecules (MW < 2 KDa), such as gonadorelin, is related to the production of bioreceptors. Small molecules do not represent good immunogens mainly due to their size (namely haptens) and elicit antibody titers only when combined with a larger carrier molecule such as bovine serum albumin (BSA), ovalbumin (OVA), keyhole limpet hemocyanin (KLH), or linked to other peptide fragments, etc. Moreover, small molecules lack multiple epitopes for response enhancement by sandwich format and therefore the assays can be designed only in a competitive mode. In the competitive assay, the antigen competes with a chemically identical molecule (competitor molecule) tethered to a signal reporter for the antibody's binding sites immobilized onto a solid microtiter plate. Up to this point, there are only a few competitive inhibition ELISA assays for gonadorelin dosage, available on the market as a research tool that might tentatively be applied in the anti-doping samples testing. In this regard, a lack of clearness transpires, from our viewpoint, about the target employed in the kit and the immunogen used to produce antibodies. Some handbook kits report the name of different peptides portions (gonadorelin, progonadoliberin-1, GAP, etc.) belonging to the prohormone but their sequences do not coincide with that of gonadorelin, for this reason understanding the kits' effectiveness in detecting gonadorelin is difficult. Moreover, the unknown antibody-binding epitope and the scarce information about the immunogen used to trigger the immune response limit the applicability of the present gonadorelin's kits.

Outside the field of sport, despite the significant role that GnRH physiologically plays, the detection of GnRH does not take place directly from blood specimens. This is related to the fact that the hypophyseal portal blood sampling, a small and relatively inaccessible blood system, is extremely difficult and invasive [82]. For this reason, examining the research literature concerning immunoassays to dose GnRH, a lot of tests have been conducted *in vivo* animal models. The pioneered immunoassay developed for GnRH quantification exploited a radioactive signal label [73]. As a first example, Morris et al. (1981) propose a radioimmunoassay (RIA) for the measurement of hypothalamic GnRH in the rat [83] while Inaba et al (1988) measured it in

canine plasma [22]. Though, regarding the safe handling of radioactive reagents, regulatory disposal, and waste of working with radioactive materials have led to the development of alternative non-isotopic labeling strategies, such as enzymatic tracers [73]. Besides, studies focused on the quantification of GnRH, through a competitive ELISA, were conducted *in vivo* by sampling hypothalamo-hypophyseal portal blood in dogs and seabreams. Inaba et al. (1994) proposed a newly competitive ELISA for GnRH detection in the canine hypothalamus and plasma, whilst Holland et al. (1998) [84] developed three competitive ELISA assays to measure various GnRH isoform (GnRH I, GnRH II, and GnRH III) in male and female seabreams' pituitary (sb) [22, 84-85]. Rodriguez et al. [86] reported the measurement of sbGnRH levels by applying the same assay methodology of Inaba et al. [22].

Immunoassays represent an established technique in the clinical field and emerge also as promising portable and high performing bioanalytical tools in the forensic field, to unmask chelating athletes. However, since current research interest is dictated by the requirement of greater throughput and sensitivity alternatives, as well as cheaper, conventional immunoassays could gradually be replaced by abiotic pseudo-ELISA assays. In this context, several efforts have been already devoted to discovering new signal reporters to increase pseudo-ELISA assays sensitivity [76] and to pinpoint capturing agents, i.e., mimetics [87-88], able to flank and/or supplant antibodies that generally are expensive and sensitive to environmental conditions.

Looking at mimetic capturing agents, the literature has highlighted aptamers and molecularly imprinted polymers (MIPs) as the most promising ones suitable for pseudo-ELISA assays. Both these mimetics can be in vitro produced and exploited to develop diagnostic "antibody-free" assays for ELISA-like format, i.e., enzyme-linked oligonucleotide assay (ELONA), where aptamers are used as mimetic receptors [79,88]; biomimetic enzyme-linked immunoassay (BELISA), pseudo-ELISA [80, 89–92], or nanoparticles-based assay (MINA) [74, 93-99]. At present, a positive imbalance of the literature is in favor of aptamers, with only few reports about MIPs starting from 2014. In addition, the ELISA format is currently a source of inspiration for many

biosensors applications [100]. But in the specific case of gonadorelin there is still an open challenge: the need for effective alternative receptors to the biological ones. To face this issue, biomimetic recognition elements (i.e., aptamers or MIPs) may be employed. A portion of the experimental study fits into this context/demand.
In the next item, we provide a broad introduction to biosensing technologies in this field and then, in connection with the point previously mentioned, an overview to give a broad picture of existing biomimetic receptors to recognize gonadorelin.

3.5.3 Biosensing technologies

Biosensing represents a well-established and extremely changeable analytical technology. Since its introduction occurred in 1956 [101], biosensors [102] have witnessed a fast growth becoming a field thriving worldwide for advancing human healthcare, for pharmaceutical companies to screen different drugs or vaccines' libraries, food, and environmental analysis, but also for anti-doping control analysis. Sensing technology gained attention over conventional analytical techniques because they enable quick and in real-time detection of a plethora of analytes (spanning from biomarkers, environmental, food and drug targets) by monitoring the interactions (qualitative ranking, calculation of kinetic and affinity constants), without the need of labeling and with a minimal (or no) sample pretreatment. Specifically, a biosensor is defined as an analytical device constituted by a biological or biomimetic element integrated within a transducer system, which may be optical, electrochemical, thermometric, piezoelectric, magnetic, or micromechanical [103]. Biosensors can be classified on the basis of biorecognition elements (e.g., tissues, microorganisms, organelles, enzymes, cell receptors, antibodies and biomimetic receptors) and signal transducers. In addition, they can be divided into two classes: the first class enclosed affinity-based biosensors established on the specific binding of an analyte to the receptor; on the other hand, the second class comprises enzyme-based

biosensors based on the enzymatic turnover, i.e., the enzyme converts the substrate into a product [104]. In a general analysis, the receptor element binds the analyte, and this recognition event is converted by the transducer into a measurable signal (signalization). The latter, in turn, is processed to a readable analytical signal by electronic devices. In the case of gonadorelin detection, only one stripping-based electrochemical sensor was described by X. Cai et al. [105]. They reported a potentiometric stripping analysis (PSA) which was successfully applied to determine gonadorelin in buffer solution (0.2 M sodium phosphate, pH 7.0) [105]. The tryptophan and tyrosine residues in the gonadorelin sequence produce two-well resolved potentiometric peaks at the corresponding potentials, tryptophan shows a peak around 0.7 V (against Ag/AgCl reference electrode) instead of tyrosine around 0.55 V. This sensing platform provides high sensitivity, down to picomole peptide level. Likewise, optical biosensors (e.g., fluorescence spectroscopy, SPR including imaging and localized, surface-enhanced Raman scattering (SERS), interferometric spectroscopy and guided mode resonance (GMR) [104] are an effective, affordable, and non-invasive alternative to electrochemical ones. Optical biosensors, especially those based on SPR principle, may offer a valid approach to expand the cohort of techniques applied to the anti-doping controls [54, 106-107], as already reported in the past for proteins of anti-doping interest and gene doping [108-109]. In this scenario, we introduce our study based on the implementation of an optical sensing platform, based on SPR transduction, alongside MIP as capturing element, to successfully quantify gonadorelin (see paragraph 3.6).

3.5.3.1 Surface Plasmon Resonance – overview of the principle

SPR and localized (L)-SPR are optical biosensors that currently constitute the ground base of the plasmonic research field [100]. The basic principle that allows the transduction is based on the coupling of the electric field of incident lights, at a certain incident angle (greater than the critical angle to achieve

the total internal reflection (TIR) optical phenomenon), with the free electrons of metallic films (SPR, typically gold layer) or metallic nanoparticles (LSPR) generating surface plasmon-polaritons or surface plasma wave (SPW). SPW, constituted by the collective oscillation of electron clouds, propagates along with the metal-dielectric interface. In detail, this self-propagating transverse wave has a magnetic vector parallel to the interface plane and is described by the propagation constant and electromagnetic field distribution [110]. The propagation constant, *β,* of an SPW is expressed as:

$$\beta = \frac{\omega}{c}\sqrt{\frac{\varepsilon_M \varepsilon_D}{\varepsilon_M + \varepsilon_D}} \quad (1)$$

where ω is the angular frequency, c is the speed of light in vacuum, ε_D and ε_M are respectively the vacuum dielectric and the metal permittivity [110]. If the real part ε_M, which describes the spatial periodicity in the direction of propagation, is negative and its absolute value is smaller than the imaginary part ε_D, describing the SPW attenuation, the above equation may describe the SPW. The electromagnetic field of SPW reaches the maximum at the metal-dielectric interface and then decreases exponentially into both media. The distance from the interface before its amplitude decayed by a factor 1/e into the dielectric is typically 100-500 nm, for metal films, and 10-50 nm for metallic nanoparticles, in the visible (source λ=630-670 nm) and near-infrared regions (source λ=850 nm) [110]. In general, the SPW propagation constant is highly sensitive to refractive change and in turn to each event occurring to the metal/dielectric interface. Hence ligand-analyte interaction (SPR fixed angle), allowing bulk sensing, and even adsorption phenomena, leading to the measurement of the film thickness absorbed on the metal surface (angle-scanning SPR), can be monitored by using the SPR technique. Undoubtedly, the core of SPR affinity biosensing is based on the study of biomolecular interactions in which recognition elements can be immobilized onto the metal surface, through various chemistry, and capture analytes

present in a sample solution, or vice versa. This carries to a measurable increase of the refractive index at the metal surface which is directly proportional to the concentration of the interacting molecules with the immobilized counterparts. The change in refractive index, Δ_{n_d}, taking place within a layer of thickness h, can be described as follows:

$$\Delta_{n_d} = (\frac{d_n}{d_c})_{vol} \frac{\Delta\Gamma}{h}$$

where $(\frac{d_n}{d_c})$ is the increase of refractive index n with the volumetric analyte concentration, c, and $\Delta\Gamma$ is the surface concentration of the molecule (analyte) being bound. A kinetic evaluation of the interactions can be accomplished thanks to the change in the coupling of incident light and SPW caused by the local change of refractive index [110-111].

In our case, the SPR equipment, namely Biacore X-100, used to develop the experimental part of this dissertation is a prism-based system. Classical microfluidic SPR instrumentation, based on Kretschmann configuration, include a glass prism coated with a flat metal layer (usually gold ~ 50 nm of thickness) in contact with the analyte solution. SPR phenomenon occurs in conducting films at the interface between media possessing different refractive index [112]. A conventional straightforward SPR sensor works at a fixed incident angle, under conditions of total internal reflection, the incident light passes through the high refractive index prism, totally reflected at the prism-metal interface, and leaks an electric evanescent decaying field across which penetrates the metal layer [111], medium of lower refractive index, and reaches the upper edge between metal-sensing medium. When the wavevector of the incident photons match with the wavevector of SPW, a characteristic absorption of energy via the evanescent wave field occurs and SPR phenomenon produces a resonance dip in the reflection spectrum. This condition is expressed by the following equation:

$$\frac{2\pi}{\lambda} n_p \theta = \beta_{ev} = Re\ (\beta_{spp})$$

where n_p is the refractive index of the dielectric prism, λ is the wavelength and θ is the angle of the incident light, β_{ev} is the propagation constant of the evanescent field [113].

Because the evanescent wave field penetrates the solution, conditions for this resonance effect are very sensitive to the refractive index, as described above [112]. Binding response is presented in a sensorgram where SPR response is measured in resonance units (RU) and plotted versus time. The sensorgram displays binding events over the entire course of an interaction and reveals association and dissociation rates of complexes, with the binding kinetics (ka, kd). The accumulated mass on the sensor chip surface (which is generally expressed as surface density pg mm^{-2}) correlates linearly with the change in the refractive index near the sensor surface measured by instrument. In Biacore instrumentation, ~8.2 resonance units (RU) correspond to 1 millidegree (m°) SPR angle shift and in addition 1 RU corresponds to exactly 10^{-6} refractive index unit (visible light). Notwithstanding that most SPR instrumentations presently commercially available hold large size (benchtop equipment), with advances in modern biosensing, few effective portable SPR kits have been developed (e.g., Plasmetrix) [114]. So gradually SPR biosensing technology evolves from off-site laboratory to on-site diagnosis, for point-of-care testing (POCT). SPR technology, in our case, represents a powerful technique to characterize novel "*household*" receptors, in terms of analytical performances, and to design novel and original abiotic assays, taking inspiration from convention ELISA assays' format. Furthermore, SPR is an interesting transduction principle i.e., label-free allowing target species quantitative measurements. Here the SPR approach has been used for development of a label free quantitative assay for gonadorelin, based on the PNE selective MIP. Further development has involved the scaling down of the experimental asset's size, versus conventional platforms assays, widely used in clinical routine analysis. This to demonstrate the applicability of the PNE

biomimetic receptor-based approach to microwelled platforms coupled to simple readers, available in most clinical diagnostic as well in antidoping laboratories.

In this dissertation, a pseudo-ELISA assay was established, which unlike SPR, involves a signal reporter. In this direction, in addition to microwelled based assay (BELISA), optofluidic POC devices' application can be foreseen, through the integration of PNE-based receptors, for example on blotting paper or nitrocellulose membranes, and eventually combined with nanomaterials. In this way sample processing, measuring, and signal output in all-in-one ready to use MIPs-based devices for *in-situ* clinical applications will be available.

3.5.4 Biomimetic receptor elements: types and features

Novel biomimetic receptor elements can be successfully synthesized and integrated for compound analysis (e.g., ELISA assays and biosensing platforms) but also for sample purification (e.g., molecularly imprinted solid-phase extraction (MISPE)) intended for forensic investigations in anti-doping. In the case study of gonadorelin, there are only few existing examples in literature of biomimetic receptors, such as aptamers and/or spiegelmers, to recognize gonadorelin. In this context, the following paragraph illustrates the existing examples of the aforementioned mimetic receptors. Subsequently, the use of MIPs, another type of mimetics, in anti-doping control area is briefly introduced prior to describing the experimental activities carried out on this topic (paragraphs 3.6 and 3.7).

3.5.4.1 Aptamers and Spiegelmers

Aptamers are short synthetic single-stranded (ss) nucleic acid sequences (DNA or RNA in the range of 15-60 nucleotides in length) able to fold into a well-defined three-dimensional structure capable of binding the target molecules non-covalently, with high affinity and selectivity [115-116]. They can also be classified as peptide aptamers, and this depends on the random sequence pools used to generate them [117]. The structural interactions

between the aptamers and the targets (via van der Walls forces, hydrogen bonds and electrostatic interactions etc.), as well as MIPs-targets, are similar to the way in which antibodies bind antigens. Unlike their natural counterparts' receptors, aptamers are synthesized *in vitro* with no animal sacrifice and in a shorter time, by reducing the batch-to-batch variability associated to distinct immune responses, and also, they are cost-effective and amenable to modifications [79]. Aptamers display an improved stability compared to antibodies, on account of the presence of robust phosphodiester backbone. Besides, they have a flexible structure (able to fold and unfold an unlimited number of times) over an extensive range of physical-chemical conditions (pH, ionic strength, T, denaturants, chemicals etc.); on the contrary antibodies are subjected to irreversible denaturation [118] in the same conditions. Chemical modifications of aptamers can impart resistance to nuclease cleavage in biological matrices. Therefore, aptamers are a versatile multifunctional instrument that find increasing application in various fields of research such as targeted therapeutic agents, as recognition elements, as affinity ligands and as a tool for cell tracking. Aptamers can be potentially generated for a multitude of macromolecules (proteins, whole cells, bacteria, and viruses) as well as for small molecules (peptides, metabolites, small drugs, metal ions, toxins etc..) that don't trigger an immune response [115, 117] but compressively, aptamers for small molecules represent a small percentage of all existing.

Traditionally, aptamers are produced via an *in vitro* screening process, namely, systematic evolution of ligands by exponential enrichment (SELEX). This process is characterized by iterative cycles consisting in the repetition of sequential steps: selection, amplification, and conditioning (purification of the relevant ssDNA) to produce selective aptamers fit for a certain non-nucleic acid target. The SELEX procedure begins with a starting "pool", a randomized library of oligonucleotides (DNA and RNA) consisting of about 10^{13} -10^{15} different sequence motifs [119-120]. Each DNA sequence is composed of a central region flanked by two constant primer binding sites, which are used for polymerase chain reaction (PCR) amplification. In a general process, at

the beginning, the pool and the target of interest are incubated in solution. Conversely, the same reaction for small molecules involves their immobilization onto a solid-support matrix to enable DNA (or RNA)-binding. Several washing steps are further employed to remove unbound sequences, to yield an enriched library, do not occur. This library is involved then for the following rounds (4-20 rounds [120]). Among SELEX methodology, other non-SELEX selection process of aptamers have been introduced that also reduce the synthesis run time, e.g., non-equilibrium capillary electrophoresis of equilibrium mixtures (NECEEM), a highly efficient affinity method [121-122]. The equilibrium dissociation constants of aptamers against macromolecules typically fall in the pico- or nano-molar range whilst Ruscito et al. report, concerning small molecules binding aptamers, that averagely recognize the low-MW targets with K_D in the low-mid micromolar range [118]. Notwithstanding, small molecules binding aptamers are still an active research field of great relevance and among these, the development of RNA-binding short elements named "riboswitches" as therapeutics and chemical probes awaked an increasing interest [123-124]. Riboswitch's structures act as regulators of gene expression through direct interaction with small molecule by triggering a conformational change in the RNA structure and this enables the transduction of the binding event straight into an output signal [123-125]. Leva et al [126] described for the first time two spiegelmers, based on L-RNA and L-DNA respectively, mirror-image aptamers. Spiegelmers are L-enantiomeric synthetic oligonucleotide, the perfect mirror image of D-oligonucleotide ligands, built of L-2'-deoxyribose unit [130]. However, the spiegelmer synthesis (SELEX) is more complicated than aptamer because it requires an appropriate non-natural mirror-image of the target [131]. These spiegelmers are able to bind GnRH with high affinity, as stated by K_D in the nM range, and with high specificity [126-129], as attested by the ability to discriminate a single amino acid exchange in the chicken GnRH sequence. In this study, spiegelmers' affinity has been tested through isothermal calorimetry, while the ligands' specificity by mean SPR analysis [125-126]. To this aim, the molecular recognition elements, 5'-biotinylated

RNA and DNA spielgemers, were immobilized on a streptavidin-coated sensor chip to test their affinity for control neuropeptides (concentration range 0.1-100 μM), such as decapeptide chicken GnRH and nonapeptide buserelin (both differing for one amino acids residue and also for the C-terminus in the case of buserelin). DNA-spielgemer did not bind buserelin while RNA-spielgemer recognized buserelin, albeit exhibited reduced affinity for it. The aptamers could be implemented into bioanalytical platform to detect gonadorelin but, till now, the attention was dedicated to the therapeutic field and in the pretreatment (peptide enrichment) of samples.

Leva et al. (2002) explored the potential application of anti-GnRH spiegelmers as a bioactive tool for cancer treatment by inhibiting the binding of GnRH to its cell surface receptor, overexpressed in hormone sensitive cancers, reducing in this way the release of the sexual hormones. A more recent study by Richards et al. proposed a DNA aptamer (NOX-1255)-based enrichment approach, after a clean-up of the equine urine investigated, to detect GnRH by means of LC-MS/MS [69, 125-126]. In particular, the effectiveness of the biotinylated L-DNA aptamer immobilized on streptavidin coated magnetic beads was explored. But a significant matrix interference, associated probably to the non-specific adsorption on the magnetic beads' surface, and a low analytical recovery (29 ± 15%) were obtained. Up to now no diagnostic aptasensors have been developed for analyzing gonadorelin which could really emphasize the biochemical properties of D-aptamers/L-aptamers presented by Leva et al. (2002). The aptamer technology has been improved over the last 20 years and represents an intriguing tool for biomimetic receptor source. However, the research in overcoming immunoassay limitation continues, eventually exploring new biomimetic approaches, based on biopolymers.

3.5.4.2 Molecular imprinting in forensic science

Molecularly imprinted polymers are a versatile tool that can be developed in multiple formats and applied in different fields. These receptors are easy to prepare and lack biological components, which leads to a far superior shelf life (see chapter 1) [130]. The possibility of tailoring the MIP to ensure the coverage of a broad range of analytes/applications, makes this technology a powerful and interesting tool in anti-doping research. They can be used directly as a recognition element in bioassay to quantify illicit drugs; or can be exploited as solid phase extraction (MIP-SPE) to clean several biological samples, which then are massively processed with analytical anti-doping election techniques (see paragraph 3.5.1) [130-133]. MIPs flexibility has led to a significant interest in the development of these analytical tools for the substances reported in the WADA prohibited list [7].

Bioanalytical portable assays in the forensic field represent an important tool for upstream in-situ screening. In this context, nowadays, the challenges rely on identifying newer rapid, specific, and sensitive strategies to quantify gonadorelin in urine samples. Hence, in response to this emerging issue, we carried out this study for gonadorelin detection. A selective MIP for gonadorelin was developed and first exploited using an optical biosensor (Surface Plasmon Resonance - SPR). It was then transferred to a disposable micro welled platform-based assay. To the best of our knowledge, no optical MIP-based sensor or MIP-based ELISA assay platform were developed to detect gonadorelin. Only a few articles have already been published using MIPs in the analysis of peptides in biological fluids and to concentrate the samples. Here, we propose a new approach to detect gonadorelin which could also be miniaturized, overcoming the pre-analytical step i.e., sample preparation, and, possibly, avoiding complex instrumentation. Our approach could be also implemented to simultaneously detect other bioactive peptides or it could also be transferred to columns to fulfill a different function in the analytical workflow, for upstream samples' extraction. The work is illustrated and discussed in the following paragraphs.

References

1. Lippi G, Franchini M, Guidi GC. Doping in competition or doping in sport? Br Med Bull. 2008; https://doi.org/10.1093/bmb/ldn014
2. Verroken M. Drug use and abuse in sport. Best Pract Res Clin Endocrinol Metab. 2000; https://doi.org/10.1053/beem.2000.0050
3. Childress AC, Komolova M, Sallee R. An update on the pharmacokinetic considerations in the treatment of ADHD with long-acting methylphenidate and amphetamine formulations. Expert Opin Drug Metab Toxicol. 2019; https://doi.org/10.1080/17425255.2019.1675636
4. Martínez-Sanz JM, Sospedra I, Ortiz CM, Baladía E, Gil-Izquierdo A, Ortiz-Moncada R. Intended or unintended doping? A review of the presence of doping substances in dietary supplements used in sports. Nutrients 2017; https://doi.org/10.3390/nu9101093
5. Backhouse, SH and Griffiths, C and McKenna, J. Tackling doping in sport: a call to take action on the dopogenic environment. British Journal of Sports Medicine. 2017; https://doi.org/10.1136/bjsports-2016-097169
6. Thevis M, Kuuranne T, Geyer H. Annual banned-substance review: analytical approaches in human sports drug testing. Drug Test Anal. 2018; https:// doi.org/10.1002/dta.2336
7. Prohibited list, https://wada-ama.org
8. Minunni M, Scarano S, Mascini M. Affinity-based biosensors as promising tools for gene doping detection. Trends Biotechnol. 2008; https://doi.org/10.1016/j.tibtech.2008.02.005
9. Scarano S, Ermini ML, Spiriti MM, Mascini M, Bogani P, Minunni M. Simultaneous Detection of Transgenic DNA by Surface Plasmon Resonance Imaging with Potential Application to Gene Doping Detection. Anal Chem. 2011; https://doi.org/10.1021/ac200877m
10. Streichert K, Seitz C, Hoffmann E, Boos I, Jelkmann W, Brunner T, Unverzagt C, Rubini M. Synthesis of Erythropoietins Site-Specifically Conjugated with Complex-Type N-Glycans. Chembiochem. 2019; https:// doi.org/10.1002/cbic.201900023
11. Kicman AT, Brooks RV, Cowan DA. Human chorionic gonadotrophin and sport. Br J Sports Med. 1991; https://doi.org/10.1136/bjsm.25.2.73
12. Thevis M, Kuuranne T, Walpurgis K, Geyer H, Schänzer W. Annual banned-substance review: analytical approaches in human sports drug testing. Drug Test Anal. 2016; https://10.1002/dta.1928

13. Simonsen D. Hormones and behavior. Horm. Behav. 2013; https://doi.org/10.2307/4510070
14. Sun Q, Zhao Z, Peptide Hormones as Tumor Markers in Clinical Practice. Enzymes 2017; https://doi.org/10.1016/bs.enz.2017.09.001
15. Ryan CA, Pearce G, Scheer J, Moura DS. Polypeptide hormones. Plant Cell. 2002; httpss://doi.org/10.1105/tpc.010484
16. Uniprot. org/uniprot/P01148 [GON1-HUMAN] (visited on 05/06/2020)
17. Sepideh K, Pegah V, "Gonadotropin Releasing Hormone," Reference Module in Biomedical Sciences, 2018; https://www.sciencedirect.com/topics/neuroscience/gnrh-antagonists
18. https://web.expasy.org/compute_pi/
19. Kang YK, Park HS. Propensities to form the β-turn and β-hairpin structures of d-Pro-Gly and Aib-d-Ala containing peptides: a computational study. 2016; https://doi.org/10.1039/C6NJ00614K
20. He Y, Zhang L, Zhu D, Song C. Design of multifunctional magnetic iron oxide nanoparticles/mitoxantrone-loaded liposomes for both magnetic resonance imaging and targeted cancer therapy. Int J Nanomedicine. 2014; https://doi.org/10.2147/IJN.S61880
21. Chevrier L, Guimiot F, de Roux N. GnRH receptor mutations in isolated gonadotropic deficiency. Mol Cell Endocrinol. 2011; https://doi.org/10.1016/j.mce.2011.04.018
22. Inaba T, Shimada S, Gonda M, Mori J, Tokunaga T, Geshi M, Torii R. Enzyme immunoassay of gonadotropin releasing hormone in the canine hypothalamus and plasma using monoclonal antibodies. Br Vet J. 1994; https://doi.org/10.1016/S0007-1935(05)80100-9
23. Okubo K, Nagahama Y. Structural and functional evolution of gonadotropin-releasing hormone in vertebrates. Acta Physiol [Oxf]. 2008; https://doi.org/10.1111/j.1748-1716.2008.01832.x
24. Casper RF. Clinical uses of gonadotropin-releasing hormone analogues. CMAJ. 1991; PMID: 1986827
25. Fontana F, Marzagalli M, Montagnani Marelli M, Raimondi M, Moretti RM, Limonta P. Gonadotropin-Releasing Hormone Receptors in Prostate Cancer: Molecular Aspects and Biological Functions. Int J Mol Sci. 2020; https://doi.org/10.3390/ijms21249511

26. Zhao J, Deng Y, Jiang Z, Qing H. G Protein-Coupled Receptors (GPCRs) in Alzheimer's Disease: A Focus on BACE1 Related GPCRs. Front Aging Neurosci. 2016; https://doi.org/10.3389/fnagi.2016.00058
27. Suo L, Chang X, Xu N, Ji H. The Anti-proliferative Activity of GnRH Through Downregulation of the Akt/ERK Pathways in Pancreatic Cancer. Front Endocrinol (Lausanne). 2019; https://doi.org/10.3389/fendo.2019.00370
28. Tsutsumi R, Webster NJ. GnRH pulsatility, the pituitary response and reproductive dysfunction. Endocr J. 2009; https://doi.org/10.1507/endocrj.k09e-185
29. Perone MJ, Castro MG. Prohormone and proneuropeptide synthesis and secretion. Histol Histopathol. 1997; PMID: 9302577
30. Park MK, Kogo H, Kawashima S, Wakabayashi K. Characterization of gonadotropin-releasing hormone (GnRH)-immunoreactive protein in the rat pineal gland. J Neurosci Res. 1995; https://doi.org/10.1002/jnr.490410311
31. Okubo K, Nagahama Y. Structural and functional evolution of gonadotropin-releasing hormone in vertebrates. Acta Physiol (Oxf). 2008; https://doi.org/10.1111/j.1748-1716.2008.01832
32. Seeburg PH, Adelman JP. Characterization of cDNA for precursor of human luteinizing hormone releasing hormone. Nature. 1984; https://doi.org/10.1038/311666a0
33. Knobil E. The neuroendocrine control of the menstrual cycle. Recent Prog Horm Res. 1980; https://doi.org/10.1016/b978-0-12-571136-4.50008-5
34. Voliotis M, Li XF, De Burgh R, Lass G, Lightman SL, O'Byrne KT, Tsaneva-Atanasova K. The Origin of GnRH Pulse Generation: An Integrative Mathematical-Experimental Approach. J Neurosci. 2019; https//doi.org/10.1523
35. Helm VJ, Müller BW. Stability of gonadorelin and triptorelin in aqueous solution. Pharm Res. 1990; https://doi.org/10.1023/a:1015981704133
36. Evans BJ, King AT, Katsifis A, Matesic L, Jamie JF. Methods to Enhance the Metabolic Stability of Peptide-Based PET Radiopharmaceuticals. Molecules. 2020; https://doi.org/10.3390/molecules25102314
37. Hoitink MA, Beijnen JH, Bult A, van der Houwen OA, Nijholt J, Underberg WJ. Degradation kinetics of gonadorelin in aqueous solution. J Pharm Sci. 1996; https://10.1021/js9601187
38. Khazeni S, Varamini P. Gonadotropin Releasing Hormone. 2018; https://doi.org/10.1016/B978-0-12-801238-3.98031-0

39. Strehlitz B, Reinemann C, Linkorn S, Stoltenburg R. Aptamers for pharmaceuticals and their application in environmental analytics. Bioanal Rev. 2012; https://doi.org/10.1007/s12566-011-0026-1
40. Clinical and Research Information on Drug-Induced Liver Injury [Internet]. Bethesda (MD): National Institute of Diabetes and Digestive and Kidney Diseases; 2012-. Gonadotropin Releasing Hormone (GnRH) Analogues. [Updated 2018 Mar 20]. Available from: https://www.ncbi.nlm.nih.gov/books/NBK547863/
41. Thomas A, Walpurgis K, Krug O, Schänzer W, Thevis M. Determination of prohibited, small peptides in urine for sports drug testing by means of nano-liquid chromatography/benchtop quadrupole orbitrap tandem-mass spectrometry. J Chromatogr A. 2012; https://doi.org/ 10.1016/j.chroma.2012.07.022
42. Zvereva I, Dudko G, Dikunets M. Determination of GnRH and its synthetic analogues' abuse in doping control: Small bioactive peptide UPLC-MS/MS method extension by addition of in vitro and in vivo metabolism data; evaluation of LH and steroid profile parameter fluctuations as suitable biomarkers. Drug Test Anal. 2018; https://doi.org/10.1002/dta.2256
43. Thibier M. Use of gonadoliberin (GnRH) or analogs in veterinary medicine. Pharmacologic and therapeutic evaluation in cattle. Ann Rech Vet. 1988; PMID: 3142332
44. Luchterhand M, Gamarra CA, Gennari RS, Carvalho PD, Barletta RV, Souza AH. Ovulation and fertility response to commercially available GnRH products in lactating cows synchronized with the Double-Ovsynch protocol. Anim Reprod Sci. 2019; https://doi.org/10.1016/j.anireprosci.2019.01.006
45. https://www.fda.gov
46. Galtd.org.au/2018-List of permanently banned substances visited on 16/01/2020)
47. Caraty A, Skinner DC. Gonadotropin-releasing hormone in third ventricular cerebrospinal fluid: Endogenous distribution and exogenous uptake. Endocrinology 2008; https://doi.org/10.1210/en.2007-1636
48. Baram T, Koch Y, Hazum E, Fridkin M. Gonadotropin-releasing hormone in milk. Science 1977; https://doi.org/10.1126/science.333582
49. Görgens C, Guddat S, Thomas A, Thevis M. Recent improvements in sports drug testing concerning the initial testing for peptidic drugs [< 2 kDa] - sample preparation, mass spectrometric detection, and data review. Drug. Test. Anal. 2018; https://doi.org/10.1002/dta.2503

50. Wada-ama.org/ WADA technical Document _ TD2019MRPL
51. Wood GC, Dass C, Iyer MR, Fleischner AM, Sheth BB. Stability of deslorelin injection. PDA J Pharm Sci Technol. 1997; PMID: 9357302.
52. Wood GC, Iyer MR, Geller AM, Fleischner AM, Sheth BB. A high-pressure liquid chromatography assay method for analysis of deslorelin and benzyl alcohol in deslorelin injection. J Liq Chrom Relat Tech 1998; https://doi.org/10.1080/10826079808006617
53. Corran PG, Sutcliffe N. Identification of gonadorelin [LHRH] derivatives: Comparison of reversed-phase high-performance liquid chromatography and micellar electrokinetic chromatography. J. Chromatogr. 1993; https://doi.org/10.1016/0021-9673(93)80060-l
54. Frasconi M, Mazzarino M, Botrè F, Mazzei F. Surface plasmon resonance immunosensor for cortisol and cortisone determination. Anal Bioanal Chem. 2009; https://doi.org/10.1007/s00216-009-2914-6
55. Hoitink MA, Beijnen JH, Boschma MUS, Bult A, Hop E, Nijholt J, Versluis C, Wiese G, Underberg, WJU. Identification of the degradation products of gonadorelin and three analogues in aqueous solution, Anal Chem. 1997; https://doi.org/10.1021/ac970634x
56. Stanová A, Marák J, Maier V, Ranc V, Znaleziona J, Sevcík J, Kaniansky D. Analysis of buserelin in urine by online combination of capillary zone electrophoresis with electrospray mass spectrometry. Electrophoresis. 2010; https://doi.org/10.1002/elps.200900422.
57. Lodén H, Amini A. Quantification of buserelin in a pharmaceutical product by multiple-injection CZE. Electrophoresis. 2007; https://doi.org/10.1002/elps.200600636
58. Tamizi E, Kenndler E, Jouyban A. A stability indicating capillary electrophoresis method for analysis of buserelin. Iran J Pharm Res. 2014; PMID: 25276180
59. Rhodes GR, Boppana VK, Rubenfield MJ. Fluorescence derivatization approaches for quantitative high-performance liquid chromatography of peptides. J Control Release 1990; https://doi.org/10.1016/0168-3659(90)90003-C
60. Thomas A, Geyer H, Kamber M, Schänzer W, Thevis M. Mass spectrometric determination of gonadotrophin-releasing hormone (GnRH) in human urine for doping control purposes by means of LC-ESI-MS/MS. J Mass Spectrom. 2008; https://doi.org/10.1002/jms.1453

61. Mazzarino, M., Calvaresi, V., de la Torre, X. et al. Development and validation of a liquid chromatography–mass spectrometry procedure after solid-phase extraction for detection of 19 doping peptides in human urine. Forensic Toxicol. 2015; https://doi.org/10.1007/s11419-015-0279-4
62. Wang Y, Chen LLH, Chien YW. HPLC analysis of gonadotropin-releasing hormone and its analogues using benzoin as a fluorogenic reagent. J Liq Chromatogr Relat Technol. 1999; https://doi.org/10.1081/JLC-100101811
63. Bi M, Bhatia KS, Singh J. A valid high performance liquid chromatography method for quantification of luteinizing hormone releasing hormone. J Liq Chromatogr Relat Technol. 1998; https://doi.org/10.1080/10826079808000530
64. Guan F, You Y, Li X, Robinson MA. A comprehensive approach to detecting multitudinous bioactive peptides in equine plasma and urine using hydrophilic interaction liquid chromatography coupled to high resolution mass spectrometry. Drug Test Anal. 2019; https://doi.org/10.1002/dta.2671
65. Görgens C, Guddat S, Thomas A, Thevis M. Recent improvements in sports drug testing concerning the initial testing for peptidic drugs (< 2 kDa) - sample preparation, mass spectrometric detection, and data review. Drug Test Anal. 2018; https://doi.org/10.1002/dta.2503.
66. Cuervo D, Loli C, Fernández-Álvarez M, Muñoz G, Carreras D. Determination of doping peptides via solid-phase microelution and accurate-mass quadrupole time-of-flight LC-MS. J Chromatogr B Analyt Technol Biomed Life Sci. 2017; https://doi.org/10.1016/j.jchromb.2017.08.044
67. Judák P, Grainger J, Goebel C, Van Eenoo P, Deventer K. DMSO Assisted Electrospray Ionization for the Detection of Small Peptide Hormones in Urine by Dilute-and-Shoot-Liquid-Chromatography-High Resolution Mass Spectrometry. J Am Soc Mass Spectrom. 2017; https://doi.org/10.1007/s13361-017-1670-7
68. Semenistaya E, Zvereva I, Krotov G, Rodchenkov G. Solid-phase extraction of small biologically active peptides on cartridges and microelution 96-well plates from human urine. Drug Test Anal. 2016; https://doi.org/10.1002/dta.1890
69. Richards SL, Cawley AT, Cavicchioli R, Suann CJ, Pickford R, Raftery MJ. Aptamer based peptide enrichment for quantitative analysis of gonadotropin-releasing hormone by LC-MS/MS. Talanta 2016; https://doi.org/10.1016/j.talanta.2016.01.006

70. Håkansson K, Emmett MR, Hendrickson CL, Marshall AG. High-sensitivity electron capture dissociation tandem FTICR mass spectrometry of microelectrosprayed peptides. Anal Chem. 2001; https://doi.org/10.1021/ac010141z
71. Vanhee C, Janvier S, Desmedt B, Meons G, Deconinck E, De Beer JO., Courselle P. Analysis of illegal peptide biopharmaceuticals frequently encountered by controlling agencies. Talanta 2015; https://doi.org/10.1016/j.talanta.2015.04.022
72. Sobhi HR, Vatansever B, Wortmann A, Grouzmann E, Rochat B. Generic approach for the sensitive absolute quantification of large undigested peptides in plasma using a particular liquid chromatography-mass spectrometry setup. J Chromatogr A. 2011 https://doi.org/10.1016/j.chroma.2011.09.072
73. L.J. Kricka, J.Y. Park, Immunochemical techniques, in: Burtis, C.A.; Ashwood, E.R.; Bruns, D.E. [Eds.] 6nd ed, Tietz textbook of clinical chemistry and molecular diagnostics, Elsevier Health Sciences, London, 2017, pp. 348-367
74. Moczko E, Díaz R, Rivas B, García C, Pereira E, Piletsky S, Cáceres C. Molecularly imprinted nanoparticles assay (MINA) in pseudo-ELISA: An alternative to detect and quantify octopamine in water and human urine samples. Polymers 2019; https://doi.org/10.3390/polym11091497
75. Lequin RM. Enzyme immunoassay (EIA)/enzyme-linked immunosorbent assay (ELISA). Clin Chem. 2005; https://doi.org/10.1373/clinchem.2005.051532
76. Gao L, Yang Q, Wu P, Li F. Recent advances in nanomaterial-enhanced enzyme-linked immunosorbent assays. Analyst 2020; https://doi.org/10.1039/d0an00597e
77. Dos Santos Maciel MO, Soares MF, Costa SF, Bragato JP, de Freitas JH, Venturin GL, Melo LM, Rebech GT, Reed S, de Lima VMF. Development of plasmonicc ELISA for the detection of anti-Leishmania sp. IgG antibodies. J Immunol Methods 2019; https://doi.org/10.1016/j.jim.2019.112664
78. Yang Q, Cai R, Xiao W, Wu Z, Liu X, Xu Y, Xu M, Zhong H, Sun G, Liu Q, Fu Q, Xiang J. Plasmonic ELISA for sensitive detection of disease biomarkers with a smart phone-based reader. Nanoscale Res Lett. 2018; https://doi.org/10.1186/s11671-018-2806-9
79. Torrini F, Palladino P, Brittoli A, Baldoneschi V, Minunni M, Scarano S. Characterization of troponin T binding aptamers for an innovative enzyme-linked oligonucleotide assay (ELONA). Anal Bioanal Chem. 2019; https://doi.org/10.1007/s00216-019-02014-7

80. Hong S, She Y, Cao X, Wang M, Zhang C, Zheng L, Wang S, Ma X, Shao H, Jin M, Jin F, Wang J. Biomimetic enzyme-linked immunoassay based on a molecularly imprinted 96-well plate for the determination of triazophos residues in real samples. RSC Adv. 2018; https://doi.org/10.1039/c8ra03531h
81. Zhdanov A, Keefe J, Franco-Waite L, Konnaiyan KR, Pyayt A. Mobile phone based ELISA (MELISA). Biosens Bioelectron. 2018; https://doi.org/10.1016/j.bios.2017.12.033
82. Gore AC. GnRH pulsatility. In: GnRH: The Master Molecule of Reproduction. Boston, MA: Kluwer, 2002, p. 29– 52
83. Morris M, Wren JA, Sundberg DK. Central neural peptides and catecholamines in spontaneous and DOCA/salt hypertension. Peptides 1981; https://doi.org/10.1016/S0196-9781(81)80035-6
84. Holland MC, Gothilf Y, Meiri I, King JA, Okuzawa K, Elizur A, Zohar Y. Levels of the native forms of GnRH in the pituitary of the gilthead seabream, Sparus aurata, at several characteristic stages of the gonadal cycle. Gen Comp Endocrinol. 1998; https//doi.org/10.1006/gcen.1998.7138
85. Kah O, Zanuy S, Pradelles P, Cerdà JL, Carrillo M. An enzyme immunoassay for salmon gonadotropin-releasing hormone and its application to the study of the effects of diet on brain and pituitary GnRH in the sea bass, Dicentrarchus labrax. Gen Comp Endocrinol. 1994; https//doi.org/10.1006/gcen.1994.1146
86. Rodríguez L, Begtashi I, Zanuy S, Carrillo M. Long-term exposure to continuous light inhibits precocity in European male sea bass (Dicentrarchus labrax, L.): hormonal aspects. Gen Comp Endocrinol. 2005; https//doi.org/10.1016/j.ygcen.2004.10.011
87. Moreno-Bondi MC, Benito-Peña E. Analytical applications of biomimetic recognition elements — an update. Anal Bioanal Chem. 2021; https://doi.org/10.1007/s00216-021-03534-x
88. Acero Sanchez JL, Henry OYF, Mairal T, Laddach N, Nygren A, Hauch S, Fetisch J, O'Sullivan CK. Colorimetric quantification of mRNA expression in rare tumour cells amplified by multiple ligation-dependent probe amplification. Anal Bioanal Chem. 2010; https://doi.org/10.1007/s00216-010-3830-5
89. Tang SP, Canfarotta F, Smolinska-Kempisty K, Piletska E, Guerreiro A, Piletsky S. A pseudo-ELISA based on molecularly imprinted nanoparticles for detection of gentamicin in real samples. Anal Methods 2017; https://doi.org/10.1039/c7ay00398f

90. Cenci L, Piotto C, Bettotti P, Bossi AM. Study on molecularly imprinted nanoparticle modified microplates for pseudo-ELISA assays. Talanta 2018; https://doi.org/10.1016/j.talanta.2017.10.018
91. Garcia Y, Smolinska-Kempisty K, Pereira E, Piletska E, Piletsky S. Development of competitive 'pseudo'-ELISA assay for measurement of cocaine and its metabolites using molecularly imprinted polymer nanoparticles. Anal Methods 2017; https://doi.org/10.1039/c7ay01523b
92. Liu G, She Y, Hong S, Wang J, Xu D. Development of ELISA-like fluorescence assay for melamine detection based on magnetic dummy molecularly imprinted polymers. Appl Sci. 2018; https://doi.org/10.3390/app8040560
93. Smolinska-Kempisty K, Guerreiro A, Canfarotta F, Cáceres C, Whitcombe MJ, Piletsky S. A comparison of the performance of molecularly imprinted polymer nanoparticles for small molecule targets and antibodies in the ELISA format. Sci Rep. 2016; https://doi.org/10.1038/srep37638
94. Esen C, Czulak J, Cowen T, Piletska E, Piletsky SA (2019) Highly efficient abiotic assay formats for methyl Parathion: molecularly imprinted polymer nanoparticle assay as an alternative to enzyme-linked immunosorbent assay. Anal Chem. 2019; https://doi.org/10.1021/acs.analchem.8b04065
95. Munawar H, Smolinska-Kempisty K, Cruz AG, Canfarotta F, Piletska E, Karim K, Piletsky SA. Molecularly imprinted polymer nanoparticle-based assay (MINA): application for fumonisin B1 determination. Analyst 2018; https://doi.org/10.1039/c8an00322j
96. Peng D, Li Z, Wang Y, Liu Z, Sheng F, Yuan Z. Enzyme-linked immunoassay based on imprinted microspheres for the detection of sulfamethazine residue. J Chromatogr A 2017; https://doi.org/10.1016/j.chroma.2017.05.016
97. Piletsky SS, Cass AEG, Piletska EV, Czulak J, Piletsky SA. A novel assay format as an alternative to ELISA: MINA test for biotin. ChemNanoMat. 2018; https://doi.org/10.1002/cnma.201800393
98. Chianella I, Guerreiro A, Moczko E, Caygill JS, Piletska E V, De Vargas Sansalvador IMP, Whitcombe MJ, Piletsky SA. Direct replacement of antibodies with molecularly imprinted polymer nanoparticles in ELISA - development of a novel assay for vancomycin. Anal Chem. 2013; https://doi.org/10.1021/ac402102j
99. Chen S, Gan N, Zhang H, Hu F, Li T, Cui H, Cao Y, Jiang Q. A portable and antibody-free sandwich assay for determination of chloramphenicol in food based

on a personal glucose meter. Anal Bioanal Chem. 2015; https://doi.org/10.1007/s00216-015-8478-8

100. Lazcka O, Del Campo FJ, Muñoz FX. Pathogen detection: a perspective of traditional methods and biosensors. Biosens Bioelectron. 2007; https://doi.org/10.1016/j.bios.2006.06.036

101. Bhalla N, Jolly P, Formisano N, Estrela P. Introduction to biosensors. Essays Biochem. 2016; hyyps://doi.org/10.1042/EBC20150001

102. M. Mascini, "A brief story of biosensor technology" in Biotechnological Applications of Photosynthetic Proteins: Biochips Biosensors and Biodevices, Boston, MA, USA:Springer, pp. 4-10, 2006

103. Liu Y, Matharu Z, Howland MC, Revzin A, Simonian AL. Affinity and enzyme-based biosensors: recent advances and emerging applications in cell analysis and point-of-care testing. Anal Bioanal Chem. 2012; https://doi.org/10.1007/s00216-012-6149-6

104. Chen Y, Fan F, Fang G, Deng Q, Wang S. Fluorometric determination of tyramine by molecularly imprinted upconversion fluorescence test strip. Mikrochim Acta 2020; https://doi.org/10.1007/s00604-020-04554-7

105. Cai X, Rivas G, Farias PAM, Shiraishi H, Wang J, Paleček E. Potentiometric stripping analysis of bioactive peptides at carbon electrodes down to subnanomolar concentrations. Anal Chim Acta 1996; https://doi.org/10.1016/0003-2670(96)00189-4

106. Gutiérrez-Gallego R, Llop E, Bosch J, Segura J. Surface plasmon resonance in doping analysis. Anal Bioanal Chem. 2011; https://doi.org/10.1007/s00216-011-4830-9

107. Mazzei F, Antiochia R, Botrè F, Favero G, Tortolini C. Affinity-based biosensors in sport medicine and doping control analysis. Bioanalysis 2014; https://doi.org/10.4155/bio.13.308

108. Scarano A, Spiriti MM, Tigli G, Bogani P, Buiatti M, Mascini M, Minunni M. Affinity Sensing for Transgenes Detection in Antidoping Control. Anal Chem. 2009; https://doi.org/10.1021/ac901445b

109. Scarano S, Ermini ML, Spiriti MM, Mascini M, Bogani P, Minunni M. Simultaneous detection of transgenic DNA by surface plasmon resonance imaging with potential application to gene doping detection. Anal Chem. 2011; https://10.1021/ac200877m

110. Homola J. Present and future of surface plasmon resonance biosensors. Anal Bioanal Chem. 2003; https://doi.org/10.1007/s00216-003-2101-0

111. Homola J. Surface plasmon resonance sensors for detection of chemical and biological species. Chem Rev. 2008; https://doi.org/10.1021/cr068107d

112. Biacore X100 Handbook BR-1008-10 Edition AC

113. Roh S, Chung T, Lee B. Overview of the Characteristics of Micro- and Nano-Structured Surface Plasmon Resonance Sensors. Sensors, 2011; https://doi.org/10.3390/s110201565

114. Zeni, L., Perri, C., Cennamo, N. et al. A portable optical-fibre-based surface plasmon resonance biosensor for the detection of therapeutic antibodies in human serum. Sci Rep. 2020; https://doi.org/10.1038/s41598-020-68050-x

115. Ruscito A, DeRosa MC. Small-Molecule Binding Aptamers: Selection Strategies, Characterization, and Applications. Front Chem. 2016; https://doi.org/10.3389/fchem.2016.00014

116. Mayer G, Jenne A. Aptamers in research and drug development. BioDrugs. 2004; https.//doi.org/10.2165/00063030-200418060-00002

117. Byun J. Recent Progress and Opportunities for Nucleic Acid Aptamers. 2021; https://doi.org/10.3390/life11030193

118. McKeague M, Derosa MC. Challenges and opportunities for small molecule aptamer development. J Nucleic Acids. 2012; https://doi.org/10.1155/2012/748913

119. Kandimalla VB, Ju h. New Horizons with A Multi Dimensional Tool for Applications in Analytical Chemistry—Aptamer. Analytical Letters 2004; https://doi.org/10.1081/AL-200028005

120. Strehlitz B, Stoltenburg R. Selex and Its Recent Optimizations. Aptamers Bioanal. 2009; http://doi.org/10.1002/9780470380772

121. Berezovski MV, Musheev MU, Drabovich AP, Jitkova JV, Krylov SN. Non-SELEX: selection of aptamers without intermediate amplification of candidate oligonucleotides. Nat Protoc. 2006; https://doi.org/10.1038/nprot.2006.200

122. Lisi S, Fiore E, Scarano S, Pascale E, Boehman Y, Ducongé F, Chierici S, Minunni M, Peyrin E, Ravelet C. Non-SELEX isolation of DNA aptamers for the homogeneous-phase fluorescence anisotropy sensing of tau Proteins. Anal Chim Acta. 2018; https://doi.org /10.1016/j.aca.2018.07.029

123. Connelly, C.M., Numata, T., Boer, R.E. et al. Synthetic ligands for PreQ1 riboswitches provide structural and mechanistic insights into targeting RNA tertiary structure. Nat Commun. 2019; https://doi.org/10.1038/s41467-019-09493-3

124. Lotz TS, Suess B. Small-Molecule-Binding Riboswitches. Microbiol Spectr. 2018; https://doi.org/10.1128/microbiolspec.RWR-0025-2018

125. Strehlitz B, Reinemann C, Linkorn S, Stoltenburg R. Aptamers for pharmaceuticals and their application in environmental analytics. Bioanal Rev. 2012; https://doi.org/10.1007/s12566-011-0026-1

126. Leva S, Lichte A, Burmeister J, Muhn P, Jahnke B, Fesser D, Erfurth J, Burgstaller P, Klussmann S. GnRH Binding RNA and DNA Spiegelmers: A Novel Approach toward GnRH Antagonism. Chem Biol. 2002; https://doi.org/10.1016/S1074-5521(02)00111-4

127. Young BE, Kundu N, Sczepanski JT. Mirror-Image Oligonucleotides: History and Emerging Applications. Chemistry. 2019; https://doi.org/10.1002/chem.201900149

128. Eulberg D, Klussmann S. Spiegelmers: biostable aptamers. Chembiochem. 2003; https://doi.org/10.1002/cbic.200300663

129. Wlotzka B, Leva S, Eschgfäller B, Burmeister J, Kleinjung F, Kaduk C, Muhn P, Hess-Stumpp H, Klussmann S. In vivo properties of an anti-GnRH Spiegelmer: an example of an oligonucleotide-based therapeutic substance class. 2002; https://doi.org/10.1073/pnas.132067399

130. Hand RA, Piletska E, Bassindale T, Morgan G, Turner N. Application of molecularly imprinted polymers in the anti-doping field: sample purification and compound analysis. Analyst 2020; https://doi.org/10.1039/d0an00682c

131. Xiao D, Jiang Y, Bi Y. Molecularly imprinted polymers for the detection of illegal drugs and additives: a review. Mikrochim. Acta. 2018; https://doi.org/10.1007/s00604-018-2735-4

132. Hasanah AN, Rahayu D, Pratiwi R, Rostinawati T, Megantara S, Saputri FA, Puspanegara KH. Extraction of atenolol from spiked blood serum using a molecularly imprinted polymer sorbent obtained by precipitation polymerization. Heliyon 2019; https/doi.org/10.1016/j.heliyon.2019.e01533

133. Soriano A.S, Herrero-Martìnez J.M., Esteve-Turrillas F.A., Armenta S. Molecularly imprinted polymer-based device for field collection of oral fluid samples for cocaine identification. J. Chromatogr. A 2020; https://doi.org/10.1016/j.chroma.2020.461629

3.6 A (bio)-sensing assay for gonadorelin detection via a PNE - based MIP

The study we are going to present is based on the following article:

- **F. Torrini**, P. Palladino, V. Baldoneschi, S. Scarano, M. Minunni. Sensitive 'two-steps' competitive assay for gonadotropin-releasing hormone detection via SPR biosensing and polynorepinephrine-based molecularly imprinted polymer, Analytica Chimica Acta 1161 (2021) 338481.

3.6.1 Aim and objectives of the study

This research study introduces an innovative sensing bioassay for the detection of gonadorelin in urine. In particular, we exploited an SPR biosensing platform to develop a label-free and regenerable device for its detection. The main novelty of the study relies on the development of a biocompatible, stable, and low-cost biomimetic receptor, the core of a sensing platform. This receptor represents an effective alternative to classic antibodies and, in the specific case of gonadorelin, is a simple and cost-effective solution to the lack of receptors (as described in the previous paragraphs). Starting from norepinephrine monomer, a highly selective and sensitive MIP was developed and optimized for optical real-time and label-free SPR biosensing. The selectivity has been addressed by testing a series of peptides, from high to low similarity, both in terms of molecular weight and primary sequence. Due to the very low molecular weight of gonadorelin (1182 Da), a two-steps competitive assay was established. Particular attention has been paid to the design of the competitor and its binding affinity constant towards the MIP, being a key step for the success of the competitive strategy. The SPR sensing assay was first optimized in standard conditions and finally applied to untreated urine samples, achieving the sensitivity required by WADA guidelines. The MIP, tested in parallel with a monoclonal antibody, the only commercially available, gave comparable results in terms of affinity constants and selectivity towards possible interfering analytes. However, the biomimetic receptor appears clearly superior in terms of sensitivity and reproducibility. This, together with its preparation simplicity,

the extremely low-cost of the monomer and its reusability for hundreds of measurements, make polynorepinephrine-based MIPs powerful rivals to immune-based approaches in the near future for similar applications.

3.6.2 Introduction

At present, the development of MIPs targeting biomolecules, such as peptides and proteins, is probably one of the most promising and challenging research areas in biosensing. In recent years, successful results were obtained by the so-called epitope imprinting (see paragraph 1.5.2) when the choice of the polymer goes in the direction of a soft and biocompatible material. In this framework, we report the development of a highly selective PNE-based MIP for the sensitive detection of gonadorelin (10 aa, 1182.33 Da) by SPR transduction. In mass-sensitive optical techniques, such as SPR, in which the bottleneck of the detection is strictly related to the molecular weight of the analyte [1], the imprinting of short peptides is mainly effective when they belong to high molecular weight (MW) biomolecules [2] able to elicit a valuable SPR response through MIP binding. Thus, in case of low MW peptides like gonadorelin (< 1200 Da) they must be detected by competitive assays [2-3] to achieve the required sensitivity. In this format, the target biomolecule competes with a chemically identical labeled molecule for the receptors' binding sites onto a solid phase, the MIP receptor in this case.

The PNE-based MIP here developed for gonadorelin recognition was exploited to set up an ultra-sensitive, label-free, and real-time competitive assay for analyses in urine and the perspective use in anti-doping controls. The main analytical parameters were accurately investigated by SPR, exploiting the competition between gonadorelin and a tailored molecule able to compete with gonadorelin for the same MIP binding cavities. The analytical performances were compared with a commercial monoclonal antibody, and with two ELISA kits on the market, evidencing the great advantages of MIP-based detection by several points of view (costs, durability, reusability, versatility etc.).

3.6.3 Experimental section: materials and methods

3.6.3.1 Reagents

Gonadorelin European Pharmacopoeia (EP) Reference Standard (acronym G) {pGLU}HWSYGLRPG-NH_2 (MW = 1182.33 Da) and L-norepinephrine hydrochloride (NE, ≧98.0%), tris(hydroxymethyl)aminomethane hydrochloride (Tris-HCl, ≧ 99.%), 4-(2-hydroxyethyl)piperazine-1-ethanesulfonic acid (HEPES), sodium chloride, hydrochloric acid, sodium acetate trihydrate, acetic acid (≧ 99.7%), sodium dodecyl sulfate (SDS), polyoxyethylene sorbitan monooleate (Tween-20), 1-ethyl-3-(dimethylaminopropyl) carbodiimide (EDAC), N-hydroxysuccinimide (NHS), ethanolamine hydrochloride (EA) were all purchased from Sigma-Aldrich (Milan, Italy). Streptavidin from *Streptomyces avidinii* was from Alfa Aesar (Waltham, MA, USA). Artificial urine prepared according to DIN EN 1616:1999, was obtained from Pickering Laboratories (Mountain View, USA) and used without any further purification. Synthetic urine composition: Urea 25.00 g L^{-1}, sodium chloride 9.00 g L^{-1}, potassium dihydrogen orthophosphate 2.50 g L^{-1}, disodium hydrogen orthophosphate anhydrous 2.50 g L^{-1}, sodium sulphite hydrated 3.00 g L^{1}, ammonium chloride 3.00 g L^{-1}, creatinine 2.00 g L^{-1}, pH 6.6+/-0.1. Ultrapure Milli-Q™ water (R ≧ 18.2 MΩ • cm) was used to prepare all the buffer solutions. Biotinylated gonadorelin (acronym BG) {pGLU}HWSYGLRPG{Lys(biotin)} (MW = 1537.75 Da) and negative control peptides: Leuprolide acetate {pGLU}HWSY{d-LEU}LRP-NHEt (MW = 1209.4 Da); PEPT-1 H_3COC-ISLAPKAQI-NH_2 (MW 981.20 Da); PEPT-2 FLDSPDR-NH_2 (MW 847.92 Da); PEPT-3 EEAKEAEDGPM (MW = 1205.25 Da) were synthesized by GenScript (Leiden, Netherlands). HBS-EP (10 mmol L^{-1} HEPES, 150 mmol L^{-1} NaCl, 3 mmol L^{-1} EDTA, 0.005% Tween-20, pH 7.4) was used as running buffer for all SPR-based experiments; HBS-EP was also used for peptides' dilutions and as buffer/solvent of the analyte and "competitor" undergoing the binding events. All chemicals used were of analytical grade. Buffered solutions were filtered through a microporous filter (0.22 μm). GnRH1 monoclonal antibody (G-mAb) was from Life Technologies

(Monza, Italy). Gold sensor chips and CM5 chips were purchased from GE Healthcare Life Sciences (Milan, Italy). All the SPR measurements were carried out by using Biacore X-100 instrumentation. A competitive inhibition enzyme immunoassay (ELISA) kit for Human Gonadotropin Releasing Hormone (GnRH) was obtained from ELISA Genie (Ireland) and used by following the manufacturer's indications.

3.6.3.2 Preparation of imprinted polymers and SPR experimental setup

Molecularly imprinted polymers (MIPs) were grafted onto gold sensor chip surface pre-cleaned with a fresh piranha solution (3:1 (v/v) H_2SO_4/H_2O_2) for 2 min, rinsed with deionized water and dried under nitrogen flow. Briefly, the chip surface was modified by dropping the polymerization mixture containing the functional monomer NE (2.00 g L^{-1} in 10 mmol L^{-1} Tris-HCl, pH 8.5) in co-presence of the G template (acronym MIP_G). Two different template (G) concentrations were used to explore different events, respectively a high G (422.9 µmol L^{-1}) concentration to study the new system and a low G (4.2 µmol L^{-1}) one to design a competitive assay. The polymerization was carried out at 25.00 ± 0.5 °C in a thermostatic oven for 5 h; then ensued a washing step with acetic acid (5 % v/v) and deionized water to remove the template from the binding cavities of the obtained MIP_G. A non-imprinted polymer (NIP) was prepared following the same procedure as for the MIP_G without G template addition. A surface passivation step was introduced for MIP_G imprinted at low template G concentration (4.2 µmol L^{-1}), theoretically leading to low density MIP_G, and NIP as follows: an aqueous solution of 1 mM cysteine, 1 mM lysine and 1 mM tris(hydroxymethyl)aminomethane was dropped onto the polynorepinephrine surface and left overnight at 25 °C by avoiding evaporation. The quinone residues of PNE interact with amine and thiol groups via Schiff base reaction and/or Michael-type addition modifying the MIP_G surface [4-77]. The molded sensor chip was inserted into the instrument and flushed with HBS-EP pH 7.4 to equilibrate the surface at a

constant flow rate of 5.00 µL min^{-1} and 25.00 ± 0.5 °C. Afterwards, a single-cycle kinetics (SCK) analysis was performed for both gonadorelin (G) and biotinylated gonadorelin (BG). SCK consists in a sequential injection of five increasing concentrations of the target molecule over the MIP_G surface, bypassing the regeneration step (flow rate: 5.00 µL min^{-1}, T = 25 °C). The five concentrations diluted in HBS-EP pH 7.4, spanning from 0.81 µmol L^{-1} to 13.00 µmol L^{-1}, were flushed over the MIP_G surface for 120 s each, followed by 30 s dissociation phase with running buffer. After each measuring cycle, the polymeric surface was regenerated by injecting short (24 s) pulses of acetic acid 5 % (v/v) aq. solution, 20 mmol L^{-1} HCl, 0.05% SDS and 20 mmol L HCl. The effectiveness of the regeneration was confirmed by the baseline level which turns to the value before the injection of the analyte.

The instrument worked with two channels in series for simultaneous measurements, and the whole analysis was completely automated by setting up a custom wizard template. The data analysis was performed by using BIAEvaluation 3.1 Software (GE Healtchare Life Sciences) to extract kinetic parameters (*ka* = association rate constant; *kd* = dissociation rate constant) and the relative equilibrium constants (K_D) from SCK analysis by using a two-state binding model fitting. All the other curves obtained were fitted to one-site binding model and the equation applied was $y=(R_{max}*X)/(K_D+X)$, where R_{max} is the maximum response (RU). The selectivity of MIP_G was evaluated by testing several peptides (4.23 µmol L^{-1}) from high to low similarity with G. The performance of MIP_G was directly compared to a standard immune-based SPR assay. For anti-G antibody (G-mAb), the immobilization protocol on a carboxymethyl dextran matrix occurs through amino coupling. After an activation step with 50 mmol L^{-1} NHS and 200 mmol L^{-1} EDAC (contact time: 420 s, flow rate: 10 µL min^{-1}), the dextran matrix was modified with G-mAb (contact time: 420 s, 10 µg mL^{-1} in 10 mmol L^{-1} acetate buffer, pH 4.0 selected by a 'pH scouting' [8]), followed by the deactivation of the surface with EA (contact time: 420 s, 10 µg mL^{-1}). Measurements were all performed at least in triplicate.

3.6.3.3 Competitive binding assay

A two-steps competitive assay to detect G was performed exploiting sequential injections of the analyte G and its competitor conjugated with streptavidin (BG:S) (flow rate: 5.00 µL min^{-1}, T = 25 °C). The latter was prepared as follows: a 4:1 molar ratio solution of BG and streptavidin in HBS-EP pH 7.4 (1.33 µmol L^{-1} and 0.33 µmol L^{-1}, respectively) was incubated for 10 min in tubes at 4 °C. Non-specific adsorption of streptavidin on MIP_G surface was tested before G testing. For SPR measurements of G, the analyte was first injected on the MIP_G for 120 s at a standard concentration and, after the washing step to remove the unbound analyte, the BG:S competitor was injected for 240 s at a fixed concentration (BG 1.33 µmol L^{-1}, and S 0.33 µmol L^{-1}) to bind eventually MIP_G remaining free cavities. G was tested within a concentration range: 0.42-13.54 nmol L^{-1}.

MIP_G was then regenerated with short pulses (24 s) of acetic acid 5% (v/v) aq. solution, 20 mmol L^{-1} HCl and 0.05% SDS. Each standard concentration was tested at least in three independent replicates. The same protocol was used to quantify G in spiked urine samples; the injection of urine samples spiked with G substituted the standard solution injections. All the SPR results collected from the competitive assays (one-step and two-steps) are here reported as the net G binding after the subtraction of the BG:S complex response, and the resulting G titration curves were fitted by using a one-site binding model.

3.6.4 Results and discussion

3.6.4.1 Imprinting of gonadorelin by NE polymerization

As recently reported by our group [9-10], norepinephrine is gaining attention as a functional monomer for MIP synthesis. This dopamine (DA) homologue shares with it most of the features, such as the capability to self-polymerize in mild conditions and leads to highly stable and adhesive nano-biofilms (or nanoparticles) on almost any surface [11-13]. However, polynorepinephrine (PNE) forms more hydrophilic and smoother surfaces [14-17]. The high

chemical similarity of NE with DA also makes PNE an efficient but still poorly explored monomer for MIP preparation, as we recently reported [9]. The superior hydrophilicity of PNE-based MIPs contributes to the drastic reduction of the well-known and undesired effect of non-specific adsorption on the receptor surface [9-18], paving the way for recording the selective binding signal only from the target on the MIP_G surface, even in complex matrices.
The whole procedure here carried out for the preparation of PNE-based MIPs (Scheme 3.1) is fast (5 h), simple (by direct drop casting of the polymerizing NE solution on the SPR gold chip, see Material and Method section), and a hundred times cheaper than an ELISA assay (*per* sample). The so-prepared MIPs, moreover, display high reusability and stability. The MIP-based sensor chip can be reused on average 40 complete experiments, considering that one experiment comprises at least five sample injections at different concentrations, each in triplicate, and the regeneration steps required. Once prepared, the MIP-based sensor is stable for at least six months (to the best of our knowledge), if properly regenerated at the end of each experiment, and then stored at 4°C in Milli-Q water to prevent the biopolymer from drying out. The MIP stability is also confirmed by the average value of the sensorgram baseline (recorded along six months and on three different chips), which displays a CV_{av}% of 2.16. These experimental evidences, taken together, make this PNE-based MIP extremely promising and advantageous with respect to classic antibodies, presenting the well-known limitations of protein reagents in terms of stability to temperature and reaction aggressive/denaturing conditions (as the case of environmental analysis). However, as previously demonstrated, the analytical performances and reliability of a synthetic receptor/ligand system in biosensing is strictly related to its rational design for both nucleic acid- and amino acid-based molecules [19-22]. At this regard, for a wider application of PNE to peptide/protein analysis, it is important to underline how the *a priori* estimation of MIP feasibility requires a deep understanding of the system which is still under study for a wider application of PNE to peptide/protein analysis. Collected evidences [9,23] indicate that the primary sequence of the peptide plays a

key role in the imprinting event, but a higher number of case studies is necessary to draw a general guideline for the synthesis of PNE/PDA-based MIPs for the detection of peptides/proteins.

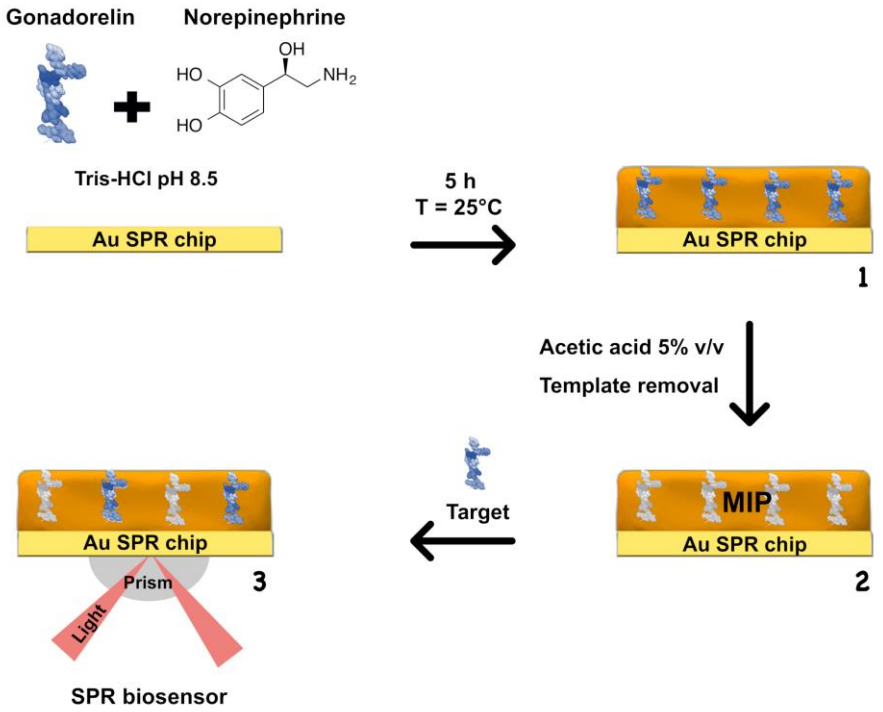

Scheme. 3.1 Schematic representation of the imprinting strategy on SPR gold chip surface. (1) The functional monomer (norepinephrine), in co-presence of the template (gonadorelin), was polymerized. (2) The template is removed from the resulting polymer matrix by leaving binding sites able to recognize (3) the target (gonadorelin).

3.6.4.2 Binding evaluation of gonadorelin and biotinylated gonadorelin on MIP for competitive assay development

Despite the low-molecular weight of G (1182 Da), a first explorative direct analysis involving the analyte G and its competitor BG, consisting in a biotinylated G, in their ability to bind MIP_G (G/BG - MIP_G) was conducted (Fig. 3.2). The direct binding assay has displayed a well-measurable SPR signal,

allowing to obtain a calibration curve in buffer and the relative equilibrium dissociation affinity constants (K_D = 6.59 ± 0.24 µmol L^{-1} for G and K_D = 6.00 ± 0.25 µmol L^{-1} for BG). Fig. 3.2 reports the sensorgrams obtained by a single-cycle kinetic (SCK) analysis method on the MIP surface. This method provides sequential injections of five increasing concentrations of G (0.81–13.0 µmol L^{-1}, blue line) over the surface receptor (here MIP) bypassing the regeneration step. For this reason, the SPR signal increases in the sensorgram by increasing G concentration. A single final regeneration step allows us to repeat the SCK method on the same chip for several times [24-25]. In the perspective of developing a competitive assay, the competitor peptide BG has been also tested in the same format. As shown in Fig. 3.2, we also verified the ability of BG (red line) in binding the MIP_G with comparable efficacy to unmodified G, when subjected to SCK protocol. This is a key step in the good functioning of a competitive assay and the results confirm this possibility. The biotin residue theoretically allows to obtain a 4:1 biotinylated G:streptavidin (BG:S) complex. The four-sites specifically bind BG through biotin (K_D in the order of 10^{-15}), and streptavidin (ca. 61.50 kDa) allows to increase the BG molecular weight. Consequently, the SPR signal inferred by the BG:S complex, competing with the G analyte for MIP_G recognition sites, significantly increases.

The calibration curves for G (blue) and BG (red) were obtained by plotting the binding level against the concentrations tested and were fitted with a one-site binding model. Although binding curves are not superimposable, the fitting provided very close K_D values for G (K_D = 6.59 ± 0.24 µmol L^{-1}) and BG (K_D = 6.00 ± 0.25 µmol L^{-1}), indicating a marginal interference of the biotin on molecular recognition and binding. Consequently, the BG can be properly employed in a competitive assay with target G. The estimated limits of detection (LOD) and quantification (LOQ), calculated as three times or ten times the standard deviation of the blank samples interpolated in the curves, were LOD_G = 0.10 ± 0.01 µmol L^{-1} and LOQ_G= 0.44 ± 0.04 µmol L^{-1} for G, while the LOD_{BG} = 0.12 ± 0.01 µmol L^{-1} and LOQ_{BG} = 0.44 ± 0.05 µmol L^{-1} for BG, respectively. In light of the findings obtained, we can state that the

direct binding of G and BG on MIP_G was highly successful. However, to achieve anti-doping tests requirements (Minimum Required Performance Level, MRPL = 2.00 ng mL^{-1}, 1.69 nmol L^{-1}) [26-27] it is necessary to attain lower limit of detection, here limited to the low micromolar range, which can be reached by a competitive assay including a high MW competitor able to produce enhanced SPR signals.

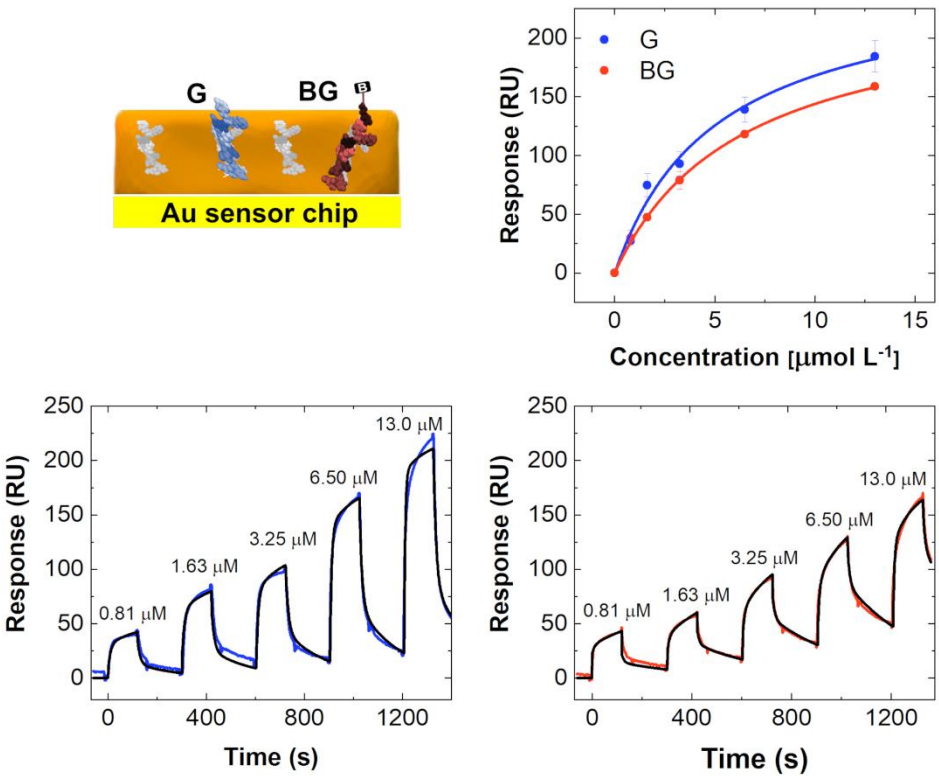

Fig. 3.2 In clockwise: representation of G/BG-MIP_G interaction; affinity curves for the direct detection of G (blue) and BG (red) on MIP_G; binding sensorgrams of the kinetic analysis (SCK), same colors

3.6.4.3 Comparison of SPR-based sensing using MIP_G and monoclonal anti-G antibody modified surfaces

To have a reference assay for the MIP_G performance, a monoclonal anti-G antibody (G-mAb) was immobilized (immobilization level = 7278.10 RU) and tested following a classic SPR protocol (see material and methods section) in a direct assay format i.e., flowing the analyte on the modified surface with the MIP_G (see above 4.6.3.2 section) or the G-mAb receptor. Fig. 3.3 reports the sensorgrams obtained for the G-mAb, and a manual run analysis was performed since the SCK method failed due to a prompt saturation of the receptor surface. In this case, we hence injected different concentrations (13.0-0.81 μmol L^{-1}) following a decreasing trend. After each concentration, a short regeneration step was carried out. The G-mAb shows a slightly higher binding ability in terms of surface loading (Fig. 3.3). However, the K_D values (7.48 ± 4.25 μmol L^{-1} for G, and 5.65 ± 0.50 μmol L^{-1} for BG) resulted very close to those obtained on MIP_G. Even if typical K_D values for mAb directed versus proteins fall in the low nanomolar range, mAbs versus low immunogenic analytes, such as short peptides, often do not display good binding ability [28-30], as we also previously reported with other short peptides of interest in anti-doping controls [31]. The overall decrease of the sensorgram baseline, shown in Fig. 3.3, is associated with an instability of the immobilized antibody (G-mAb). In this frame, our biomimetic receptor MIP_G competes with much more expensive G-mAbs in terms of G and BG binding affinity constants. However, compared to MIP_G, the anti-G mAb resulted more sensitive (LOD_G = 16.63 ± 3.11 nmol L^{-1} and LOQ_G = 55.42 ± 10.4 nmol L^{-1}; LOD_{BG} 11.71 ± 0.890 nmol L^{-1} and LOD_{BG} = 19.24 ± 3.60 nmol L^{-1}) and reproducible ($\%CV_{avG}$ = 5.00%, $\%CV_{avBG}$ = 4.78%) in the direct detection of G, as we can expect by a monoclonal antibody. However, not even the G-mAb resulted sensitive enough for the MRPL limit achievement required by WADA.

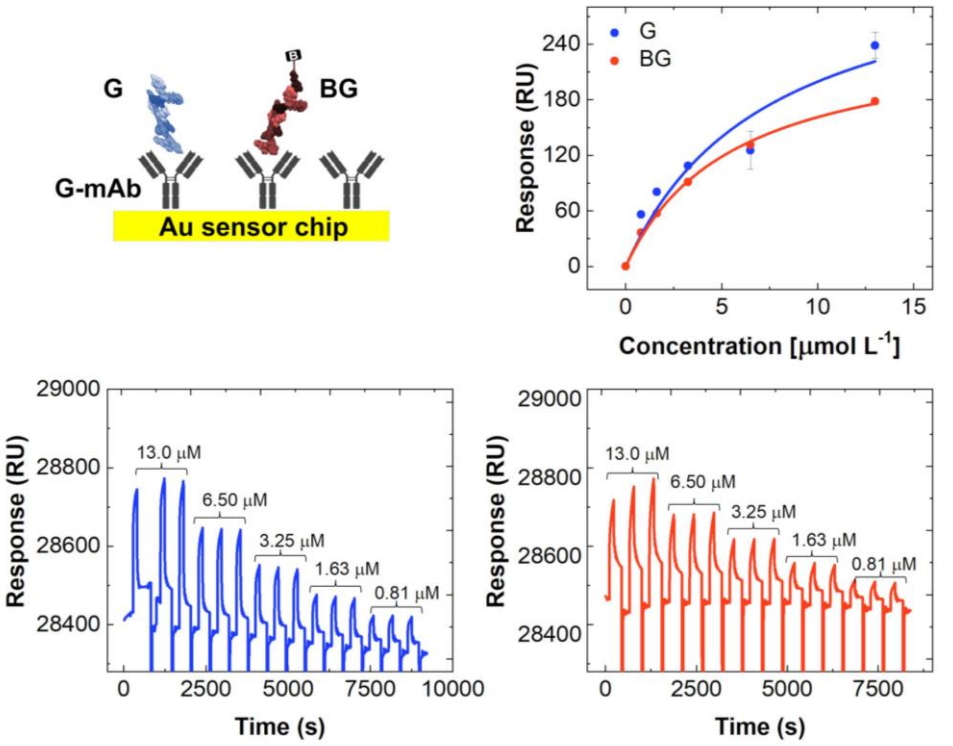

Fig. 3.3 In clockwise: representation of G/BG-mAb interaction; affinity curves for the direct manual run of G (blue) and BG (red) on mAb; binding sensorgrams (manual run analysis) of G-mAb (blue) and BG-mAb (red) interactions

3.6.4.4 Choice of gonadorelin concentration for MIP imprinting

The concentration of the G template, theoretically reflecting the density of binding sites obtained on the MIP surface, was also evaluated. In fact, a successful surface competition may occur only if limited binding sites are available on the receptor surface: the target (G) and the competitor peptide complex with streptavidin (here BG:S) must thus compete for a discrete number of cavities; otherwise, the competitive reaction does not take place since there are enough binding sites to accommodate both G and BG:S. Hence, the choice of a proper template concentration to be used in the imprinting procedure is a mandatory step. Different MIP_G densities were obtained by using three G concentrations during the imprinting procedures

i.e., 423, 42.3, and 4.23 μmol L^{-1} (corresponding to 500, 50, and 5 ppm), likely giving MIPs with a decreasing G binding sites density and an increased non-imprinted surface area of the polymer. A passivation step was integrated in the polymer preparation, before the template G removal, to avoid any possible unspecific adsorption during the real sample analysis. Testing the MIP_G surfaces reported above with BG:S, the best binding ability for G template was observed for the lower density of imprinting (template 4.23 μmol L^{-1}). Tentatively, we ascribe such behavior to the steric crowding of the binding molecules (BG:S), which depends on template concentration, leading to a more efficient binding and a higher SPR signal (Fig. 3.4). Considering also the economic savings derived from this choice, subsequent experiments were conducted using G = 4.23 μmol L^{-1} as template concentration for MIP_G preparation. The BG calibration curves obtained at the lowest (4.23 μmol L^{-1}) and the highest (423 μmol L^{-1}) concentration of template G, are compared in Fig. 3.4. Even if not directly deductible, a further reduction of the template could lead to even more stringent conditions for the competition, which can be studied in the next future.

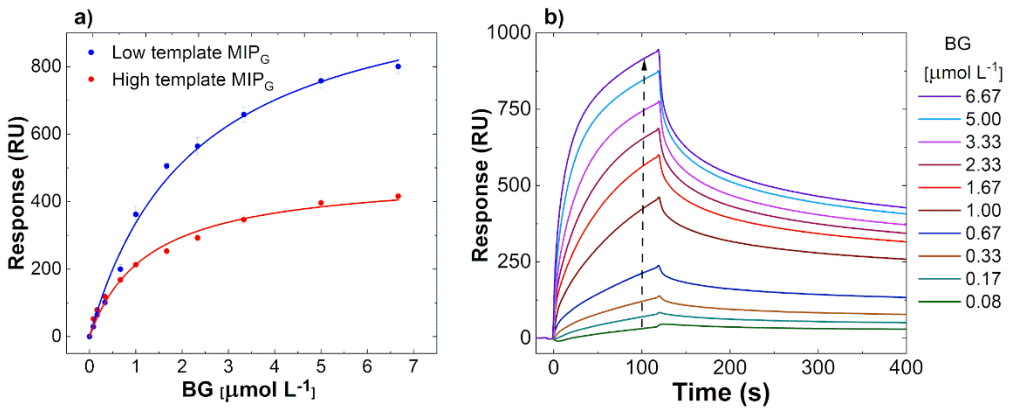

Fig. 3.4 (a) Binding curves of 4:1 BG:S competitor on MIP_G imprinted with high (423 μmol L^{-1}; red circles and lines) and low (4.23 μmol L^{-1}; blue circles and lines) concentration of template G, respectively. BG:S concentration spans from 0.08 to 6.67 μmol L^{-1}. (b) Sensorgrams of BG:S - MIP_G interaction on MIP_G imprinted with the lowest concentration of G (4.23 μmol L^{-1})

3.6.4.5 Optimization of the BG:S competitor concentration

Another key step in a surface competitive assay development is the right choice of the competitor concentration, that should be set near its K_D. Thus BG:S calibration on the optimized MIP_G at low density of G sites (4.23 µmol L^{-1}) was performed. Then the fitting by the one-site binding model was performed by using BIAEvaluation 3.1 Software (GE Healtchare Life Sciences) (see materials and methods). The $R_{max,}$ experimentally obtained from the saturation curve reported in Fig. 3.4 (R_{max} = 1094.61 ± 55.69 RU), allowed to calculate the K_D (2.25 ± 0.27 µmol L^{-1}) and, hence, to select the most effective BG:S concentration in the competitive assay equal to 1.33 µmol L^{-1} for BG and 0.33 µmol L^{-1} for S.

3.6.4.6 Selectivity of MIP_G in gonadorelin recognition

The selectivity study of MIP_G towards gonadorelin recognition was investigated by testing Leuprolide (LEU), a second peptide of anti-doping interest with high similarity to G, and three unrelated peptides as negative controls. Beside MIP_G, a NIP (non-imprinted polymer) as control surface, and G-mAb (section 3.6.3.1) for conventional antibody-based assay chip, were also prepared and tested in the same manner for comparison. MIP_G and NIP modified surfaces were treated with an additional passivation step to reduce the possible non-specific adsorption of peptides. All the peptides (4.20 µmol L^{-1} each, Table 3.2 were selected with comparable molecular weight and number of amino acid residues to gonadorelin and were tested under the same experimental conditions. LEU is a peptide hormone analogue of GnRH also used as doping agent and reported in the S2 class of the WADA list [31-33]. PEPT-1, PEPT-2 and PEPT-3 have no sequence similarity to the target G and should not be recognized by MIP_G. As shown in Fig. 3.5, MIP_G and G-mAb exhibit an excellent selectivity against G and BG, while some interaction is observed with LEU and no significant signals are recorded for the selected peptides (PEPT-1, PEPT-2 and PEPT-3) on both MIP_G and G-mAb modified surfaces. For the same peptides, negligible responses were observed on the

NIP surface. This behavior, on one hand, may be ascribable to the low affinity of the peptides' primary sequence for the catecholamine-based polymers (PNE). On the other hand, it may be associated with the highly selectivity of the MIP_G and the good chemical modification (passivation) of the polynorepinephrine surface, as NIP results corroborate. The Cross-Reactivity (%CR) for LEU peptide, expressed as percentage ratio between LEU and G response, results of 68% for LEU on MIP_G and 32 % for mAb, compatible with the use of the immunoreagent (mAb). However, considering the high homology among the two sequences, these findings confirm the effectiveness of the imprinting strategy adopted in producing MIPs for gonadorelin (reference standard) able to discriminate peptides differing for only one amino acid. The binding signals recorded for all the peptides (G/BG and LEU) were largely suppressed on a NIP surface in comparison to the MIP_G responses. This behavior supports the usefulness of the passivation step using small molecules (section 3.6.3.2) on the PNE surface.

Table 3.2 Sequence, number of amino acids and molecular weight of each peptide tested

Name	**Sequence**	**Size (aa)**	**MW (Da)**
G	p{GLU}HWSYGLRPG-NH_2	10	1182.33
BG	{pGLU}HWSYGLRPG-{Lys(biotin)}	11	1537.75
LEU	{pGLU}HWSY{d-LEU}LRP-NHEt	9	1209.40
PEPT-1	Ac-ISLAPKAQI-NH_2	9	981.20
PEPT-2	FLDSPDR-NH_2	7	847.92
PEPT-3	EEAKEAEDGPM	11	1205.25

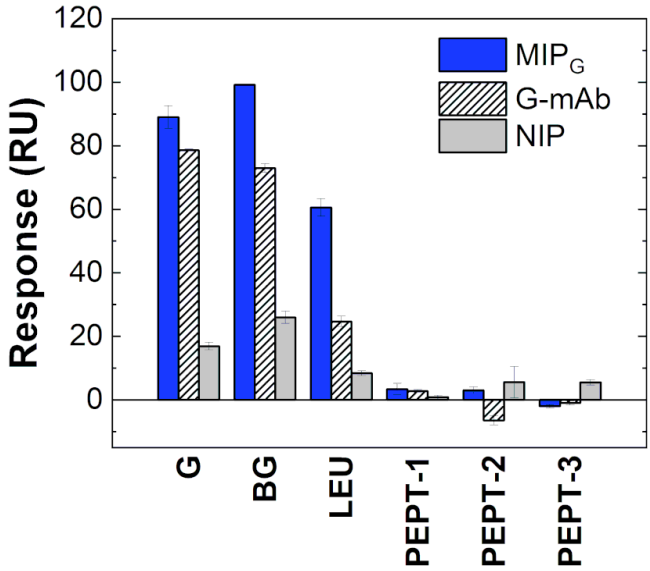

Fig. 3.5 Specificity test performed respectively on MIP_G (blue bars), NIP (grey bars) and G-mAb (dashed bars), against LEU, a homologue peptide of anti-doping interest, and unrelated peptides (PEPT-1, PEPT-2, PEPT-3) by SPR. The bar-chart indicates SPR responses ± SD recorded for the target (G), the competitor (BG), and all the tested peptides (PEPT-X), all at 4.20 µmol L^{-1}

3.6.4.7 Surface competitive assay for gonadorelin

Finally, the competitive heterogenous assay format was set. This approach, suitable for small molecules such as gonadorelin, is based on the competition for a limited number of binding sites [93] between the analyte G and a fixed amount of the detecting molecule (here BG:S). Most of the direct competitive assays' protocols, named 'one-step' format, involve the simultaneous addition of the target analyte and the competitor on the binding surface with the receptors. However, some literature reports the advantage of sequential competitive assay (named 'two-steps' format) [34-39], in which the analyte and the competitor interact subsequently with the surface receptor. In these conditions, the target is firstly injected onto the receptor surface (here MIP) and binds the recognition sites. Then, the detecting molecule is added to occupy the remaining free binding sites. Thus, the higher amount of target is present in the sample, the lower amount of detecting molecule binds the

receptor and, therefore, a lower analytical signal is recorded (turn-off assay). Using the two-steps assay format, a larger amount of target is capable of binding to the receptor (here MIP) than in the one-step assay (or simultaneous assay), and therefore this strategy provides an improvement of the assay sensitivity [37]. We performed both, 'one step' and 'two-steps' competition assays, to evaluate the best protocol to be adopted in the final assay, remembering here that both G and BG present similar affinity constants. For practical reason, to calculate the LOD of the competitive assays, the total SPR signal (SPR signal of competitor BG:S and target G) was directly subtracted from the SPR signal of the BG:S competitor alone. The resulting curves were fitted by using a simple one-site binding model reported in paragraph 3.6.3.2. The one step protocol was first performed in standard solutions and then in spiked urine. In standard solutions this approach displayed a limited dynamic range at micromolar concentration, together with a high variability among assays, expressed as standard deviation (Fig. 3.6), and poor repeatability (%CV_{av} = 15.00%).

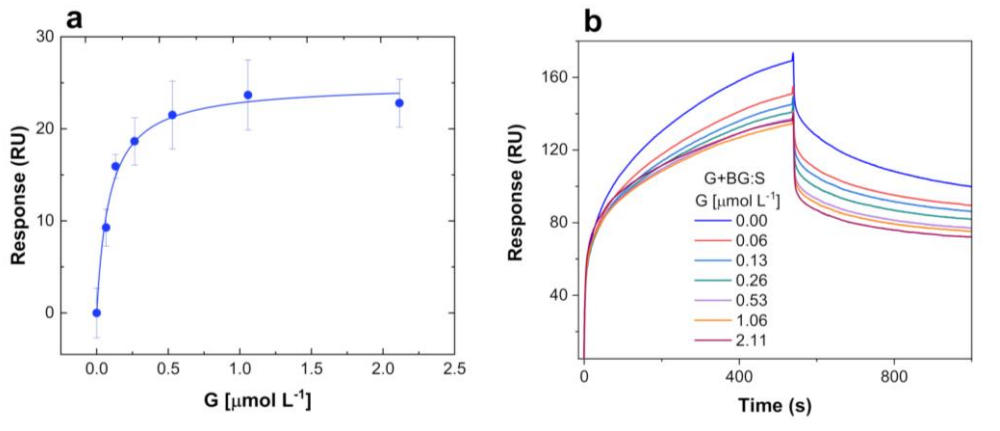

Fig. 3.6 (a) Dose-response curve in buffer of the 'one step' competitive assay in buffer, where G (0.07-2.11 μmol L^{-1}) and BG:S are simultaneously injected over MIP_G surface. SPR signals in the graph are expressed as subtraction between responses from BG:S (zero target G concentration) and BG:S + G. (b) Representative sensorgrams of G interaction in competition with BG:S

Moreover, to establish a competition reaction, a high concentration of the detecting molecule (BG = 6.66 μmol L^{-1} and S = 1.66 μmol L^{-1}) was necessary with long analysis time (contact time: 540 s). SPR signals resulted also very low and, compared to data obtained by direct detection of G (Fig. 3.2), we think that the steric hindrance due to the larger competitor BG:S mass, co-present in solution with G, could prevent the analyte G binding. Therefore, despite the benefit of the competitive one-step format leading to G detection with a higher sensitivity (LOD = 25.50 $\pm$ 3.90 nmol L^{-1} and LOQ = 87.00 $\pm$ 0.010 nmol L^{-1}) compared to the direct format (LOD = 0.10 $\pm$ 0.01 μmol L^{-1}, see 3.6.3.2 section), there is still room to improve the system performances to fulfill the anti-doping tests requirements. Then the two-steps protocol provided the results reported in Fig. 3.7. The calibration curves were obtained both in buffer and spiked urine (Fig. 3.8). In this case the competition with G occurred in the very low nanomolar range (0.42 – 13.54 nmol L^{-1}), with excellent repeatability (%CV_{av} = 2.45% in buffer and %CV_{av} = 1.40% in urine). The range of G concentrations was finely tuned. In fact, G concentrations in the low micromolar range (10 – 211 nmol L^{-1}), gave a calibration curve in buffer with a saturation profile already at 50 nmol L^{-1} (Fig. 3.7) and a wide change in SPR signal between zero and the lowest G concentration analyzed (10 nmol L^{-1}) that suggested to decrease the G concentrations to be tested. This clue was successfully confirmed by subsequent results, which exhibited a well-defined dose response curve, typical of a competitive assay (Fig. 3.8).

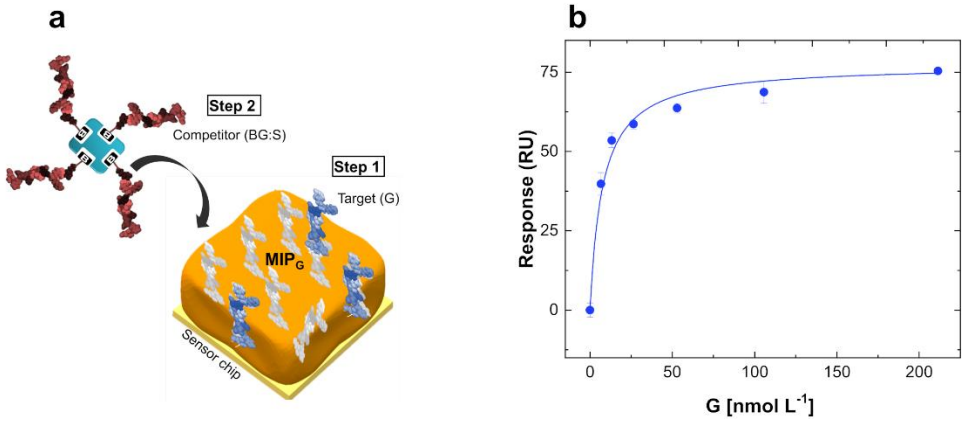

Fig. 3.7 (a) Sketched representation of the 'two-steps' assay. (b) Dose-response curve in buffer for the assay where G and BG:S are injected in sequence over the MIP_G surface. G concentrations ranges from 10 to 211 nmol L^{-1}. SPR signals in the graph are expressed as subtraction between responses from BG:S (zero target G concentration) and BG:S + G.

The competitive 'two-steps' assay was applied in complex matrix, i.e., artificial urine with the addition of G in the range 0.42 - 13.54 nmol L^{-1}. The selected operating analytical range is suitable for gonadorelin detection in doping application. The average percentage recovery of the assay for G was 95.00%, calculated from SPR signals in urine and buffer ($(SPR_{urine}/SPR_{buffer})*100$). The calculated limit of detection and quantification ($LOD = 3\sigma*K_D/R_{max}$ and $LOQ = 10\sigma*K_D/R_{max}$ where sigma is the standard deviation of the mean RU of the blank solution) resulted respectively 44.0 ± 5.0 pmol L^{-1} and 146.8 ± 15.8 pmol L^{-1} in buffer, while LOD = 52.0 ± 6.0 pmol L^{-1} and LOQ = 188.5 ± 20.3 pmol L^{-1} in undiluted artificial urine. In both cases, the estimated LOD is in line with the Minimum Required Performance Level (MRPL = 1.69 nmol L^{-1}) [26-27] at which all the Word Anti-Doping (WADA)-accredited laboratories must operate to assure the harmonization of the methods' analytical performance applied to detect non-threshold prohibited substances (e.g., drugs in class S2.2.1 "Gonadotropin (CG/LH) Releasing Factors"), according to TD2019MRPL [27].

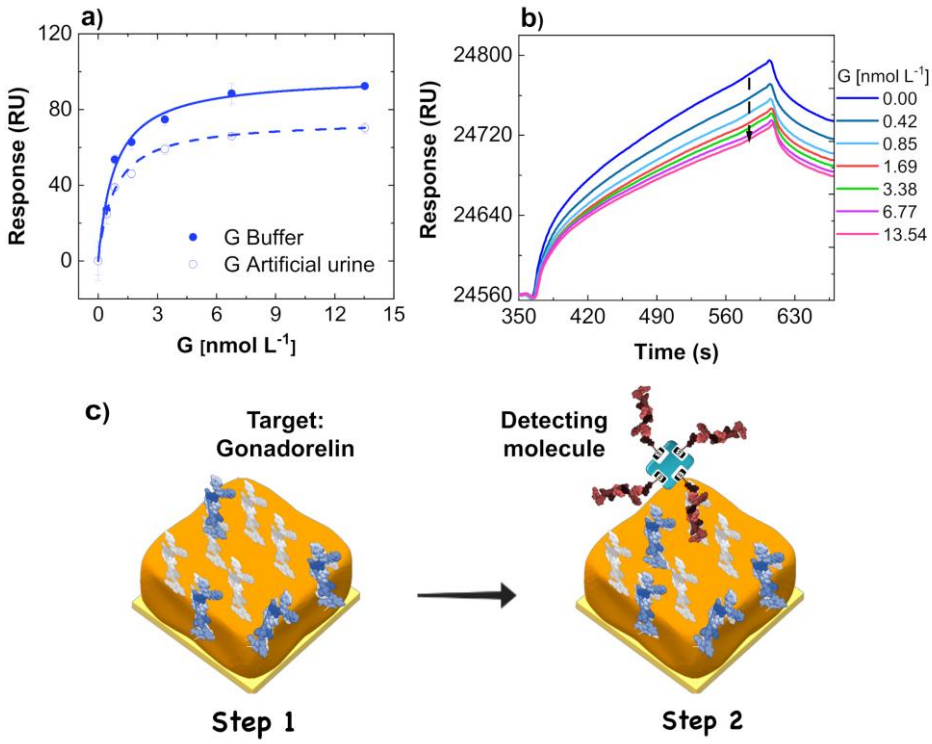

Fig. 3.8 (a) Two-steps competitive assay: comparison of dose-response curves for G (0.42 – 13.54 nmol L^{-1}) in buffer and artificial spiked urine samples. Each point is representative of 3 replicates (RU_{mean} ± SD). SPR signals are expressed as subtraction between responses from BG:S (zero target G concentration) and BG:S + G. (b) SPR sensorgrams of the assay in urine. (c) Sketched representation of the assay

Besides, an artificial urine sample spiked with gonadorelin (EP Reference Standard, 845.8 pmol L^{-1}) was analyzed in parallel with our MIP-based assay and with a commercial competitive enzyme-linked immunosorbent assay (ELISA), respectively. Briefly in detail, the ELISA kit protocol relies on the competition between the target (GnRH) and the competitor molecule for a limited number of antibody binding sites. These were sequentially added onto the 96-well plate pre-coated with antibodies and incubated 1h at 37°C. Then, multiple washing steps were accomplished and the signal output, resulting in a colored enzymatic reaction, is measured at λ= 450 nm.

While our assay resulted highly accurate (%error = 5.19%) in detecting gonadorelin, with the ELISA kit we faced a saturated signal error (Abs@450nm = 2.66 ± 0.11), impairing any quantification. To troubleshoot this, we tested the ELISA kit with the calibrator concentrations (1.16 - 845.8 pmol L^{-1}) suggested by the manufacturer and subsequently we tried to dose the same concentrations of gonadorelin (EP Reference Standard) by using the same diluent/washing buffers. Also, in this case, we faced saturated signals attributable only to the binding of the competitor molecule (without analyte, see Fig. 3.9). Probably gonadorelin (EP Reference Standard) is not able to trigger a proper competitive reaction with the competitor molecule provided by the kit and this impaired any further comparison (Fig. 3.9).

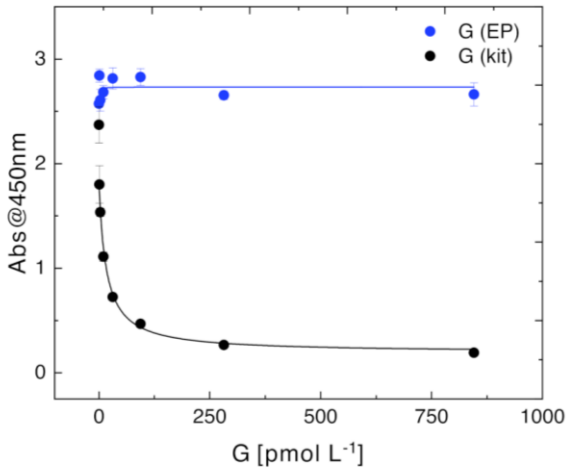

Fig. 3.9 Dose-response of competitive ELISA kits performed with the calibrators supplied by the manufacturer (black dots), and with gonadorelin (EP standard reference, blue dots). Each point is representative of 3 replicates (RU_{mean} ± SD).

Finally, it is worthy to highlight that the MIP-based competitive assay here designed represents the first example of highly performing biosensing method (antibody-free) to detect a small biomolecule of anti-doping interest. Real samples from athletes are not yet available (private communication with

Prof. Botrè, Director of the Italian WADA laboratory), but we rely on this possibility in the near future.

3.6.5 Conclusions

In this study, we developed a novel polynorepinephrine-based MIP for the detection of the peptide hormone gonadorelin, through SPR biosensing, for anti-doping purposes. To the best of our knowledge, this is the first report about gonadorelin detection based on optical biosensing and on a catecholamine-based MIP. The analytical performances of the biosensor were characterized by evaluating the binding capacity of gonadorelin (G), the biotinylated competitor (BG), and random peptides as negative controls. The results allowed the further optimization of a 'two-steps' competitive assay, in which the target (G) and the detecting molecule (BG:S) complex sequentially compete for a limited number of binding sites of the MIP. The selectivity of the detection resulted excellent, showing the ability in discriminating one single amino acid change over the peptide sequence. The optimized assay achieves a high sensitivity (LOD = 52.0 ± 6.0 pmol L^{-1}) and an excellent repeatability (%CV_{av} = 1.40%) in untreated urine, in line with WADA analytical requirements. A direct comparison with a commercial monoclonal antibody in terms of selectivity, reusability and cost highlighted the overall excellent features of this polynorepinephrine-based MIP. The strength of the reported method is further reinforced by the difficulty to find ELISA kit on the market for testing the EP G Reference Standard, as required by WADA. Moreover, the only methods currently existing in the research literature for G quantification rely on expensive liquid chromatography tandem-MS techniques (LC-MS/MS) requiring highly trained personnel and long pre-treatments of the samples. Last, but not least, the reported protocol to fabricate PNE-based MIPs is about 100 times cheaper than an ELISA assay, and ongoing tests are displaying their resistance to very drastic environmental conditions, prohibitive for antibodies. The imprinting process may be translated to other peptides/proteins of interest, and from SPR to

other diagnostic platforms, such as multi-well microplates or other systems conventionally used in immuno-based assays.

References

1. P. Palladino, A.M. Aura, G. Spoto, Surface plasmon resonance for the label-free detection of Alzheimer's β-amyloid peptide aggregation. Anal. Bioanal. Chem. 408 (2016) 849-854.
2. R. Karlsson, Real-time competitive kinetic analysis of interactions between low-molecular weight ligands in solution and surface-immobilized receptors. Anal. Biochem. 221 (1994) 142-151.
3. P. Du, M. Jin, G. Chen, C. Zhang, Z. Jang, Y. Zhang, P. Zou, Y. She, F. Jin, H. Shao, S. Wang, L. Zheng, J. Wang, A competitive bio-barcode amplification immunoassay for small molecules based on nanoparticles. Sci. Rep. 6 (2016) 38114.
4. X. Tan, P. Gao, Y. Li, P. Qi, J. Liu, R. Shen, L. Wang, N. Huang, K. Xiong, W. Tian, Q. Tu, Poly-dopamine, poly-levodopa, and poly-norepinephrine coatings: Comparison of physico-chemical and biological properties with focus on the application for blood-contacting devices, Bioact. Mater. 6 (2021) 285-296.
5. C.-Y. Liu, C.-J. Huang, Functionalization of polydopamine via the aza-michael reaction for antimicrobial interfaces. Langmuir 32 (2016) 5019-5028.
6. J. Sherwood, Y. Xu, K. Lovas, Y. Qin, Y. Bao, Surface functionalization of dopamine coated iron oxide nanoparticles for various surface functionalities. J. Magn. Magn. Mater. 427 (2017) 220-224.
7. B.P. Tripathi, P. Das, F. Simon, M. Stamm, Ultralow fouling membranes by surface modification with functional polydopamine. Eur. Polym. J. 99 (2018) 80-89.
8. Biacore X100 Handbook BR-1008-10 Edition AC.
9. V. Baldoneschi, P. Palladino, M. Banchini, M. Minunni, S. Scarano, Norepinephrine as new functional monomer for molecular imprinting: an applicative study for the optical sensing of cardiac biomarkers, Biosens. Bioelectron. 1 (2020) 112161.
10. V. Baldoneschi, P. Palladino, S. Scarano, M. Minunni, Polynorepinephrine: state-of-the-art and perspective applications in biosensing and molecular recognition. Anal. Bioanal. Chem. 412 (2020) 5945-5954.
11. T. Iwasaki, Y. Tamai, M. Yamamoto, T. Taniguchi, K. Kishikawa, M. Kohri, Melanin precursor influence on structural colors from artificial melanin particles:

polyDOPA, polydopamine, and polynorepinephrine, Langmuir 34 (2018) 11814-11821.

12. X. Liu, Z. Xie, W. Shi, Z. He, Y. Liu, H. Su, Y. Sun, D. Ge, Polynorepinephrine nanoparticles: A novel photothermal nanoagent for chemo-photothermal cancer therapy, Appl. Mater. Interfaces 11 (2019) 19763-19773.
13. X. Xiao, Y. Zhang, J. Wu, L. Jia, Poly[norepinephrine]-coated open tubular column for the separation of proteins and recombination human erythropoietin by capillary electrochromatography, J. Sep. Sci. 40 (2017) 4477-4660.
14. Z. Lu, A.M. Douek, A.M. Rozario, R.F. Tabor, J. Kaslin, B. Follink, B.M. Teo, Bioinspired polynorepinephrine nanoparticles as an efficient vehicle for enhanced drug delivery, J. Mater. Chem. B 8 (2020) 961.
15. X. Xiao, Y. Zhang, J. Wu, L. Jia, Poly[norepinephrine]-coated open tubular column for the separation of proteins and recombination human erythropoietin by capillary electrochromatography, J. Sep. Sci. 40 (2017) 4477-4660.
16. S. Hong, J. Kim, Y.S. Na, J. Park, S. Kim, K. Singha, G.-I. Im, D. Han, W.J. Kim, H. Lee, Poly(norepinephrine): Ultrasmooth material-independent surface chemistry and nanodepot for nitric oxide. Angew. Chem. Int. Ed. 52 (2013) 9187–9191.
17. X. Tan, P. Gao, Y. Li, P. Qi, J. Liu, R. Shen, L. Wang, N. Huang, K. Xiong, W. Tian, Q. Tu, Poly-dopamine, poly-levodopa, and poly-norepinephrine coatings: Comparison of physico-chemical and biological properties with focus on the application for blood-contacting devices, Bioact. Mater. 6 (2021) 285-296.
18. R.-P. Liang, C.-Y. Xiang, J.-Y. Wang, J.-D. Qui, Preparation of polynorepinephrine adhesive coating via one-step self-polymerization for enantioselective capillary electrochromatography coupled with electrogenerated chemiluminesense detection, J. Chromatogr. A 1284 (2013) 194-201.
19. M.L. Ermini, S. Scarano,R. Bini, M. Banchelli, D. Berti, M. Mascini, M. Minunni, A rational approach in probe design for nucleic acid-based biosensing. Biosens. Bioelectron. 26 (2011) 4785-4790.
20. A. Accardo, A. Morisco, P. Palladino, R. Palumbo, D. Tesauro, G. Morelli, Amphiphilic CCK peptides assembled in supramolecular aggregates: structural investigations and in vitro studies. Mol. Biosys. 7 (2011) 862-870.
21. P. Palladino, G.L. Scaglione, A. Arcovito, R. Maria Vitale, P. Amodeo, B. Vallone, M. Brunori, E. Benedetti, F. Rossi, Neuroglobin–prion protein interaction: what's the function?. J. Pept. Sci. 17 (2011) 387-391.

22. P. Palladino, L. Portella, G. Colonna, R. Raucci, G. Saviano, F. Rossi, M. Napolitano, S. Scala, G. Castello, S. Costantini, The N-terminal Region of CXCL11 as structural template for CXCR3 molecular recognition: Synthesis, conformational analysis, and binding studies. Chem. Biol. Drug Des. 80 (2012) 254–265.
23. P. Palladino, M. Minunni, S. Scarano, Cardiac Troponin T capture and detection in real-time via epitope-imprinted polymer and optical biosensing, Biosens. Bioelectron. 106 (2018) 93–98.
24. R. Karlsson, P.S. Katsamba, H. Nordin, E. Pol, D.G. Myszka, Analyzing a kinetic titration series using affinity biosensors. Anal. Biochem. 349 (2006) 136-147.
25. W. Palau, C. Di Primo, Simulated single-cycle kinetics improves the design of surface plasmon resonance assays, Talanta 114 (2013) 211-216.
26. C Görgens, S. Guddat, A. Thomas, M. Thevis, Recent improvements in sports drug testing concerning the initial testing for peptidic drugs [< 2 kDa] - sample preparation, mass spectrometric detection, and data review. Drug. Test. Anal. 10 (2018) 1755-1760.
27. Wada-ama.org/ WADA technical Document _ TD2019MRPL.
28. B. Fromme, P. Eftekhari, M.V. Regenmortel, J. Hoebeke, A. Katz, R. Millar, A novel retro-inverso gonadotropin-releasing hormone [GnRH] immunogen elicits antibodies that neutralize the activity of native GnRH. Endocrinology 144 (2003) 3262-3269.
29. P. Gomes, E. Giralt, D. Andreu, Direct single-step surface plasmon resonance analysis of interactions between small peptides and immobilized monoclonal antibodies. J. Immunol. Methods 235 (2000) 101-111.
30. F.A. Raymond, A.F. Williams, H.R. Behrman, D.L. Wolin, Ovarian Gonadotropin-Releasing Hormone-Like Protein[s]: Demonstration and Characterization. Endocrinology 118 (1986) 961-967.
31. A.C. Wilson, S.V. Meethal, R.L. Bowen, C.S. Atwood, Leuprolide acetate: a drug of diverse clinical applications. Expert Opin. Investig. Drugs, 16 (2007) 1851-1863.
32. Wada-ama.org/2020-List of prohibited substances (visited on 16/01/2020).
33. I. Zvereva, G. Dudko, M. Dikunets, Determination of GnRH and its synthetic analogues' abuse in doping control: Small bioactive peptide UPLC–MS/MS method extension by addition of in vitro and in vivo metabolism data.; evaluation of LH

and steroid profile parameter fluctuations as suitable biomarkers. Drug Test Anal. 10 (2018) 711-722.

34. N. Kobayashi, J. Goto, J.; Noncompetitive immunoassays for small molecules with high sensitivity and specificity, Adv. Clin. Chem. 36 (2001) 139-170.
35. D.S. Hage, D.H. Thomas, M.S. Beck, Theory of a sequential addition competitive binding immunoassay based on high-performance immunoaffinity chromatography. Anal. Chem. 65 (1993) 1622-1630.
36. T. Ito, N. Aoki, S. Kaneko, K. Suzuki, High-sensitive and rapid sequential cortisol detection using twin sensor QCM. Anal. Methods 6 (2014) 7469-7474.
37. L.J. Kricka, J.Y. Park, Immunochemical techniques, in: Burtis, C.A.; Ashwood, E.R.; Bruns, D.E. [Eds.] 6nd ed, Tietz textbook of clinical chemistry and molecular diagnostics, Elsevier Health Sciences, London, 2017, pp. 348-367.
38. M. Nilsson, H. Håkanson, B. Mattiasson, Process monitoring by flow-injection immunoassay: Evaluation of a sequential competitive binding assay. J. Chromatogr. A 597 (1992) 383-389.

3.7 A portable biomimetic-based platform: beyond bench

The study we are going to present is based on the following article:

- **F. Torrini**, L. Caponi, A. Bertolini, P. Palladino, F. Cipolli, A. Saba, A. Paolicchi, S. Scarano, M. Minunni. A biomimetic enzyme-linked immunosorbent assay (BELISA) for the analysis of gonadorelin by using molecularly imprinted polymer-coated microplates, Analytical and Bioanalytical Chemistry (2022), https://doi.org/10.1007/s00216-021-03867-7.

3.7.1 Aim and objectives of the study

An original biomimetic enzyme-linked immunoassay (BELISA) to target the small peptide hormone gonadorelin is presented. We proposed a BELISA assay which involves the growth of a PNE-based MIP directly on microwells. Gonadorelin quantification was accomplished via a colorimetric indirect competitive bioassay involving the competition between biotinylated gonadorelin linked to the signal reporter and the unlabeled analyte. These compete for the same MIP binding sites resulting in an inverse correlation between gonadorelin concentration and the output color signal (λ = 450 nm). A detection limit of 277 pmol L^{-1} was achieved with very good repeatability in standard solutions ($_{av}$CV% = 4.07%) and in urine samples ($_{av}$CV% = 5.24%). The selectivity of the assay resulted adequate for biological specimens and non-specific control peptides. In addition, the analytical figures of merit were successfully validated by mass-spectrometry, the reference anti-doping benchtop platform for the analyte. This BELISA assay was aimed to open real perspectives for PNE-based MIPs as alternatives to antibodies, especially when the target analyte is a poorly or non-immunogenic small molecule, such as gonadorelin.

3.7.2 Introduction

In this study, we successfully report and demonstrate the versatility of the developed PNE-based MIP, as capturing receptor, for gonadorelin (acronym G), moving from a benchtop instrumental asset (i.e., SPR) towards a portable, low-cost and very widely used bioanalytical platform, i.e., ELISA reader. The capturing receptor, PNE-based MIP, was previously developed, optimized and coupled to a SPR transduction to set up a sensitive and selective 'two-step' competitive assay for anti-doping controls [1], described in the previous paragraph 3.6. To this aim, the MIP for G has been adapted to play the role of the capturing antibody in 96-well microplates, obtaining a very sensitive and selective BELISA test in a competitive format [2]. The assay exploits one of the most common ELISA readout strategies, i.e., the use of horseradish peroxidase (HRP) as a signal reporter, and tetramethylbenzidine (TMB) as substrate, developing the well-known optical signal in the visible range. The colorimetric PNE-based BELISA assay succeeded in quantifying gonadorelin directly from untreated (except for 1:10 dilution) human urine, the most sampled matrix in anti-doping controls. The BELISA results on real samples correlate well with those obtained using high-performance liquid chromatography-tandem mass spectrometry, which represents the gold standard technique for anti-doping analysis. These results represent one of the first answers to the need, in forensic and other diagnostic fields, of developing versatile and cost-effective 'antibody-free' analytical platforms, to be used in decentralized testing labs for athletes' monitoring and, in general, for diagnostics. We believe that this new generation of MIPs based on natural and biocompatible polymers will have a noteworthy impact on bioanalysis, especially in terms of reagents cost and stability, simplicity of handling and in opening new chances toward the effective synthesis of mimetic receptors for low or non-immunogenic target analytes.

3.7.3 Experimental section: materials and methods

3.7.3.1 Reagents

Gonadorelin European Pharmacopoeia (EP) Reference Standard (acronym G) {pGLU}HWSYGLRPG-NH2 (MW = 1182.33 Da), L-norepinephrine hydrochloride (NE, ≧98.0%), L-lysine (≧98.0%) tris(hydroxymethyl)aminomethane hydrochloride (Tris-HCl, ≧ 99.%), L-cysteine hydrochloride monohydrate (≧ 98.%), 4-(2-hydroxyethyl)piperazine-1-ethanesulfonic acid (HEPES), sodium chloride, hydrochloric acid, acetic acid (≧ 99.7%), polyoxyethylene sorbitan monooleate (Tween-20), bovine serum albumin (BSA), streptavidin-horseradish peroxidase conjugate (S-HRP), methanol LC-MS grade (99.8%), water LC-MS grade, acetonitrile (ACN), ammonium hydroxide (NH_4OH) and formic acid (FA ≧ 95%) were all obtained from Sigma-Aldrich (Milan, Italy). 3,3',5,5'-tretramethylbenzidine (TMB) substrate and stop solution were from Thermo Fisher Scientific (Waltham, MA, USA).

Biotinylated gonadorelin (acronym BG) {pGLU}HWSYGLRPG{Lys(biotin)} (MW = 1537.75 Da) and non-specific control peptides: PEP_A Ac-ISLAPKAQIK-NH2 (MW = 1109.37 Da) and PEP_B {pGLU}HWSY{d-LEU}LRP (MW = 1182.34 Da) were synthesized by GenScript (Leiden, Netherlands). Dilution buffer (DB) (10 mmol L^{-1} HEPES, 150 mmol L^{-1} NaCl, pH 7.4) and washing buffer (WB) (10 mmol L^{-1} HEPES, 150 mmol L^{-1} NaCl, 0.0001% BSA and 0.1% Tween-20, pH 7.4) were used for peptides' dilutions and for wells' washing, respectively. All buffer solutions were prepared using ultrapure Milli-Q™ water (18.2 MΩ • cm) and were filtered through a microporous filter (Millipore, pore size of 0.22 μm). All chemicals used were of analytical grade. 96-well flat-bottom microtest plates and acetate foil for 96-well plates were obtained by Sarstedt (Nümbrecht, Germany). OASIS cartridges (hydrophilic-lipophilic-balanced [HLB], 60 mg, $3cm^3$) were acquired from Waters (Milford, MA, USA).

The internal standard (ISTD) (Des-Pyr^{1})-GnRH (MW = 1071.21 Da), used in mass spectrometry analysis, was obtained from Bachem (Bubendorf, Switzerland).

3.7.3.2 Preparation of imprinted polymers on microplates

MIPs were directly growth (via a bulk polymerization) onto disposable 96-well microplates by dropping a fresh polymerization mixture (100 µL/well) composed by the functional monomer NE (2.00 g L^{-1} in 10 mmol L^{-1} Tris-HCl, pH 8.50) in co-presence of the template G (4.23 nmol L^{-1}). The plates were left upside down for 5 hours at a fixed temperature (T = 25.0 ± 0.5 °C), under static conditions, to obtain the polymeric film formation both on the base and walls of each microplate well. Then a surface passivation step was performed to minimize possible non-specific binding of biomolecules, mainly present in biological fluids, such as human urine or serum, to the polymeric surface. An aqueous solution containing 10 mM cysteine (Cys), 10 mM lysine (Lys), and 10 mM tris(hydroxymethyl)aminomethane (Tris) was dropped onto the PNE surface (200 µL/well) and left overnight at 25 °C by avoiding evaporation. This passivation step was allowed by aza-and thiol- Michael addition reactions through the amines and thiol contained in the used compounds (Cys, Lys, Tris). Washing steps with acetic acid (5 % v/v, 200 µL/well for 3 times) and deionized water (200 µL/well for 3 times) were accomplished to remove the template from the polymeric binding cavities and any residual oligomers. Between washes, the plates were inverted and blotted against absorbent paper.

3.7.3.3 Competitive assay for gonadorelin analysis

The competitive BELISA for the quantitative detection of G in standard solutions and human urine was designed by employing a two-steps assay architecture over the MIP (see Scheme 1). The first part of the study involved the preliminary assessment of the BG binding affinity to the synthesized MIP (see paragraph a below). Afterward, the competition was established by

sequential incubations of the analyte G in water and its competitor BG conjugated with streptavidin-HRP (see paragraph b below), respectively. The last step involved the enzyme S-HRP cascade process to obtain a colorimetric read-out signal. In detail, the S-HRP optimization was carried out using two blocking solutions, 0.0001 % BSA and 0.1 % Tween-20, contained in the WB which contribute to minimize possible non-specific binding by avoiding any masking of the MIP cavities. The blocking reagents, 0.0001 % BSA and 0.1 % Tween-20, used in this bioassay were estimated using the approach proposed by Steinitz [3] as a compromise between high specific signal and low nonspecific background signal.

a) Biotinylated gonadorelin calibration

The protocol for calibrating BG is listed below: the MIP-coated wells were first conditioned by washing with WB (200 µL/well) followed by incubating BG at different concentrations (0.20 – 13.00 µmol L^{-1} diluted in DB). BG solutions were dispensed in triplicate into the modified wells. The microplate was gently stirred for 10 min and incubated at 4°C for 40 min. A washing step with WB (200 µL/well) was then performed, followed by streptavidin-HRP enzyme (0.20 mg L^{-1}) incubation (detecting molecule S-HRP, 200 µL/well) for 30 min at 4°C. The wells were finally washed with WB (200 µL/well for three times) and TMB reagent (100 µL/well) was added and incubated for 5 min before the enzymatic reaction was stopped by the addition of 0.16 M H_2SO_4 (stop solution, 100 µL/well). The absorbance was measured by using iMark™ microplate absorbance reader (Bio-Rad, Milan, Italy) at λ = 450 nm.

b) Competitive inhibition MIP-based assay

The PNE-based MIP was used in a competitive BELISA assay to quantify G through a competition between a different concentration of free G and a fixed amount of BG. The free analyte G diluted in DB, in the concentration range $8.46 \bullet 10^{-5}$-8.46 µmol L^{-1}, was dispensed into each well (100 µL/well) of the microplate. The solution was blended, incubated at 4°C for 20 min, and then

washed with WB (200 µL/well). Subsequently, the procedure continues as described in the paragraph above by exploiting a fixed concentration of BG (6.50 µmol L^{-1}, 100 µL/well). Besides, the MIP selectivity was assessed in the competitive BELISA assay by measuring the response of unrelated peptides (PEP_A and PEP_B, see details in materials paragraph) which replace the analyte G incubation.

3.7.3.4 Analysis of gonadorelin in human urine samples

The two-steps competitive assay was tested on human urines from healthy volunteers (see ethical standard). Samples were chosen among those intended for disposal at the Clinical Pathology Laboratory of the University Hospital in Pisa. Detailing, samples were selected among those that did not present significant amounts of proteins, as verified by nephelometric measurements, and which contained negligible G concentration (see mass spectrometric analysis of unspiked urine). The use of the selected biological samples has been approved by the local Ethics Committee (CEAVNO), Pisa, Italy (19/02/2020). Hence the urine samples were diluted 1:10 in water and spiked with a known amount of gonadorelin spanning from 0.084 to 846 nmol L^{-1} to simulate post-administered human urine specimens. Spiked and unspiked samples were explored following the same experimental procedure, except for G addition, to evaluate the possible occurrence of matrix effects.

3.7.3.5 Urine samples analysis by LC-MS/MS

Mass spectrometry was used as an analytical gold standard technique for G quantification to validate the designed competitive BELISA. To this aim, blank and G-spiked urine samples from healthy volunteers were analyzed by LC-MS/MS and BELISA test in parallel. For LC-MS/MS, the samples were diluted 1:10 in a water/methanol/formic acid (97:2.9:0.1; v/v/v) solution and spiked with G at different concentrations (0 – 0.084 – 0.423 and 4.23 nmol L^{-1}). The ISTD (Des-Pyr1)-GnRH was added to these fortified urine samples to obtain a fixed concentration of 100 ng mL^{-1} and then extracted and purified via solid

phase extraction (SPE) using Waters Oasis-HLBTM cartridges (3 mL, 60 mg), as previously reported by Zvereva et al. [4]. Before the sample elution, the cartridges were preconditioned by flowing methanol (2 mL) and water (2 mL) and by rinsing with NH_4OH/H_2O (5:95 v/v, 2 mL) and with ACN/H_2O (20:80 v/v, 2 mL). The sample elution was performed with 5% FA (2 mL) in an ACN/H_2O (75:25 v/v) solution and the eluates, thermostated at 45°C, were evaporated to dryness under a nitrogen stream and reconstituted with diluent solution. Referring to Thomas et al. [5], an implemented mass spectrometry method was here developed. Sample analysis was performed on a LC-MS/MS instrumental layout composed of an Agilent (Santa Clara, CA, USA) 1290 UHPLC system which comprehends a binary pump, a column oven set to 60°C and a thermostated autosampler. This is coupled with an AB Sciex (Concord, Ontario, Canada) QTRAP 6500+ mass spectrometer working as a triple quadrupole and equipped with an IonDrive™ Turbo V source. Chromatographic separation was achieved by using an Agilent Zorbax StableBond 300 C18, 1 x 50 mm, 3.5 µm column, while the integrated switching valve was used to discard both head and tail of the HPLC runs.

The mobile phases were constituted of (A) 0.1% FA in methanol and (B) 0.1% formic acid in water and the gradient elution (100 µL/min flow rate) was performed as follows: 0.0 min (A) 5%, 5.2 min (A) 50%, 6.2-7.2 min (A) 90%, 7.7-10.5 (A) 5% (volume injection = 5 µL). A mass spectrometry selected reaction monitoring (SRM) method was operated in positive ion mode. For each compound, after the optimization of declustering potential (DP), collision energy (CE) and collision exit potential (CXP), three transitions were considered in the analysis. Based on the highest signal/noise ratios, one of them was used as quantifier (Q) and the others as qualifiers (q) (see Table 3.3). Additional operative parameters were set as follows: collision gas (CAD) nitrogen; operative pression with CAD gas ON, 3.6 mPa; curtain gas (CUR) = 20 arbitrary units; gas source 1 (GS1) = 40 arbitrary units; gas source 2 (GS2) = 45 arbitrary units; ion spray voltage (ISV) = 5.5 kV; source temperature (TEM) = 550 °C; entrance potential (EP) = 10.3 V and DP = 70 V.

Table 3.3 MS operative parameters

Analyte	SRM transition (Da)	CE (V)	CXP (V)
G	592.1 → 221.1 (q)	44	6.4
	592.1 → 248.9 (Q)	38	7.1
	592.1 → 748.1 (q)	31	9.8
(Des-Pyr^{1})-GnRH	536.4 → 110.2 (q)	32	5.7
	536.4 → 110.2 (Q)	71	5.5
	536.4 → 934.5 (q)	29	12.2

3.7.4 Results and discussion

In this study a PNE-based mimetic receptor to capture the small peptide G was fabricated, as a first attempt, onto disposable 96-wells microplates (see Scheme 1). The binding capacity, as well as synthesis conditions, of the MIP towards G was previously characterized through a benchtop sensing platform (Surface Plasmon Resonance- SPR) by growing the polymer layer onto a planar gold support (see paragraph 3.6). The MIP showed very interesting analytical behavior, overall, in terms of K_D and LOD. Thus, the opportunity to adapt the PNE-based mimetic assay to an ELISA-like test, arose. For this purpose, the synthesis conditions and dilution buffer (DB) were slightly modified according to the previous study to be tailored to the different support structure, here polystyrene microplates, and assay mode (static conditions instead of continuous flow in SPR). To the best of our knowledge, up to this point, there are only a few competitive ELISA tests based on antibodies for the detection of gonadorelin, available on the market as a research tool, which could be tentatively applied in the anti-doping field. Nevertheless, the unknown antibody-binding epitope and the scarce information about the immunogen used to elicit the immune response limit their applicability. So, the main novelty of this study, with respect to the current literature, relies on synthesizing for the first time a PNE-based mimetic receptor onto microplates, and setting-up a BELISA, by exploiting disposable miniaturized platforms for easier and cost-effective detection of poorly or non-immunogenic small molecule, here G. This assay is like the

conventional ELISA, but the traditional bioreceptor, i.e., the antibody, is replaced with a "household" PNE-mimetic receptor, showing several advantages in terms of ease and speed of preparation, low cost, temperature stability, versatility and the synthesis in vitro, avoiding any animal use. In detail, a colorimetric two-steps competitive assay to quantify the analyte G was directly carried out on the MIP surface. For this purpose, a fixed concentration of the competitor molecule, the biotinylated G (BG) conjugated to the signal reporter (S-HRP), was involved in the assay to trigger a competitive reaction with G for the same MIP cavities. The whole BELISA assay was designed to maintain the compatibility with one of the most widely used readout that involves horseradish peroxidase (HRP) enzyme as a signal reporter and TMB as a substrate that, in its classical use, leads to a final yellow color with a maximum absorbance peak at λ = 450 nm. Thus, the colorimetric signal obtained was directly related to the amount of G and it was measured by a simple absorbance reader, as those commonly present in clinical laboratories.

The BELISA assay development has required the optimization of several parameters, from the buffer composition for the washing steps (WB) and binding interaction with the MIP (DB), to the optimal concentration of the BG competitor, as well as the concentration of the detecting molecule S-HRP. The working temperature and the incubation times for the different steps (MIP-analyte, -BG, and BG-S-HRP interactions) were tried out to optimize the assay. Finally, the developed BELISA was calibrated and applied to human urine fortified with G. Mass spectrometric analysis was separately settled and eventually performed to validate the BELISA test.

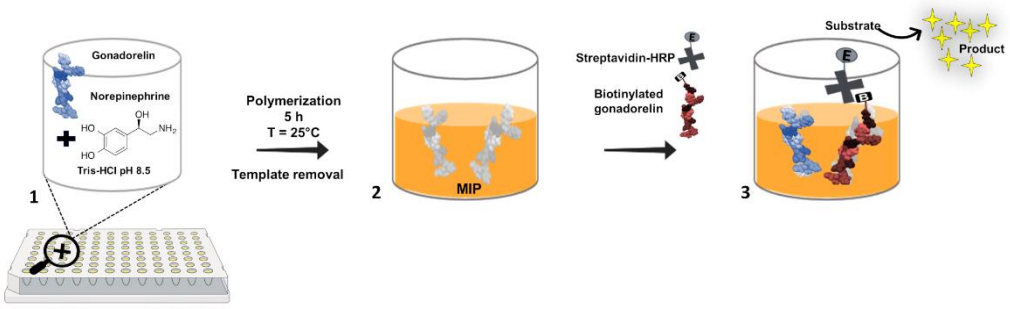

Scheme. 3.2 Sketched illustration of the imprinting process onto a micro-welled plate. (1) The functional monomer (norepinephrine) and the template (gonadorelin) were dropped as a mixture onto the wells' microplate and the polymerization process occurred for 5 h at 25 °C. (2) Then, the template was washed out the polymeric matrix, and the 'two-steps' competitive BELISA (3) was set up

3.7.4.1 Evaluation of factors affecting the bioassay and BG binding test

To exclude possible optical artifacts due to the sole presence of S-HRP, TMB, and/or the reaction cascade involved in the readout step on the MIP, a dose-response test was first carried out. To this aim, various S-HRP enzyme concentrations in WB were dispensed into the MIP-coated wells and kept at 4°C for 30 min, followed by three washing steps with the same buffer (200 µL/well). Fig. 3.10 displays the curve obtained after S-HRP addition at increasing concentration. Accordingly, we selected the optimal S-HRP concentration giving the lowest Abs@450 nm, which significantly differs from the blank (no S-HRP added into the wells), resulting in 0.20 µg mL^{-1} (dilution ratio 1:5000 in WB). This concentration was thus employed for all further experiments. This first step demonstrated that the polymer does not interfere with the enzyme-based optical detection, and this is the prerequisite to go further in the assay development.

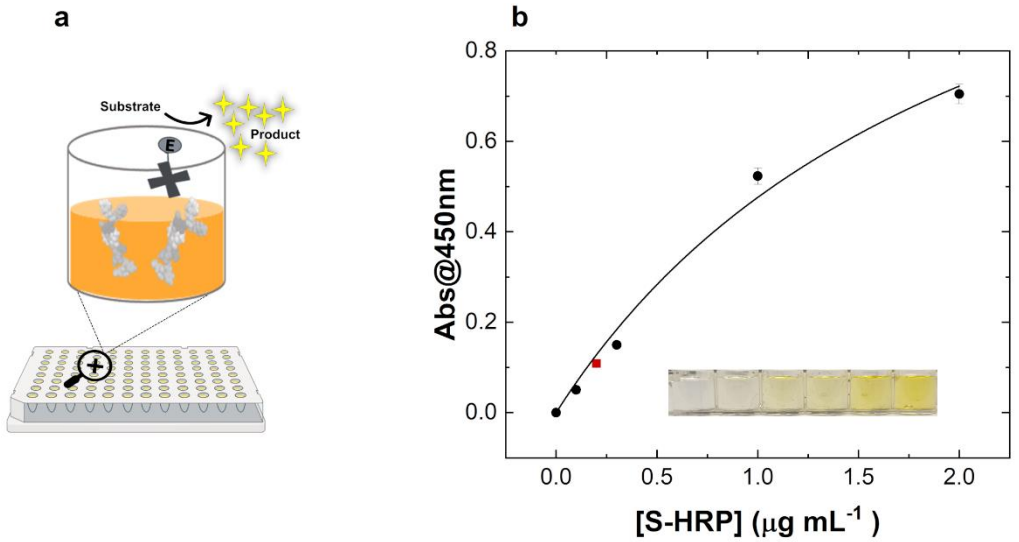

Fig. 3.10 (a) Schematic depiction of the assay setup to select the S-HRP concentration (0.20 μg mL^{-1}); (b) Calibration curve of the enzyme conjugated to streptavidin (S-HRP) on the MIP-coated microplate

Thereafter, the BG calibration, the competitor molecule, was tested and optimized. Two temperatures, 4 °C and 25°C, were compared in terms of BG binding efficacy on the PNE-based MIP (Fig. 3.11). These temperatures were selected since they are most used in standard ELISA protocols for reagents' incubation. Regarding this, we aimed to simplify the conventional ELISA kit, by substituting the natural receptors with biomimetics, while minimizing the standard ELISA protocol in terms of incubation temperatures, operative steps, and laboratory equipment required. Besides, these temperatures are also chiefly used for the storage of substrates modified with natural inspired polymers (e.g., PNE and PDA). The calibration curves were obtained by plotting the Abs@450 nm against the concentrations tested both at T = 4°C (solid line) and T= 25°C (dashed line), as displayed in Fig. 3.11.

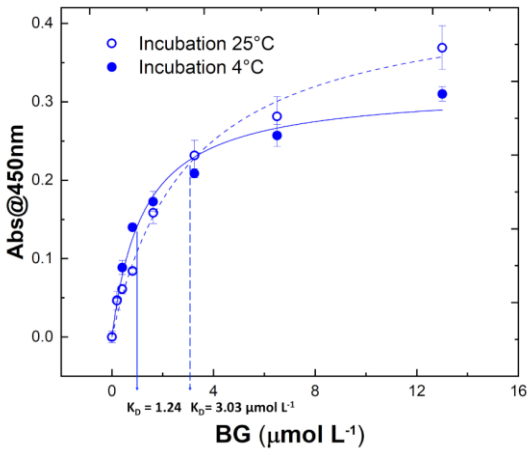

Fig. 3.11 Comparison of BG calibration curves performed at 4°C (solid line) and 25°C (dashed line), respectively

In this case, the test performed at T= 25°C provides a saturation level higher (around 13.00 µmol L^{-1}) than the curve resulting from a 4°C incubation experiment (around 6.50 µmol L^{-1}). Nonetheless, these data (T =25°C) are affected by a higher standard deviation. According to the latter evidence, the overall assay repeatability at 4°C resulted slightly improved, as inferred by the intra-assay average coefficient of variation (% coefficient of variation = 100* standard deviation/mean), $_{av}$CV% (25°C) = 4.40 % and $_{av}$CV% (4°C) = 3.44 %, respectively. This, in addition to being well compatible with routine ELISA incubation temperature, allows avoiding local temperature fluctuations over seasons and among different laboratories, improving the assay repeatability. This bestows robustness to the assay, as also denoted by the good inter-laboratory reproducibility which was estimated $_{av}CV\%_{4°C}$= 4.8% at 4°C. Lastly, the equilibrium dissociation constant, K_D, were extrapolated from the saturation curves obtained by measuring the direct BG-MIP binding interaction. In this case, the two datasets (Fig. 3.11) were fitted with a Langmuir binding model (1:1) by the equation $y=(R_{Absmax}*X)/(K_D+X)$ (Origin 2019b), where R_{Absmax} is the maximum response (Abs@450nm) and K_D is the equilibrium dissociation constant that was estimated for the curves. From this evaluation, R_{max} and K_D values resulted as follows: R_{max} (25°C) = 0.440 ±

0.023, K_D (25°C) = 3.03 ± 0.42 µmol L^{-1} and R_{max} (4°C) = 0.317 ± 0.015, K_D (4°C) = 1.24 ± 0.20 µmol L^{-1}.

Finally, for achieving an efficient competition, the optimal competitor molecule (BG) concentration has been selected after its calibration. In this case, the BG concentration was derived from the K_D estimation at 4°C (see Fig. 3.12) and experimentally selected at 6.50 µmol L^{-1}. To note that the estimated K_D value of the interaction MIP-BG extrapolated from the BELISA is in the same order of magnitude to the one previously inferred by the SPR biosensor (paragraph 3.6). This finding is very interesting since the surface binding sites (surface capacity) of the two assay substrates (polystyrene microwell vs gold chip) are very different in size and material, encouraging further applications of PNE-based mimetics on both the platforms.

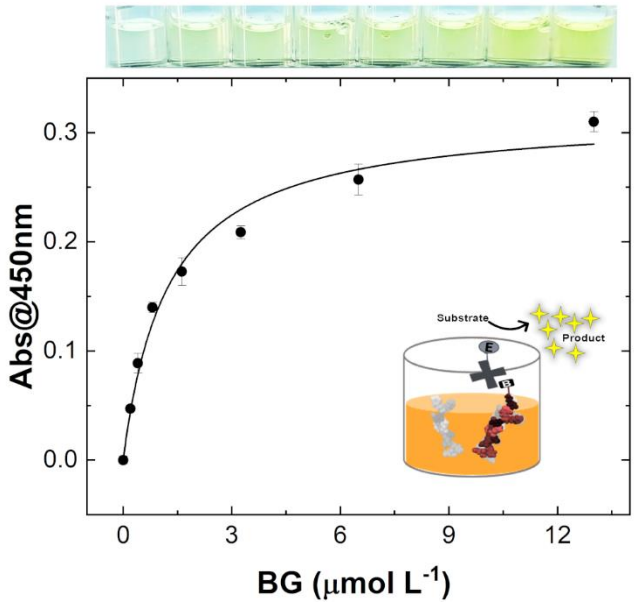

Fig. 3.12 Saturation binding curve for BG where the BG concentration (0.20-13.00 µmol L^{-1}) was plotted against Abs@450nm. Each point indicates the mean response ± SD of quadruplicate measures. The inset figure reports the BG calibration scheme. An illustrative photo (at the top of the figure) reports the wells color development for an increasing series of BG concentrations (from left to right)

3.7.4.2 Competitive binding assay on MIP-coated microplates

Once optimized the main experimental conditions, we moved forward with the actual 'two-steps' competitive assay by calibrating gonadorelin in buffer condition first and, finally, in real matrix, *i.e.*, human urine. In the first step, the analyte is incubated in the MIP-coated microplate wells (as detailed in the experimental section (b)); thereafter, a fixed amount of the competitor molecule (BG) is sequentially incubated at the defined optimal concentration, followed by washing step and a standard HRP/TMB-based readout protocol. The standard curve obtained in buffer (Fig. 3.13) within the range $8.46 \bullet 10^{-5}$-8.46 μmol L^{-1} showed an evident inhibition of the absorbance signals with the increase of G concentration, demonstrating the ability of G to compete with BG. This is a key result obtained by successfully tuning the BG concentration to be used in the assay, as aforementioned. The signals measured (Abs@450nm) were expressed as the percent of analyte G bound to the MIP binding sites (A) divided by the maximal binding of the competitor molecule BG (A_0) to the MIP surface, measured in absence of the analyte (blank) (%A/A_0). In detail, data are reported in Fig. 3.13 as a semilogarithmic plot to display the typical S-shaped sigmoidal curve of the competitive BELISA assay. The curve is fitted with a 4-parameters logistic (4PL) regression (R^2 = 0.989) by the equation $y = \frac{(A_1 - A_2)}{1+(x/x_0)^p} + A_2$ where A_1 is the theoretical response at zero G concentration (A_1 = 106.3 ± 6.5 μmol L^{-1}) and A_2 the theoretical response at infinite concentration (A_1 = 19.4 ± 7.1 μmol L^{-1}); p is the slope factor (p = 0.36 ± 0.09 μmol L^{-1}) and x_0 is the mid-range concentration (inflection point, x_0 = 0.011 ± 0.005 μmol L^{-1}).

The assay (sigmoidal-shaped curve) showed a linear response in the concentration range spanning from 0.42 to 846 nmol L^{-1} (Fig. 3.14).

The limit of detection (LOD) and quantification (LOQ) were calculated as three times and ten times, respectively, of the standard deviation for the blank samples interpolated in the sigmoidal curve, namely LOD = 277 pmol L^{-1} and LOQ = 14.1 nmol L^{-1}. In addition, in terms of repeatability, the BELISA assay performed very well, with $_{av}$CV% = 4.07.

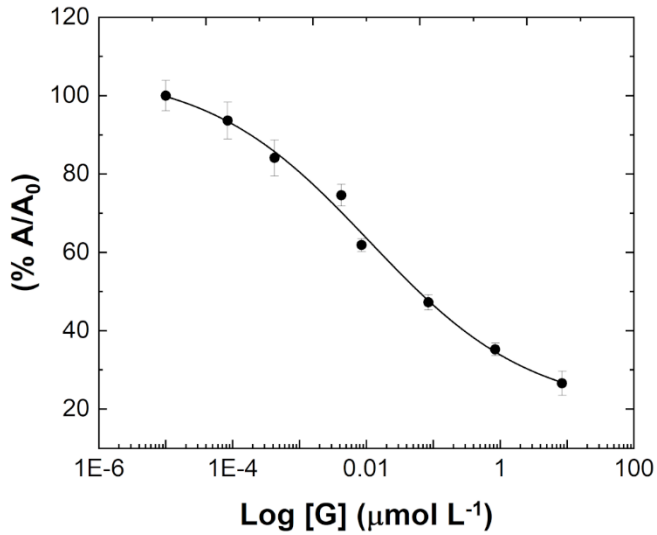

Fig. 3.13 MIP-based competitive inhibition BELISA: typical S-shaped curve (x-axis logarithmically transformed) for gonadorelin spiked in standard solutions over the concentration range of 8.46•10-5-8.46 μmol L^{-1}. The curve was fitted by using a 4-parameters (4PL) logistic regression

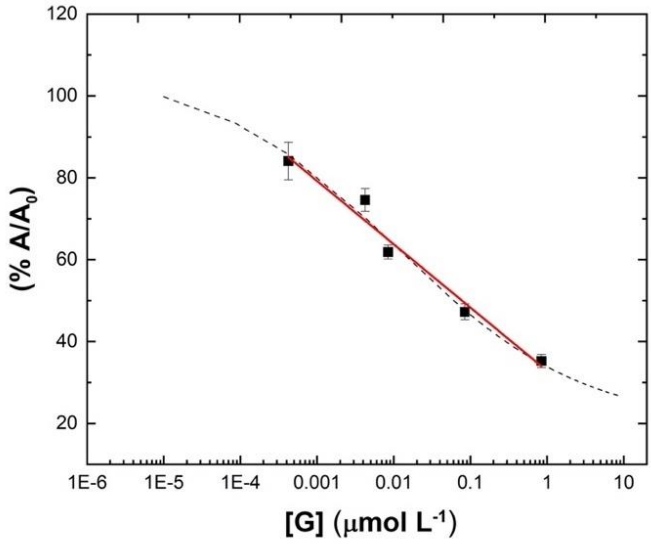

Fig. 3.14 The linear range of the sigmoid-shaped curve (0.42 to 850 nmol L^{-1}) obtained by analyzing G spiked standard solutions was highlighted in red

3.7.4.3 Selectivity of the BELISA assay for gonadorelin

The selectivity of the assay towards the analyte G was assessed by measuring the BELISA response (Abs@450nm) to two different control non-related peptides with comparable molecular weight and number of amino acids to the analyte G (see Table in Fig. 3.15). To this, the two peptides were added to the MIP surface as the first step in place of the analyte. Compared to G behavior (Fig. 3.15), almost negligible inhibition responses (less than 10%, expressed as A/A0 * 100) were found for both the unrelated peptides A and B. This means that the BG competitor may bind the MIP at the same level in all the cases and very low or no competition with the nonspecific peptides occurs. Therefore, non-related peptides compete very poorly with BG for the same MIP cavities, confirming the very good selectivity of the assay for the imprinted target. This also demonstrates that the PNE-based mimetic retains this feature also in batch (static) conditions, consolidating data previously obtained on the SPR biosensor [1].

a

Name	Sequence	Size (aa)	MW (Da)
G	p{GLU}HWSYGLRPG-NH2	10	1182.33
PEPT-A	Ac-ISLAPKAQIK-NH2	10	1109.37
PEPT-B	{pGLU}HWSY{d-LEU}LRP	9	1182.34

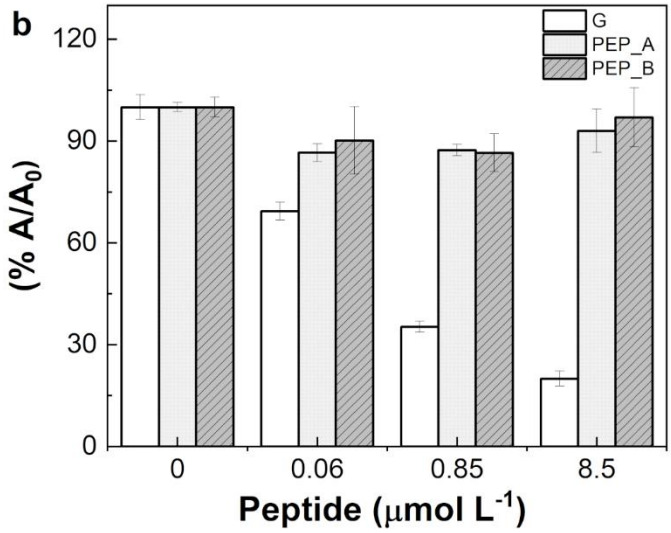

Fig. 3.15 Selectivity test performed on MIP-coated microplates. (a) Sequence, number of amino acids, and molecular weight of each peptide tested; (b) the competitive assay was performed with the target G (white color) and unrelated control peptides (PEP_A, grey bars, and PEP_B, grey striped bars)

3.7.4.4 Analysis of gonadorelin in human urine by BELISA

To evaluate the applicability of the novel competitive MIP-based BELISA, human urine samples from two healthy volunteers were tested. Preliminary experiments were conducted on untreated urine since the direct analysis of samples without the need of pre-analytical steps is one of the most important requirements in ELISA-like assays. However, the *'as it is'* urine testing resulted in no signal development possibly due to some urine component that impaired the test function. The stumbling-block has been overcome with a 1:10 dilution of the urine fortified with G (0.084-846 nmol L^{-1} in aqueous solution), significantly improving the output signal (Fig. 3.16).

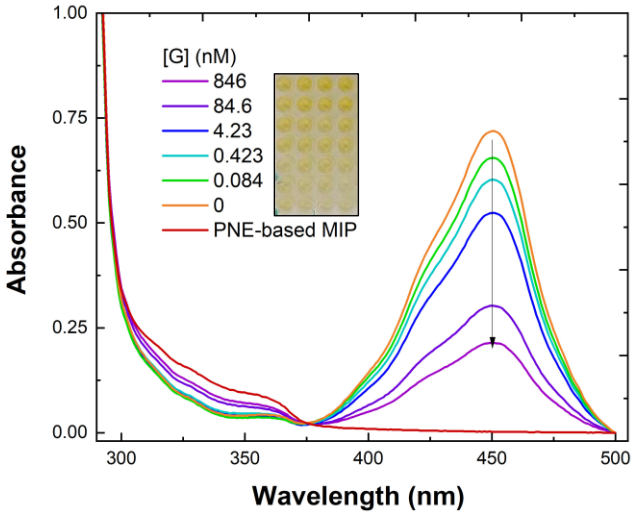

Fig. 3.16 Representative UV-vis absorption spectra of the BELISA assay, before data elaboration, and an illustrative inset image of the assay.

The diluted urine samples were thus dispensed into the microplate and then the assay procedure proceeds as described above (as detailed in the Materials and Methods section (b)). In this case, a successful competition occurred (Fig. 3.17), and the concentration of G in urine specimens was determined using the calibration obtained in buffer (Fig. 3.13), performed on the same day, to estimate the mean recovery. The mean recovery, expressing the closeness of the concentration values obtained in biological samples, with respect to the nominal spiked concentration, was calculated by the following formula $_{av}$recovery% = %(measured concentration-basal concentration/added concentration [6]). The basal G concentration in urine specimens is almost zero (see the following LC-MS/MS analysis), thus the resulting $_{av}$recovery% was equal to 91 ± 19 % for the urine sample 1 and 96 ± 25 % for the urine sample 2. The values obtained indicate a good recovery albeit a recovery overestimation occurred at the lowest concentration tested (recovery% = 118% for sample 1 and 124% for sample 2). Moreover, the repeatability on real samples resulted very good, namely $_{av}$CV% = 3.49 for sample 1 and $_{av}$CV% = 5.24 for sample 2. Lastly, the BELISA was validated

by mass spectrometry which is the reference analytical technique required by WADA in anti-doping controls.

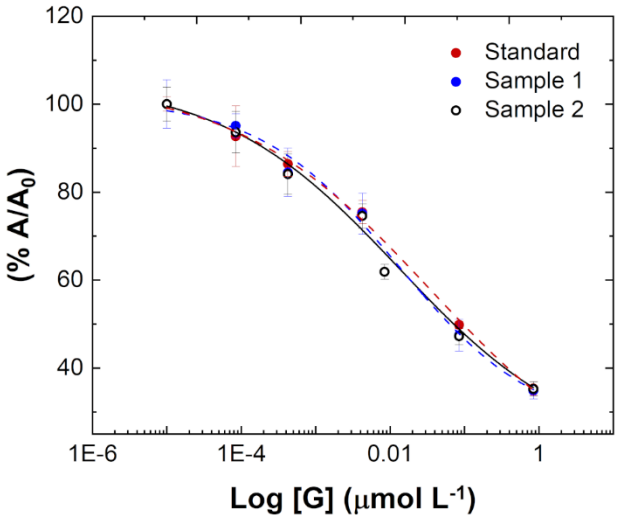

Fig. 3.17 (a) Competitive inhibition curve obtained by performing the MIP-based BELISA on human urine samples and standard solution fortified with gonadorelin, spanning from 0.084 to 846 nmol L^{-1}

3.7.4.5 LC-MS/MS method validation

LC-MS/MS analysis was set-up by modifying a previous protocol reported by Thomas et al. [5]. Human urine samples were in parallel analyzed with BELISA and LC tandem mass spectrometry, in this case in compliance with European Medicines Agency (EMA) guidelines to assure the quantitative performance of the assay (including selectivity, linearity, sensitivity, and accuracy) [7]. Firstly, a calibration curve built with standard solutions of G in water diluted urine (1:10), in the concentration range spanning from 0.084 to 8.46 nmol L^{-1}, was performed by LC-MS/MS (Fig. 3.19). Then the spiked urine samples were analyzed, and the G concentrations were estimated based on the response of the instrument to the known G standard solutions. All the figures of merit were estimated. Initially, the selectivity of the proposed method was assessed by performing repeated injections of urine samples,

with and without analyte G, into the chromatographic system and the retention time (RT) was monitored, RT (G) = 4.58 min and RT (ISTD) = 3.88 min (Fig. 3.18).

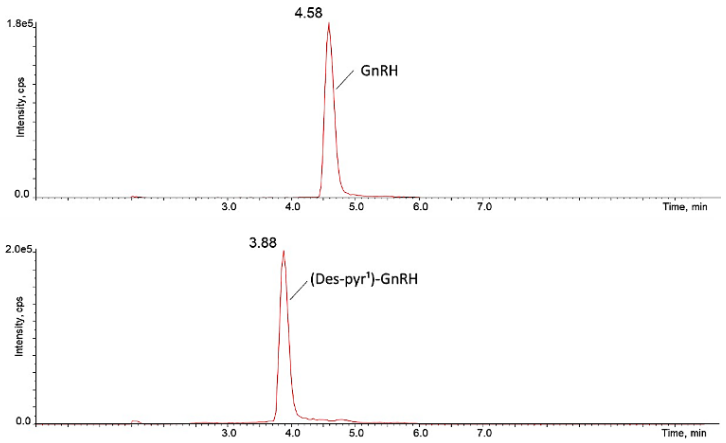

Fig. 3.18 Chromatographic profiles of G (aka GnRH) and ISTD (Des-pyr^1)-GnRH (from top to bottom) and relative retention times

No interferences in the selected transitions occurred, demonstrating the selectivity of the method. The linearity of the method was evaluated for the G calibration curve (y = a + bx, where a = -0.022 ± 0.006 and b = 0.551 ± 0.003), carried out in standard solutions, and it was expressed as correlation coefficient (R) ≥ 0.999 (Fig. 3.19). The G concentrations in standard solutions providing a "signal-to-noise" (S/N) ratio close to 3 and 10, calculated using a specific tool of ABSciex Analyst® software, were assumed as LOD and LOQ, respectively. The LOD achieved corresponds to 21 pmol L^{-1} while the LOQ is equal to 84 pmol L^{-1}. The accuracy (%) was determined in human urine samples diluted 1:10 in water at 0.11, 0.61 and 1.27 nmol L^{-1} and it was calculated by the following formula % (measured concentration/nominal spiked concentration). Thus, the resulting accuracy was found in the optimal range of 85-115% as indicated by EMA [7]. Besides, recovery (%) and matrix effect were studied as reported by Matuszewski et al. [8]. The mean percent recovery was established by comparing the peak areas of G and those of

ISTD which were added respectively before and after the extraction procedure. The obtained recovery (%) for G was equal to 36.25 ± 1.05 while the recovery (%) for ISDT corresponded to 60.1 ± 0.8. In addition, the matrix effect (%ME) was calculated by comparing the peak areas of the ISTD and those of the analyte G which were respectively added to water (A) and urine (B) samples [%(B/A)], both previously subjected to extraction procedure ($\%ME_G$= 47.4 ± 9.9 and $\%ME_{ISTD}$ = 88.1 ± 16.3). The recovery ratio (RR) between the analyte G and the ISTD (Des-pyr1)-GnRH was eventually found constant and concentration-independent. Therefore, RR is able to provide a correct analysis and quantification of G in human urine samples.

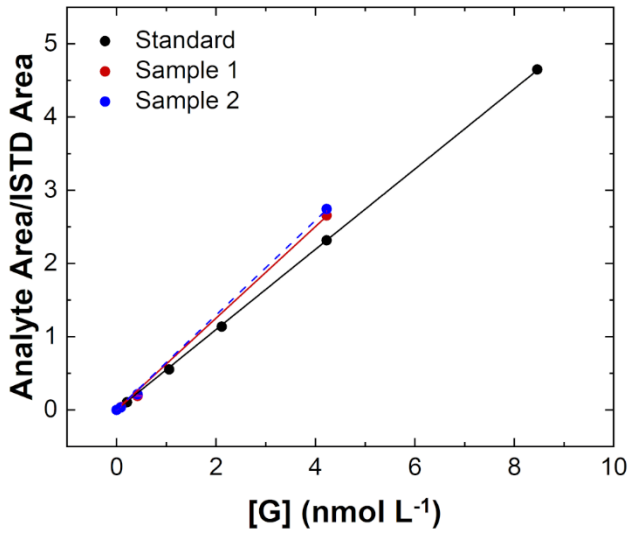

Fig. 3.19 Calibration curve for the LC-MS/MS analysis of gonadorelin (G) in standard solutions (concentration range: 0.084-8.46 nmol L^{-1}, black dots) and results (red and blue dots) of urine specimens spiked with G at 0.084, 0.423 and 4.23 nmol L^{-1}

Additional experiments were executed to study the stability of GnRH and ISTD (Des-pyr1)-GnRH as a result of freeze-thaw cycles. Aliquots of freshly gonadorelin at a low, medium, and high concentration were prepared in water and were divided into two aliquots. The first aliquot was quickly injected into

the instrument while the second one was frozen at −20 °C and thawed at room temperature before being analyzed. The acquired results were compared and no peptide (G) and/or ISTD degradation was detected. This is an important information confirming the stability of the reference lyophilized peptide reconstituted in water and stored at -20°C which was then be gradually used in the assay's trials.

3.7.4.6 Bland-Altman analysis

The correlation between the BELISA test (A) here developed and the reference method by LC-MS/MS (B) was assessed using a Bland-Altman plot (aka Tukey mean-difference plot) [9]. This is a simple method of data plotting used both in analytical chemistry and biomedicine to compare two different analytical strategies. In this case, the agreement between two quantitative measurements were evaluated by constructing a scatter plot, in which the y-axis reports the difference between the two measurements (A-B) while the x-axis describes the mean of the value-pair ((A+B)/2). On this basis, the correlation between the paired data reported in Fig. 3.20 shows that all xy scatter points lie within a predetermined interval of ± 2SD of the mean difference [10] suggesting that the confidence level between the two methods is equal to 95%. In this case, a good agreement between BELISA assay and the LC-MS/MS method was achieved.

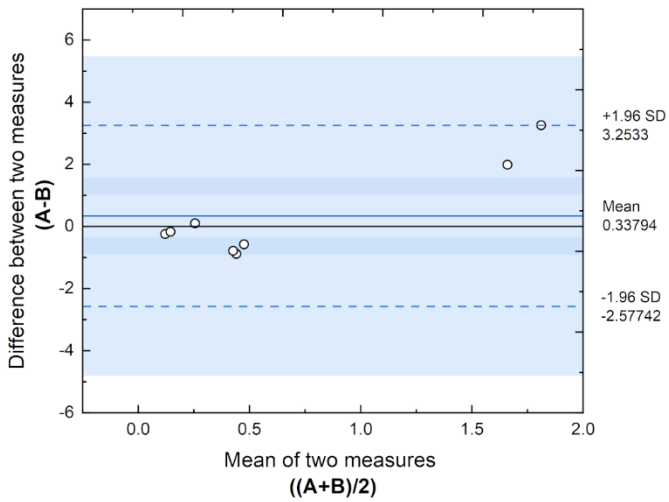

Fig. 3.20 Bland-Altman plot displays the regression line between measurements performed by BELISA assay (A) and the LC-MS/MS reference method (B). The difference of each value pair (A-B) is plotted on y-axis against the mean of each value-pair on the x-axis ((A+B)/2)

3.7.5 Conclusions

Antibodies, poly- and mono-clonal ones, have revolutionized the history of bioanalytic and the related diagnostic fields since the 1980s. Alongside the numerous and assessed advantages in using this naturally evolved tool to fulfill specific biomolecular recognition, they also display well-known limitations. ELISA tests are undoubtedly one of the most widely used bioanalytical methods which have benefited enormously from the incessant development in the immunological field, since antibodies in ELISA tests almost always play both the role of receptor and signal reporter molecules. However, they present environmental sensitivity, short lifetime even in correct storage conditions, high costs and long production times, the need of animals/cells use, and sometimes display low selectivity. For very low molecular targets, such as chemicals and short peptides, sometimes there is a lack of effective antibodies due to the scarce or absent immunogenicity of the antigen itself. In this framework, the perspective development of mimetic receptors alternative to antibodies in ELISA-like tests is an extremely exciting

and challenging task for the bioanalytic field. This is also in line with the EU Directive (2020/63/EU) on the protection of animals used for scientific purposes and the recent EURL ECVAM recommendations on non-animal-derived antibodies [11]. Here, an antibody-free competitive Biomimetic-ELISA assay (BELISA) based on a nature-inspired molecularly imprinted polymer as a recognition element was developed for the successful quantitation of the short peptide gonadorelin. The aim of the study was the conservation of a routine ELISA-type test protocol coupled to a classical enzyme-based readout at λ_{max} = 450 nm, except for the need of antibodies. According to our knowledge, this is the first example of a BELISA test involving a molecularly imprinted polymer based on polynorepinephrine, and able to detect the analyte (gonadorelin, G) in buffer and untreated (except for 1:10 dilution) human urine. The BELISA assay allows the sensitive and selective measurement of this potential doping peptide, G, in representative urine samples with very good performance. The results obtained in standards solutions and urine samples showed a good repeatability ($_{av}$CV%=4.07% for standard solutions, $_{av}$CV% (sample 1) = 3.49% and $_{av}$CV% (sample 2) = 5.24%, a challenging task considering that all the receptors were manually drop casted and polymerized in each microplate well. The prospective improvement of this parameter can therefore be figured out by automating, for example, the microwells preparation under highly controlled conditions. To validate the BELISA test, simulated blinded urine samples spiked with G were simultaneously dosed by BELISA and LC/MS-MS, the reference benchtop platform in anti-doping analysis for such type of analytes. In both cases, the detection limit achieved in standard solutions (LOD_{BELISA}= 277 pmolL^{-1} and $LOD_{LC\text{-}MS/MS}$ = 21 pmol L^{-1}) for G detection resulted in line with the Minimum Required Performance Level (MRPL = 1.69 nmol L-1) at which all the World Anti-Doping (WADA)-accredited laboratories must operate. The results from the two platforms correlate well by performing a simple statistical Bland-Altman analysis. The LC-MS/MS method resulted more sensitive than the BELISA, as expected from a gold standard method. Nevertheless, the BELISA assay may be largely enhanced, if needed, by

involving more sensitive detection strategies (e.g. fluorescence or chemiluminescence). As a whole, catecholamine-based MIPs, PNE in this case, have shown (here for the G case study) to be an excellent candidate material to imagine ELISA-like tests of the near future, antibody-free, extremely cheap, able to be prepared for a large variety of targets (even small non-immunogenic), very stable to environmental conditions, and highly versatile. This approach could further open new possibilities as abiotic point-of-care testing to make multiplexing biological samples analysis by integrating the smartphone technology which can be also extendable to several analytes.

References

1. Torrini F, Palladino P, Baldoneschi V, Scarano S, Minunni M. Sensitive 'two-steps' competitive assay for gonadotropin-releasing hormone detection via SPR biosensing and polynorepinephrine-based molecularly imprinted polymer. Anal Chim Acta 2021; https://doi.org/10.1016/j.aca.2021.338481
2. He Y, Hong S, Wang M, Wang J, Abd El-Aty AM, Hacimuftuoglu A, Khan M, She Y. Development of fluorescent lateral flow test strips based on an electrospun molecularly imprinted membrane for detection of triazophos residues in tap water. New J Chem. 2020; https://doi.org/10.1039/d0nj00269k
3. Steinitz M. Quantitation of the blocking effect of tween 20 and bovine serum albumin in ELISA microwells. Anal Biochem. 2020; https://doi.org/10.1006/abio.2000.4602
4. Zvereva I, Dudko G, Dikunets M. Determination of GnRH and its synthetic analogues' abuse in doping control: Small bioactive peptide UPLC-MS/MS method extension by addition of in vitro and in vivo metabolism data; evaluation of LH and steroid profile parameter fluctuations as suitable biomarkers. Drug Test Anal. 2018; https://doi.org/10.1002/dta.2256. Epub 2017 Sep 28
5. Thomas A, Geyer H, Kamber M, Schänzer W, Thevis M. Mass spectrometric determination of gonadotrophin-releasing hormone (GnRH) in human urine for doping control purposes by means of LC-ESI-MS/MS. J Mass Spectrom. 2008; https://doi.org/10.1002/jms.1453

6. Tripathi BP, Das P, Simon F, Stamm M. Ultralow fouling membranes by surface modification with functional polydopamine. Eur Polym J. 2018; https://doi.org/10.1016/j.eurpolymj.2017.12.006
7. Guideline on bioanalytical method validation, European Medicines Agency 2011
8. Matuszewski BK, Constanzer ML, Chavez-Eng CM. Strategies for the assessment of matrix effect in quantitative bioanalytical methods based on HPLC-MS/MS. Anal Chem 2003; https://doi.org/10.1021/ac020361s
9. Giavarina D. Understanding Bland Altman analysis. Biochem Med. 2015; https://doi.org/10.11613/bm. 2015.015
10. www.originlab.com/Bland-Altman-Plots
11. Viegas Barroso JF, Halder ME, Whelan M. EURL ECVAM recommendation on non-animal-derived antibodies. EUR 30185 EN, Publications Office of the European Union 2020; https://doi.org/10.2760/091625

CHAPTER 4

Moving towards nano-sized imprinted polymers as artificial antibodies

4.1 Nanomedicine: from films towards nano-therapeutics

Nanomedicine……is medicine at the nanoscale [1]!

Like for any breakthrough technology, the promising possibilities that nanomedicine offers in the future must be balanced against risks. Nanomedicine products are regulated, in terms of toxicity assessment and multi-stage trials, and clinically evaluated for their benefit/risk ratio for the patients. It is of utmost importance to examine upfront all possible side effects to human beings and the environment. In this scenario, biocompatibility and sustainability are crucial factors for specific applications in the biomedical field. Nanotechnology offers multiple benefits to achieve innovation in healthcare with impact in all fields of medicine from diagnostics and therapeutics, going through medical imaging, vaccines, and regenerative medicine. The field of nanomedicine primarily blossomed with the potential of *in vivo* delivering drugs but now is spreading also for the treatment and

follow-up of various diseases, for tissues and organs regeneration, and for the early diagnosis at the nanoscale. Nanomedicine provides important cutting-edge tools to deal with the actual clinical requests directed towards personalization medicine. In this broad scenario, it is an urgent need to explore many biomaterials which possess unique advantages, such as low toxicity, low price, and biocompatibility. It's all about breaking old barriers, indeed they are intended to pave the way as potential substitutes for nano-metals. Poly(catecholamines) (pCAs) showed excellent biocompatibility and can significantly decrease the occurrence of adverse effects, as demonstrated by a few testing studies performed in vitro [2]. In the case of pCAs, their ability to self-assemble, in one step, into nanostructures, but also to coat non-planar surfaces, makes them a potential soft, non-toxic, biocompatible, and sustainable tool to be exploited in different fields of nanomedicine. Moving from nanofilms towards nanostructures, different properties change, and we briefly detail these considerations in the following experimental section.

In this section, we get an overview mainly on the current applicative state-of-art of PNE@NPs (in terms of core-shell) and PNE-NPs (pure polymer NPs). In order to progress beyond this, we briefly discuss our view concerning the molecular imprinting at the nanoscale, bringing attention to the recent existing progresses in this field. Few recent studies show that PNE can be efficiently involved in the construction of drug delivery systems for small therapeutics such as nitric oxide and chemotherapeutics, specifically for chemo-photothermal cancer therapy. Among other fields of MIP applications, drug delivery is considered an excellent and promising method of drug-controlled release to achieve therapeutic results [3]. Two different architectural structures are reported; from one side, a core-shell approach was exploited by coating polystyrene beads nanoparticles with a PNE layer with the function of store NO [4]. The same approach was also used concerning chemo-photothermal cancer therapy, where FeOOH-NPs were coated with PNE and then loaded with the drug, artemisinin [5].

On the other side, always about chemo-photothermal cancer therapy, PNE nanoparticles have been synthesized by one-pot method modified with polyethylene glycol moieties (PNE PEG-based NPs) and loaded with doxorubicin ((DOX)-loaded PNE-PEG based NPs). This DOX@system under irradiation with a near-IR laser, or at acidic pH like in the tumor microenvironment, releases DOX exhibiting an enhanced chemotherapeutic efficacy [6]. We focus, as outlook for the near future, and comprehensively explain the potential of the nano-imprinted biopolymers (nano-IBPs), starting from PNE and then moving forward with polyserotonin (PSE) for diagnostics, bioanalytical applications, and therapeutics of the future. Molecular imprinting has been identified as the most efficient and promising path to synthesize artificial receptors, as an alternative to their natural counterparts (antibodies). Therefore, increasing efforts have progressed in this direction.

4.2 Introduction and objective of the study

Soft and green nano-imprinted biopolymers (nano-IBPs), represent excellent candidates for mimic receptors to be exploited in future biomedical applications. In particular, nano-IBPs can be a valid alternative to immune checkpoint antibodies, a "hot" topic in cancer immunotherapy, in order to block programmed cell death 1 receptor (PD-1) and/or programmed cell death ligand 1 (PD-L1) [7]. These are two important targeting sites to develop effective therapeutic strategies. PD-1, also known as CD279 (cluster of differentiation 279), regulates T cell-mediated immune responses through which cancer cells evade the immune system promoting tumor progression [8-9]; it is highly expressed on T cells in patient tumors. PD-L1, also known as CD274, is a membrane protein that binds PD-1 on the effector T cells, overexpressed on tumor cell surfaces to escape immunosuppression [10], transducing immunosuppressive signals. Nano-IBPs enabled sensors which represent an appealing technology, simple and low-cost, for the highly specific and sensitive detection of clinical biomarkers directly from samples (e.g., biological, and environmental samples). Moreover, nano-IBPs are promising alternatives to capture and reporter antibodies, commonly joined

in diagnostic platforms i.e., sensing, and bioanalytical devices. By addressing these two tasks, on one side nano-IBPs can be integrated as receptor elements, also replacing IBPs films, to enhance the assay sensitivity by increasing the specific surface area. Likewise, on the other side, nano-IBPs can be used as reporter elements when the bioanalytical assay is properly designed to achieve a sandwich architecture bringing along an impressive improvement of the assay sensitivity. To the best of our knowledge, no study on PNE based nano-IBPs or core-shell IBPs, involving PNE in the hierarchical structure, has been reported. Several cases about PDA-based core-shell nano-MIPs were described in the scientific literature by employing a two-steps synthesis. In particular, almost all the cases that have been reported involve PDA to build the shell structure around an inorganic core particle. Regarding this, two explicative cases are described below. To date, Chen et al. [11] synthesized hollow MIPs for horseradish peroxidase (HRP) recognition using a SiO_2@NH_2 core, showing an excellent specificity towards the analyte, after that the dissolution of the core silica NPs, was occurred. Chaowana et al. [12] presented, for the first time, a nanocomposite probe based on a core@shell imprinted PDA@quantum dot (QD). This probe was applied as an opto-sensor (fluorescent probe) for effective sarafloxacin, an antimicrobial agent, recognition in chicken meat samples. The quantitative detection of sarafloxacin was performed through fluorescence intensity quenching by the analyte recognition event.

Herein we briefly report the characterization of the NPs that we have started to synthesize and characterize by using a combination of dynamic light scattering (DLS) and scanning electron microscopy (SEM) to provide information on the morphology and size at the nanoscale. All these measurements were performed in collaboration with Prof. Emiliano Fratini and Dott. Giovanni Ferraro (University of Florence). In addition, we introduce a preliminary promising test on the use of poly(catecholamines) based nano-IBPs as mimetic receptors via SPR platform (see paragraph 3.5.3.1) to capture gonadorelin (see chapter 3).

4.3 Experimental section: materials and methods

4.3.1 Chemicals and instrumentation for the characterization

Dopamine hydrochloride (DA, ≥ 98.0%), norepinephrine hydrochloride (NE, ≥ 98.0%), and NaOH were from Merck. Ultrapure Millli-Q™ water (R ≥ 18.2 MΩ • cm) was used throughout all of the NPs synthesis. N-hydroxysuccinimide (NHS), 1-ethyl-3-(dimethylaminopropyl) carbodiimide (EDAC), ethanolamine (EA) and CM7 sensor chip was purchased from Cytivia Sweden AB. 4-(2-hydroxyethyl)piperazine-1-ethanesulfonic acid (HEPES), sodium chloride, acetic acid (≧ 99.7%), polyoxyethylene sorbitan monooleate (Tween-20) were obtained from Sigma-Aldrich (Milan, Italy).

Dynamic light scattering (DLS) is a non-invasive technique to size particles by measuring the random changes in the intensity of light scattered from a suspension or solution. The measurements were performed by a Brookhaven Instruments 90Plus Nanoparticle Size Analyzer apparatus. The light scattered from the sample was collected at 90° with respect to the incident 659 nm laser light radiation The NPs samples were prepared by dilution to minimize multiple scattering effects associated with the high concentration of the particulate.

Characterization by field emission scanning electron microscopy (FE-SEM) was performed using a high-resolution scanning electron Zeiss SIGMA microscopy (Carl Zeiss Microscopy GmbH, German) equipped with GEMINI Field-Emission SEM column (Carl Zeiss). It consists of a high-brightness Schottky field emission source, a beam booster, and in-lens secondary electron detector. Measurements were conducted on uncoated samples with an acceleration potential of 2 kV and at a working distance of about 2-3 mm. The analysis of SEM micrographs was conducted to determine the mean particle dimensions using ImageJ 1.52t software. Figure images were converted into binary images by setting a threshold and then analyzed using the macros included in the software. 100 individual nanoparticle measurements were considered, and the size distribution below 10 nm was not included because it was too close to the pixel size.

Optical measurements: UV–Vis absorption spectra were recorded by a UV-visible spectrophotometer Evolution 201 from Thermo Scientific at 25.0 °C, by using quartz cells.

4.3.2 Synthesis of bio-nanoparticles

Polydopamine and polynorepinephrine nanoparticles were prepared via one-pot, as a result of polymerization-induced precipitation, according to the procedure reported by Wang et al. (2019) [13] for PDA with some improvements. In a glass vial, the monomer (DA or NE, 10.55 mM) was diluted to 10 mL with ultrapure water. After the temperature and magnetic stirring were set up at 50°C and 700 rpm, respectively, 84 µL of a NaOH solution (1 M) was quickly added to the mixing reaction. The reaction proceeded for 3 h and NPs were then collected by centrifugation (20000 g, 5 min), sonicated (2 minutes), and washed two times with deionized water to remove unreacted dopamine and/or small oligomers. The collected pellet and supernatant solution were stored at 4°C.

4.3.3 Synthesis of core-shell nanostructures

Core-shell molecularly imprinted polymer-based nanostructures were synthesized, for the first time, entirely constituted by polycatecholamines. The PNE core structure (d= 80 ± 11) was composited with MIP via a copolymerization process. Firstly, 4.3 mg of the template molecule, gonadorelin (see chapter 3), and 2.8 mg of NE were dissolved in a solution of 10 mM Tris-HCl pH=8.5 containing 0.01 g L^{-1} of PNE-NPs and stirred for 5 h at 25°C (700 rpm). In this case, we considered a shell growth of around 5 nm to estimate the amount of monomer to be added in the imprinting step, by calculating the total surface areas exposed by the particles per unit mass of sample. Core-shell non-imprinted BPs were synthesized under the same experimental conditions, without the addition of the template molecule.

4.3.4 SPR experiment

SPR binding testes were carried out with a Biacore X™ (Biacore AB, Cytivia Sweden AB) instrument, with a flow rate of 5 µL min^{-1}, using a CM7 sensor chip modified with a carboxymethyl-dextran matrix. HBS-EP (composition: 10 mM HEPES, 150 mM NaCl, 3 mM EDTA, and 0.0005% Tween-20, pH 7.4) was used as running and immobilization buffer. The covalent immobilization of gonadorelin (G) to the carboxymethyl-dextran matrix occurred via the amine-coupling method, which is constituted by three sequential steps: 1) activation of carboxymethyl groups with 50 mM NHS and 200 mM EDC (1:1 v/v, 35 µL); 2) G immobilization in HBS-EP pH 7.4 (423 µmol L^{-1}, 100 µL); 3) deactivation of the remaining reactive hydroxysuccinimide esters with EA. The immobilization of gonadorelin can occur randomly via the primary amine on the N-terminal moiety or via the -OH group of the reactive serine. The latter reaction takes place if there is a neighboring histidine residue, as in this case, {pGLU}HWSYGLRPG-NH_2. In this first explorative test, after G immobilization, nano-IBPs and non-imprinted IBPs were separately injected (without dilution, 10 µL) four times. The regeneration among each injection was performed with 10 mM NaOH (10 µL).

4.4 Results and outlook for future research

In the experimental conditions described above a first synthesis of PDA NPs was carried out. This first trial was considered "a model reaction" to go further with the study of the catecholamine-based NPs. The UV-vis spectroscopic characterization of PDA NPs (pellet sample), DA, and the supernatant solution was executed to follow the synthesis, *i.e.*, the monomer consumption with the polymer growth. By looking at the UV absorption spectra in Fig. 4.1a, the peak of DA monomer (10.55 mM in water) is clearly observed at 280 nm (red dashed line). During PDA NPs preparation, this peak is going to fade off, while a broad absorption band (green line) between 200 and 700 nm (here the spectrum arbitrarily ends at 350 nm), typical of the PDA polymer, gradually increases. The absorption trend of supernatant displays an intermediate

behavior between DA and PDA (PDA oligomers), but a certain monomer component is evident. The hydrodynamic diameter was estimated by DLS and a cumulant analysis, to analyze the correlation function (here not discussed), a polydispersity index (PDI) related to the width of the distribution, was performed.

The hydrodynamic diameter and the polydispersity of the NPs were measured at time zero and after one day (Fig. 4.1), giving the values shown in Table 4.1. The samples resulted to be low polydisperse, as the PDI value is lower than 0.1 [14]. Afterward, a morphology analysis by SEM was performed for all the NPs studied. SEM micrographs at different magnifications are shown in Fig. 4.1 and, overall, they spotlight low polydispersity spherical primary units with a diameter 112 ± 14 nm.

Table 4.1 DLS results summaries obtained on a NPs PDA sample

	Diameter (mean ± SD)	**Half width (nm)** (mean ± SD)	**Polydispersity** (mean ± SD)
0 day	162.9 ± 1.8	38.7 ± 9.9	0.077 ± 0.032
1 day	188.6 ± 2.1	56.7 ± 5.7	0.099 ± 0.015

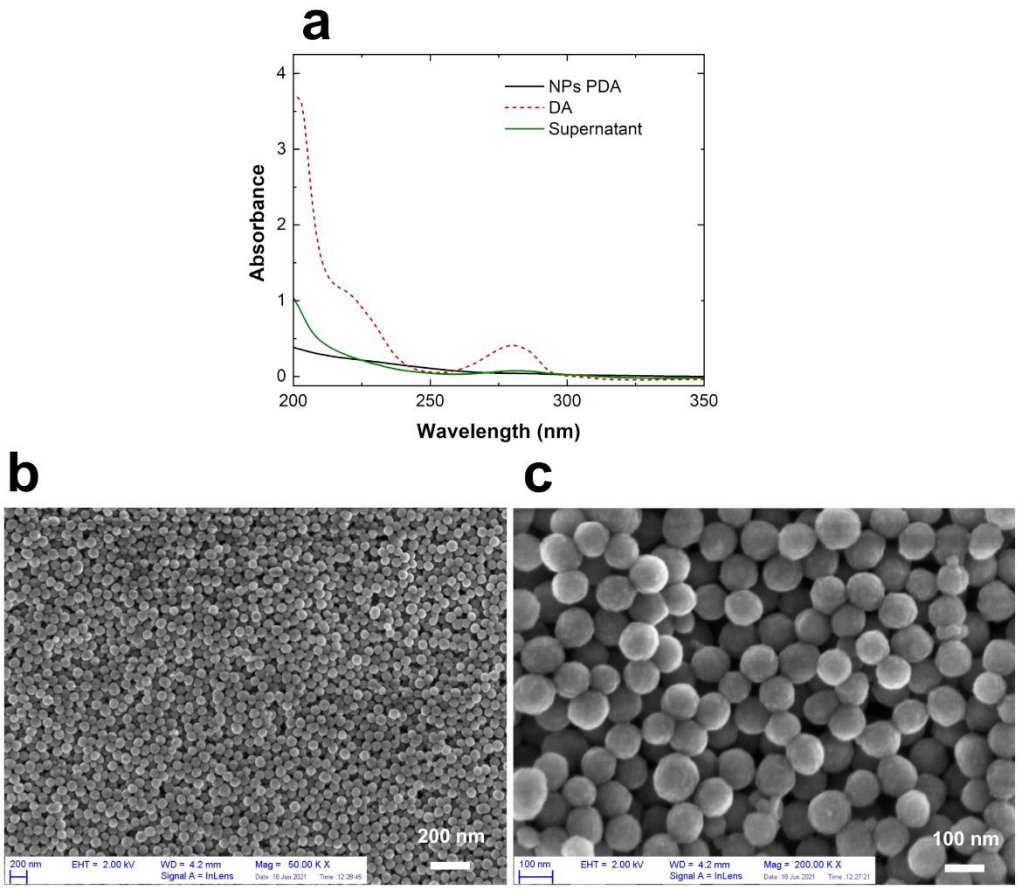

Fig. 4.1 (**a**) UV absorption spectra of DA, NPs PDA, and supernatant solution, respectively are displayed; SEM micrographs showing low polydispersity spherical NPs nanoparticles taken at 50000 kX (scale bar 200 nm) (b) and 20000 kX (c) magnifications (scale bar 100 nm), respectively

The reproducibility of the synthesis reaction was also evaluated by estimating the mean diameter and the $\%CV_{mean}$ of the different NPs batches over three different days. The mean diameter corresponds to 112 ± 12 nm, while an excellent reproducibility was obtained $\%CV_{mean}$ equal to 10.7 (Fig. 4.2).

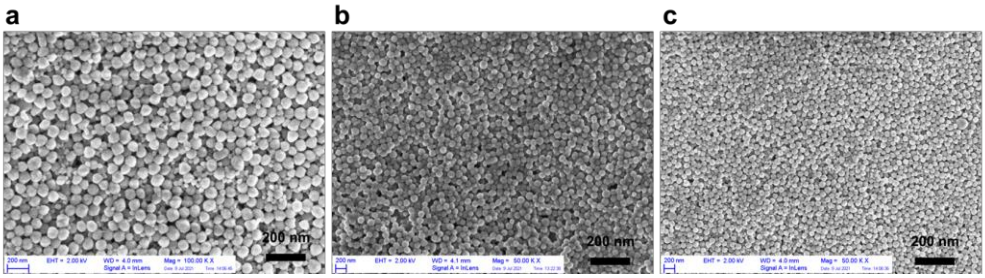

Fig. 4.2 (**a**) Morphology of PDA NPs over three days.
SEM micrographs (scale bar 200 nm) showing low polydispersity spherical NPs nanoparticles taken at 10000 kX (a) and 50000 kX (b-c). The estimated diameter for each sample is respectively equal to, left-to right direction: 112 ± 14 nm (a), 124 ± 25 nm (b) and 100 ± 11 nm (c)

PNE nanoparticles were synthesized following the same procedure for PDA. In particular, the growth of PDA and PNE NPs during the synthesis was monitored, as well as pH (pH range during synthesis: 8.6-8.3), by analyzing NPs samples produced at different reaction times (Fig. 4.3). As shown in Figure 4.3, the PDA nanoparticles gradually grow (from 60 to 310 nm) by increasing the synthesis time. The capability to tune the size of the nanoparticles, only as a function of time, is an interesting result that deserves a more in-depth investigation. In the case of PNE, it seems that the kinetic growth of seeds occurs slower compared to PDA. This first assumption is a consequence of a simple experimental observation. PNE NPs subjected to a synthesis process of less than 5 h, during the centrifugation (20 000 g) remain in solution. In addition, morphological characterization will be performed to complete the observation. The PNE NPs diameter, estimated through ImageJ software, results smaller compared to their PDA homologues, as verified by SEM (Fig. 4.3).

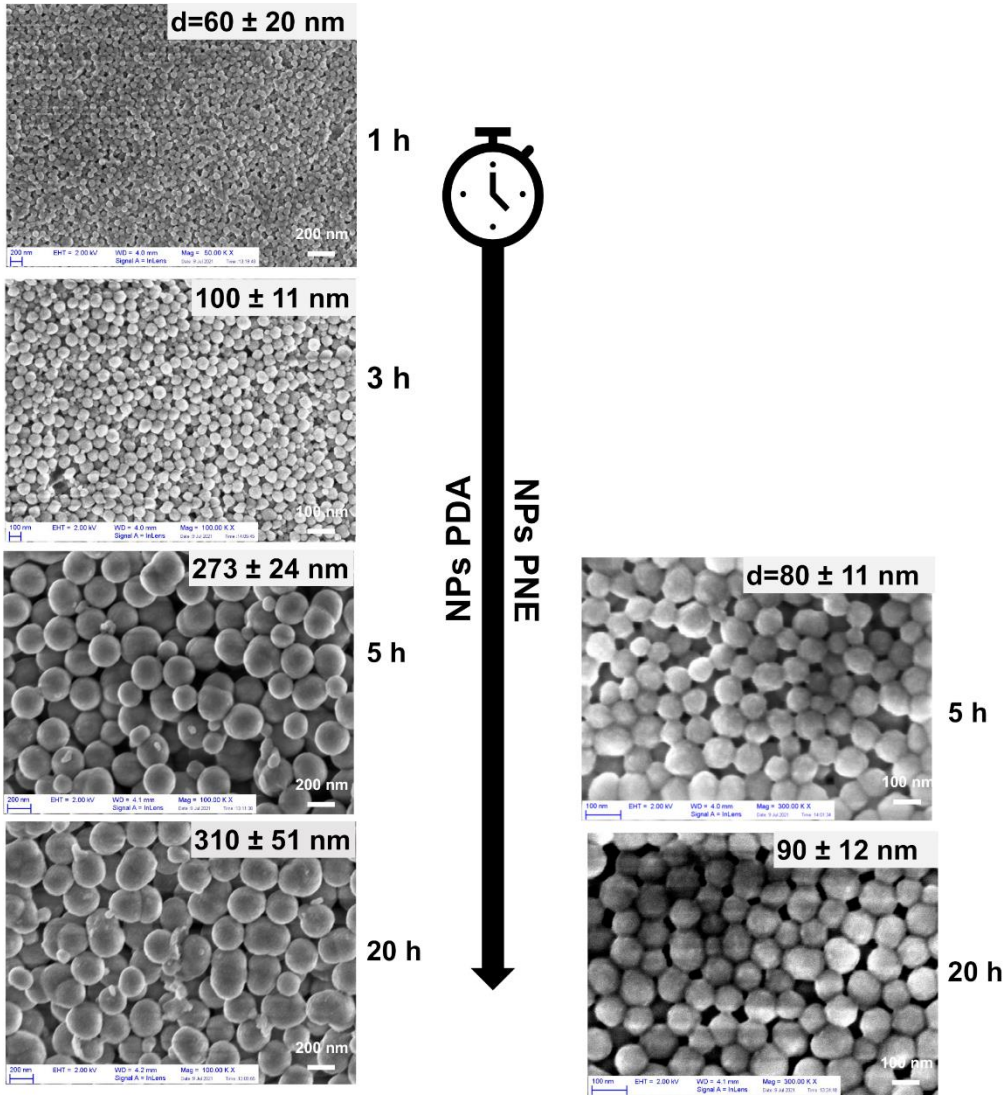

Fig. 4.3 SEM images acquired at different "time synthesis". On the left SEM micrographs for PDA while on the right SEM micrographs for PNE. The estimated diameter for each sample is shown in the SEM figures

Thereafter, we carried out the first attempts to make core-shell nanoparticles completely biocompatible, by avoiding the metal-based core. In this case, the procedure was constituted of two steps. The first step consists in the core synthesis (PDA or PNE), here described so far, a non-imprinted polymer, which after the washing steps were lyophilized for longer storage. A

morphological evaluation, pre (Fig. 4.4a) and post (Fig. 4.4b) freeze drying process was performed on the PDA NPs revealing that this did not affect the morphology and particles' size (see Fig. 4.4). The second step consists in a subsequent polymerization in co-presence of the seeds (core NPs), a functional monomer (DA or NE) diluted in Tris-HCl buffer pH 8.5, to obtain an external shell that covers the core. In Fig. 4.4 two different combinations of core-shell NPs are presented: PDA@PNE (left) and PNE@PNE (right). A significant increase in size (from 80 to 241 nm), comparing the core and the core-shell structures, was observed only for the second combination, PNE@PNE core-shell although clusters of two-three PNE NPs may be observed. An interesting point that will be addressed, in terms of physical-chemical properties, is the combination of different pCAs into the same structure. The core-shell design will be optimized by well weighting the monomers' concentration to cover a single particle (considering the number of particles) in order to be able then to print the shell itself.

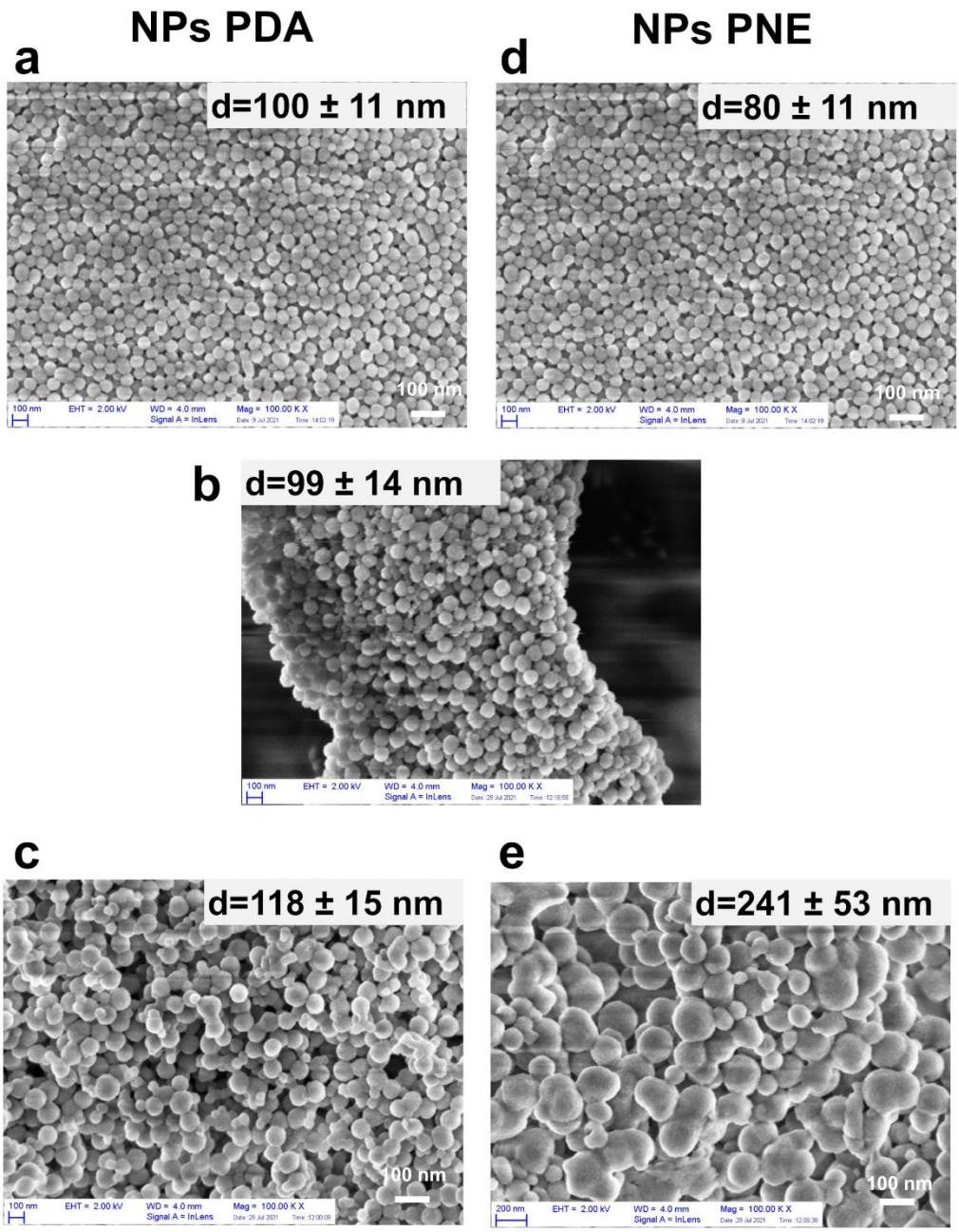

Fig. 4.4 SEM images of the PDA core (a), the freeze-dried core (b) and "core-shell" PDA@PNE structures (c). On the right, SEM images of the PNE core (d) and core-shell" PDA@PNE structures (e)

4.4.1 SPR binding interaction analysis of nano-IBPs

Although a more-in depth nanostructure optimization, as well as characterization, is needed, a first explorative binding test of nano-IBP was performed. A direct binding analysis involving gonadorelin, immobilized on the sensor chip with a suitable chemistry (gonadorelin immobilization level= 413.3 RU), and nano-IBPs was carried out.

The direct binding nano-IBPs test has displayed a well-measurable SPR signal (88.9 ± 2.6) with very good repeatability (%CV_{av}= 2.9, Fig. 4.5). Non-imprinted BPs, as control surfaces, were also tested in the same manner. In this second case, the analytical signal recorded is lower than nano-IBPs (Fig. 4.5). The results gathered during this SPR experiment (Fig. 4.5) strongly suggested that the imprinting process was indeed successful and that gonadorelin is reversibly bound to the cavities on the nano-IBPs. This behavior may be associated with the selectivity of the nano-IBPs towards the template gonadorelin. These "objects" proved to be extremely promising in this first trial to undertake further studies in a multidisciplinary field.

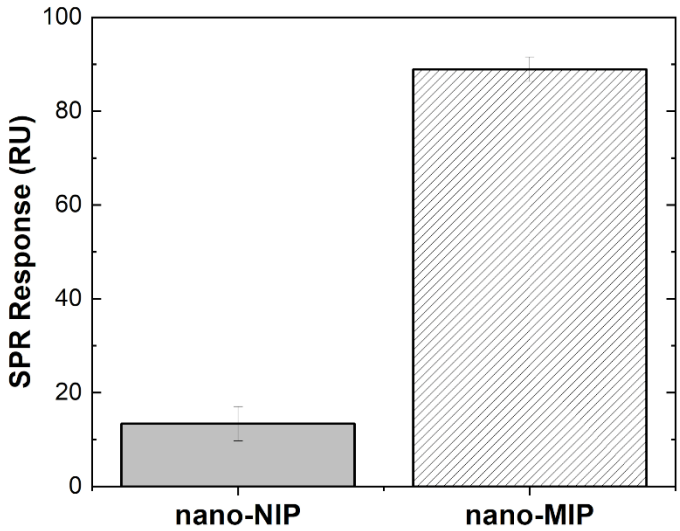

Fig. 4.5 SPR responses comparison for the nano-IBP (or nano-MIP) and non-imprinted BP (or nano-NIP) versus the analyte, gonadorelin, covalently immobilized onto a sensor surface chip

References

1. https://nanomedicine.eu
2. Liu Y, Ai K, Lu L. Polydopamine and its derivative materials: Synthesis and promising applications in energy, environmental, and biomedical fields. Chem Rev. 2014; https://doi.org/10.1021/cr400407a
3. Zaidi SA, Molecular imprinting: A useful approach for drug delivery. Mater Sci Technol. 2020; https://doi.org/10.1016/j.mset.2019.10.012
4. Liu X, Xie Z, Shi W, He Z, Liu Y, Su H, et al. Polynorepinephrine nanoparticles: a novel photothermal nanoagent for chemophotothermal cancer therapy. ACS Appl Mater Interfaces 2019; https://doi.org/10.1021/acsami.9b03458
5. He Z, Su H, Shen Y, Shi W, Liu X, Liu Y, et al. Poly(norepinephrine)-coated FeOOH nanoparticles as carriers of artemisinin for cancer photothermal-chemical combination therapy. RSC Adv. 2019; https://doi.org/10.1039/c9ra01289c
6. Luo D, Carter KA, Miranda D, Lovell JF. Chemophototherapy: an emerging treatment option for solid tumors. Adv Sci. 2017; https://doi.org/10.1002/advs.201600106
7. Fessas P, Lee H, Ikemizu S, Janowitz T. A molecular and preclinical comparison of the PD-1 targeted T-cell checkpoint inhibitors nivolumab and pembrolizumab, Semin Oncol. 2017; https://doi.org/10.1053/j.seminoncol.2017.06.002
8. Akinleye A, Rasool Z. Immune checkpoint inhibitors of PD-L1 as cancer therapeutics, J Hematol Oncol. 2019; https://doi.org/10.1186/s13045-019-0779-5
9. Horita S, Nomura Y, Sato Y, Shimamura T, Iwata S, Nomura N. High-resolution crystal structure of the therapeutic antibody pembrolizumab bound to the human PD-1. Sci Rep. 2016; https://doi.org/ 10.1038/srep35297
10. Jiang Y, Chen M, Nie H, Yuan Y, PD-1 and PD-L1 in cancer immunotherapy: clinical implications and future considerations. Hum. Vaccines Immunother. 2019; https://doi.org/10.1080/21645515.2019.1571892
11. Chen W, Fu X, Zhu X, Liu Q. Protein recognition by polydopamine-based molecularly imprinted hollow spheres. Biosens Bioelectron. 2019; https://doi.org/10.1016/j.bios.2019.111492
12. Chaowana R, Bunkoed O. A nanocomposite probe of polydopamine/molecularly imprinted polymer/quantum dots for trace

sarafloxacin detection in chicken meat. Anal Bioanal Chem. 2019; https://doi.org/10.1007/s00216-019-01993-x

13. Wang X, Wang N , Yang Y , Wang X , Liang J , Tian X , Zhang H , Leng X . Polydopamine nanoparticles carrying tumor cell lysate as a potential vaccine for colorectal cancer immunotherapy. Biomater Sci. 2019; https://doi.org/10.1039/c9bm00010k
14. Amaro-Gahete J, Benítez A, Otero R, Esquivel D, Jiménez-Sanchidrián C, Morales J, Caballero Á, Romero-Salguero FJ. A Comparative Study of Particle Size Distribution of Graphene Nanosheets Synthesized by an Ultrasound-Assisted Method Nanomaterials 2019; https://doi.org/10.3390/nano9020152

CHAPTER 5

Catecholamines – based bioanalytical tests on microplates

Microplates, also known as microwell plates, are one of the most widespread and straightforward tools employed in the biomedical field, as well as conceived and designed by G. Takatsy in 1950 (Hungary) as an 8 x 12 matrix of wells (96 total wells) [1]. These types of platforms are extensively used since the 1970s for immunological testing assays (such as ELISA) along with a rapidly growing, in recent years, for various biological measurements, thanks also to the optimization of the automation technology. Moreover, they are largely employed in clinical and analytical workflows to streamline and miniaturize bioassays eventually *a priori* optimized and tested with benchtop instrumentation. In our case, the strategy to move from benchtop optical spectroscopic platforms towards their miniaturization, to accomplish *in-situ* measurements, is a valid and ambitious goal to pursue (as described in Chapter 3).

This strategy allows reducing the costs of the overall analysis as fewer reagents are required due to the lower well volume (micro-scale well features). Moreover, microplates allow high-throughput screening of multiple samples, simultaneously. This type of substrate is generally very useful to develop the most disparate assays (liquid or solid-phase assays) limited only by the research imagination. In this context, colorimetric assays (colorimetry) have a prominent role in the bioanalytical field research for detecting the presence of various analytes. These assays involved responses that cause naked-eye visible and measurable color changes (intensity of electromagnetic radiation in the visible region of the spectrum) due to enzymatic, chemical, or plasmon-mediated chemical reactions between spotted reagents and/or biological or mimetics receptors, analytes or chemicals, previously deposited onto the microplate.

Motivated by the need for decentralized, simple, and low-cost platforms, some research studies described in this PhD dissertation were dedicated to addressing clinical problems that need diagnostic tests to guarantee quick decision-making. The selection of a microplate, in terms of well shape and polymeric composition, follows the choice of assay technology. In all experiments, we have employed microplates constituted by common untreated polystyrene (PS), an unsaturated hydrocarbon-based polymer partially positive and negatively charged due to the presence of aromatic substituents, which is capable of sticking to proteins. Moreover, the microplates selected own flat-bottom wells that are well-suited for bottom-reading applications, as our absorbance microplate reader [1].

In detail, two original colorimetric bioassays, which do not involve enzymatic labels, were designed for detecting different analytes, by evaluating for all the analytical figures of merit. Moreover, the tests developed are joined by the role of the catecholamine DA (see chapter 2). The strategies designed were also validated with commercial kits or the related reference methods, when available, to highlight the positive and promising features of these simple colorimetric microplate-based assays in order to expand their practical use.

References

1. Auld DS, Coassin PA, Coussens NP, Hensley P *et al*. Microplate selection and recommended practices in high-throughput screening and quantitative biology. 2020; In: Markossian S, Grossman A, Brimacombe K, et al., editors. Assay Guidance Manual. Bethesda (MD): Eli Lilly & Company and the National Center for Advancing Translational Sciences; 2004-.

The two case studies investigated were outlined below:

• A model screening tool was developed to detect hypochlorous acid, produced by myeloperoxidase during inflammation, which is characteristic of several neurodegenerative disorders. Physiologically, chlorinated byproducts of dopamine (dopamine-quinones) were generated in neurons and were observed in brains affected by Parkinson's disease.

• A PDA-based method for the quantification of human serum albumin (HSA), a "*biochemical doorbell"* of kidney damage, directly from urine samples.

5.1 Preliminary screening tool for hypochlorous acid of neuronal oxidative stress

Based on the following study:

P. Palladino, **F. Torrini**, S. Scarano, M. Minunni. Colorimetric analysis of the early oxidation of dopamine by hypochlorous acid as preliminary screening tool for chemical determinants of neuronal oxidative stress, Journal of Pharmaceutical and Biomedical Analysis 179 (2020) 113016.

5.1.1 Aim and objectives of the study

The hypochlorous acid produced by the innate immune system during inflammation characteristic of several neurodegenerative disorders is responsible for the generation of chlorinated byproducts of dopamine in neurons where this neurotransmitter reaches the highest concentration. Therefore, this physiological acid could play a key role in neuronal oxidative stress associated to aberrant dopamine-quinones (DQ) production. Here we report a model study simulating simplified conditions of HOCl reaction with dopamine (DA) in neurons, showing for the first time that DA is immediately converted by HOCl to the yellow colored DQ molecule. The DQ originated from dopamine oxidation results directly proportional to the total amount of the oxidant with excellent reproducibility. Furthermore, following the several evidences of the interplay between cytosolic dopamine and calcium in neurodegenerative disorders, we have verified that the presence of calcium cation influences the dopamine oxidation pathway likely due to the metal chelation by semiquinone formed in the early stage of dopamine oxidation. This experimental approach, based on the isolation of the highly reactive DQ molecule, could be useful for prelaminar investigation of the (putative) determinants of dopamine-poisoning derivatives formation.

Graphical abstract

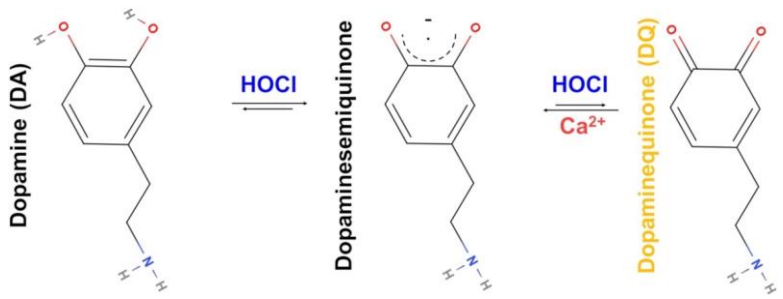

5.1.2 Introduction

The history of dopamine (DA) investigation starts at the beginning of the 20th century with the chemical synthesis [1]. Later on, DA was identified in human body, together with the description of the DA metabolism in the brain and peripheral areas that allowed the explanation of age-related synthetic decline, the recognition of pathologies associated with concentration anomalies of DA and subsequent associated-drugs application in several medical conditions [2,3]. Finally, there was the reawakening of synthetic dopamine at the beginning of the 21st century [4–6], when the non-enzymatic oxidation to *ortho*-quinone and the subsequent self-polymerization has generated several applications in medicine, (bio)analytical chemistry, and materials science [7–11]. However, the largest body of research is still focusing on the neuronal oxidative reactions of dopamine that have been postulated to be involved in Parkinson's disease (PD), according to the theory of the conversion of neurotransmitters into cytotoxic molecules during cerebral inflammation. In detail, DA is synthesized in the cytoplasm of dopaminergic neurons, where it is transported into synaptic vesicles and released by exocytosis; alternatively, DA serves as a precursor for the synthesis of other catecholamine neurotransmitters. The excess of cytosolic DA is catabolized by monoamine oxidase or sequestered into the lysosomes forming neuromelanin starting from the oxidation of DA to dopamine- ortho-quinone (DQ) (see Fig. 5.1) [4,12–14].The redistribution of DA from the

synaptic vesicles, where it is maintained in a reduced state by the low pH, to the cytosol can lead to cellular damage, for example inducing α-synuclein misfolding and aggregation [15], with a mechanism common to other proteins associated to neurodegenerative disorders [16,17], that could lead to an unrestrained DA cytosolic accumulation and further oxidative stress [14,18–20]. Particularly interesting appears the role of hypochlorous acid (HOCl), which is produced by the myeloperoxidase (MPO) during inflammation and generates the chlorinated byproducts of dopamine observed in brains affected by PD [21]. Although MPO is also able to directly oxidize dopamine without producing HOCl, the latter could play a main role in neuronal oxidative stress associated to aberrant DQ production. Accordingly, here we propose a fundamental study on the early oxidation of dopamine by means of visible spectroscopy, showing for the first time that DA is immediately converted by HOCl to the yellow colored DQ molecule. Furthermore, we have verified that the presence of calcium cation, involved in α-synuclein stability and PD insurgence [22–24], effectively affects the DQ formation likely due to its chelation by dopamine semiquinone formed in the early stage of DA oxidation to DQ [4,12–14], whereas the time evolution of the DQ interconversion to aminochrome (AC) indicates that the presence of Ca^{2+} does not influence the kinetics of this transformation. More in general, this colorimetric assay could be useful for preliminary analytical screening of putative chemical determinants of dopamine-poisoning derivatives formation in presence of oxidative stress before any study in much more complex biological models of neuronal environment [12,14,18,19,21,25].

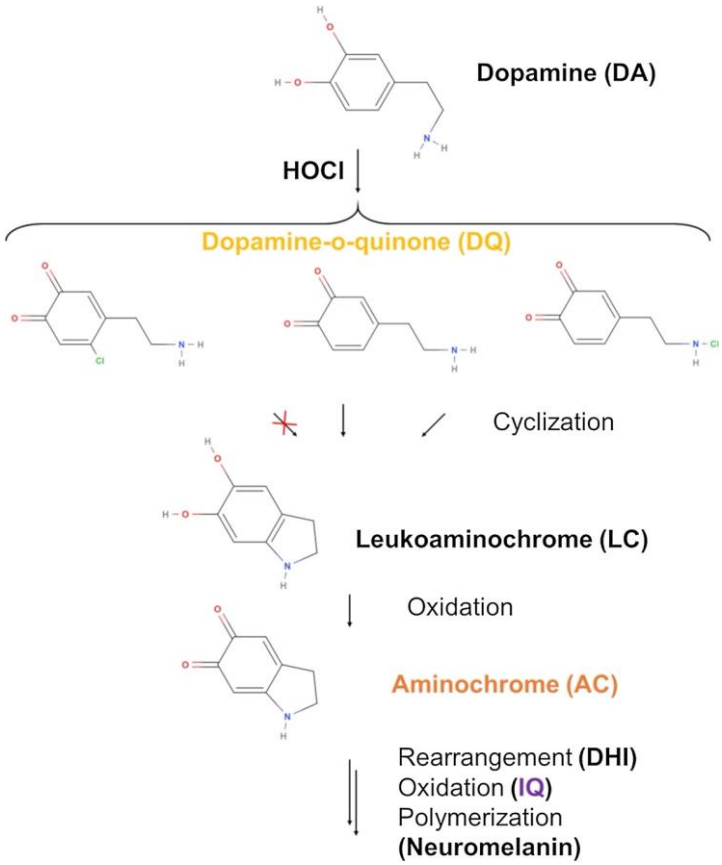

Fig. 5.1 Schematic representation of dopamine oxidation, and hypothetical chlorination, by HOCl according to literature [4,12–14]. The initial oxidation of dopamine (DA) produces the corresponding dopamine-ortho-quinone (DQ). The following DQ cyclization step gives leukoaminochrome (LC) that is subsequently oxidized to aminochrome (AC). Then, AC rearranges to 5,6-dihydroxyindole (DHI), which can be oxidized to indole-5,6-quinone (IQ) and polymerize to form neuromelanin

5.1.3 Materials and methods

5.1.3.1 Chemicals and reagents

Salts, dopamine hydrochloride, ethylenediaminetetraacetic acid disodium salt dihydrate (EDTA), and spectrophotometer cuvettes disposable polystyrene (PS) were purchased from Sigma Aldrich (Milan, Italy). Sodium hypochlorite solution was purchased from Merck KGaA (Germany) (Lot number: K50436114, containing 120 g L^{-1} of active chlorine as calculated from

iodometric titration). All reagents were used without further purification. Water used for all preparations was obtained from a Milli-Q system (Millipore Corporation, MA, USA) to avoid metal-induced oxidative processes on DA.

5.1.3.2 UV–Vis spectroscopy

Absorbance spectra were recorded on a Thermo Scientific Evolution 220 UV–vis spectrophotometer. Optical measurements were performed at 20 ˚C using quartz cells for kinetics for the wave- length range of 190÷680 nm with optical path length of 1.0 cm and PS cuvettes with optical path length of 1.0 cm for titration in visible region only. All the experiments were recorded with a 30-s delay. Titration experiments were performed adding freshly prepared oxidant solution of NaClO or $Ca(ClO)_2$ in H_2O to several dopamine-containing PS-cuvettes with a final concentration of DA 1.2 mM in KH_2PO_4 0.5 M pH 3.8, with three replicas for each oxidant concentration. Kinetics experiments were performed keeping constant both concentrations of dopamine and oxidant. Data were analyzed with Origin® software.

5.1.4 Results and discussion

5.1.4.1 The relevance of acidic pH in dopamine oxidation

Catecholaminergic neurons synthetize dopamine in the cytosol, where the pH is neutral; then it is readily transported into the synaptic vesicles and stored in an acidic environment where it is stable towards oxidation unless in presence of high temperature and pressure, UV irradiation, transitions metals, or other strong oxidants [26]. The latter two are the most physiologically relevant enzyme-free conditions for aberrant quinones production in the cell. In particular, the stability of dopamine at acidic pH could be undermined in presence of HOCl generated by the innate immune system during the inflammation process that is characteristic of several neurodegenerative disorders [21]. Accordingly, to simulate the synaptic environment and relevant reactions, we decided to study the first stage of dopamine oxidation at acidic pH by HOCl to attempt for the first time the

isolation, in ideal conditions, of the DQ monomeric species. Otherwise, the auto-oxidation at neutral/basic pH would skip the DQ formation stage in favor of AC and subsequent oxidations steps up to polydopamine (PDA) formation. Considering that the relative concentrations of HOCl and its conjugate base (OCl^-) are strongly dependent on pH (pKa 7.5 at 25°C), herein several salts have been tested to keep the pH of sample solutions around 4 where HOCl virtually represents the total chlorine present in solution [27], therefore excluding the contribution of OCl^- that is about equimolar to HOCl at the neutral pH of cytosol, whereas should be a negligible component in the acidic medium of synaptic vesicles here simulated for the screening of hypothetical chemical determinants of dopamine oxidation. Among acetic acid/sodium acetate, citric acid/sodium citrate (data not shown), and KH_2PO_4 (final concentration 0.5 M, pH 3.8) the latter resulted the best in terms of UV–vis data repeatability, somehow reinforcing the previously reported evidence that phosphate salts do not alter the rate of dopamine oxidation in water, whereas other buffers resulted unsuitable because inhibiting or accelerating the dopamine oxidation [13].

5.1.4.2 Dopamine titration with HOCl at acidic pH

Dopamine-*ortho*-quinone has been previously observed by oxidation of DA by using $NaIO_4$ in water or MnO_2 in aqueous acidic solution (HCl 30 %) [14,28]. Early analysis of dopamine reaction with hypochlorous acid were performed at neutral or basic pH, where large amount of chlorine is present as ClO^- [27], without characterization of DQ intermediate [21]. Therefore, this is the first report showing that DA is immediately converted by real HOCl to the yellow colored DQ (λ_{max} 395 nm). The titrations of dopamine solution with HOCl are reported in Fig. 5.2. The color intensity of DQ solutions is directly proportional to HOCl concentration (R^2 = 0.996, see Table 5.1) up to a maximum corresponding to two equivalents of oxidant (Fig. 5.3) with very good repeatability ($CV\%_{mean}$=2.97 between 31.2 µM and 5.00 mM), virtually covering the amount of HOCl estimated in diseased brains (20 ÷ 400 µM) [29], which could correspond to both the complete two-electrons conversion

of catecholamine to ortho-quinone, and DA chlorination. Additional oxidant leads to color lost in proportion to the new amount of active chlorine added in solution, likely due to further oxidation of DA to not-visible end products, e.g., leukochrome (λ_{max} 296 nm) and 5,6-dihydroxyindole (λ_{max} 320 nm), which are part of the electro- chemical and chemical reaction pathway of PDA formation (Fig. 5.1). Furthermore, the observation of the same cuvettes after 60min shows the appearance of AC peak (λ_{max} 480 nm) together with a decreased intensity of DQ peak, plus broad absorbance at high wavelengths indicative of dopamine polymerization. Notably, at higher concentrations of HOCl (Fig. 5.2, right panels) AC formation is slightly visible, and, more interestingly, the decreased intensity of DQ peak seems not accompanied by dopamine polymerization. Accordingly, we infer that high HOCl concentration could lead to dopamine ring chlorination, likely in position 5, that impairs the DQ cyclization (Fig. 5.1) [21]. Thus, the relative concentration of HOCl and dopamine could be determinant in the oxidation pathway.

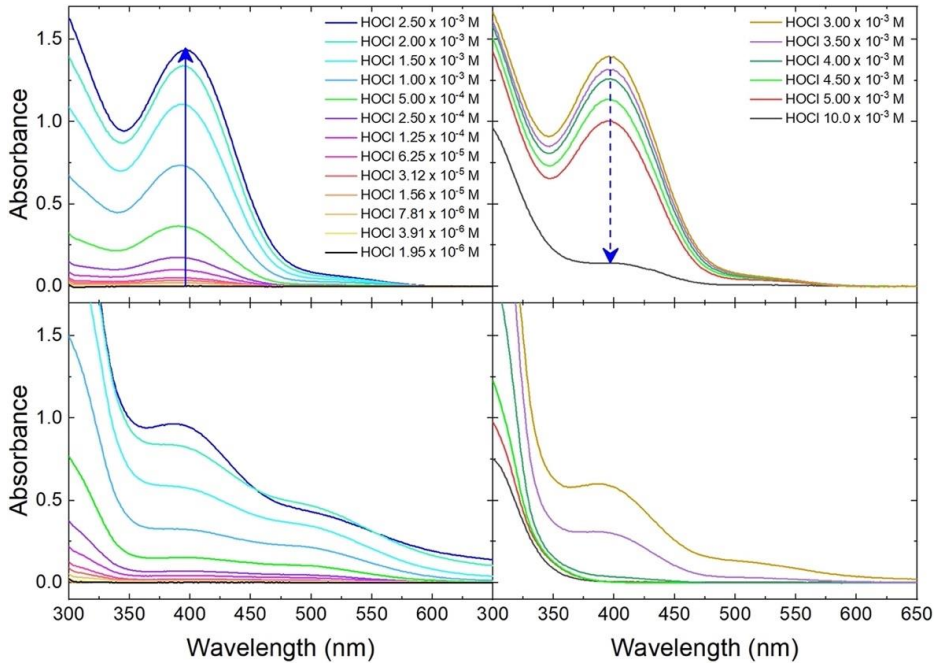

Fig. 5.2 Dopamine oxidation by HOCl at pH 3.8 analyzed by optical spectroscopy. UV-vis spectra solutions containing a fixed concentration of DA (1.2 mM) with increasing concentrations of HOCl from NaClO (1.95 µM to 2.5 mM on the left, and 3.0–10.0 mM on the right) recorded with a delay of 0.5 min (upper panels) and after 60 min (lower panels)

Table 5.1 DQ formation in dependence of oxidant concentration at 0.5 min and 60 min

Oxidant	time (min)	Range (10^{-3} M)	Intercept ± SD	Slope ± SD	R^2
NaClO	**0.5**	0–1.5	0.003 ± 0.001	0.753 ± 0.015	0.996
		3.0–10	2.011 ± 0.014	−0.190 ± 0.002	0.999
	60	**0–2.5**	−0.005 ± 0.009	0.389 ± 0.009	0.993
		2.5–4.0	2.451 ± 0.106	−0.609 ± 0.032	0.994
$Ca(ClO)_2$	**0.5**	0–1.5	0.003 ± 0.003	0.261 ± 0.005	0.996
		3.0–10	0.545 ± 0.068	0.023 ± 0.013	0.436
	60	**0–5.0**	0.011 ± 0.006	0.158 ± 0.003	0.996
		5.0–10	N.A.	N.A.	N.A.

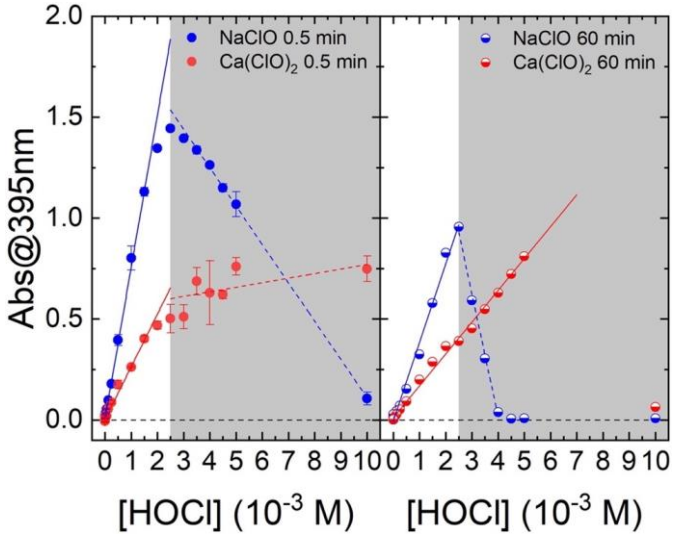

Fig. 5.3 Dopamine oxidation by HOCl at pH 3.8. The absorbance at 395 nm corresponds to DQ formed by DA oxidation (1.2 mM) in presence of HOCl from NaClO (blue lines and circles) or $Ca(ClO)_2$ (red lines and circles) in cuvettes after 0.5 min (left panel) and 60 min (right panel) (For interpretation of the references to colour in this figure legend, the reader is referred to the web version of this article).

5.1.4.3 Calcium effect on dopamine titration with HOCl at acidic pH

There are several evidence of the interplay between cytosolic dopamine and calcium in neurodegenerative disorders [22–25].

Accordingly, we have verified the direct influence of this cation in dopamine oxidation too in a model system. The titration reported in Fig. 5.2 has been repeated in presence of Ca^{2+} introduced by using $Ca(ClO)_2$ instead of NaClO to be quantitatively converted in HOCl at pH 3.8. Fig. 5.4 clearly shows the reduced amount of DQ formed in presence of Ca^{2+} in comparison with above reported experiments. Moreover, additional important aspects appear from data analysis in Fig. 5.3 and Table 5.1. Although reduced in presence of calcium, the amount of DQ produced recalls a saturation curve, without any decrease during all the HOCl titration. Furthermore, the same solutions observed after 60 min show an increase of DQ intensity in presence of Ca^{2+} up to 5 mM of HOCl, which is the opposite behavior observed without Ca^{2+}. We try to rationalize these results considering the chelating effect of the

semiquinone formed in the early stage of dopamine oxidation to DQ [28]. This anion would act as calcium sequestrant resulting stabilized and thus slowing down the rate of DQ synthesis and subsequent reactions reported in Fig. 5.1. At the same time, this kinetic trap would represent a reservoir that generates larger amount of the DQ observed after 60 min.

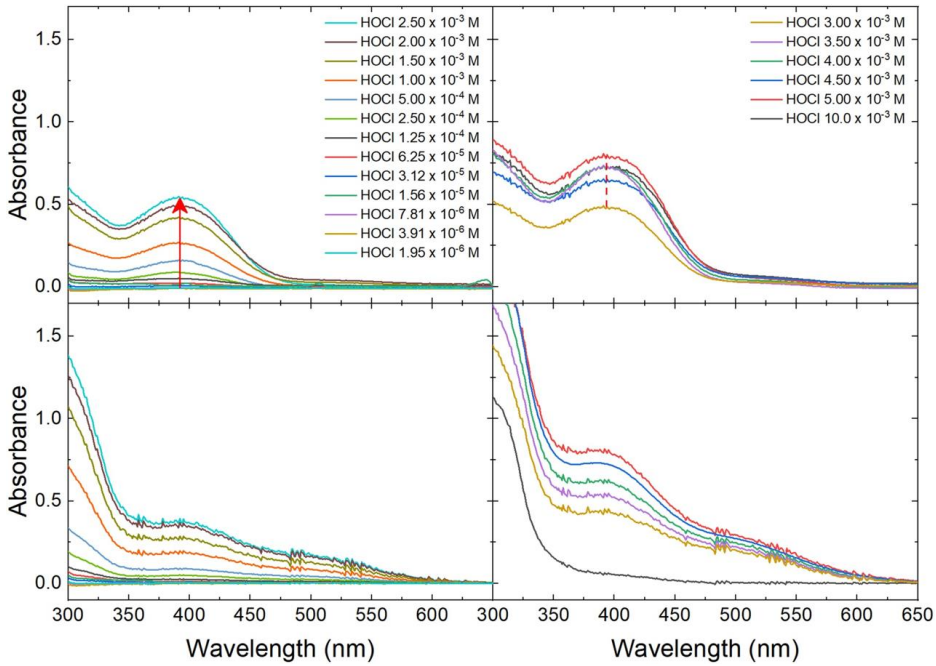

Fig. 5.4 Dopamine oxidation by HOCl at pH 3.8 in presence of Ca^{2+}. UV-vis spectra solutions containing a fixed concentration of DA (1.2 mM) with increasing concentrations of HOCl from $Ca(ClO)_2$ (from 1.95 μM to 2.5 mM on the left, and 3.0–10.0 mM on the right) recorded with a delay of 0.5 min (upper panels) and after 60 min (lower panels).

5.1.4.4 Kinetics of dopamine oxidation by HOCl

Upon HOCl addition at DA acid solution, the catecholamine is visibly converted in yellow DQ within few seconds, whereas the acidic pH delays the AC formation. This simplified system allows to observe the time evolution of the DQ interconversion to AC by means of UV–vis spectroscopy without isolation steps. Fig. 5.5 shows equimolar amount of DA and HOCl (1.2 mM)

at pH 3.8. The initial DQ absorption at 395 nm decreases and results progressively replaced by AC with a maximum absorbance at 480 nm and a shoulder around 307 nm. The isosbestic points clearly visible in Fig. 5.5 ensure the presence of only two molecular species during the experiments here described. Such behavior is qualitatively preserved in presence of calcium ions derived from $Ca(ClO)_2$. However, the intensity of each characteristic peak is much lower, confirming the observation from dopamine titration experiments (see above). Notably, the presence of EDTA, used as calcium chelator, increases the absorbances, almost restoring the spectra obtained in absence of Ca^{2+}. Moreover, the kinetic analysis of DQ rearrangement has been reported in Fig. 5.6 considering a first-order reaction according to Eq. (1):

$$\boldsymbol{Abs^{t}_{395nm} = A + (B - A) \times e^{-k \times t}} \qquad (1)$$

where B is the absorbance of DQ at 395 nm and t^0, i.e., prior of any molecular rearrangement ($B = \varepsilon^{DQ}_{395nm} \times [DQ]_0$), whereas A is the absorbance at the same wavelength after fully conversion to AC ($A = \varepsilon^{AC}_{395nm} \times [DQ]_0$). Data fitting resulted very good, and the associated parameters are reported in Table 5.2. The first-order rate constants appear identical within the error, clearly indicating that the presence of Ca^{2+} does not influence the kinetics of DQ-to-AC transformation but only the DA oxidation to DQ.

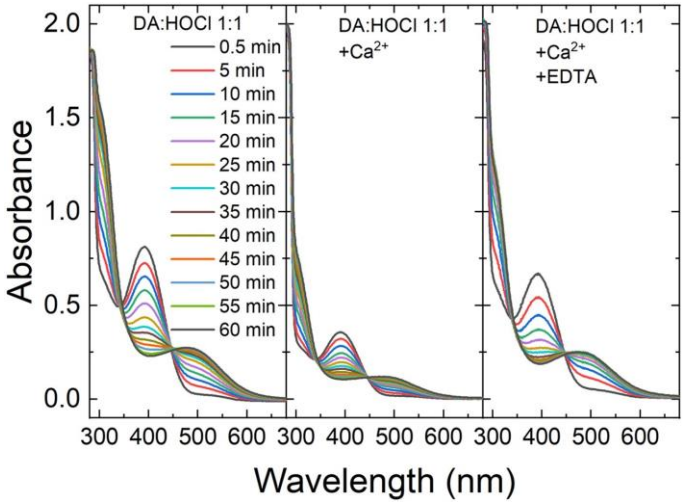

Fig. 5.5 DQ interconversion to AC inpresence of Na^+, Ca^{2+}, and EDTA. UV–vis spectra of DA (1.2 mM) in presence of equimolar HOCl at pH 3.8 from 0.5– 60 min (left panel). The same experiment is reported in presence of calcium ions derived from $Ca(ClO)_2$ (middle panel), or in the presence of both calcium ions derived from $Ca(ClO)_2$ and EDTA (right panel).

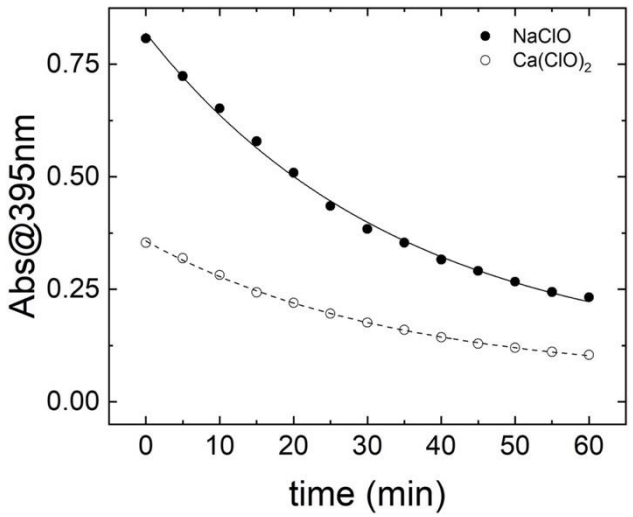

Fig. 5.6 Data analysis of DQ interconversion to AC. Absorbance values at 395 nm for DA solution (1.2 mM) in presence of equimolar hypochlorite from NaClO (solid line and black circles) or $Ca(ClO)_2$ (dashed line and white circles). Data have been fitted considering a first-order reaction (Eq. (1)). Results of data fitting are reported in Table 5.2.

Table 5.2 First-order kinetics of DQ interconversion to AC in presence of Na^+ or Ca^{2+}

Oxidant	A ± SD	B ± SD	k ± SD (min^{-1})	R^2
NaClO	0.095 ± 0.025	0.820 ± 0.009	0.029 ± 0.002	0.997
$Ca(ClO)_2$	0.052 ± 0.006	0.357 ± 0.002	0.030 ± 0.001	0.999

5.1.4 Conclusions

To the best of our knowledge, this study represents the first report on the ability of HOCl, a naturally occurring oxidant in neurons, in forming dopamine-*ortho*-quinone (DQ) from dopamine. The impact of this pathway is clinically relevant since aberrant DQ levels are connected to neurodegenerative disorders. As a model system, to study the first stage of dopamine oxidation isolating the DQ molecule, the experiments have been performed in presence of HOCl at acidic pH to avoid the DA autooxidation. The oxidation reaction was carried out at pH = 3.8 that is lower than the pH expected for the neuronal cytosol but guarantees that the chlorine in solution is quantitatively converted to HOCl [27]. DQ has been kinetically isolated, and quantitatively determined as a linearly correlated product of HOCl concentration (R^2 = 0.996), with excellent averaged repeatability ($CV\%_{mean}$ = 2.97). Moreover, following the several evidences of the interplay between cytosolic dopamine and calcium in neurodegenerative disorders, the influence of calcium cation in dopamine oxidation has been investigated. A reduced amount of DQ formed in presence of Ca^{2+} after few seconds together with an increase of DQ intensity after 60 min has been evidenced. This is likely due to the chelating effect of semiquinone formed in the early stage of dopamine oxidation that could decrease the rate of DQ synthesis. Finally, we have observed the time evolution of the DQ interconversion to AC, confirming the intensity decrease in presence of calcium ions that is restored in presence of EDTA. Remarkably, the first-order rate constants with and without calcium ions (R^2 = 0.999 and 0.997, respectively) appear identical, indicating that this cation does not influence the kinetics of DQ-to-AC transformation but

only the DA oxidation to DQ. Our experimental conditions do not pretend to represent the molecular complexity and heterogenicity of dopaminergic neuron content even for health individuals [30], where, for example, the local DA concentration ranges from 10^{-1} M in vesicles to 10^{-6} M in cytosol [31,32], whereas it is about 10^{-9} M in extracellular fluid in brain [33]. However, our experimental approach, based on the isolation of the highly reactive DQ molecule, could be useful as a preliminary screening tool to study the influence of other aberrant chemical determinants of oxidative stress on dopamine-poisoning derivatives formation (e.g., redox active metal cations, thiols, and other organic reducing agents) before to deal with much more complex biological models of neuronal environment.

References

1 G. Barger, H.H. Dale, Chemical Structure and sympathomimetic action of amines, J. Physiol. (Paris) 41 (1910) 19–59, http://dx.doi.org/10.1113/jphysiol.1910.sp001392

2 C. Sarkar, B. Basu, D. Chakroborty, P.S. Dasgupta, S. Basu, The immunoregulatory role of dopamine: an update, Brain Behav. Immun. 24 (2010) 525–528, http://dx.doi.org/10.1016/j.bbi.2009.10.015

3 S. Fahn, The history of dopamine and levodopa in the treatment of Parkinson's disease, Mov. Disord. 23 (2008) S497–S508, http://dx.doi.org/10.1002/mds.22028

4 Y. Li, M. Liu, C. Xiang, Q. Xie, S. Yao, Electrochemical quartz crystal microbalance study on growth and property of the polymer deposit at gold electrodes during oxidation of dopamine in aqueous solutions, Thin Solid Films 497 (2006) 270–278, http://dx.doi.org/10.1016/j.tsf.2005.10.048

5 K. Liu, W.-Z. Wei, J.-X. Zeng, X.-Y. Liu, Y.-P. Gao, Application of a novel electrosynthesized polydopamine-imprinted film to the capacitive sensing of nicotine, Anal. Bioanal. Chem. 385 (2006) 724–729, http://dx.doi.org/10.1007/s00216-006-0489-z

6 H. Lee, S.M. Dellatore, W.M. Miller, P.B. Messersmith, Mussel-inspired surface chemistry for multifunctional coatings, Science 318 (2007) 426–430, http://dx.doi.org/10.1126/science.1147241

7 S. Scarano, E. Pascale, P. Palladino, E. Fratini, M. Minunni, Determination of fermentable sugars in beer wort by gold nanoparticles@polydopamine: a layer-by-layer approach for Localized Surface Plasmon Resonance measurements at fixed wavelength, Talanta 183 (2018) 24–32, http://dx.doi.org/10.1016/j.talanta.2018.02.044

8 P. Palladino, M. Minunni, S. Scarano, Cardiac Troponin T capture and detection in real-time via epitope-imprinted polymer and optical biosensing, Biosens. Bioelectron. 106 (2018) 93–98, http://dx.doi.org/10.1016/j.bios.2018.01.068

9 S. Scarano, P. Palladino, E. Pascale, A. Brittoli, M. Minunni, Colorimetric determination of p-nitrophenol by using ELISA microwells modified with an adhesive polydopamine nanofilm containing catalytically active gold nanoparticles, Microchim. Acta 186 (2019) 146, http://dx.doi.org/10.1007/s00604-019-3259-2

10 P. Palladino, A. Brittoli, E. Pascale, M. Minunni, S. Scarano, Colorimetric determination of total protein content in serum based on the polydopamine/protein adsorption competition on microplates, Talanta 198 (2019) 15–22, http://dx.doi.org/10.1016/j.talanta.2019.01.095

11 P. Palladino, F. Bettazzi, S. Scarano, Polydopamine: surface coating, molecular imprinting, and electrochemistry-successful applications and future perspectives in (bio)analysis, Anal. Bioanal. Chem. 411 (2019) 4327–4338, http://dx.doi.org/10.1007/s00216-019-01665-w

12 W. Linert, E. Herlinger, R.F. Jameson, E. Kienzl, K. Jellinger, M.B. Youdim, Dopamine, 6-hydroxydopamine, iron, and dioxygen-their mutual interactions and possible implication in the development of Parkinson's disease, Biochim. Biophys. Acta 1316 (1996) 160–168, http://dx.doi.org/10.1016/0925- 4439(96)00020-8

13 E. Herlinger, R.F. Jameson, W. Linert, Spontaneous autoxidation of dopamine, J. Chem. Soc. Perkin Trans. I 2 (1995) 259–263, http://dx.doi.org/10.1039/p29950000259

14 M. Bisaglia, S. Mammi, L. Bubacco, Kinetic and structural analysis of the early oxidation products of dopamine analysis of the interactions with □-synuclein, J. Biol. Chem. 282 (2007) 15597–15605, http://dx.doi.org/10.1074/jbc.M610893200

15 M. Bisaglia, R. Filograna, M. Beltramini, L. Bubacco, Are dopamine derivatives implicated in the pathogenesis of Parkinson's disease? Ageing Res. Rev. 13 (2014) 107–114, http://dx.doi.org/10.1016/j.arr.2013.12.009

16 P. Palladino, G.L. Scaglione, A. Arcovito, R.M. Vitale, P. Amodeo, B. Vallone, M. Brunori, E. Benedetti, F. Rossi, Neuroglobin–prion protein interaction: what's the function? J. Pept. Sci. 17 (2011) 387–391, http://dx.doi.org/10.1002/psc. 1333

17 P. Palladino, A.M. Aura, G. Spoto, Surface plasmon resonance for the label-free detection of Alzheimer's β-amyloid peptide aggregation, Anal. Bioanal. Chem. 408 (2016) 849–854, http://dx.doi.org/10.1007/s00216-015-9172-6

18 J.E. Galvin, Interaction of alpha-synuclein and dopamine metabolites in the pathogenesis of Parkinson's disease: a case for the selective vulnerability of the substantia nigra, Acta Neuropathol. (Berl.) 112 (2006) 115–126, http://dx. doi.org/10.1007/s00401-006-0096-2

19 S.L. Leong, R. Cappai, K.J. Barnham, C.L. Pham, Modulation of alpha-synuclein aggregation by dopamine: a review, Neurochem. Res. 34 (2009) 1838–1846, http://dx.doi.org/10.1007/s11064-009-9986-8

20 J. Lotharius, P. Brundin, Pathogenesis of Parkinson's disease: dopamine, vesicles and α-synuclein, Nat. Rev. Neurosci. 3 (2002) 932–942, http://dx.doi. org/10.1038/nrn983

21 T.M. Jeitner, M. Kalogiannis, B.F. Krasnikov, I. Gomlin, M.R. Peltier, G.R. Moran, Linking inflammation and Parkinson disease: hypochlorous acid generates parkinsonian poisons, Toxicol. Sci. 151 (2016) 388–402, http://dx.doi.org/10. 1093/toxsci/kfw052

22 S. Nath, J. Goodwin, Y. Engelborghs, D.L. Pountney, Raised calcium promotes α - synuclein aggregate formation, Mol. Cell. Neurosci. 46 (2011) 516–526, http://dx.doi.org/10.1016/j.mcn.2010.12.004

23 A. Rcom-H'cheo-Gauthier, J. Goodwin, D. Pountney, Interactions between calcium and alpha-synuclein in neurodegeneration, Biomolecules 4 (2014) 795–811, http://dx.doi.org/10.3390/biom4030795

24 J. Lautenschlager, A.D. Stephens, G. Fusco, et al., C-terminal calcium binding of alpha-synuclein modulates synaptic vesicle interaction, Nat. Commun. 9 (2018) 712, http://dx.doi.org/10.1038/s41467-018-03111-4

25 B. Liss, J. Striessnig, The potential of L-type calcium channels as a drug target for neuroprotective therapy in Parkinson's disease, Annu. Rev. Pharmacol. Toxicol. 59 (2019) 263–289, http://dx.doi.org/10.1146/annurev-pharmtox- 010818-021214

26 M.O. Salomäki, T. Ouvinen, L. Marttila, H. Kivelä, J. Leiro, E. Mäkilä, J.O. Lukkari, Polydopamine nanoparticles prepared using redox active transition metals, J. Phys. Chem. B 123 (2019) 2513–2524, http://dx.doi.org/10.1021/acs.jpcb.8b11994

27 Y. Feng, D.W. Smith, J.R. Bolton, Photolysis of aqueous free chlorine species (HOCl and OCl) with 254 nm ultraviolet light, J. Environ. Eng. Sci. 6 (2007) 277–284, http://dx.doi.org/10.1139/s06-052

28 W.J. Barreto, S. Ponzoni, P. Sassi, A Raman and UV-Vis study of catecholamines oxidized with Mn (III), Spectrochim. Acta A. 55 (1998) 65–72, http://dx.doi.org/10.1016/S1386-1425(98)00164-4

29 Y.W. Yap, M. Whiteman, B.H. Bay, Y. Li, F.S. Sheu, R.Z. Qi, C.H. Tan, N.S. Cheung, Hypochlorous acid induces apoptosis of cultured cortical neurons through activation of calpains and rupture of lysosomes, J. Neurochem. 98 (2006) 1597–1609, http://dx.doi.org/10.1111/j.1471-4159.2006.03996.x

30 J.F. Poulin, J. Zou, J. Drouin-Ouellet, K.Y.A. Kim, F. Cicchetti, R.B. Awatramani, Defining midbrain dopaminergic neuron diversity by single-cell gene expression profiling, Cell Rep. 9 (2014) 930–943, http://dx.doi.org/10.1016/j.celrep.2014.10.008

31 D.M. Omiatek, A.J. Bressler, A.-S. Cans, A.M. Andrews, M.L. Heien, A.G. Ewing, The real catecholamine content of secretory vesicles in the CNS revealed by electrochemical cytometry, Sci. Rep. 3 (2013) 1447, http://dx.doi.org/10.1038/srep01447

32 T.M. Olefirowicz, A.G. Ewing, Dopamine concentration in the cytoplasmic compartment of single neurons determined by capillary electrophoresis, J. Neurosci. Meth. 34 (1990) 11–15, http://dx.doi.org/10.1016/0165-0270(90)90036-F

33 M.-Y. Zhang, C.E. Beyer, Measurement of neurotransmitters from extracellular fluid in brain by in vivo microdialysis and chromatography–mass spectrometry, J. Pharmaceut. Biomed. Anal. 40 (2006) 492–499, http://dx.doi.org/10.1016/j.jpba.2005.07.025.

5.2 Quantification of human serum albumin (HSA) in urine samples with a polydopamine (PDA)-based method

Based on the following study:

F. Torrini, S. Scarano, P. Palladino, M. Minunni. Polydopamine-based quantitation of albuminuria for the assessment of kidney damage, Analytical and Bioanalytical Chemistry (2021) 2217-24. 413

5.2.1 Aim and objectives of the study

Proteinuria is considered indicative of kidney damage that can be related to various adverse outcomes. Nowadays, there is a huge demand for routine urine screening methods to assess health risks in clinical setting without expensive procedures and long pretreatment of the sample. To address this issue, a polydopamine-based colorimetric assay to determine urinary albumin concentration in real samples is proposed here. The core of this approach relies on the established competitive adsorption of polydopamine film and human serum albumin onto the polystyrene surface of ELISA plates. Herein, we investigated the influence of temperature and the Tris-HCl buffer concentration on the polydopamine film growth. The absorbance of polydopamine film, after 24 h at 25 °C, decreases with the increase of HSA concentration, allowing the selective detection of HSA down to 0.036 ± 0.001 g L^{-1} in untreated urine. This simple and low-cost bioanalytical assay exhibited very good repeatability, $\%CV_{mean}$ = 2 in human urine, and was superior in terms of analytical performances to some standard methods available on the market, especially in comparison to the Bradford assay, for early screening and assessment of kidney damage.

Graphical abstract

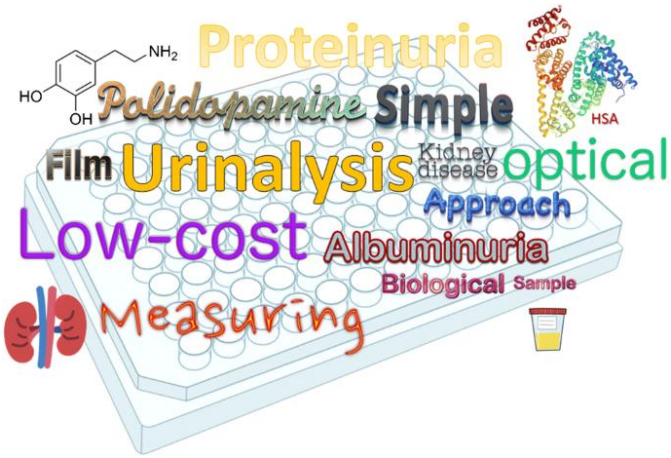

5.2.2 Introduction

Urinalysis plays a pivotal role in routine clinical practice, along with other exams, to detect the level of biomarkers used for disease diagnosis and monitoring, including infections, diabetes, liver, and kidney disorders [1]. Timely and accurate assessment of kidney disease, a harmful and outspread pathology, is extremely important for a prompt diagnosis and management of the health risks [2]. In particular, the chronic kidney disease affects almost 10% of the population, which makes it the ninth leading cause of death in the world, largely linked to elevated albumin in urine [3, 4]. Such proteinuria may originate primarily from kidney damage and can be transient or persistent [5–8]. A transient increase of proteins in urine may be correlated to non-renal pathology, like intensive physical exercise, fever or sepsis, anemia, and urinary tract infection. Conversely, a persistently high level of protein excretion has a relevant impact on the clinical outcome, like cardiovascular diseases, infections, metabolic and endocrine disorders, frailty, and cognitive impairment. Among the possible causes of this condition may be encountered glomerulonephritis, polycystic kidney disease, diabetes, obesity, or ischemia. Furthermore, nowadays, clinical trials are focused on a possible association between proteinuria and cancer incidence [4, 9, 10]. In

clinical setting, proteinuria is classified as "selective" when albumin, the most abundant protein of the human blood plasma, constitutes a substantial majority of the urinary protein [5]. In this study, we considered the aforementioned condition. Currently, albuminuria is mainly assessed by using a semi-quantitative dipstick, alternatively by electrophoresis, colorimetric, or turbidimetric assays [1, 5, 11]. The concentration of albumin in urine during clinical exam is expressed as concentration of human serum albumin (HSA), or as urinary albumin-to-creatinine ratio [12]. The latter value is extremely useful when a sample is analyzed randomly because the concentration of creatinine, a metabolic waste product, represents the normalization factor that compensates some usual variation in the urine excretion over the course of the day [5]. In this framework, we looked at the specific application of a simple polydopamine (PDA)-based colorimetric platform described by Palladino et al. [13], which essentially relies on the competitive isothermal adsorption of a polydopamine layer and proteins on polystyrene surface of multi-well plate. In particular, it has been reported that the PDA absorbance in the visible region decreases with the increase of protein concentration, allowing the analytical quantification of biomarkers like albumin here examined. Here, we have investigated the influence of two fundamental but unexplored parameters of dopamine polymerization other than its concentration, namely temperature and salt concentration of the ordinary buffer for pH control. This allowed to achieve further insights into physicochemical determinants of PDA formation from its monomer by providing a better overview and control of medium determinants of PDA growth in the presence of real samples without pretreatments. Accordingly, here we present a very simple, low-cost, and robust experimental asset for high-throughput urine single spot screening of albuminuria condition, from micro- ($0.02\ g\ L^{-1} < [HSA] < 0.2\ g\ L^{-1}$) to macroalbuminuria ($[HSA] > 0.2\ g\ L^{-1}$), without sample treatments, including dilution [14–17]. As proof of concept, the proposed methodology is compared with some commercial colorimetric methods for proteinuria analysis covering different working ranges, overlaying the dynamic range reported above, namely ELISA assay

(0.003–0.240 g L^{-1}), dipstick test (0.02–0.10 g L^{-1}), and Bradford assay (0.1– 1.4 g L^{-1}). The analytical performances of PDA-based colorimetric approach have been evaluated by testing artificial and real human urine samples spiked with HSA to cover the reference values reported above for micro- and macro- albuminuria and used in the clinical practice to identify the severity level of renal injury. The results obtained showed good reproducibility, offering a complementary bioanalytical assay in clinical proteomics, and appearing especially superior to the Bradford assay, for early screening and assessment of kidney damage.

5.2.3 Experimental section

5.2.3.1 Materials and chemicals

Dopamine hydrochloride, sodium chloride, glacial acetic acid, tris(hydroxymethyl)aminomethane hydrochloride (Tris-HCl, purity >99%), and human serum albumin were purchased from Sigma-Aldrich (Milan, Italy). Ultrapure water (resistivity 18.2 MΩ cm Millipore corporation, USA) was used for all experiments. Buffers were filtered by using vacuum filter cups (0.22 μm pore size). All the trials were carried out by setting a fixed temperature through a thermostatic oven. Artificial urine for testing sterile urethral catheters, ready-to-use solution prepared according to DIN EN 1616:1999, was acquired from Pickering Laboratories (Mountain View, USA). Artificial urine composition (pH 6.6 ± 0.1): 25.00 g L^{-1} urea, 9.00 g L^{-1} sodium chloride, 2.50 g L^{-1} potassium dihydrogen orthophosphate, 2.50 g L^{-1} disodium hydrogen orthophosphate anhydrous, 3.00 g L^{-1} sodium sulfite hydrated, 3.00 g L^{-1} ammonium chloride, and 2.00 g L^{-1} creatinine. Disposable 96-well microtest plate flat-bottom, with low binding polystyrene solid surface, and acetate foil for 96-well were obtained by Sarstedt (Nümbrecht, Germany). Bradford protein assay was from Bio-Rad (Milan, Italy) with a linear range from 0.1 to 1.4 g L^{-1}. Human microalbumin ELISA kit was purchased from Bioassay Technology Laboratory (Shanghai, China) with a standard curve range from 0.003 to 0.240 g L^{-1}. Micral urine test strips (0.02–0.10 g L^{-1}) were purchased from Roche diagnostics (Monza, Italy).

5.2.4 Methods and instrumentation

5.2.4.1 The effect of temperature on the PDA film growth

Polydopamine films were prepared on a disposable microwell platform by dropping a freshly prepared solution of 5.00 g L^{-1} dopamine in 20 mM Tris-HCl pH 8.50 (100 µL/well). The platform was left upside down for 24 h at a fixed temperature on a thermostatic oven under static condition to achieve the polymeric film formation. The dependence of PDA growth on temperature has been determined at 5 °C, 15 °C, 20 °C, 25 °C, 30 °C, 35 °C, 40 °C, and 45 °C with eight replicas for each temperature. In this context, to prevent the dehydration of the PDA film at high temperature, the microwell platforms were properly sealed with an acetate foil. The polymerization was followed by four washing steps. The wells were rinsed with deionized water and then emptied onto absorbent paper. Lastly, the wells were filled with 100 µL/well of deionized water for optical density measurements at different wavelengths (415, 450, 490, 555, 595, 655, 750 nm) by using iMark™ microplate absorbance reader.

5.2.4.2 The effect of buffer concentration on the PDA film growth

Polydopamine films were prepared on a disposable microwell platform by dropping a freshly prepared solution of 5.00 g L^{-1} dopamine in Tris-HCl pH 8.50 (100 µL/well), at several concentrations (160 mM, 80.0 mM, 40.0 mM, 20.0 mM, 10.0 mM, 5.00 mM, 2.50 mM, 1.25 mM, 0.625 mM), or H_2O. The platform was left upside down for 24 h at 25 °C in a thermostatic oven under static condition to achieve the polymeric film formation. The polymerization, washing, and reading steps were the same reported above to monitor the temperature effect on the growth of the PDA film.

5.2.4.3 The effect of urine matrix on the PDA film growth

The potential urine matrix interference in the measurements of the urinary HSA content was tested by measuring the influence of artificial and human urine samples on PDA growth from dopamine. Moreover, the same

experiments were repeated in the presence of the target macromolecule and the results were compared to the blank (dopamine in buffer only). The samples of urine (50 µL/well) were carefully added to wells and gently mixed, to avoid foaming, with 10.00 g L^{-1} dopamine in 320 mM Tris-HCl pH 8.50, with or without HSA (2.00 g L^{-1}) (50 µL/well). The plates were flipped for 24 h at a controlled temperature of 25 °C under static condition and then washed as mentioned in the previous section. The wells were filled with 100 µL/each of deionized water and the optical density measurements were conducted at a fixed wavelength (415 nm).

5.2.4.4 The analysis of artificial and human urine samples

The study focused on the examination of standard artificial urine, and real matrix samples collected from a healthy volunteer. The artificial and real urine samples were spiked with HSA at different concentrations spanning from 0.02 to 1.00 g L^{-1}. Spiked and unspiked urine sample aliquots were subjected to the same experimental procedure except for HSA addition. No preserving agent was added to the urine real samples, since they were immediately analyzed. The standard artificial urine is not stabilized but stored at − 20 °C. The samples (50 µL/well) were carefully added to wells and gently mixed, to avoid foaming, with 10.00 g L^{-1} dopamine (50 µL/well) in 40 mM or 320 mM Tris-HCl pH 8.50. The procedure continues as described in the previous section. The same urine samples have been analyzed with some commercial kits/analytical methods, i.e., Bradford protein assay, ELISA kit, and dipstick test kit specific for urine analysis, according to the standard operating procedure reported by each supplier. In particular, the Bradford assay protocol consists of mixing 5 µL of protein sample with 145 µL of Bradford reagent (Coomassie blue) on the microwell plate (150 µL/well), reading the color developed by solution at λ = 595 nm.

5.2.4 Results and discussion

With the aim to develop a robust method with large applicability for polydopamine-based quantitation of albuminuria, here we have preliminary

investigated two fundamental environmental factors, other than dopamine concentration previously explored [13], influencing dopamine polymerization and its adsorption onto the surface. In detail, we have studied a broad range of conditions for temperature and buffer concentration that normally could change between different laboratories or set of experiments, and potentially affecting the reproducibility of the urine analysis. Subsequently, we have studied the effect of the urine matrix on PDA growth prior to analyze real human urine samples also in comparison with common analytical methods for urine analysis.

5.2.4.1 PDA growth as function of temperature

Here, we conducted, for the first time to our knowledge, a systematic study of the polydopamine growth as function of the temperature at fixed concentration of dopamine (5 g L^{-1}), by measuring the absorbance of the polymeric film grafted to polystyrene microwell plates. Temperature effect was investigated over the range 5 to 45 °C that covers the ambient operating temperatures. Figure 5.7a shows the increase of the optical density with the temperature, recorded on the visible range, likely due to thicker layer formation of PDA onto polystyrene surface. In particular, the absorbance at 415 nm, most indicative of PDA formation, follows a sigmoidal trend increasing with the temperature. The sigmoid shows the inflection point around 25 °C, with a larger relative increase between 15 and 35 °C, whereas below 15 °C and above 35 °C, the relative growth of PDA film is less marked than between these temperatures (Fig. 5.7b). The same behavior has been observed at any wavelength (data not shown). These results appear particularly significative underlying that temperature variability, typically encountered among analytical laboratories, can largely affect the dopamine polymerization and deposition. Accordingly, we have chosen 25 °C as the working temperature, fixed by a thermostatic oven for subsequent experiments, because this condition ensures absorbance readability, high repeatability, and limited incorporation of irregular aggregates which can potentially be formed at higher temperature due to drying. The complete

dataset for experiments in dependence of temperature in Fig. 5.7 is reported in tables 5.3 and 5.4.

Table 5.3 Coefficient of variation (%CV) for PDA absorbance values (Dopamine 5.00 g L^{-1} in 20 mM Tris-HCl) vs wavelength (λ) from Fig. 5.7a

	%CV of A_{PDA} @ different λ							
λ (nm)	5 °C	15 °C	20 °C	25 °C	30 °C	35 °C	40 °C	45 °C
415	23	10	5	4	3	4.7	3	2
450	23	11	6	4	6	5.4	3	5
490	24	12	7	5	5	5	4	5
555	27	14	8	6	7	7	4	6
595	27	14	8	6	1	6	4	7
655	29	16	9	7	5	7	5	8
750	28	17	12	8	9	9	6	9
$\%CV_{mean}$	26	13	8	6	5	6	4	6

Table 5.4 PDA Absorbance (Dopamine 5.00 g L^{-1} in 20 mM Tris-HCl) at 415 nm (mean ± SD) and related Coefficient of variation (%CV) *vs* Temperature (°C) from Fig. 5.7b

T (°C)	A_{PDA}@415nm	%CV
5	0.056 ± 0.013	23
15	0.077 ± 0.008	10
20	0.132 ± 0.006	5
25	0.185 ± 0.007	4
30	0.208 ± 0.006	3
35	0.232 ± 0.011	4.7
40	0.239 ± 0.008	3
45	0.251 ± 0.005	2
	$\%CV_{mean}$	7

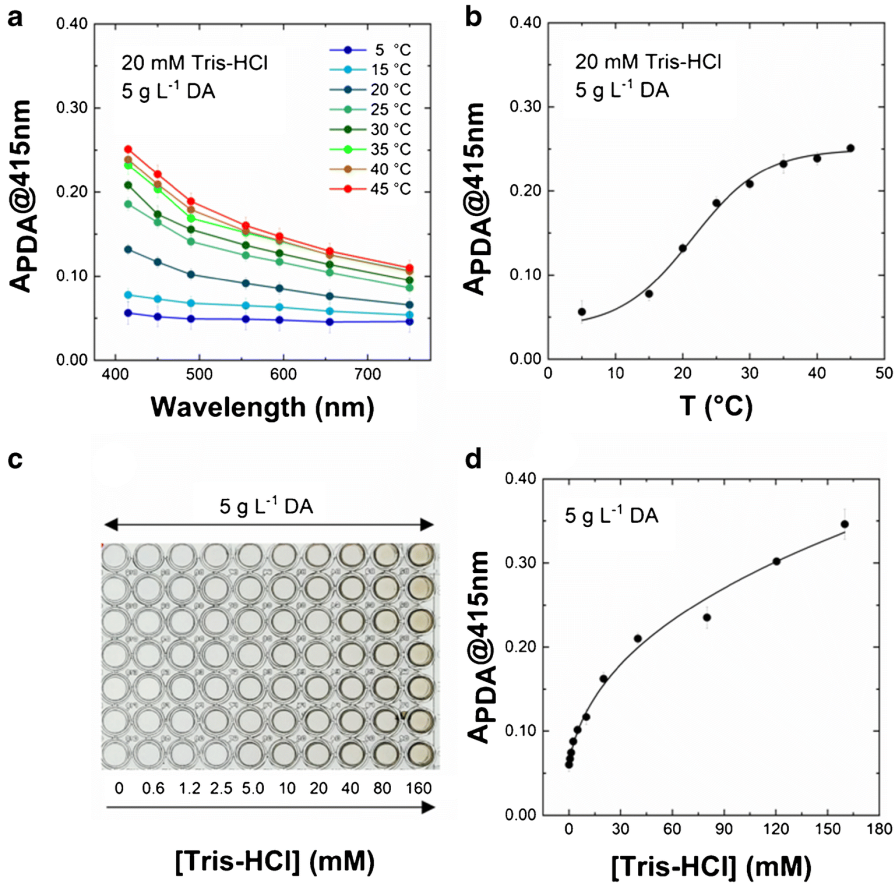

Fig. 5.7 Polydopamine film growth onto the surface of polystyrene multi-well plates. **a)** Absorbance of PDA film recorded on a plate reader in the visible range after 24 h of dopamine 5.00 g L^{-1} polymerization in 20 mM Tris-HCl pH 8.50, and **b)** its dependence on temperature at 415 nm. **c**) Microwell plate after 24 h at 25 °C with 5.00 g L^{-1} dopamine at increasing Tris-HCl buffer concentration and d its absorbance dependence on buffer concentration at 415 nm. The lines in **a**, **b**, and **d** are inserted to guide the eye. Each point represents the average of eight measurements ± standard deviation

5.2.4.2 PDA growth as function of buffer concentration

Herein, we reported the polydopamine growth as a function of the Tris-HCl concentration, the typical buffer for PDA preparation. The pKa of Tris-HCl is 8.07 at 25 °C, showing a good buffer capacity between 7.1 and 9.1 (pKa ± 1). Of course, its resistance to pH change is directly proportional to buffer concentration [18] and this aspect is particularly important for PDA formation

because, generally, buffer solutions reported in PDA literature are about 10–20 mM, which is practically equimolar to the typical dopamine hydrochloride concentrations (2–5 g L^{-1}, 10 – 26 mM) used in polymerization experiments [13, 19–22]. Consequently, dopamine alters the solution pH which determines the equilibrium concentration of the different dopamine species [23], potentially affecting the PDA formation. Here, we have quantified this buffer effect by studying the polydopamine growth as function of the buffer concentration, fixing both the temperature (25 °C) and the concentration of dopamine (5.00 g L^{-1}), and measuring the absorbance of the polymeric film growth onto the microwell plates as depicted in Fig. 5.7c. Figure 5.7d shows the progressive increase of the absorbance with the buffer concentration, probably due to larger deprotonation and self-polymerization of dopamine at higher pH, as expected. Again, these results appear particularly useful to achieve high reproducibility for the PDA film formation and its absorbance in the visible range by avoiding concentration variability of buffer encountered in different experimental protocols. Moreover, it is also fundamental to minimize the possible result discrepancies due to unknown composition and pH of real samples like urine [24] by using an efficient buffer. Accordingly, we have chosen dopamine 5.00 g L^{-1}, 25 °C, and 160 mM Tris-HCl pH 8.5 as the working conditions for subsequent experiments, conferring larger buffer capacity to solution and higher optical absorbance values for PDA film compared to literature data [13]. The complete dataset for experiments in dependence of buffer concentration in Fig. 5.7 is available in Table 5.5.

Table 5.5 PDA Absorbance (Dopamine 5.00 g L^{-1}) at 415 nm (mean ± SD) and related coefficient of variation (%CV) vs [Tris-HCl] at 25 °C from Fig. 5.7d (artificial urine)

[Tris-HCl] (mM)	A_{PDA}@415nm	%CV
0.000	0.060 ± 0.008	13
0.625	0.067 ± 0.010	15
1.250	0.074 ± 0.006	8
2.500	0.088 ± 0.002	2
5.000	0.101 ± 0.006	6
10.00	0.117 ± 0.009	8
20.00	0.162 ± 0.008	5
40.00	0.210 ± 0.007	3
80.00	0.235 ± 0.013	5.5
160.0	0.346 ± 0.018	5.2
	$\%CV_{mean}$	7

5.2.4.3 PDA growth in the presence of artificial and real urine matrix

In this study, we analyzed the potential interference of matrix on the detection of selective albuminuria condition. In particular, we have evaluated the contribution of artificial (see Materials and chemicals for composition) and real matrix to PDA film formation via optical spectroscopy, by fixing the dopamine concentration at 5.00 g L^{-1}, the temperature at 25 °C, and choosing 160 mM Tris-HCl pH 8.5 as buffer. The absorbance was recorded at 415 nm, corresponding to maximum absorbance wavelength for polydopamine film as reported in Fig. 5.7a.

The mean absorbance values of PDA film onto microplates without interferent (blank, dopamine in buffer) or formed from dopamine in artificial (orange) or human (yellow) urine, whose components could compete/interfere with PDA formation and adsorption onto plate surface, are plotted as histograms in Fig. 5.8. Furthermore, absorbance values were also recorded for PDA film formed from the same urinary matrices with the addition of human serum albumin (1.00 g L^{-1} HSA), simulating a sample from a patient with severe kidney damage and a consequent macroalbuminuria. Figure 5.8 shows that artificial and human urine matrices have almost no effect on PDA formation, even in the presence of 2 g L^{-1} of glucose (green), giving a matrix-independent

absorbance within the experimental errors, which represents undoubtedly a good result for HSA quantification in the real specimens. On the contrary, matrices spiked with HSA show a large absorbance decrease due to high competition with PDA for adsorption onto surface of polystyrene. These results are qualitatively in line with our recent findings at lower buffer concentration but with a different dependence on protein concentration of the PDA absorbance (vide infra) [13].

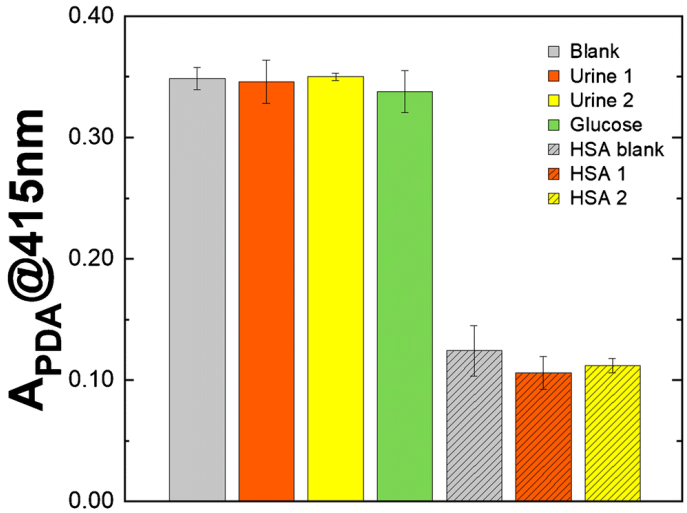

Fig. 5.8 Polydopamine film growth onto the surface of multi-well plates after 24 h at 25 °C by using dopamine 5.00 g L^{-1} in blank solution (160 mM Tris-HCl pH 8.5) without (gray) or in the presence of artificial urine (orange), human urine (yellow), or artificial urine spiked with 2 g L^{-1} of glucose (green) samples. Bars with stripes represent the PDA film growth in the presence of HSA (1 g L^{-1}) in blank solution (gray), artificial urine (orange), and urine (yellow). PDA absorbance at 415 nm has been measured for each solution, reporting the mean value (± SD) calculated on three replicates

5.2.4.4 Artificial and synthetic urine analysis

We have investigated and compared the effect of spiking artificial standard and real human urine samples with different concentration of HSA (Fig. 5.9). The range of HSA concentration was chosen to span from microalbuminuria (0.02 g L^{-1} < [HSA] < 0.2 g L^{-1}) to macroalbuminuria ([HSA] > 0.2 g L^{-1}), which are conditions associated with kidney damage [17]. The human urine

sample collected has shown a pH around 6, whereas the artificial urine has a certified pH = 6.6 ± 0.1. The pH of both samples is similar and within the normal range of pH for urine, usually ranging from 4.5 to 8.0 [16, 20]. Figure 5.9 displays the effect of the competitive adsorption at 25 °C at different concentrations of HSA in the copresence of dopamine (5.00 g L^{-1}) in 160 mM Tris-HCl pH 8.5. The absorbance of polydopamine film decreases upon the increase of HSA concentration. This experimental evidence has been ascribed to decreased thickness of the adhesive PDA layer onto the polystyrene surface for increased amount of protein in solution due to a competitive adsorption process, as extensively discussed by Palladino et al. [13]. Besides, it is necessary to mention that tris molecules are getting incorporated into poly(catecholamine) (here PDA) films due to the reactivity of amine groups towards quinone. It is possible that by increasing tris concentration, the crosslinking of the polymeric film gradually increased. In this context, we can ascribe that a competitive intrinsic reaction between the amine groups of tris molecules and HSA for the quinones modulate the polymer formation, negatively affecting the PDA film when a higher HSA concentration is absorbed to the solid surface [25]. However, for a better comparison with Bradford protein assay (vide infra), Fig. 5.9a is presented as absorbance of blank (PDA formed in matrix without HSA) minus absorbance of samples in the presence of this protein, obtaining an excellent linear trend (R^2 = 0.994), almost superimposable for human and artificial urine, with excellent repeatability ($\%CV_{mean}$ = 2 and 4, respectively) over the HSA concentration range 0.00 to 1.00 g L^{-1} (see Table 5.6). Although this result was expected based on our recent literature [13], such large linear dynamic range achieved in 160 mM Tris-HCl pH 8.5 appears easier to handle than the Langmuir-shaped curve previously obtained [13], and here replicated, at lower buffer concentration (20 mM Tris- HCl pH 8.5) as reported in Fig. 5.10.

5.2.4.5 Comparative analysis of colorimetric bioanalytical assays for albuminuria detection

Different standard and commercial analytical methods for albumin detection in urine samples have been tested for comparison with the PDA-based quantitation of albuminuria here proposed. Namely, Sandwich ELISA kit and dipstick test, in addition to Bradford protein assay, have been used to analyze the same samples tested with the PDA-based strategy.

Unfortunately, in our hands, the commercial ELISA kit for microalbuminuria failed to give useful results for the analysis of the urine samples spiked with HSA. The enzyme was completely saturated during the experiment and no differences between concentrations have been highlighted by measuring the absorbance at 450 nm both within the standard curve range (0.003–0.240 g L^{-1}) or, as expected, above it (data not shown). For the other assays, the results of the analyses of human and artificial and urine samples spiked with HSA are reported in Fig. 5.9, Tables 5.6, 5.7 and 5.8. Figure 5.9b shows a significative matrix-dependent behavior for the Bradford protein colorimetric assay, which is based on the absorbance at 595 nm of Coomassie brilliant blue G-250 (A_{G250}@595 nm), with a much larger difference between the curves for urine and artificial urine samples in comparison with the PDA strategy applied at the same samples reported in Fig. 5.9a. The analysis of such data shows better analytical parameters for PDA-based method, as detailed in Tables 5.6 and 5.7. Specifically, there is a lower relative variability of data, demonstrated by lower mean coefficient of variation ($\%CV_{mean}$ for HSA in urine = 2 for PDA assay and 4 for Bradford assay), and larger values of the coefficient of determination (R^2 for HSA in urine = 0.994 for PDA assay and 0.982 for Bradford assay), confirming the visible superior goodness of linear fit for the PDA-based method with respect to the Bradford assay in this HSA concentration range. Moreover, the dynamic range for PDA reaches a lower analyte concentration, as indicated by lower limit of detection (LOD) values for HSA spiked in human or artificial urine (0.036 ± 0.001 g L^{-1} and 0.053 ± 0.001 g L^{-1}, respectively), near to the threshold between normo-

and microalbuminuria [15–17], whereas the LOD values achieved by using the Bradford assay are closer the threshold between micro- and macro-albuminuria in both matrices (0.147 ± 0.005 g L^{-1} and 0.204 ± 0.007 g L^{-1}, respectively) [15–17]. Notably, as clearly shown in Fig. 5.9b, for the Bradford protein assay, a sigmoidal fit (red lines) represents better the piecewise trend than the linear fitting (black lines) suggested by the supplier. Differently, for PDA data, there is no such large practical advantage in applying the sigmoidal fit (red lines in Fig. 5.9a) instead of the linear one that covers very well the whole dynamic range (black lines in Fig. 5.9a, and Table 5.8). Finally, Fig. 5.9c shows the images of semi-quantitative commercial dipstick strips tested against human urine spiked with HSA. The main advantage of this colorimetric immunoassay is the test rapidity (60 s), whereas the PDA strategy currently takes 24 h. Accordingly, a different modulation of buffer to accelerate the polymerization and deposition will be the subject of future work to shorten the assay time. However, because of the presence of a monoclonal antibody and gold nanoparticles, the cost of dipstick test is about 100 times higher than that of the PDA-based strategy. Moreover, the application of these semi-quantitative strips is limited to the microalbuminuria concentration range, requiring sample dilution for higher analyte concentration, and it is much more difficult to appreciate the analyte concentration solely by the naked eye comparison of color intensities of such strips with a limited reference color scale [26].

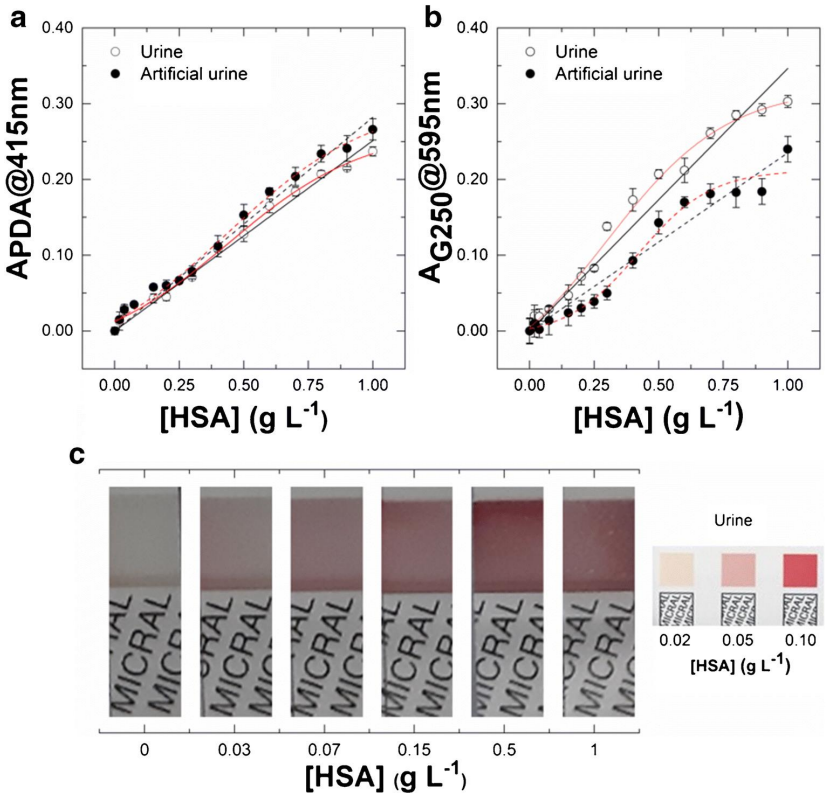

Fig. 5.9 Analysis of human and artificial urine spiked with HSA. (**a**) Absorbance at 415 nm of PDA layer (A_{PDA}@415 nm) from dopamine 5.00 g L^{-1} in 160 mM Tris-HCl pH 8.5 at 25 °C presented as absorbance of blank (PDA formed in matrix without HSA) minus absorbance of samples in the presence of increasing concentration of HSA, spanning from 0.02 to 1.00 g L^{-1}, spiked into human (open circle) or artificial (black circles) urine samples. (**b**) Absorbance at 595 nm, after blank subtraction, of Coomassie brilliant blue G-250 (AG_{250}@595 nm) from Bradford protein assay applied to the same spiked urine reported above. The least-squares fitting for the linear regression (black lines; see Table 1) or sigmoidal (red lines; see Table 5.8) analysis of data in a and b was achieved by using OriginPro 2019b. Absorbance values are reported as the mean value (± SD) calculated on three replicates. (**c**) Images of dipstick strip test for albumin applied to human urine sample spiked with HSA, and the related color reference scale

Table 5.6 Analytical parameters for PDA-based method (Fig. 5.3a) both tested in human and artificial urine samples

	PDA-based method (A_{PDA}@415 nm)					
Parameters	Urine			Artificial urine		
m (g^{-1} L)	0.251 ± 0.005			0.282 ± 0.006		
LOD (g L^{-1})	0.036 ± 0.001			0.053 ± 0.001		
R^2	0.994			0.994		
[HSA] (g L^{-1})	Mean	SD	%CV	Mean	SD	%CV
0.00	0.350	0.003	0.9	0.372	0.005	1
0.02	0.337	0.012	3.6	0.357	0.003	0.8
0.04	0.320	0.001	0.3	0.344	0.007	2
0.08	0.315	0.003	1	0.337	0.002	0.6
0.15	0.307	0.006	2	0.314	0.004	1
0.20	0.305	0.005	2	0.312	0.007	2
0.25	0.284	0.002	0.7	0.305	0.004	1
0.30	0.279	0.002	0.7	0.293	0.007	2
0.40	0.242	0.003	1	0.260	0.014	5.4
0.50	0.222	0.010	4.5	0.219	0.014	6.4
0.60	0.185	0.009	5	0.188	0.005	3
0.70	0.166	0.006	4	0.168	0.012	7.1
0.80	0.143	0.005	4	0.138	0.011	8.0
0.90	0.135	0.002	1	0.131	0.017	13
1.00	0.113	0.006	5	0.106	0.014	13
$\%CV_{mean}$			2			4

Table 5.7 Analytical parameters for Bradford protein assay (Fig. 5.3b) both tested in human and artificial urine samples

	Bradford assay (A_{G250}@595 nm)					
Parameters	Urine			Artificial urine		
m (g^{-1} L)	0.251 ± 0.005			0.282 ± 0.006		
LOD (g L^{-1})	0.036 ± 0.001			0.053 ± 0.001		
R^2	0.994			0.994		
[HSA] (g L^{-1})	Mean	SD	%CV	Mean	SD	%CV
0.00	0.173	0.017	9.8	0.181	0.016	8.8
0.02	0.193	0.014	7.3	0.191	0.018	9.4
0.04	0.192	0.010	5.2	0.183	0.011	6.0
0.08	0.202	0.003	1	0.195	0.019	9.7
0.15	0.220	0.014	6.4	0.205	0.017	8.3
0.20	0.245	0.011	4.5	0.211	0.010	4.7
0.25	0.256	0.004	2	0.220	0.009	4
0.30	0.311	0.005	2	0.231	0.009	4
0.40	0.346	0.015	4.3	0.274	0.010	3.7
0.50	0.380	0.006	2	0.324	0.015	4.6
0.60	0.385	0.016	4.2	0.351	0.007	2
0.70	0.434	0.007	2	0.362	0.013	3.6
0.80	0.458	0.006	1	0.364	0.020	5.5
0.90	0.465	0.008	2	0.365	0.017	4.7
1.00	0.476	0.008	2	0.421	0.017	4.0
$\%CV_{mean}$			4			6

Table 5.8 Sigmoidal fitting parameters for HSA (0.02 - 1.00 g L^{-1}) from Fig. 5.9

$$Boltzmann\ model$$

$$y = \frac{A1 - A2}{1 + e^{(x - x_0)/dx}} + A_2$$

	PDA-based method (A_{PDA}@415nm)		*Bradford-assay (A_{G250}@595nm)*	
Parameters	Urine	Artificial urine	Urine	Artificial urine
A1	-0.037 ± 0.028	-0.007 ± 0.014	-0.083 ± 0.055	-0.050 ± 0.036
A2	0.268 ± 0.023	0.212 ± 0.012	0.321 ± 0.020	0.306 ± 0.028
x0	0.438 ± 0.038	0.422 ± 0.030	0.299 ± 0.057	0.432 ± 0.040
dx	0.269 ± 0.060	0.141 ± 0.031	0.234 ± 0.054	0.284 ± 0.066
R^2	0.992	0.974	0.989	0.992

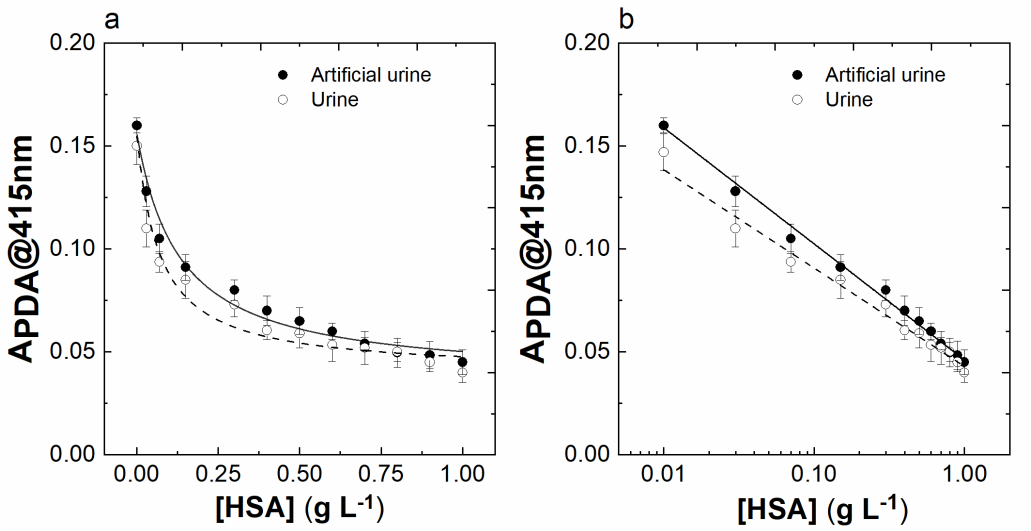

Fig. 5.10 Competitive adsorption isotherms for HSA (0.03 - 1.00 g L^{-1})/PDA (Dopamine 5.00 g L^{-1} in 20 mM Tris-HCl) in urine and artificial urine. (a) Absorbance recorded at 415 nm for PDA layer grafted onto ELISA plate. (b) Linear regression curves resulting from semilogarithmic plot of data in Table 5.9 and Fig. 5.1a. Absorbance values are reported as the mean value (± SD) calculated on three replicates

Table 5.9 Linear fitting parameters for HSA (0.03 - 1.00 g L^{-1})/PDA (Dopamine 5.00 g L^{-1} in 20 mM Tris-HCl) from Fig. 5.4b

Calibration curve: $Abs_{\lambda max} = Abs^{0}_{\lambda max} + m \times [\mathrm{HSA}]$; $Abs^{0}_{\lambda max} is\ the\ intercept\ at\ [\mathrm{HSA}] = 0\ and\ m\ is\ the\ slope$						
Sample	Urine			Artificial urine		
m (g L^{-1})	-0.048 ± 0.002			-0.056 ± 0.001		
$Abs^{0}_{\lambda max}$	0.043 ± 0.001			0.046 ± 0.001		
LOD (g L^{-1})	0.562			0.193		
R^2	0.980			0.996		
[HSA] (g L^{-1})	Mean	SD	%CV	Mean	SD	%CV
0.00	0.160	0.004	3	0.150	0.009	6
0.03	0.128	0.008	6	0.110	0.009	8
0.07	0.105	0.007	7	0.094	0.005	5
0.15	0.091	0.006	7	0.085	0.009	11
0.30	0.080	0.005	6	0.073	0.006	8
0.40	0.070	0.007	10	0.061	0.005	8
0.50	0.065	0.007	11	0.059	0.007	12
0.60	0.060	0.004	7	0.053	0.008	15
0.70	0.054	0.003	6	0.052	0.008	15
0.80	0.050	0.007	14	0.050	0.005	10
0.90	0.048	0.007	15	0.045	0.005	11
1.00	0.045	0.006	13	0.040	0.005	13
$\%CV_{mean}$			9			10

5.2.5 Conclusions

Albuminuria is considered a potential diagnostic marker for early renal damage. Here, we propose a colorimetric method to quantify the urinary albumin concentration based on the competitive adsorption of a polydopamine layer and human serum albumin (HSA) onto the polystyrene surface of ELISA plates. The method has been optimized by evaluating the effect of temperature and buffer concentration variability, typically encountered among analytical laboratories, on PDA film formation and, consequently, on the reproducibility of the analysis. Furthermore, it has shown the limited matrix effect on the optical measurements. Accordingly, the analytical performances of this approach have been successfully evaluated testing artificial and human urine samples spiked with HSA, covering the whole reference concentration range required by the clinical

practice to identify both micro- and macroalbuminuria. The results obtained showed excellent repeatability ($\%CV_{mean}$ = 2 for human urine), with a broad linear dynamic range up to 1 g L^{-1}, and superior analytical performances in comparison with some standard and commercial colorimetric analytical methods, like dipstick test or Bradford protein assay. As a whole, the method here reported results in a flexible and cost-effective bioassay, based on a common optical platform, for routine screening and assessment of selective albuminuria in urine without the pretreatment of the samples.

References

1. Yeasmin S, Ammanath G, Ali Y, Boehm BO, Yildiz UH, Palaniappan A, et al. Colorimetric urinalysis for on-site detection of metabolic biomarkers. ACS Appl Mater Interfaces. 2020. https:// doi.org/10.1021/acsami.0c09179
2. Résimont G, Piéroni L, Bigot-Corbel E, Cavalier E, Delanaye P. Urinary strips for protein assays: easy to do but difficult to interpret! J Nephrol. 2020. https://doi.org/10.1007/s40620-020-00735-y
3. Rhee C, Kovesdy C. Spotlight on CKD deaths—increasing mortal- ity worldwide. Nat Rev Nephrol. 2015. https://doi.org/10.1038/ nrneph.2015.25
4. Mok Y, Ballew SH, Sang Y, Coresh J, Joshu CE, Platz EA, et al. Albuminuria, kidney function, and cancer risk in the community. Am J Epidemiol. 2015. https://doi.org/10.1093/aje/kwaa043
5. Julian BA, Suzuki H, Suzuki Y, Tomino Y, Spasovski G, Novak J. Sources of urinary proteins and their analysis by urinary proteomics for the detection of biomarkers of disease. Proteomics Clin Appl. 2009. https://doi.org/10.1002/prca.200800243.
6. Pollak MR, Quaggin SE, Hoenig MP, Dworkin LD. The glomeru- lus: the sphere of influence. Clin J Am Soc Nephrol. 2014. https:// doi.org/10.2215/CJN.09400913.
7. Makanjuola D, Lapsley M. In Marshall W, Lapsley M, Day A, Ayling R, editors. Clinical biochemistry: metabolic and clinical aspects. 3rd ed. Churchill Livingstone; 2014. pp. 124–151. https://doi.org/10.1016/B978-0-7020-5140-1.00007-9
8. Persson F, Rossing P. Diagnosis of diabetic kidney disease: state of the art and future perspective. Kidney Int Suppl. 2018. https://doi.org/10.1016/j.kisu.2017.10.003

9. Kim MJ, Kang YU, Kim CS, Choi JS, Bae EH, Ma SK, et al. Proteinuria as a risk factor for mortality in patients with colorectal cancer. Yonsei Med J. 2013. https://doi.org/10.3349/ymj.2013.54. 5.1194
10. Jørgensen L, Heuch I, Jenssen T, Jacobsen BK. Association of albuminuria and cancer incidence. J Am Soc Nephrol. 2008. https://doi.org/10.1681/ASN.2007060712
11. Viswanathan G, Upadhyay A. Assessment of proteinuria. Adv Chronic Kidney Dis. 2011. https://doi.org/10.1053/j.ackd.2011. 03.002
12. Shuvy M, Zwas DR, Lotan C, Keren A, Gotsman I. Albuminuria: associated with heart failure severity and impaired clinical out- comes. Can J Cardiol. 2020. https://doi.org/10.1016/j.cjca.2019. 09.001
13. Palladino P, Brittoli A, Pascale E, Minunni M, Scarano S. Colorimetric determination of total protein content in serum based on the polydopamine/protein adsorption competition on microplates. Talanta. 2019. https://doi.org/10.1016/j.talanta.2019.01. 095
14. Sorich MJ, Rowland A, Kichenadasse G, Woodman RJ, Mangoni AA. Risk factors of proteinuria in renal cell carcinoma patients treated with VEGF inhibitors: a secondary analysis of pooled clinical trial data. Br J Cancer. 2016. https://doi.org/10.1038/bjc.2016. 147
15. Adamczak M, Masajtis-Zagajewska A, Mazanowska O, Madziarska K, Stompór T, Więcek A. Diagnosis and treatment of metabolic acidosis in patients with chronic kidney disease – position statement of the working group of the polish society of nephrology. Kidney Blood Press Res. 2018. https://doi.org/10.1159/ 000490475
16. Ruggenenti P, Remuzzi G. Time to abandon microalbuminuria? Kidney Int. 2006. https://doi.org/10.1038/sj.ki.5001729
17. Heerspink HJL, Brantsma AH, Zeeuw DD, Bakker SJL, Jong PED, Gansevoort RT. Albuminuria assessed from first-morning-void urine samples versus 24-hour urine collections as a predictor of cardiovascular morbidity and mortality. Am J Epidemiol. 2008. https://doi.org/10.1093/aje/kwn209
18. Urbansky ET, Schock MR. Understanding, deriving, and computing buffer capacity. J Chem Educ. 2000. https://doi.org/10.1021/ed077p1640
19. Scarano S, Pascale E, Palladino P, Fratini E, Minunni M. Determination of fermentable sugars in beer wort by gold nanoparticles@polydopamine: a layer-by-layer approach for localized surface plasmon resonance measurements at fixed wavelength. Talanta. 2018. https://doi.org/10.1016/j.talanta.2018.02.044

20. Palladino P, Minunni M, Scarano S. Cardiac Troponin T capture and detection in real-time via epitope-imprinted polymer and optical biosensing. Biosens Bioelectron. 2018. https://doi.org/10.1016/ j.bios.2018.01.068
21. Scarano S, Palladino P, Pascale E, Brittoli A, Minunni M. Colorimetric determination of p-nitrophenol by using ELISA microwells modified with an adhesive polydopamine nanofilm containing catalytically active gold nanoparticles. Microchim Acta. 2019. https://doi.org/10.1007/s00604-019-3259-2
22. Palladino P, Bettazzi F, Scarano S. Polydopamine: surface coating, molecular imprinting, and electrochemistry-successful applications and future perspectives in (bio)analysis. Anal Bioanal Chem. 2019. https://doi.org/10.1007/s00216-019-01665-w
23. Sánchez-Rivera AE, Corona-Avendano S, Alarcón-Angeles G, Rojas-Hernández A, Ramırez-Silva MT, Romero-Romo MA. Spectrophotometric study on the stability of dopamine and the determination of its acidity constants. Spectrochim Acta A. 2003. https://doi.org/10.1021/acs.jpcb.8b02304
24. Cook J, Strauss K, Caplan Y, Lodico C, Bush D. Urine pH: the effects of time and temperature after collection. J Anal Toxicol. 2007. https://doi.org/10.1093/JAT/31.8.486
25. Barclay TG, Hegab HM, Clarke SR, Ginic-Markovic M. Versatile surface modification using polydopamine and related polycatecholamines: chemistry, structure, and applications. Adv. Mater. Interfaces. 2017. https://doi.org/10.1002/admi.201601192
26. Posthuma-Trumpie GA, Korf J, van Amerongen A. Lateral flow (immuno)assay: its strengths, weaknesses, opportunities and threats. A literature survey. Anal Bioanal Chem. 2009. https://doi. org/10.1007/s00216-008-2287-2.

CHAPTER 6

Overall conclusions

The research study of these three years has focused on exploring neurotransmitter-derived biopolymers, in the analytical chemistry field, to design original diagnostic and (bio)analytical assays addressing various research questions. The focus was on the use of norepinephrine (NE) as a promising building block to produce mimetic receptors, rivaling their natural counterparts i.e., antibodies (Abs). This is a strong need in diagnostic for overcoming the wide use of animals for the routine production of antibodies, in compliance with the EU Directive on animal protection for scientific purposes (2010/63/EU). Animal-friendly polynorepinephrine (PNE)-based receptors (molecularly imprinted polymers, MIPs) may represent the entities of the future, thanks to their sustainability, easy production processing, and low cost. In this work, PNE-based MIPs were synthesized for the detection of gonadorelin, a small synthetic neuropeptide, misuse in sports settings. The PNE-based MIP displayed an interesting K_D in the low micromolar range; it was successfully integrated into a two-steps competitive bioanalytical assay

on a benchtop opto-sensing platform based on Surface Plasmon Resonance transduction. In addition, the developed biosensor was successfully applied to the label-free and real-time detection of gonadorelin in urine samples displaying very good analytical performance. The selectivity of the detection resulted excellent, showing the ability in discriminating one single amino acid change over the peptide sequence. The optimized assay achieves a high sensitivity (LOD = 52.0 pmol L^{-1}) and an excellent repeatability (%CV_{av} = 1.40%) in untreated urine, in line with WADA analytical requirements. A direct comparison with a commercial monoclonal antibody in terms of selectivity, reusability, and cost, highlighted the overall excellent features of this PNE-based MIP. The stability and versatility of this receptor also represent important features for point-of-care testing applications. In this framework we moved to apply PNE-based MIP for gonadorelin to simple analytical platforms, widely spread instrumentation available at clinical or anti-doping laboratories. Thanks to the high versatility feature of catecholamine-based biopolymers to stick to different material surfaces, as well as the transferability of the imprinting technology, allowed to miniaturize the assay for decentralized anti-doping analysis. In this case, the MIP for gonadorelin has been adapted to play the role of capturing antibodies in disposable 96-well microplates. The colorimetric PNE-based biomimetic enzyme-linked immunoassay (BELISA) developed, succeed in quantifying gonadorelin in standard solutions but also in untreated urine samples. In addition, according to our knowledge, this is the first example of a BELISA test involving a MIP based on PNE. The results obtained in standards solutions and urine samples showed good repeatability ($_{av}$CV% = 3.49 for sample 1 and $_{av}$CV% = 5.24 for sample 2), a challenging task considering that all the receptors were manually drop-casted and polymerized in each microplate well. Also in this case, the detection limit achieved in standard solutions (LOD_{BELISA}= 277 pmol L^{-1}) for gonadorelin detection resulted in line with the Minimum Required Performance Level (MRPL = 1.69 nmol L^{-1}) at which all the World Anti-Doping (WADA)-accredited laboratories must operate. Validation of BELISA has been performed using mass spectrometry, as a gold

standard technique, demonstrating the ability of BELISA to correctly achieve gonadorelin quantitative measurements. This issue is of crucial importance for further PNE-based assays with application to real problems.

The strength of the reported diagnostic platforms is further reinforced by the difficulty to find antibodies capable to bind properly gonadorelin.

Catecholamine-based MIPs, PNE in this case, have shown (here for the case study on gonadorelin) to be an excellent green and sustainable candidate material to imagine ELISA-like tests of the near future, antibody-free, extremely cheap, able to be prepared for a large variety of (even non-immunogenic) targets, very stable to environmental conditions, and highly versatile. This approach could further open new possibilities as abiotic point-of-care testing to make multiple biological samples analysis by integrating the smartphone technology which can be also extendable to several analytes. The imprinting technology (IT) may be transferred to other biomolecules, platforms, and architecture formats (layers or nanostructures) for all biomedical applications. In general, polycatecholamine-based biopolymers, represent excellent candidates for mimic receptors, indeed they are intended to pave the way for "breaking old barriers", i.e., bioreagents and classical non-sustainable polymers. In this scenario, it appears a fundamental task to leap forward, as an outlook on the future investigation, in a deeper understanding of the actual potential of the catecholamine-based biopolymers. Moreover, driven by the significant advances in nanotechnology, nano-imprinting biopolymers (IBPs) recently gained a lot of attention for therapeutic and diagnostic purposes. In this dissertation, we have started to study polydopamine and PNE nano-biopolymers (BPs) as promising tools to further extend the use of MIPs.

Smart optical catecholamine-based assays, in this case using DA/PDA, were also designed to address some clinical urgent demands. Mainly, two different (bio)analytical assays were developed. The first study produced a model screening tool to detect hypochlorous acid, produced by myeloperoxidase during inflammation, which is characteristic of several neurodegenerative disorders. Physiologically, chlorinated byproducts of DA (dopamine-

quinones) were generated in neurons and were observed in brains affected by Parkinson's disease. In this case, a creative approach was developed in which the presence of the biomarker (hypochlorous acid) drives oxidation of DA to quinone under acidic conditions, thus avoiding DA auto-oxidation and providing an easily accessible readout by UV-vis absorption. This assay could be useful as a preliminary simple screening tool to study the influence of aberrant chemical determinants of oxidative stress on dopamine-poisoning derivatives formation (e.g., redox active metal cations, thiols, and other organic reducing agents) before moving to complex biological neuronal systems. In addition, a polydopamine-based colorimetric assay was established to determine urinary human serum albumin (HSA), a biomarker of kidney damage. The core of this approach relied on competitive adsorption of PDA film and HSA onto micro welled polystyrene plates, allowing the selective UV-vis detection of HSA down to 0.036 ± 0.001 g L^{-1} in untreated urine, with very good repeatability ($\%CV_{mean}$ = 2) in human urine, eventually superior in terms of analytical performances to some standard methods available on the market (i.e., dipstick strip test, Bradford protein assay, and ELISA kits). Finally, two studies were presented in the appendix which do not involve catecholamine-based strategies for quantitative analytical applications. However, they refer to the "research line" of our group based on the development of smart, cheap, sensitive, and low-cost quantitative assays. Two more colorimetric-based assays on microplates are reported. In the first study 3,3',5,5'-tetramethylbenzidine is used as a multi-colorimetric indicator of chlorine in water; in the second, the selective quantification of anthocyanin with catechol/pyrogallol moiety in edible plants upon zinc complexation is illustrated.

APPENDIX

The scientific activities so far described in the present dissertation were addressed primarily on the use of catecholamines to design MIPs and bioassays. Besides, here, other studies flanking this pathway, are reported.

• Appendix 1: Determination of chlorine via a multichromatic 3,3',5,5'-tetramethylbenzidine -based method.

Based on the following study (A) and patent (B):

A) P. Palladino, **F. Torrini**, S. Scarano, M. Minunni. 3,3',5,5'-tetramethylbenzidine as multi-colorimetric indicator of chlorine in water in line with health guideline values, Analytical and Bioanalytical Chemistry 412 (2020), 7861-69.

B) Kit for colorimetric determination of chlorine level in water used for recreational purposes. Inventors: P. Palladino, M. Minunni, **F. Torrini**, S. Scarano. Priority number: 102019000024778 (IT)
Filed: December 19, 2014. Date of Patent: October 29, 2020. Assignee: University of Florence.

• Appendix 2: Colorimetric selective quantification of anthocyanins with catechol/pyrogallol moiety in edible plants upon zinc complexation

Based on the following study:

F. Torrini, L. Renai, S. Scarano, P. Palladino, M. Del Bubba, M. Minunni, Colorimetric selective quantification of anthocyanins with catechol/pyrogallol moiety in edible plants upon zinc complexation, Talanta 240 (2022) 123156.

Appendix 1

Determination of chlorine via a multichromatic 3,3',5,5'-tetramethylbenzidine -based method

3,3',5,5'-tetramethylbenzidine as multi-colorimetric indicator of chlorine in water in line with health guideline values

Pasquale Palladino*, Francesca Torrini, Simona Scarano, Maria Minunni

Department of Chemistry 'Ugo Schiff', University of Florence, Via della Lastruccia 3-13, 50019 Sesto Fiorentino, Italy

*Corresponding author: pasquale.palladino@unifi.it

A1.1 Abstract

Sanitizing solutions against bacterial and viral pathogens are of utmost importance in general, and in particular in these times of pandemic due to Sars-Cov2. They frequently consist of chlorine-based solutions, or in the direct input of a certain amount of chlorine in water supply systems and swimming pools. Colorimetry is one of the techniques used to measure the crucial persistence of chlorine in water, including household chlorine test kits commonly based on colorimetric indicators. Here we show a simple and cheap colorimetric method based on 3,3',5,5'-tetramethylbenzidine (TMB), commonly used as chromogenic reagent for enzyme-linked immunosorbent assays. TMB is converted by chlorine to a colored molecule though a pH-dependent multi-step oxidation process where the chromaticity of TMB is directly proportional to chlorine content. This molecule offers several advantages over other commonly used reagents in terms of safety, sensitivity and, peculiarly, hue modulation, giving rise to the detection of chlorine in water with a multi-color change of the indicator solution (transparent/blue/green/yellow). Moreover, through the appropriate setting of reaction conditions, such coloration is finely tunable to cover the range of

chlorine concentration recommended by international health agencies for treatment of drinking water and swimming pools and to test home-made solutions prepared by dilution of household bleach during health emergency events such as during the current pandemic.

Graphical abstract

A1.2 Introduction

Chlorine and chlorine-based compounds are widely used for oxidative inactivation of several disease-causing viruses and bacteria in water treatments, for food preservation, and during other cleaning procedures [1,2]. In all cases, the presence of chlorine residual is required to ensure the protection from recontamination. The range of chlorine concentrations recommended by international health or environmental agencies depends on the application, spanning several orders of magnitude from drinking water to sanitizing or disinfecting solutions. In detail, chlorine can be added to drinking water or swimming pools to achieve a minimum level of 0.2-0.5 mg L^{-1} (expressed as Cl_2) for an effective disinfection and residual concentration but should stay below 4-5 mg L^{-1} to avoid eye/nose irritation and stomach discomfort [3,4]. Whereas, sanitizing solutions applied to reduce germs for example on food contact surfaces or mouthed toys are obtained by dilution of concentrated chlorine bleach to 50-200 mg L^{-1}. Finally, disinfecting concentration for toilet or diapering areas should be larger than 2400 mg L^{-1}. The standard analytical methods for the determination of chlorine in natural

and treated waters are based on electrochemical techniques, iodometry, and absorption spectrophotometry [5,6], usually requiring devices for signal transduction or UV-lamp for fluorescence emission [7-9]. However, several kits for household chlorine test are present on the market for naked-eye quantification of chlorine concentration based on monochromatic indicators [10]. Here we introduce a peculiar use of 3,3',5,5'-tetramethylbenzidine (TMB) as multi-colorimetric indicator for determination of chlorine in aqueous solution. TMB is still one of the most commonly used chromogenic reagent for enzyme-linked immunosorbent assays (ELISAs) 46 years after its first synthesis as safer substitute for carcinogenic benzidine in the detection of occult blood [11-14]. This molecule gives rise to non-colored solution in reduced state that becomes blue upon oxidation (diamine). Further oxidation leads to a green stage, which is a mixture of the blue stage and the yellow endpoint (diimine). Notably, the blue colored product has been characterized as the diamine/diimine charge-transfer complex in equilibrium with the cation-radical and diamine/diamine mixture, as reported in Fig. A1 [15,16]. This reaction sequence is sensitive to several factors, like pH [16], solvent, temperature [17,18], and catalyst [14,19,20]. The application of TMB as an analytical reagent outside the field of clinical chemistry started long time ago thanks to good stability of the reaction product and high sensitivity and selectivity of such analytical methods [21-24]. Notably, thanks to ion-masking salts, TMB-based assays have shown high tolerance for potential interfering species in drinking water (including Cl^-, I^-, NO^{3-}, SO_4^{2-}, CO_3^{2-}, $H2PO^{4-}$, $P2O7^{4-}$, Na^+, K^+, Mg^{2+}, Ca2+, Zn2+, Fe^{3+} and H_2O_2) being the common and permitted concentrations of these molecules below the respective limits of interference elsewhere described [21-24]. Consequently, the reactions reported in Fig. A1 have been used for quantitative measurements of chlorine in water [21-25], under organic matter-rich conditions [26], or generated by myeloperoxidase of neutrophils [27-29], reaching an enhanced degree of automation, reduced reagent consumption and waste production [23]. Although a rigorous control of pH is not necessary, the pH range determines the color development. In detail, pH 1-

2 allows to follow the yellow TMB-diimine formation only (Fig. A1C) [21-23,25], whereas pH 4-6 has been used to track the blue TMB charge-transfer complex formation (Fig. A1B) [24]. In both conditions, the color intensity is directly proportional to the total amount of the chlorine present in the solution, reporting a limit of detection as low as 2 μg L^{-1} at pH 1.5 and 4 μg L^{-1} at pH 4.5 [22]. TMB presents several advantages in terms of sensitivity and safety over the other reagents used for colorimetric analysis of chlorine in water like o-tolidine (OTO), syringaldazine, N,N-diethyl-p-phenylenediamine (DPD), and dopamine [9,10,21,22,30]. Here we report the experimental tuning of TMB concentration, according to one-to-one stoichiometry for oxidant/substrate system [15], to achieve the visual and spectroscopic detection of chlorine by means of the color change of solution from blue to yellow (Fig. A1) like a universal indicator that covers the entire range of chlorine concentrations recommended for drinking water and swimming pools treatment [3,4]. This method appears superior to common household chlorine test kits for drinking water and swimming pools, which are based on monochromatic indicators, and could offer a useful tool to check home-made chlorine-based sanitizing solutions, which become rare during public health emergency events due to large demand.

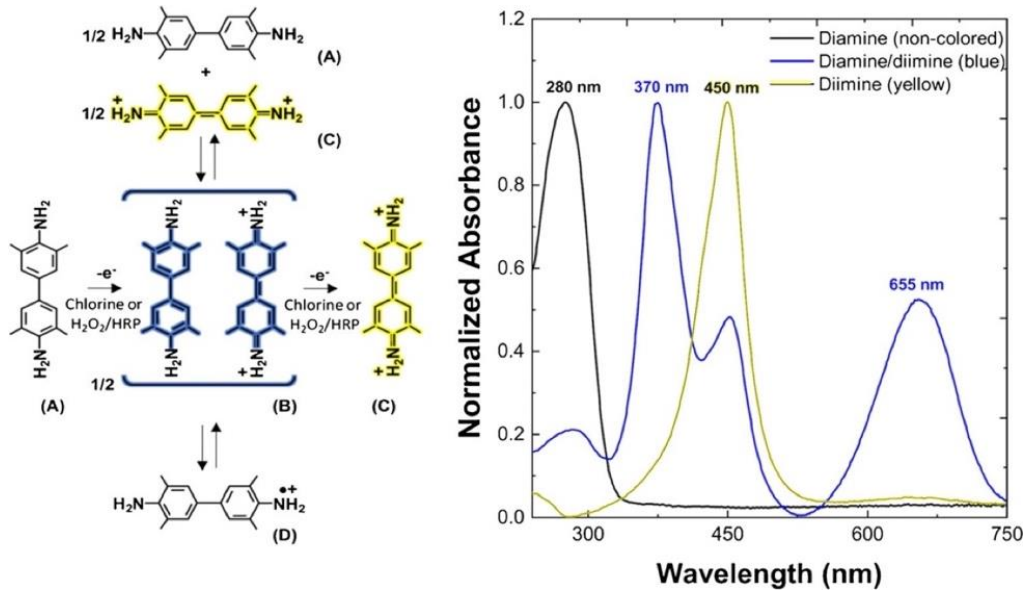

Fig. A1 The reaction sequence of TMB oxidation by chlorine (this work) [24, 25], or by H_2O_2 in presence of peroxidase catalyst (HRP) [15, 16, 18, 19], as elsewhere identified by means of optical spectroscopy, electron spin resonance spectroscopy, and resonance Raman scattering spectroscopy [15, 16, 18, 19, 24, 25]. **A)** Non-colored reduced state (diamine). **B)** Blue charge-transfer complex (diamine/diimine). **C)** Yellow two-electron oxidation product (diimine). **D)** One-electron oxidation product (cation-radical). The most representative UV-Vis spectra for the TMB species upon oxidation by chlorine (this work) are reported on the right

A1.3 Materials and methods

A1.3.1 Reagents and materials

Disposable low-binding 96-microplates were purchased from Sarstedt (Germany). Absorption suprasil® quartz cuvettes of 10 mm pathlength and 1400 µL chamber volume were provided by Hellma GmbH & Co. KG (Germany). Sodium hypochlorite solution was purchased from Merck KGaA (Germany) (Lot number: K50436114, originally containing 120 g L^{-1} of active chlorine as calculated from iodometric titration) and used to prepare stock solutions based on the intrinsic UV-absorbance of ClO^- [31]. DPD1 free chlorine test kit was purchased from Powehaus24® GmbH & Co. KG (Germany). TMB and other chemicals were purchased from Sigma Aldrich (Milan, Italy). A stock solution of about 1 mM TMB has been prepared in

ethanol/H_2O 1:1 v/v and left overnight at Room Temperature (RT) until completely dissolved before storing it at 4 °C in a dark bottle. All reagents were used as received without any further purification. Milli-Q water with a resistivity of 18.2 MΩ cm at 25.0 °C was degassed and used in preparation of all the solutions (Merck Millipore, Italy).

A1.3.2 UV-Vis Spectroscopy

Optical measurements have been performed on a UV-visible spectrophotometer Evolution 201 from Thermo Scientific at 25.0 °C, by using quartz cells also for determination of hypochlorite concentration of stock solution, and on a microplate absorbance visible reader iMark™ from Bio-Rad at room temperature, by using 96-well polystyrene microplates. Acetic acid/sodium acetate 200.0 mM in presence of tetrasodium diphosphate 40.0 mM (Na4P2O7), referred to hereinafter as buffer 1, or disodium dihydrogen diphosphate 20.0 mM ($Na_2H_2P_2O_7$), referred to hereinafter as buffer 2, have been chosen to stabilize TMB solution around pH 4.5. Spectrophotometric measurements have been carried out by filling the quartz cuvette with 700 µL of TMB 42.3 x 10^{-6} M plus 700 µL of freshly prepared H_2O or tap-water samples containing chlorine in the range 0.25 – 5.00 mg L^{-1} with three replicas for each chlorine concentration. After the analysis of each chlorine concentration, the cuvette has been emptied and thoroughly washed. Analogously, microplates experiments have been performed adding 150 µL of freshly prepared H_2O or tap-water samples to each well containing chlorine in the range 0.25 – 5.00 mg L^{-1} with 4 replicas for each chlorine concentration. All the wells have been preloaded with 150 µL of TMB 42.3 x 10^{-6} M, which is equimolar to 3.00 mg L^{-1} of active chlorine for drinking water or swimming pool simulation. Finally, DPD1 chlorine test kit has been used following the manufacturer instructions. Data were analyzed with OriginLab Corporation software.

A1.4 Results and discussion

A1.4.1 Chlorine titration experiments

Titration curve of TMB with H2O2 (50 x 10^{-6} M at pH 5.0) in presence of horseradish peroxidase catalyst (HRP) has been elsewhere reported [15], showing that the blue charge-transfer complex formation and subsequent destruction is nearly symmetrical about the midpoint. The endpoint has been found to correspond to about equimolar peroxide and TMB, obtaining the full conversion to diimine and thus confirming a one-to-one stoichiometry for this catalyzed TMB/oxidant reaction. Analogously, here we follow spectrophotometrically all the stages of reaction in Fig. A1 exploiting the full potential of the catalyst-free TMB reaction with active chlorine by titration, in polystyrene plates or quartz cuvettes, in mild acidic buffer that controls chlorine speciation and TMB reactivity.

In detail, molecular chlorine (Cl_2) in mostly present at pH < 2, hypochlorous acid (HOCl) dominates the equilibrium at 4 < pH < 6, and hypochlorite (ClO^-) is predominant at pH > 8 [29,31]. Buffering the sample solutions in one of these pH ranges can limit the variability of results due to different reactivity of chlorine species. However, mild acidic buffer guarantees the best conditions to measure the chlorine content in real samples by tracking all the non-catalytic oxidation stages of TMB (Fig. A1). In fact, it has been demonstrated that a pH below 2 prevents the formation of the blue TMB charge-transfer complex formation (Fig. A1B) in favor of yellow TMB-diimine formation only (Fig. A1C). Analogously, it has been reported that the charge-transfer complex formation is significantly reduced at pH above 6. Therefore, we have performed experiments stabilizing TMB solution at pH 4.5 with diphosphate salts (see Materials and method), thus preventing interference from redox active ions like Fe(III) potentially present in water supply systems, as elsewhere demonstrated by extensive interference studies [21-24]. Differently from previously reported single-color intensity estimation with TMB (either yellow or blue) or DPD (magenta) [21-26,29], this method allows the naked-eye quantification of chlorine by multi-color changes of TMB

solution. This approach for the first time proposes TMB as a universal indicator for the selected range of chlorine concentrations, from a minimum blue level for an effective disinfection, through an optimal green level, up to the safe yellow guideline level corresponding to equimolar chlorine and TMB (see below).

A1.4.2 TMB reaction with active chlorine in H_2O and tap water

Fig. A2A shows preliminary experiments of color development for TMB test solution in buffer 1 (pH 4.5, see Materials and method) with chlorine samples in H_2O in quartz cuvettes. The main representative absorbances selected from UV-visible spectra at 25.0 °C have been acquired in a kinetic rate mode and reported in Fig. A2B. In detail, after 30 seconds of incubation necessary for sample preparation, three fixed wavelengths (280 nm, 450 nm and 655 nm) have been recorded every 10 s for a total accumulation time of 300 s. The solution of a fixed amount of TMB 42.3 x 10^{-6} M is initially transparent due to UV absorbance only of diamine (λ_{max} 280 nm, Fig. A1A) that decreases along with chlorine accumulation (Fig. A2C). Simultaneously, the solution develops a blue color of increasing intensity in the presence of chlorine from 0.25 mg L^{-1} to 1.00 mg L^{-1}. This visible band corresponds to the blue diamine/diimine charge-transfer complex (λ_{max} 655 nm, Fig. A1B). The titration curve at 655 nm shows the formation and subsequent disappearance of the blue product (Fig. 2C). Higher concentrations of chlorine lead to the appearance of green color, due to blue/yellow absorbance mixing. A yellow solution due to yellow diimine form of TMB (λ_{max} 450 nm, Fig. A1C) is obtained at higher chlorine concentration up to 3.00 mg L^{-1} of Cl_2. Finally, the solution becomes orange when chlorine reaches the 5.00 mg $L^{-}1$ (70.5 x 10^{-6} M), which is the guideline value that could lead to potential health effects from long-term exposure [3,4]. Data show a good reproducibility, obtaining a mean coefficient of variation of 4.72 % for absorbance values at 280 nm, 3.91 % at 450 nm, and 3.52 % at 655 nm over the entire range of chlorine concentrations after 0 seconds, for example (Table A1). All the reactions appear complete within 1

minute in agreement with previous observations of blue color development obtained in similar conditions but with a large excess of TMB [24]. The time evolution plots of main absorbance bands are reported in Fig. A2D showing quite stable colors at 25.0 °C. Similar results were obtained in buffer 2, however absorbance values appear less stable after 15 minutes (data not shown). The same experiments performed by using tap water for chlorine dilutions instead of H_2O have been reported in Fig. A3, showing a limited matrix effect (likely due to foreign ions) on colors appearance and intensity along chlorine titration with respect to H_2O alone, confirming the good reproducibility, obtaining, for example, a mean coefficient of variation of 3.18 % for absorbance values at 280 nm, 3.23 % at 450 nm, and 2.66 % at 655 nm after 0 seconds (Table A1). The complete dataset, for H_2O or tap water, in dependence of time, chlorine concentration, and λmax is available on request.

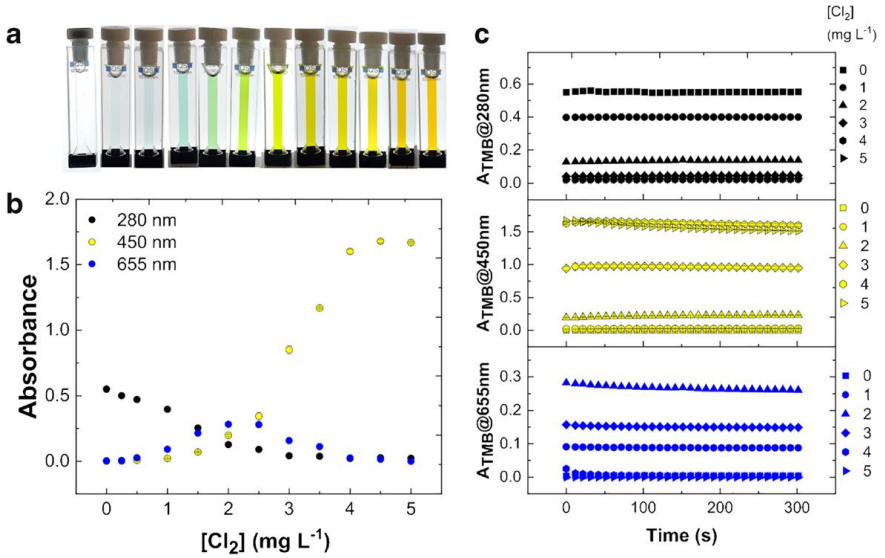

Fig. A2 Reaction of TMB solution in buffer 1 (pH 4.5) with active chlorine in H_2O at 25.0 °C. **a)** Color development for TMB oxidation by chlorine in quartz cuvettes. **b)** Absorbance at 280 nm, 450 nm and 655 nm. **c)** Time evolution plot for the TMB absorbance at different wavelengths after reaction with chlorine. The absorbances are reported as mean value of three replicates for each chlorine concentration

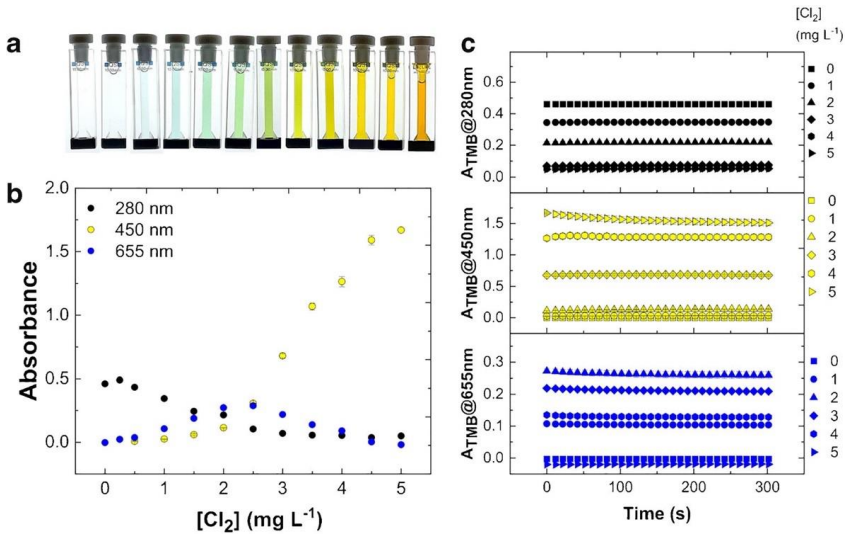

Fig. A3 Reaction of TMB solution in buffer 1 (pH 4.5) with active chlorine in tap water at 25.0 °C. **a)** Color development for TMB oxidation by chlorine in quartz cuvettes. **b)** Absorbance at 280 nm, 450 nm, and 655 nm. **c)** Time evolution plot for the TMB absorbance at different wavelengths after reaction with chlorine. The absorbances are reported as mean value of three replicates for each chlorine concentration

Table A1. Coefficient of variation (%CV) for Absorbance values *vs* [Cl_2] from Fig. 2A (H_2O) and 3A (Tap water)

Time 0 (s)	**Absorbance H_2O (%CV)**			**Absorbance in tap water (%CV)**		
[Cl_2] mg L^1	**280 nm**	**450 nm**	**655 nm**	**280 nm**	**450 nm**	**655 nm**
0.00	0.92	4.89	1.55	0.29	8.25	1.06
0.25	1.00	3.73	2.34	3.51	0.50	7.58
0.50	0.71	4.80	2.50	0.88	3.11	4.23
1.00	1.00	9.58	8.08	2.02	4.16	4.72
1.50	4.86	5.77	1.69	1.11	9.99	3.93
2.00	6.02	2.86	1.06	5.03	0.69	2.69
2.50	1.72	9.18	1.07	0.47	0.77	0.62
3.00	14.5	3.35	1.91	1.27	2.51	0.05
3.50	2.37	0.49	2.70	1.07	2.58	1.98
4.00	1.44	1.00	3.39	5.85	3.15	1.39
4.50	15.9	0.77	5.60	13.8	2.42	3.31
5.00	6.17	0.54	10.3	2.87	0.60	0.30
$\%CV_{mean}$	**4.72**	**3.91**	**3.52**	**3.18**	**3.23**	**2.66**

A1.4.3 Comparison of TMB method with a DPD1 chlorine test kit

96-well polystyrene microplates have been used for the optimization of the method, enabling the experimental procedure described for quartz cuvettes to be carried out on 96 samples simultaneously, with minor volume consumption and thus more replicates for each chlorine concentration. Furthermore, taking the advantage of distinct visible λ_{max} absorbances for TMB oxidation products by reaction with chlorine, we have used a filter-based plate reader instead of a spectrophotometer preliminarily used for greater flexibility due to wavelength scanning capability from UV to visible. In detail, DPD-containing tablets from a commercial test kit have been compared to TMB solution in buffer 1 here formulated for the naked-eye sensing of chlorine concentration in water samples. Figure A4A shows a polystyrene microplate containing Cl_2 in H_2O, including the range of concentrations recommended for drinking water treatment, about 0.25-3.00 mg L^{-1} [3,4], in presence of a fixed amount of DPD or TMB. DPD solutions have been prepared mimicking a swimming pool test, i.e., using one DPD tablet for 13 mL of water, which is the volume of the commercial test tube. Such chlorine solutions present a magenta color with intensity depending on chlorine content and here ideally representing the color reference scale for a chlorine sample test with DPD. However, it seems difficult to distinguish the analyte concentration solely by naked eye comparison of color intensities. On the contrary, the same chlorine solutions give different colors in presence of TMB, from light blue to bright yellow through green hues, depicting the color reference scale for a chlorine test with this TMB formulation, which allows an easier visual sensing and estimation of chlorine content, behaving like a universal indicator within the chosen range of chlorine concentration. The same results have been obtained by using tap water for chlorine dilutions (Fig. A4B). The representative absorbances of the main molecular species and colors are reported in Figs. A4C and A4D for H_2O and tap water solutions, respectively. As expected, the absorbances of TMB solution recorded at 450 nm (yellow) and 655 nm (blue) follow the trend observed in quartz cuvettes with optimal results in terms of reproducibility expressed as percent coefficient of variation (%CV in Table

A2). In particular, the titration curve at 655 nm shows the formation and subsequent disappearance of the blue product with a bell-shaped trend symmetrical about the midpoint corresponding to 0.50 mol chlorine/mol of TMB, i.e., 1.50 mg L^{-1} (Fig. A4C), as theoretically expected and previously shown for another oxidant system [15]. The yellow diimine absorbance (λ_{max} 450 nm) reaches the maximum when the oxidant concentration is equimolar with TMB, i.e., 3.00 mg L^{-1} of Cl_2 chosen as maximum safe concentration for active chlorine in water, whereas at same chlorine concentration the blue color contribution from charge-transfer complex returns to the minimum level and the green color disappears from the plate with it (Figs. A4A and A4B). Conversely, the absorbance of DPD solutions recorded at 555 nm (magenta) shows a monotone increase with chlorine concentration, as expected (Figs. A4C and A4D), also presenting a reproducibility worse than TMB (Table A2). Finally, in agreement with previous studies describing the better precision, sensitivity, and safety of TMB over the other reagents used for colorimetric analysis of chlorine [21,22], here we report a comparison at *t* 0 s of the proposed method based on TMB, and commercial method based on DPD. The analytical parameters have been obtained on three chlorine concentration ranges by using the piecewise linear fitting implemented in the Originlab software (Fig. A5). In detail, Table A3 show the best detection limit for the linear fitting of TMB blue color development (λ_{max} 655 nm) for lower chlorine concentrations (0.00-1.50 mg L^{-1}) in H_2O and tap water. Moreover, the sensitivity represented by the slope (m) of the calibration curve, and the reproducibility reported as %CVmean appear both superior for TMB (both at λ_{max} 655 nm and 450 nm) over DPD method, in H_2O and tap water, within the working range for chlorine determination (0.00-3.00 mg L^{-1}).

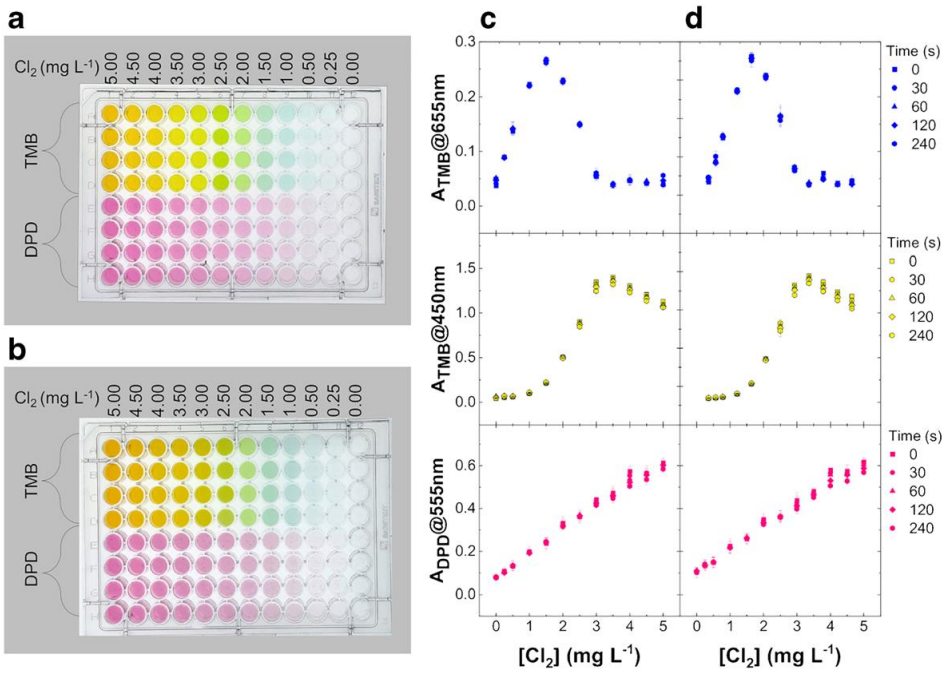

Fig. A4 TMB prepared in buffer1 versus DPD test kit for chlorine detection by microplate visible reader. Chlorine concentration ranges from 0.25 to 5.00 mg L^{-1} with four replicas for each chlorine solution in H2O **(a)** or tap water **(b)**. Each well of a 96-well polystyrene microplate contains 300 µL of sample solution with a final concentration of 1 tablet of DPD for 13 mL of water, as required by original commercial test, or TMB equimolar to 3.00 mg L^{-1} of Cl_2 in buffer. The absorbances at 450 nm and 655 nm (TMB), and 555 nm (DPD) for chlorine in H_2O **(c)** or tap water **(d)** are reported as mean value of four replicates for each chlorine concentration

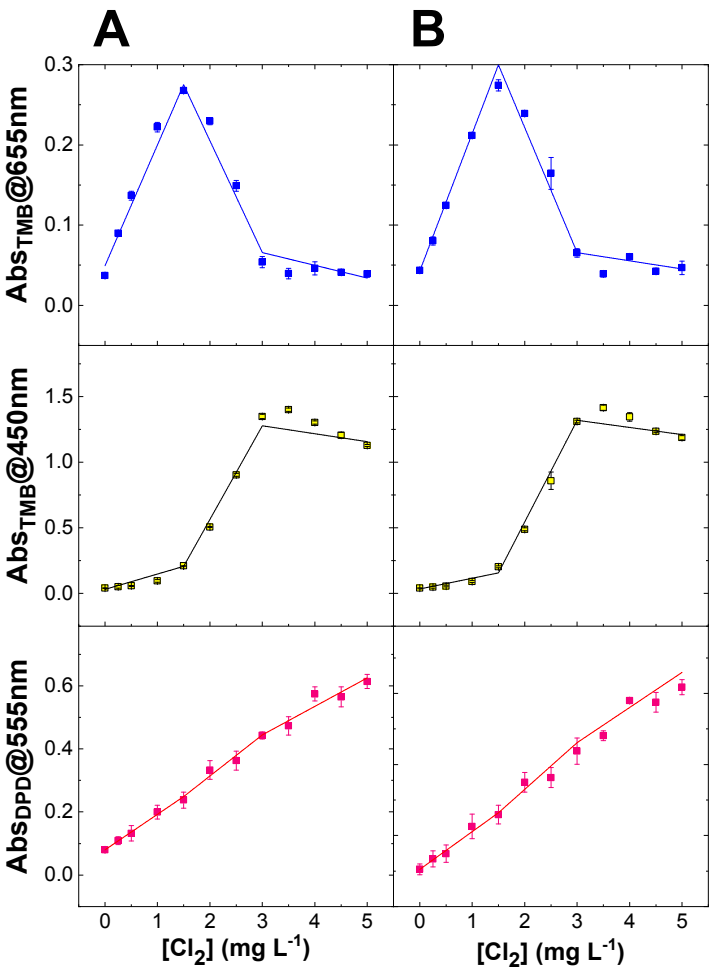

Fig. A5 Piecewise linear fitting for TMB and DPD titration experiments with chlorine in H_2O **(A)** and tap water **(B)** at *t* 0 s. Data and fitting parameters are reported in the main text in Figure A4 and Tables A3/A4, respectively. The chlorine concentration ranges are 0.00-1.50 mg L^{-1}, 1.50-3.00 mg L^{-1}, and 3.00-5.00 mg L^{-1}

Table A2 Coefficient of variation (%CV) for Absorbance values vs [Cl2] from Fig. A4c (H_2O) and Fig. A4d (tap water)

Time 0 (s)	**Absorbance H_2O (%CV)**			**Absorbance in tap water (%CV)**		
	DPD	**TMB**		**DPD**	**TMB**	
$[Cl_2]$ mg L^1	**555 nm**	**450 nm**	**655 nm**	**555 nm**	**450 nm**	**655 nm**
0.00	5.89	5.29	5.41	14.7	7.64	2.56
0.25	11.0	17.9	1.11	16.9	17.5	6.54
0.50	18.4	6.05	4.07	16.2	9.79	1.78
1.00	11.1	10.7	2.66	15.3	9.43	1.57
1.50	10.9	0.48	0.71	10.2	3.77	2.53
2.00	8.86	0.81	1.83	7.94	2.21	1.45
2.50	8.19	1.28	4.58	7.83	7.62	12.0
3.00	2.57	1.25	13.1	8.46	0.75	8.25
3.50	6.20	0.93	16.6	2.84	1.38	9.59
4.00	3.92	0.97	18.0	1.32	2.44	29.2
4.50	5.68	1.81	4.88	4.84	0.64	2.92
5.00	3.60	0.66	10.3	3.44	1.38	17.9
$\%CV_{mean}$	**8.03**	**4.01**	**6.94**	**9.16**	**5.38**	**8.02**

Table A3 Comparison of the proposed (TMB) and commercial (DPD) methods at *t* 0 s. The analytical parameters of the proposed method (TMB), at *t* 0 s, have been obtained on three chlorine concentration ranges by using the piecewise linear fitting implemented in the Originlab software (Fig. A5)

TMB					
		H_2O	Tap water	H_2O	Tap water
$[Cl_2]$ (mg L^{-1})	Analytical parameters	λ_{max} 450 nm (yellow)		λ_{max} 655 nm (blue)	
0.00-1.50	$Abs^0_{\lambda max}$	0.03 ± 0.02	0.03 ± 0.01	0.05 ± 0.01	0.04 ± 0.01
	$m\ (mg^{-1}L)$	0.12 ± 0.01	0.08 ± 0.02	0.15 ± 0.01	0.17 ± 0.01
	$\%CV_{mean}$ (n =4)	8.08	9.62	2.79	3.00
	LOD (mg L^{-1})	0.05	0.11	0.04	0.02
1.50-3.00	$Abs^0_{\lambda max}$	-0.87 ± 0.07	-1.01 ± 0.06	0.48 ± 0.02	0.53 ± 0.02
	$m\ (mg^{-1}L)$	0.71 ± 0.04	0.77 ± 0.03	-0.14 ± 0.01	-0.16 ± 0.01
	$\%CV_{mean}$ (n =4)	0.95	3.59	5.06	6.05
3.00-5.00	$Abs^0_{\lambda max}$	1.46 ± 0.19	1.48 ± 0.12	0.11 ± 0.05	0.10 ± 0.04
	$m\ (mg^{-1}L)$	-0.06 ± 0.05	-0.05 ± 0.03	-0.01 ± 0.01	-0.01 ± 0.01
	$\%CV_{mean}$ (n =4)	1.12	1.32	12.57	9.48
R^2		0.99	0.99	0.98	0.98

Table A4 The analytical parameters of the commercial method (DPD), at *t* 0s, have been obtained on three chlorine concentration ranges by using the piecewise linear fitting implemented in the Originlab software (Fig. A5)

DPD			
$[Cl_2]$ (mg L^{-1})	Analytical parameters	H_2O	Tap water
		λ_{max} 555 nm (magenta)	
0.00-1.50	$Abs^0_{\lambda max}$	0.08 ± 0.01	0.10± 0.02
	$m\ (mg^{-1}L)$	0.11 ± 0.01	0.11 ± 0.03
	$\%CV_{mean}$ (n =4)	11.47	14.64
	LOD (mg L^{-1})	0.13	0.42
1.50-3.00	$Abs^0_{\lambda max}$	0.05 ± 0.03	0.07 ± 0.07
	$m\ (mg^{-1}L)$	0.13 ± 0.01	0.13 ± 0.03
	$\%CV_{mean}$ (n =4)	7.63	8.60
3.00-5.00	$Abs^0_{\lambda max}$	0.17 ± 0.03	0.16 ± 0.09
	$m\ (mg^{-1}L)$	0.09 ± 0.01	0.10 ± 0.22
	$\%CV_{mean}$ (n =4)	4.40	4.18
R^2		1.00	0.98

A1.5 Conclusions

This work contributes to the field of the colorimetric determination of free chlorine in water by using TMB, which is the safer chromogenic substitute of benzidine in clinical chemistry assays, already shown to have a precision and sensitivity higher than other common colorimetric methods and offering the further advantage of hue modulation upon oxidation. The latter feature of TMB solutions have been exploited here for spectroscopic detection of chlorine in water, and even naked eye sensing appears possible through the recognition of typical color of each oxidation stage of TMB in diphosphate-

based buffer at pH 4.5, which is also able to mask potential redox active ions, e.g. Fe(III), commonly present in drinking water and swimming pools. The key novelty of this work lies in the appropriate setting of reaction conditions, showing for the first time that it is possible to finely tune the TMB colors change to cover exactly the range of chlorine concentration recommended by international health agencies for treatment of drinking water and swimming pools. The assay relies on the simple tuning of TMB final concentration to be equimolar to chlorine concentration value with limited potential health effects from long-term exposure. Therefore, obtaining a multi-colorimetric indicator of chlorine in water working between minimum value, to achieve an effective disinfection, and maximum health guideline value, to avoid irritations or discomfort. Consequently, the improvement of the current detection limit of chlorine concentration in water, well below guideline concentrations, is clearly out of the scope of this paper. In detail, TMB solutions produce a yellow color at the maximum safe concentration of chlorine, a green color at intermediate and recommended optimal chlorine values, and a blue color at the prescribed lower end concentration of chlorine in water. The method has been also successfully applied in tap water and appears superior to a commercial test kit for visual sensing and quantification of chlorine in swimming pools that are instead based on monochromatic chromophores like DPD. Finally, this analytical method could offer a practical tool to test home-made sanitizing solutions, and their "shelf life", necessarily prepared by serial dilution of household chlorine bleach during supply shortage for public health emergency events such as pandemic influenza, as we did here to prepare a stock solution from concentrated chlorine bleach bottle, pointing out the significance of this work in human healthcare. A different modulation of TMB assay for a direct measure of higher chlorine concentration will be the subject of future work.

References

1. Bruchet A, Duguet JP. Role of oxidants and disinfectants on the removal, masking and generation of tastes and odours. Water Sci Technol. 2004; https://doi.org/10.2166/wst.2004.0589
2. Deborde M, Von Gunten URS. Reactions of chlorine with inorganic and organic compounds during water treatment-kinetics and mechanisms: a critical review. Water Res. 2008; https://doi.org/10.1016/j.watres.2007.07.025
3. EPA, United States Environmental Protection Agency, Office of Ground Water and Drinking Water. National Primary Drinking Water Regulations https://www.epa.gov/ground-water-and-drinking-water/national-primary-drinking-water-regulations. Accessed 03 July 2020
4. WHO, World Health Organization. In: Guidelines for drinking-water quality. 4th ed. 2011. https://www.who.int/water_sanitation_health/publications/gdwq4-with-add1-chapters/en/. Accessed 03 July 2020
5. Nagy G, Nagy L. Halogens. In: Nollet LM, De Gelder LS, editors. Handbook of water analysis. CRC press; 2000. pp. 189-199
6. Rice EW, Baird RB, Eaton AD, editors. APHA, American Public Health Association Publisher, Standard Methods for the Examination of Water and Wastewater 23rd edition, Part 4500-Cl, Chlorine (Residual) 4-61-4-74. 2017
7. O'Riordan A, O'Sullivan B, Lovera P, Seymour I, Rohan J. Electrochemical Detection of Free-Chlorine in Water Samples Facilitated by In-Situ pH Control Using Interdigitated Microelectrodes. ChemRxiv. 2020; Preprint: https://doi.org/10.26434/chemrxiv.11898126.v1
8. Nandi S., Shyam B. A diamino functionalized metal-organic framework for fluorometric recognition of free chlorine in environmental water samples. Micropor Mesopor Mat. 2020; https://doi.org/10.1016/j.micromeso.2020.110116
9. Dou J, Shang J, Kang Q, Shen D. Field analysis free chlorine in water samples by a smartphone-based colorimetric device with improved sensitivity and accuracy. Microchem J. 2019; https://doi.org/10.1016/j.microc.2019.104200
10. Schwenke KU, Spiehl D, Krauße M et al. Analysis of free chlorine in aqueous solution at very low concentration with lateral flow tests. Sci Rep. 2019; https://doi.org/10.1038/s41598-019-53687-0

11. Holland VR., Saunders BC, Rose FL, Walpole AL. A safer substitute for benzidine in the detection of blood. Tetrahedron. 1974; https://doi.org/10.1016/S0040-4020(01)97504-0
12. Goda Y, Kobayashi A, Fujimoto S, Toyoda Y, Miyagawa KI, Ike M, Fujita M. Development of enzyme-linked immunosorbent assay for detection of alkylphenol polyethoxylates and their biodegradation products. Water Res. 2004; https://doi.org/10.1016/j.watres.2004.07.030
13. Hintemann T, Schneider C, Schöler HF, Schneider RJ. Field study using two immunoassays for the determination of estradiol and ethinylestradiol in the aquatic environment. Water Res. 2006; https://doi.org/10.1016/j.watres.2006.04.028
14. Wu L, Li G, Xu X, Zhu L, Huang R, Chen X. Application of nano-ELISA in food analysis: recent advances and challenges. Trends Anal Chem. 2019; https://doi.org/10.1016/j.trac.2019.02.002
15. Josephy PD, Eling T, Mason RP. The horseradish peroxidase-catalyzed oxidation of 3,5,3',5'-tetramethylbenzidine. Free radical and charge-transfer complex intermediates. J Biol Chem. 1982; 257: 3669-3675
16. Bally RA, Gribnau TCJ. Some aspects of the chromogen 3,3',5,5'-tetramethylbenzidine as hydrogen donor in a horseradish peroxidase assay. Clin Chem Lab Med. 1989; https://doi.org/10.1515/cclm.1989.27.10.791
17. Awano H, Ohigashi H. Absorption spectra of the cationic radical salt of 3,3',5,5'-tetramethylbenzidine in acetonitrile. Bull Chem Soc Jpn. 1990; https://doi.org/10.1246/bcsj.63.2101
18. Misono Y, Ohkata Y, Morikawa T, Itoh K. Resonance raman and absorption spectroscopic studies on the electrochemical oxidation processes of 3,3',5,5'-tetramethylbenzidine. J Electroanal Chem. 1997; https://doi.org/10.1016/S0022-0728(97)00305-7
19. Li B, Du Y, Li T, Dong S. Investigation of 3,3',5,5'-tetramethylbenzidine as colorimetric substrate for a peroxidatic DNAzyme. Anal Chim Acta. 2009; https://doi.org/10.1016/j.aca.2009.09.009
20. Drozd M, Pietrzak M, Parzuchowski PG, Malinowska E. Pitfalls and capabilities of various hydrogen donors in evaluation of peroxidase-like activity of gold nanoparticles. Anal Bioanal Chem. 2016; https://doi.org/10.1007/s00216-016-9976-z

21. Serrat FB. Colorimetric method for determination of chlorine with 3,3′,5,5′-tetramethylbenzidine. Talanta. 1994; https://doi.org/10.1016/0039-9140(94)00184-7
22. Serrat FB, Morell GB, Polo DR. Comparison of methods and kits for colorimetric determination of residual chlorine in water. J. AOAC Int. 1997; 80: 1117–1121.
23. Mesquita RB, Noronha MLF, Pereira AI, Santos AC, Torres AF, Cerdà V, Rangel AO. Use of tetramethylbenzidine for the spectrophotometric sequential injection determination of free chlorine in waters. Talanta. 2007; https://doi.org/10.1016/j.talanta.2007.01.010
24. Guo Y, Ma Q, Cao F, Zhao Q, Ji X. Colorimetric detection of hypochlorite in tap water based on the oxidation of 3,3′,5,5′-tetramethyl benzidine. Anal Methods. 2015; https://doi.org/10.1039/c5ay00735f
25. Zhang J, Yang X. A simple yet effective chromogenic reagent for the rapid estimation of bromate and hypochlorite in drinking water. Analyst. 2013; https://doi.org/10.1039/c2an36287b
26. Yamaoka H, Nakayama-Imaohji H., Horiuchi I, Yamasaki H, Nagao T, Fujita Y, Maeda H, Goda H, Kuwahara T. Tetramethylbenzidine method for monitoring the free available chlorine and microbicidal activity of chlorite-based sanitizers under organic-matter-rich environments. Lett Appl Microbiol. 2016; https://doi.org/10.1111/lam.12506
27. Andrews PC, Krinsky NI. Quantitative determination of myeloperoxidase using tetramethylbenzidine as substrate. Anal Biochem. 1982; https://doi.org/10.1016/0003-2697(82)90185-3
28. Freitas M, Lima JL, Fernandes E. Optical probes for detection and quantification of neutrophils' oxidative burst. A review. Anal Chim Acta. 2009; https://doi.org/10.1016/j.aca.2009.06.063
29. Kettle AJ, Albrett AM, Chapman AL, Dickerhof N, Forbes LV, Khalilova I, Turner R. Measuring chlorine bleach in biology and medicine. Biochim Biophys Acta. 2014; https://doi.org/10.1016/j.bbagen.2013.07.004
30. Palladino P, Torrini F, Scarano S, Minunni M. Colorimetric analysis of the early oxidation of dopamine by hypochlorous acid as preliminary screening tool for chemical determinants of neuronal oxidative stress. J Pharmaceut Biomed Anal. 2020; https://doi.org/10.1016/j.jpba.2019.113016

31. Feng Y, Smith DW, Bolton JR. Photolysis of aqueous free chlorine species (HOCl and OCl) with 254 nm ultraviolet light. J Environ Eng Sci. 2007; https://doi.org/10.1139/s06-052

Appendix 2

Colorimetric selective quantification of anthocyanins with catechol/pyrogallol moiety in edible plants upon zinc complexation

Francesca Torrini, Lapo Renai, Simona Scarano, Massimo Del Bubba, Pasquale Palladino*, Maria Minunni

Department of Chemistry 'Ugo Schiff', University of Florence, Via della Lastruccia 3-13, 50019 Sesto Fiorentino, Italy

*Corresponding author: pasquale.palladino@unifi.it

A2.1 Abstract

Here is examined the colour development from common anthocyanins (i.e., cyanidin, delphinidin, malvidin, and pelargonidin glycosides) and from anthocyanins-rich extracts (i.e., bilberries, strawberries, and raspberries), using zinc-anthocyanin complexes as molecular probe. We have observed the absorbance increase in the blue region in presence of large excess of zinc ion at acidic pH for cyanidin and delphinidin derivatives, likely due to quinoidal base stabilization from catechol and pyrogallol moiety. The assay conditions were studied and applied to natural extracts containing these compounds. The same behavior was observed for bilberry and, to a minor extent, for raspberry extracts, due to the larger cyanidin/delphinidin contents in the former than in the latter. Anthocyanin standard UV–Vis analysis in buffer has shown a very good linear correlation for cyanidin and delphinidin (R^2 = 0.995 and 0.997, respectively), good precision (CV% = 7.4% and 5.3% respectively), high sensitivity (Cyε_{600nm} = 8300 M^{-1} cm^{-1}, LOD = 0.264 ± 0.005 mg L^{-1}, LOQ = 0.478 ± 0.007 mg L^{-1}, and Dpε_{600nm} = 15,900 M^{-1} cm^{-1}, LOD = 0.143 ± 0.002 mg L^{-1}, LOQ = 0.478 ± 0.007 mg L^{-1}). The effectiveness of this colorimetric method for the selective quantification of catechol/pyrogallol-based anthocyanins has been demonstrated in the aforementioned complex real matrices and compared to LC-MS/MS analysis

and pH- differential method, offering a valuable tool to characterize plant and food extracts particularly rich in zinc- coordinating anthocyanins.

Graphical abstract

A2.2 Introduction

Anthocyanins (ACs) are water-soluble plant pigments well-known for their antioxidant properties and largely used to colour foods and beverages. Hundreds of ACs have been isolated, according to the kind of glycosylation (with hexose and/or pentose) and/or hydroxyl/methoxy substitution of the three aromatic rings of the shared flavylium chromophore (Fig. A1) [1–3]. ACs with *ortho* hydroxyl substitutions in the B ring, such as cyanidin- (Cy), delphinidin- (Dp), and petunidin- (Pt)-derivatives, can coordinate metal cations. Other ACs such as pelargonidin- (Pg), peonidin- (Pn), or malvidin- (Mv)-derivatives have only a single hydroxyl group in the B ring with much weaker metal-chelating properties. The structure of ACs strictly depends on pH. Briefly, the flavylium cation (red colour), which predominates at pH < 2, is prone to water addition at pH range approximately from 3 to 6, leading to neutral carbinol/chalcone pseudobase (colourless).

Moreover, pH ≥ 8 favors the formation of the anionic quinoidal base (blue colour), which is stabilized by metal cations (M^{n+}) coordination [1,4–6]. Accordingly, together with liquid chromatography [7,8] and electrochemistry [9], a common analytical approach for the determination of total ACs

concentration (TAC) is the pH-differential colorimetric method [10,11], which is based on the different absorbance (A) of AC-rich extracts at pH 1.0 (red color) and pH 4.5 (colorless), according to equation (1). Therefore, the concentration of ACs is calculated considering the molar absorptivity of the most abundant anthocyanin in the sample [1,10,11].

$$A = (A_{\lambda max} - A_{700nm})_{pH1.0} - (A_{\lambda max} - A_{700nm})_{pH4.5} \quad (1)$$

In this framework, the metal-binding ability of ACs has been exploited for colorimetric determination of several metal cations, mainly by using cyanidin as chromophore [1,12], and for color development for food applications [5,13-15]. These methods are based on the bathochromic shift of the maximum absorption wavelength in the visible spectrum and the increase of absorbance, due to decrease of the electron transition energy in ACs π-conjugated system upon metal coordination. At the best of our knowledge, there are very few reports on quantitative determination of ACs by using a metal-complex as probe and UV–Vis spectroscopy as analytical tool [16,17]. In these studies, the ACs determination is based on the stable blue color expression of catechol/pyrogallol systems in presence of hundreds-fold excess of Al^{3+} at acidic pH [13], where the large excess of metal ion is necessary due to pH-dependent competition with H^+ for the binding site of ACs [14]. Following this approach, Bernal et al. developed a method for the spectrophotometric determination of Cy-3-glucoside in edible plants, through the formation of purple-colored solutions. This method is very sensitive, achieving a LOD = 0.186 mg L^{-1} for Cy-3-glucoside, but not truly selective, *i.e.,* it cannot easily/visually discriminate anthocyanins bringing different hydroxyl/methoxy substitution of B-ring, because any AC gives intense color in presence of Al^{3+} with comparable molar extinction coefficients, although with distinct λ_{max} [16].

Based on these considerations, this study has been devoted to develop a colorimetric method for more selective determination of catechol/pyrogallol content in fruits, i.e., for quantification of ACs with ortho hydroxyl

substitutions in the B ring by using a similar strategy of neutral/anionic quinoidal base stabilization, but using for the first time AC-Zn^{2+} complex as molecular probe [13,14,17]. The color development has been preliminarily investigated for some anthocyanin standards, with or without ortho hydroxyl substitutions, in presence of large excess of Zn^{2+}, in analogy to Al^{3+} studies [13,14], by means of UV–Vis spectroscopy. Subsequently, the same procedure has been applied to fruit extracts, namely, common bilberries (*Vaccinium myrtillus*), strawberries (*Fragaria* × *ananassa Duch*.), raspberries (*Rubus idaeus*), and persimmon (*Diospyros kaki*), to prove the effectiveness of such method also in complex real matrices in comparison with the TAC determined by the pH-differential colorimetric method and liquid chromatography-tandem mass spectrometry (LC-MS/MS) analysis. Accordingly, the colorimetric assay here developed appears a valuable tool to further discriminate and study catechol/pyrogallol-rich plants and foods, complementarily to conventional colorimetric and chromatographic methodologies, with potential industrial applicability.

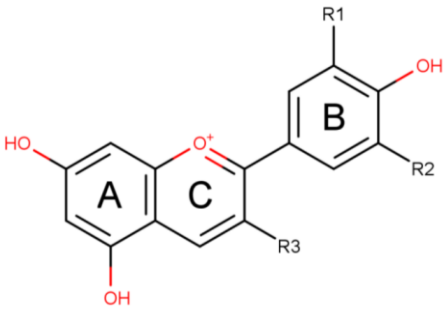

	R1	R2	R3
Cyanidin	OH	H	OH
Cy-3-Glycoside	OH	H	*O*-Glycoside
Delphinidin	OH	OH	OH
Dp-3-Glycoside	OH	OH	*O*-Glycoside
Malvidin	OCH_3	OCH_3	OH
Mv-3-Glycoside	OCH_3	OCH_3	*O*-Glycoside
Pelargonidin	H	H	OH
Pg-3-Glycoside	H	H	*O*-Glycoside

Fig. A1 Chemical structure of some anthocyanidins (R3 = OH), and corresponding anthocyanins (R3 = *O*-Glycoside) here investigated

A2.3 Experimental section

A2.3.1 Materials and chemicals

The anthocyanins standards have been purchased from Extrasynthese (Genay, France). Zinc acetate dihydrate 99+%, methanol anhydrous 99.8%, sodium fluoride has been obtained from Sigma-Aldrich (St. Louis, MO, USA). All chemicals have been used as received without any further purification. Ultrapure water (resistivity of 18.2 MΩ cm at 25.0 °C) filtered by using vacuum filter cups, 0.22 μm pore size, has been used for the preparation of all solutions (Merck Millipore, Italy).

A2.3.2 Sample origin and extraction

Bilberries (*Vaccinium myrtillus*) were collected in Tuscan Apennines, whereas strawberries (*Fragaria* × *ananassa* Duch. cv. Camarosa), raspberries (*Rubus idaeus* cv. Tulameen), and persimmons (Diospyros Kaki kaki cv. Farmacista honoratiHonorati), were purchased in a local supermarket.

Fruit samples were frozen in liquid nitrogen and subsequently freeze-dried until constant weight, and finally grinded to obtain a homogeneous powder. The samples were finally stored at 20 ◦C until analyses were performed. The extraction was performed on each type of fruit sample according to the procedure reported by Ancillotti et al. [18]. Briefly, three independent aliquots (500 mg dry weight, d.w.) of each freeze-dried sample were extracted for 15 min with a methanol/water solution 80/20 (v/v), in ice bath under magnetic stirring, containing 10 mM NaF to inactivate polyphenol oxidase. Then, samples were centrifuged at 8000×g for 10 min and the supernatant recovered. This method was tested by a recovery evaluation procedure on three sequential extractions of each independent aliquots of each fruit sample, applying the total monomeric anthocyanin assay (TMA) with the pH differential method described by Ancillotti et al. [18], and using reference standards as follows: cyanidin-3-glucoside for bilberries, pelargonidin-3-glucoside for strawberries, and cyanidin-3-O-sophoroside for raspberries. TMA was performed in each sequential extract, and the results

showed that the third extraction, in comparison with the first two steps, provided a recovery in the ranges of 3.4–4.9% for bilberry samples, 3.1–4.5% for strawberry samples, and 3.0–5.8% for raspberry samples [18,19]. Accordingly, the first two sequential extractions were combined for spectrophotometric and LC-MS/MS analyses.

A2.3.3 UV-Vis optical measurements

Stock solutions of each anthocyanin standard have been prepared in methanol/water 80/20 (v/v) at 100 mg L^{-1}. Freeze-dried fruits aliquots (500 mg dry weight, d.w.) have been sequentially extracted two-times with methanol/water (including 10 mM NaF) solution 80/20 (v/v) in ice bath under magnetic stirring.

Optical measurements have been carried out in quartz cuvettes at 25.0 °C by using Evolution™ 201 UV–visible spectrophotometer (Thermo Scientific) by properly diluting and mixing anthocyanins and fruit extracts with zinc or sodium acetate 200 mM (pH 5.5) in methanol/ water 80/20 (v/v), according to new methodology here presented, or with KCl 25 mM (pH 1.0) or sodium acetate 400 mM (pH 4.5), according to conventional pH-differential protocol. The absorbance has been measured in the range 250–800 nm, against a negative control prepared in the same manner reported above, without the addition of anthocyanins reference standards or fruit extracts. Further measurements have been carried out in disposable polystyrene 96-well micro-test plates (Sarstedt, Milan, Italy) by using iMark™ microplate visible absorbance reader with optical filters (Bio-Rad, Milan, Italy), with 595 nm representing the best available filter for the blue colour (λ_{max} 600 nm) from Dp-3-glucoside (*vide infra*).

A2.3.4 Liquid chromatography-tandem mass spectrometry analysis

Samples were filtered at 0.2 μm with nylon membranes before chromatographic analysis, and bilberry extracts were diluted 1:1000 with ultrapure water to avoid system saturation. The LC apparatus consisted of a low-pressure gradient quaternary pump Nexera X2 LC- 30AD, a CTO/20AC

thermostatted column compartment, a SIL-30AC autosampler, a DGU-20A 5R degassing unit and a CBM-20A module controller (Shimadzu, Kyoto, Japan). The LC system was coupled with a 5500 QTrap™ mass spectrometer (Sciex, Ontario, Canada) by a Turbo VTM interface equipped with an ESI probe. Chromatograms were elaborated by the Sciex Analyst software (release 1.6.2). The chromatographic separation was performed on a Phenomenex (Torrance, USA) Kinetex XB-C18 column (150 × 2.1 mm i.d., particle size 2.6 µm) equipped with a guard column containing the same stationary phase. Chromatographic analysis was performed at 50 °C with water/formic acid 95/5 (v/v%) (eluent A) and methanol/formic acid 95/5 (v/v%) (eluent B), according to the following gradient: 0.1–10 min linear gradient 7–17% B, 10–20 min linear gradient 17–22% B, 20–22 min liner gradient up to 95% B 22–27 min isocratic 95% B. The flow rate was 0.3 mL min^{-1} and the injection volume was 5 µL for all standard solutions and samples. Targeted MS/MS analysis was carried out using the Multiple Reaction Monitoring mode (MRM) in positive ionization mode. Source dependent parameters were optimized in flow injection analysis at optimal LC flow and mobile phase composition, and were as follows: curtain gas 30, CAD gas medium, temperature 600 °C, gas 1 40, gas 2 65, interface heater on and ion spray voltage 5500 V. For each investigated compound, the most intense transition was used for quantification and the second most intense for confirming identification (Decision 2002/ 657/CE). Compound dependent parameters were optimized by direct infusion of properly diluted target analyte standard solutions (see Table A1). The principal figures of merit of the LC-MS/MS method are shown in Table A2.

Table A1 Optimized MS parameters for the investigated polyphenols. Numbers 1 and 2/3 refer to quantifier and qualifier transitions, respectively. (Q1) Precursor ion (m/z); (Q3) product ion (m/z); (DP) declustering potential (V); (EP) entrance potential (V); (CE) collision energy (V); (CXP) collision exit potential (V)

Compound	Q1	Q3	DP	EP	CE	CXP
Cyanidin-3-*O*-glucoside 1	449	287	120	10	40	20
Cyanidin-3-*O*-glucoside 2	449	137	120	10	75	12
Cyanidin-3-*O*-glucoside 3	449	213	120	10	75	20
Cyanidin-3-*O*-sophoroside 1	611	287	110	10	45	15
Cyanidin-3-*O*-sophoroside 2	611	449	110	10	70	20
Pelargonidin-3-*O*-glucoside 1	433	271	100	10	35	20
Pelargonidin-3-*O*-glucoside 2	433	121	100	10	80	15
Pelargonidin-3-*O*-rutinoside 1	579	271	100	10	35	20
Pelargonidin-3-*O*-rutinoside 2	579	121	100	10	80	15
Delphinidin-3-*O*-glucoside 1	465	303	100	10	40	25
Delphinidin-3-*O*-glucoside 2	465	229	100	10	70	25
Malvidin-3-*O*-glucoside 1	493	331	100	10	35	25
Malvidin-3-*O*-glucoside 2	493	315	100	10	65	15

Table A2 Figures of merit of the LC-MS/MS analytical method adopted in this study. Instrumental detection limits (IDLs), linearity ranges, and correlation coefficients (R^2)

	IDL (μg L^{-1})	**[1]Linearity Range (μg L^{-1})**	**R^2**
Cyanidin-3-*O*-glucoside	0.02	0.06-2000	0.997
Cyanidin-3-O-sophoroside	0.005	0.02-2000	0.999
Pelargonidin-3-O-glucoside	0.01	0.05-2000	0.999
Pelargonidin-3-*O*-rutinoside	0.01	0.05-2000	0.998
Delphinidin-3-*O*-glucoside	0.1	0.3-2000	0.992
Malvidin-3-*O*-glucoside	0.02	0.1-2000	0.999

[1]The bottom limit of the linearity range represents the Instrumental Quantitation Limit.

A2.4 Results and discussion

A2.4.1 Method development

We have recently noticed the influence of several cations in solution at high millimolar range on the oxidation, polymerization, and color development of naturally occurring catecholamines due to the well- known metal coordination capability of catechol moiety [20]. Inspired by this observation, we have applied the same conditions also for solutions of some anthocyanins that contain an analogous functional group (Fig. A1); in particular it has been preliminary observed, on 96-well polystyrene microplates spectrophotometrically analyzed by filter-based plate reader, that large excess of zinc ion at slightly acidic pH was able to induce color development from Cy-3-glucoside and Dp-3-glucoside solutions, whereas Mv-3-glucoside, and Pg-3-glucoside solutions remained essentially uncolored as in absence of zinc acetate (Fig. A2).

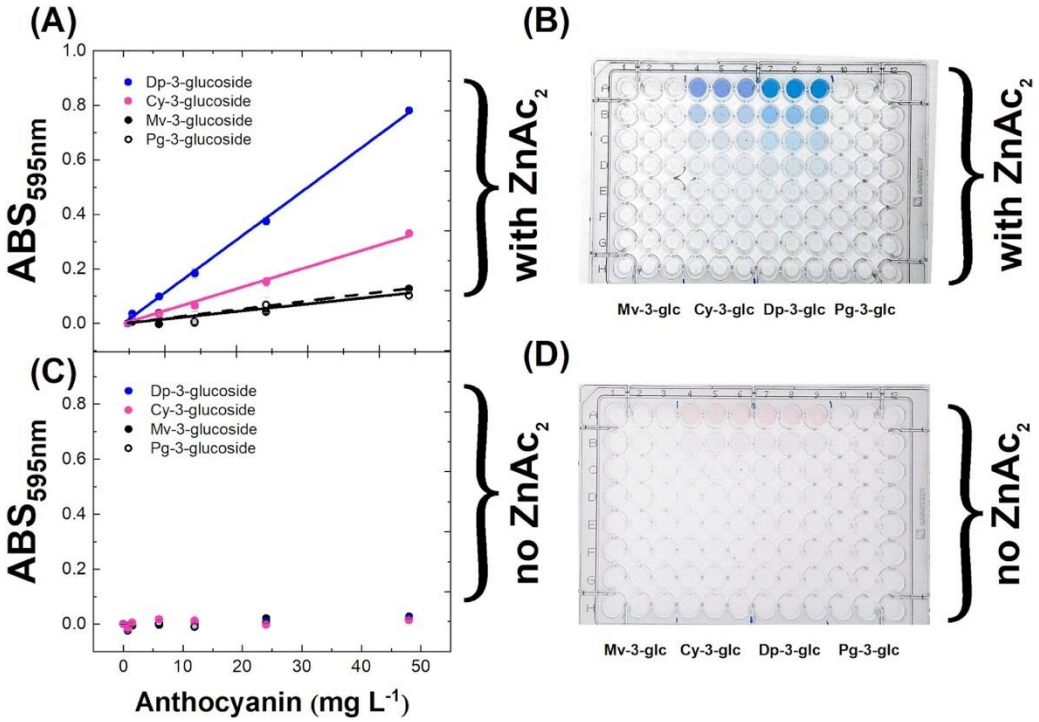

Fig. A2 Absorbance at 595 nm by filter-based plate reader for anthocyanins Dp-3-glucoside (blue circles), Cy-3-glucoside (pink circles), Mv-3-glucoside (black circles), and Pg-3-glucoside (white circles) solutions up to 50 mg L^{-1} at pH 6.4 with (A and B) and without (C and D) zinc acetate 150 mM at 25 °C in MeOH/H_2O 80/ 20 (v/v). (For interpretation of the references to color in this figure legend, the reader is referred to the Web version of this article.)

Such encouraging results were the basis of the successive method development. First, several anthocyanin standards were tested to evaluate the relative colorimetric test response; Further, fruit extracts at different qualitative-quantitative ACs content were analyzed. In detail, this raw method was preliminarily applied to anthocyanins-rich (bilberry and strawberry) and anthocyanin-free (persimmon) fruit extracts, obtaining a bright blue color from bilberry only (Fig. A3).

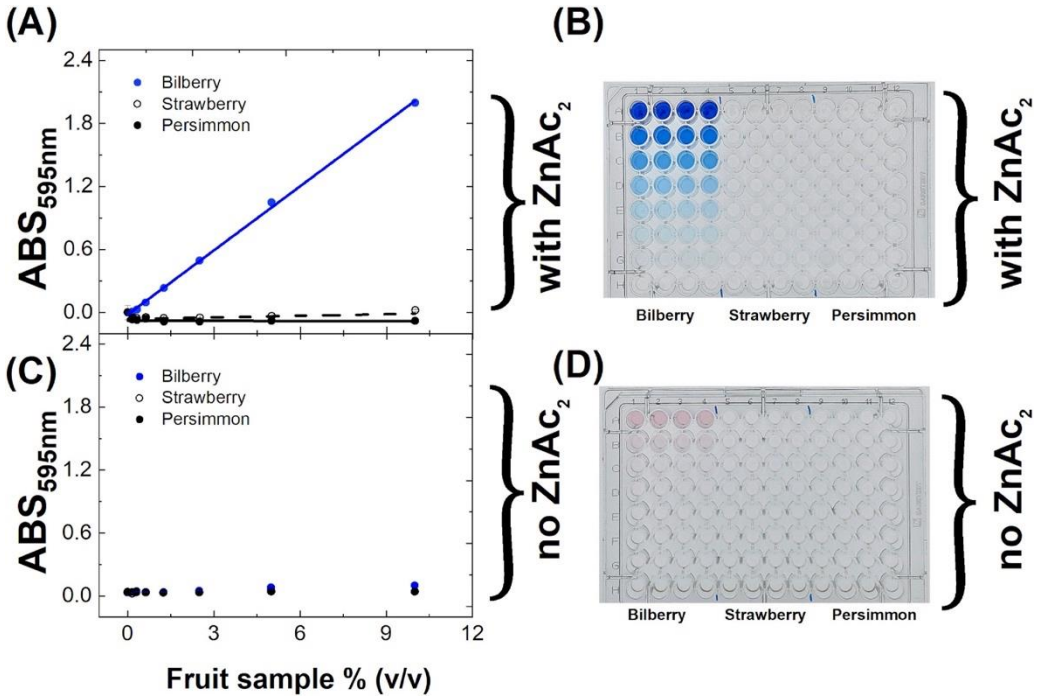

Fig. A3 Absorbance at 595 nm from filter-based plate reader for bilberry (blue circles), strawberry (white circles), and persimmon (black circles) fruit extracts diluted in MeOH/H_2O 80/20 (v/v) with (A and B) and without (C and D) zinc acetate 150 mM at 25 °C and pH 6.4. (For interpretation of the references to color in this figure legend, the reader is referred to the Web version of this article.)

Moreover, although other cations were tested (Mg^{2+}, Ca^{2+}, and Ba^{2+}), the blue color was obtained in presence of zinc ions only (Fig. 4A and B), being stable over 1 h (Fig. 4C). Furthermore, it was observed a red and hyperchromic shift increasing the methanol content from zero to 80% in the solvent (Fig. A4D).

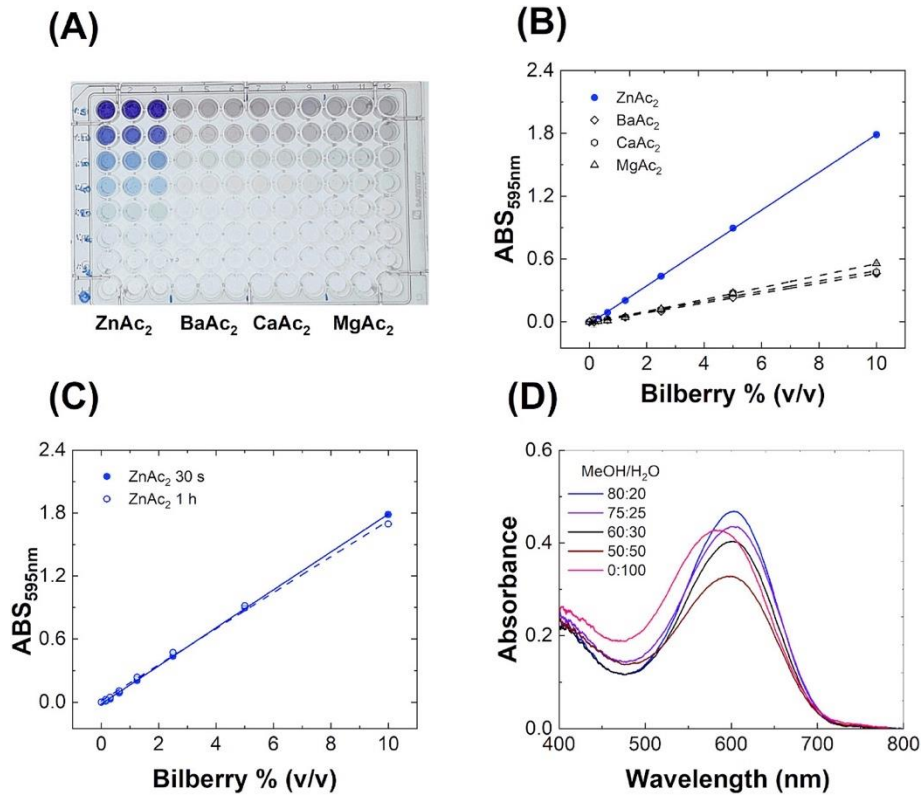

Fig. A4 Optical measurements of bilberry extract and blue colour development depending on solution composition at 25 °C. (A) Bilberry solutions on 96- well polystyrene microplate, and (B) their absorbance at 595 nm, in presence of (from left to right) 150 mM zinc acetate (blue circles), barium acetate (white squares), calcium acetate (white circles), or magnesium acetate (white triangles) in MeOH/H_2O 80/20 (v/v) at pH 6.4. (C) Bilberry solutions absorbance at 595 nm in 150 mM zinc acetate in MeOH/ H_2O 80/20 (v/v) at pH 6.4 after 30 s (blue circles) or 1 h (white circles). (D) Methanol-dependent visible spectrum of bilberry solutions in 150 mM zinc acetate in MeOH/H_2O from 0/100 (pink line) to 80/20 (blue line) (v/v) at pH 6.4. (For interpretation of the references to color in this figure legend, the reader is referred to the Web version of this article.)

Finally, the influence of pH and zinc acetate concentration was verified (Fig. A5), finding that the best condition for larger absorbance and good linearity was achieved by using 100 mM $ZnAc_2$ and pH 5.5. However, it is worth noting that even at pH 4.3, which is close to the reference value of the pH-differential method corresponding to the colorless pseudobase form of anthocyanin, the presence of zinc gives rise to blue/purple colors of bilberry solutions.

Overall, these results indicate zinc acetate 100 mM at pH 5.5 in MeOH/H_2O 80/20 (v/v) as the best colorimetric assay condition for anthocyanin analysis as detailed in the following paragraphs. Thus pH 5.5 was further used in the experiments.

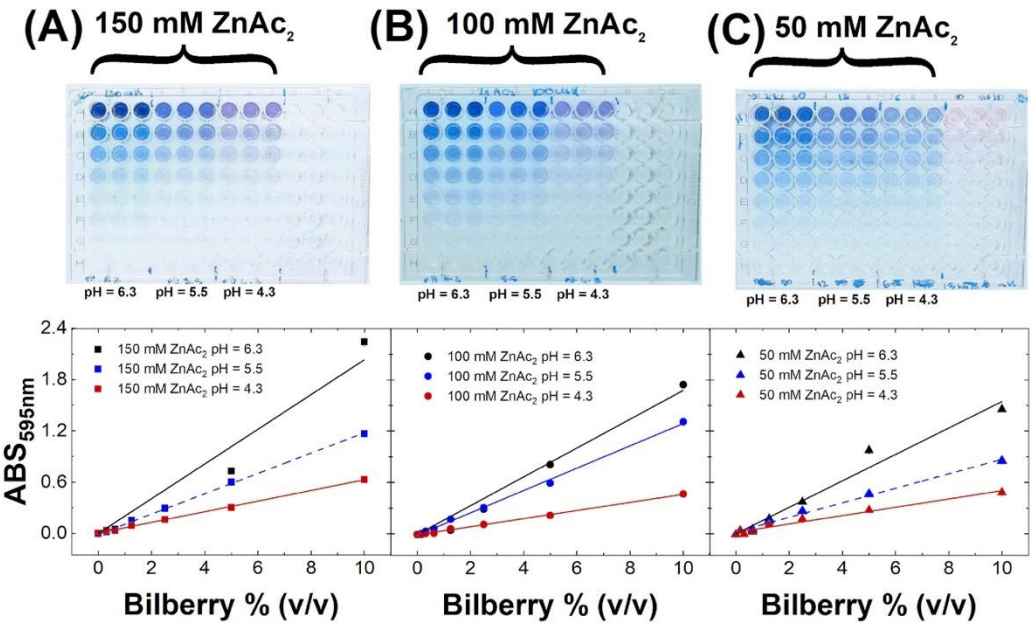

Fig. A5 Optical measurements at 595 nm on filter-based plate reader of bilberry extract at 25 °C in MeOH/H_2O 80/20 (v/v) in dependence of zinc acetate concentration. (Upper panels) 96-well microplates containing 150 mM (A), 100 mM (B), and 50 mM (C) $ZnAc_2$ at pH 6.3, 5.5, or 4.3 (from left to right). (Lower panels) Absorbance at 595 nm for bilberry solutions in $ZnAc_2$ 150 mM (squares), 100 mM (circles), or 50 mM (triangles), and pH 6.3 (black), 5.5 (blue), or 4.3 (red). (For interpretation of the references to color in this figure legend, the reader is referred to the Web version of this article.)

A2.4.2 Anthocyanin color development in presence of zinc acetate

Although several metal ions and metalloids have been found to induce color expression for ACs [13,21–24], to the best of our knowledge this is the first paper exploiting the effect of Zn^{2+} on color development of ACs by metal chelation of the anionic form to develop an analytical method [13,14,17,25–30].

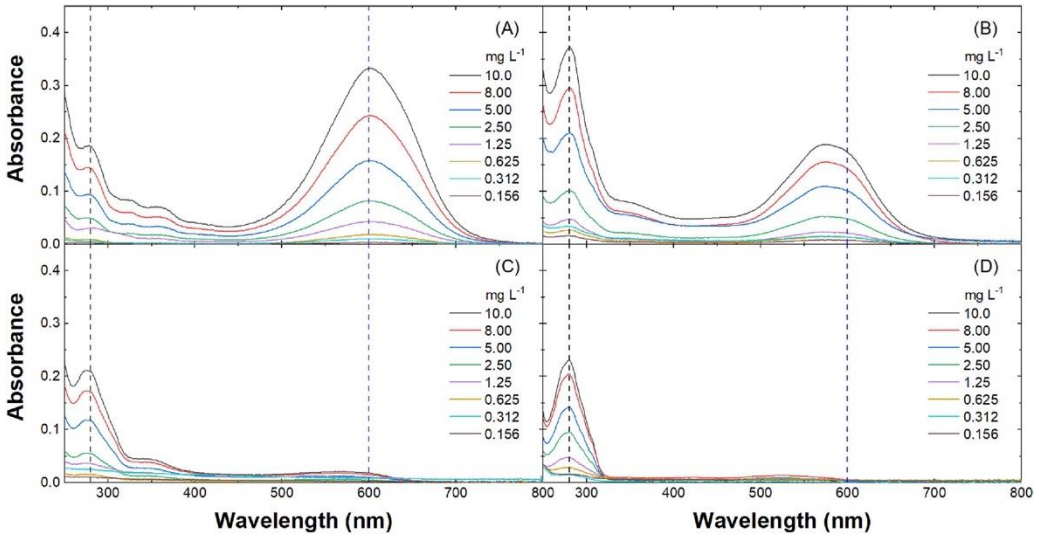

Fig. A6 UV–Vis spectra of anthocyanins Dp-3-glucoside (A), Cy-3-glucoside (B), Mv-3-glucoside (C), and Pg-3-glucoside (D) up to 10 mg L^{-1} in presence of zinc acetate 100 mM at pH 5.5 at 25 °C in MeOH/H_2O 80/20 (v/v). Black and blue reference lines indicate absorbance at 280 nm and 600 nm, respectively. All measurements have been performed in triplicate. (For interpretation of the references to color in this figure legend, the reader is referred to the Web version of this article.)

In detail, Fig. A6 shows the UV–Vis spectra of anthocyanins Cy-3-glucoside, Dp-3-glucoside, Mv-3-glucoside, and Pg-3-glucoside up to 10 mg L^{-1} in presence of zinc acetate 100 mM at pH 5.5 at 25.0 °C in MeOH/H2O 80/20 (v/v). The hyperchromic shift in the visible region is only induced on AC bearing catechol (Cy-) or pyrogallol (Dp-) moieties on the B ring (Fig. A1), because Zn^{2+} complexation and hydrogen ions displacement, strictly pH-dependent [14], lead to the formation of colored quinoidal bases conferring purple color to Cy-3-glucoside solutions (λ_{max} 575 nm) and more intense blue color to Dp-3-glucoside ones (λ_{max} 600 nm). Conversely, Mv-3-glucoside and Pg-3-glucoside solutions remain essentially uncolored, thus evidencing a strong selectivity of the proposed method for catechol/pyrogallol ACs. This behavior is different from that elsewhere reported for Al^{3+}, which shows the largest absorbance for Cy-glycosides at λ_{max} = 575 nm and equal absorbance for Dp-and Mv-glycosides under the same experimental conditions [16],

indicating the occurrence of Al^{3+}-coordination also by ortho-dioxygenated B-ring (Fig. A1). Accordingly, this novel analytical method based on zinc ions can be applied to further discriminate anthocyanins differing in the number and position of hydroxyl groups, which is relevant for fruits and/or vegetables with different ACs composition.

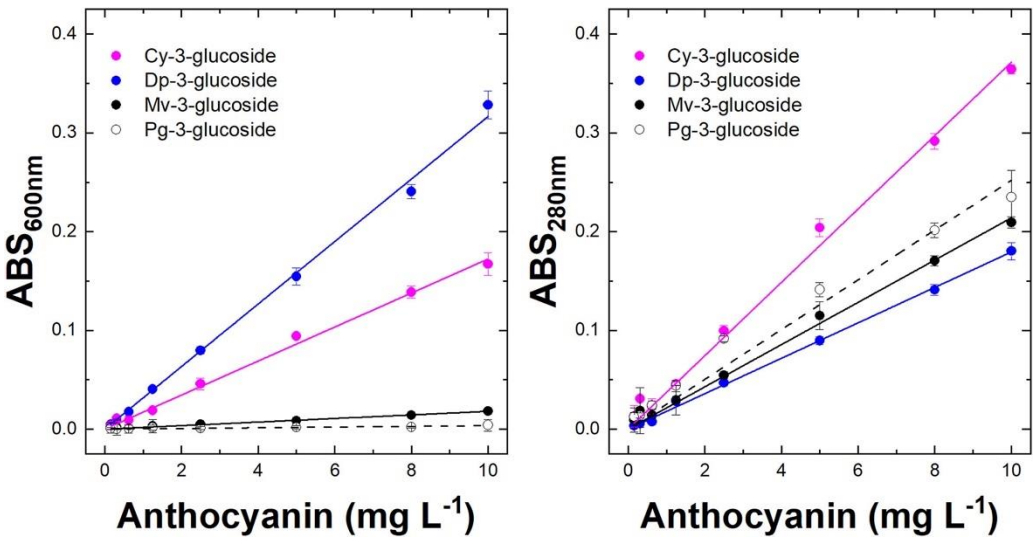

Fig. A7 Calibration curves of anthocyanins Cy-3-glucoside (blue circles), Dp-3-glucoside (pink circles), Mv-3-glucoside (black circles), and Pg-3-glucoside (white circles) up to 10 mgL^{-1} in presence of 100 mM zinc acetate at pH 5.5 at 25°C in MeOH/H_2O 80/20(v/v) by using absorbance values at 600 nm (left panel) and 280 nm (right panel) from UV–Vis spectra in Fig. A6. All measurements have been performed in triplicate. (For interpretation of the references to color in this figure legend, the reader is referred to the Web version of this article.)

Fig. A7 shows the calibration curves for each anthocyanin standard here analyzed in presence of zinc ion, by using the absorbance values from Fig. A6 as a function of ACs concentration. In particular, the absorbance at 600 nm is strictly dependent on catechol/pyrogallol content, whereas the absorbance at 280 nm is indicative, in this case, of the total anthocyanin content. The analytical parameters for Cy-3-glucoside and Dp-3-glucoside have been reported in Table A3, showing a very good linear correlation

between absorbance at 600 nm and concentration of anthocyanin (R^2 = 0.995 and 0.997, respectively), with good repeatability above the limit of quantification (LOQ = 0.88 ± 0.02 and 0.478 ± 0.007 mg L^{-1}, respectively) and high sensitivity (ε_{600nm} = 8300 and 15,900 M^{-1} cm^{-1}, respectively). The different ε600nm/ε280nm ratio for these two anthocyanins is reflected into the different color of respective solutions.

Table A3 Fitting parameters for Cy-3-Glucoside and Dp-3-Glucoside calibration curves by using absorbance values at 600 nm and 280 nm from UV-Vis spectra in Fig. A6

Anthocyanin	Cy-3-Glucoside	Dp-3-Glucoside	Cy-3-Glucoside	Dp-3-Glucoside
λ_{max}	600 nm	600 nm	280 nm	280 nm
R^2	0.995	0.997	0.991	0.997
[a]%CV_{mean}	7.8	5.3	3.5	4.1
[b]m (mg^{-1} L)	0.0172 ± 0.0003	0.0317 ± 0.0005	0.0371 ± 0.0008	0.0179 ± 0.0002
[c]LOD (mg L^{-1})	0.264 ± 0.005	0.143 ± 0.002	0.288 ± 0.006	0.596 ± 0.007
[d]LOQ (mg L^{-1})	0.88 ± 0.02	0.478 ± 0.007	0.96 ± 0.02	1.99 ± 0.02
[e]ε (M^{-1} cm^{-1})	8300 ± 150	15,900 ± 250	18,000 ± 390	9000 ± 100

[a]Above the LOQ
[b]m is the slope of each calibration curve
[c]LOD = 3 X SD_{blank}/m
[d]LOQ = 10 X SD_{blank}/m
[e]ε = 1000 x Anthocyanin MW x m/pathlength

A2.4.3 Quantification of anthocyanins in fruit extract samples

Although the reference method to determine the anthocyanin content in foods is represented by LC hyphenated with spectrophotometric or mass spectrometric detection, using anthocyanin(s) as external standards, it has been shown that the results obtained with this analytical approach is highly correlated [30]. However, the main disadvantage of the spectrophotometric pH-differential method is that it cannot clearly distinguish among different classes of anthocyanins because of large absorbance overlap at acidic pH. Differently, the colorimetric method here developed is suitable to selectively determine catechol and pyrogallol in copresence of other ACs classes thanks

to the peculiar absorbance at about 600 nm of catechol/pyrogallol moieties, which provide a specific metal ion coordination capability (Figs. A2 and A3). Accordingly, we evaluated the applicability of the developed analytical method to real fruit extract samples, analyzing the same samples also by pH-differential method and LC-MS/MS.

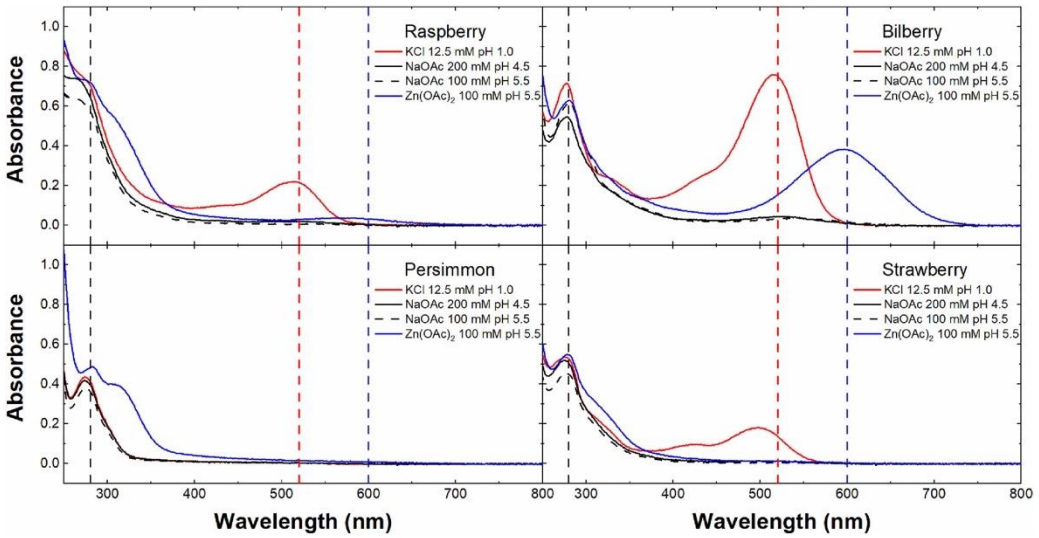

Fig. A8 UV–Vis absorbance spectra of fruit extracts from raspberry (upper left), bilberry (upper right), persimmon (lower left), and strawberry (lower right) analyzed with classical pH differential method (12.5 mM KCl pH = 1.00 or 200 mM NaOAc pH = 4.5) and with new zinc method (100 mM NaOAc pH = 5.5, or 100 mM $Zn(OAc)_2$ pH = 5.5) at 25 °C in MeOH/H_2O 80/20 (v/v). Vertical lines indicate the wavelength characteristic of maximum absorbance for phenols (280 nm, black dashed line), cyanidin at acidic pH (520 nm, red dashed line), and delphinidin in presence of zinc ion (600 nm, blue dashed line). All measurements have been performed in triplicate. (For interpretation of the references to color in this figure legend, the reader is referred to the Web version of this article.)

Fig. 8 shows representative UV–visible absorbance spectra of extracts from raspberry, bilberry, persimmon, and strawberry fruit samples. The reaction requires about 1 min and is stable at least for 1 h (Fig. 4C).

All sample extracts, including persimmon (i.e., the negative control), show the maximum of absorbance at about 280 nm, which is characteristic of

phenols content (vertical dashed black line). The absorbance at this wavelength is not sensitive to pH change from 1.0 (red trace) to 4.5 (black trace), as reported in literature for pH-differential method [10]. Differently, the effect of the presence of zinc ion at 280 nm is clearly distinguishable in all samples, including the one of persimmon that shows a new absorbance maximum at about 320 nm. This finding must be ascribed to the presence of zinc (added as acetate, blue trace), since when sodium acetate was used no absorbance maximum was evidenced at 320 nm (dashed black trace). However, the most relevant result for this work is the difference of visible response of fruit extracts to the pH-differential method with respect to the zinc method here proposed. In detail, at pH 1.0 (red trace) only extracts of fruits containing anthocyanins give rise to red solutions with a maximum of absorbance depending on the main anthocyanins occurring in the fruit, *i.e.*, about 520 nm for raspberry and bilberry (containing mainly cyanidin and delphinidin, respectively), and about 496 nm for strawberry (major AC pelargonidin), as expected [10]. Conversely, the pH-differential method does not discriminate the catechol/pyrogallol-based ACs content from total anthocyanin content (TAC). Differently, in presence of zinc acetate at pH 5.5 (blue trace), only fruit extracts containing cyanidin (raspberry) or delphinidin (bilberry) show a new absorbance maximum at about 600 nm and a purple/blue color, thus allowing the naked eye discrimination of raspberry/bilberry fruit extracts from the others and above-all catechol/pyrogallol colorimetric quantification according to equation (2) that is analogue of equation (1) used for the pH differential method [1,10,11], but with the further advantage of using the same pH, the same cation concentration, and the same solvent, for both absorbing and not absorbing reference condition.

$$A = (A_{600nm} - A_{800nm})_{Zn(II)\ pH5.5} - (A_{600nm} - A_{800nm})_{Na(I)\ pH5.5} \qquad (2)$$

Table A4 shows the concentrations of (i) selected single anthocyanin determined in fruit extracts by using LC-MS/MS, (ii) conventional pH-

differential method (TAC), and (iii) the Zn-coordinating anthocyanins (TMCA) analyzed by the colorimetric method here developed. As expected, for persimmon the anthocyanins are not detectable and therefore not reported. LC-MS analysis of raspberry extract has detected about 30 mg L^{-1} of Cy-3-glucoside and Cy-3-sophoroside. However, upon zinc ion coordination at pH 5.5 is possible to estimate a TMCA value of 38 ± 3 mgL^{-1}, expressed as Cy-3-glucoside chloride equivalents for the same extract, and the TAC value is even larger, also detecting non coordinating anthocyanins. Differently, LC-MS analysis of bilberry samples has detected more than 300 mg L^{-1} of anthocyanin, including Dp-3-glucoside, Cy-3-glucoside, and Mv-3-glucoside, each one larger than whole raspberry extract content. In this case, we estimate a TMCA value of 428 ± 14 mg L^{-1} expressed as Cy-3-glucoside chloride equivalents, very close to the TAC value for the same extract. Finally, LC-MS/ MS analysis of strawberry samples has mainly detected pelargonidins, plus a minor amount Cy-3-glucoside. Only the latter component is detected by using zinc solution giving 9 ± 3 mg L^{-1} that is very close to LC-MS/MS estimation. Also in this case the TAC value is larger, indicating the presence of other ACs not-detected by LC-MS/MS.

Table A4 Estimation of anthocyanin content in fruit extracts by using LC-MS/MS, pH-differential method, and absorbance values from UV-Vis spectra in presence of zinc acetate at pH 5.5

	LC-MS Anthocyanin (mg L^{-1})					
	Cy-3-	Dp-3-	Mv-3-	Pg-3-	[a]TAC (mg L^{-1})	[b]TMCA (mg L^{-1})
Raspberry	17 ± 1 [c](GLU) 12 ± 1 [c](SOP)	n.d.	n.d.	n.d.	56 ± 2	38 ± 3
Bilberry	61 ± 5 [c](GLU) 47 ± 7 [c](GLU)	220 ± 41 [c](GLU)	45 ± 3 [c](GLU)	n.d.	406 ± 6	428 ± 14
Strawberry	8 ± 1 [c](GLU)	n.d.	n.d.	215 ± 23 [c](GLU) 27 ± 1 [c](RUT)	387 ± 12	9 ± 3

n.d. Not detected. Values below the detection limit

[a] Total anthocyanin content (TAC) from pH-differential analysis expressed as Cy-3-glucoside chloride equivalents.

[b] Total metal-coordinating anthocyanin content (TMCA) from Zn-based colorimetric analysis expressed as Cy-3-Glucoside Chloride equivalents.

[c] GLU (glucoside), SOP (sophoroside), GAL (galactoside), RUT (rutinoside).

A2.5 Conclusions

Common anthocyanins with different substitution pattern and different fruit extracts with different anthocyanin content have been used to develop a colorimetric method for catechol/pyrogallol anthocyanin quantification in real matrix. The assay developed here responds to the need of simple, low cost, sensitive and reproducible analytical platforms, eventually moving to greener analysis, by reducing the solvent use and complex instrumentation. The assay is based on the selective zinc ion coordination of anthocyanins like cyanidin- and, preferentially, delphinidin-derivatives that can be recognized by naked eye by purple and blue color appearance, respectively, differently from not-coordinating and uncolored solutions containing anthocyanins like

malvidin- and pelargonidin-derivatives in the same conditions. The method shows a very good linear correlation between concentration and visible absorbance (R^2 = 0.995 for cyanidin and 0.997 for delphinidin), with good reproducibility (CV% = 7.4% for cyanidin and 5.3% for delphinidin), and high sensitivity (LOD = 0.264 ± 0.005 mg L^{-1} for cyanidin, and 0.143 ± 0.002 mg L^{-1} for delphinidin). The procedure has been applied to fruits extract of bilberries strawberry, raspberry, and persimmon and compared to LC-MS/MS analysis and classic pH-differential method. The bilberry samples, very rich in delphinidin-3-glucoside, has shown the largest color development in presence of zinc ions with a good accordance between classic and new methodology. These results are different from, and even more sensitive than, the recent Al^{3+} -based assay for anthocyanins, showing instead cyanidin-3-glucoside largest absorbance and coordination and color development also by *ortho*-dioxygenated B-ring like in case of malvidin. Accordingly, this novel colorimetric assay based on Zn^{2+} appears a valuable tool to further discriminate and study catechol/pyrogallol-rich natural products and foods, appearing complementary to conventional colorimetric and chromatographic methodologies.

References

1. V.S. Fedenko, S.A. Shemet, M. Landi, UV–vis spectroscopy and colorimetric models for detecting anthocyanin-metal complexes in plants: an overview of in vitro and in vivo techniques, J. Plant Physiol. 212 (2017) 13–28.
2. L. Guidi, P. Penella, M. Landi, Anthocyanins in Mediterranean diet: common and innovative sources, in: L.H. Warner (Ed.), Handbook of Anthocyanins: Food Sources, Chemical Application and Health Benefit, Nova Publisher, New York, 2015, pp. 1–50.
3. O.M. Andersen, K.R. Markham, Flavonoids – Chemistry, Biochemistry and Applications, CRC Taylor & Francis, Boca Raton, FL, USA, 2006.
4. F. Pina, M.J. Melo, C.A. Laia, A.J. Parola, J.C. Lima, Chemistry and applications of flavylium compounds: a handful of colours, Chem. Soc. Rev. 41 (2) (2012) 869–908.

5. P. Trouillas, J.C. Sancho-García, V. De Freitas, J. Gierschner, M. Otyepka, O. Dangles, Stabilizing and modulating color by copigmentation: insights from theory and experiment, Chem. Rev. 116 (9) (2016) 4937–4982.
6. R. Brouillard, Chemical Structure of Anthocyanins, Anthocyanins as food colors, 1982, pp. 1–40.
7. R. Eder, in: L.M.L. Pigments, Nollet (Eds.), Food Analysis by HPLC , Marcel Dekker, New York, 2000, pp. 825–880.
8. L. Renai, F. Tozzi, C.V. Scordo, E. Giordani, M.C. Bruzzoniti, D. Fibbi, L. Mandi, N. Ouazzani, M. Del Bubba, Productivity and nutritional and nutraceutical value of strawberry fruits (Fragaria x ananassa Duch.) cultivated under irrigation with treated wastewaters, J. Sci. Food Agric. 101 (3) (2021) 1239–1246.
9. A. Romani, M. Minunni, N. Mulinacci, P. Pinelli, F. Vincieri, M. Del Carlo, M. Mascini, Comparison among differential pulse voltammetry, amperometric biosensor, and HPLC/DAD analysis for polyphenol determination, J. Agric. Food Chem. 48 (4) (2000) 1197–1203.
10. M.M. Giusti, R.E. Wrolstad, Characterization and measurement of anthocyanins by UV-visible spectroscopy, Curr. Protocol. Fool Anal. Chem. 1 (2001) F1. 2.1–F1. 2.13.
11. J. Lee, R.W. Durst, R.E. Wrolstad, Determination of total monomeric anthocyanin pigment content of fruit juices, beverages, natural colorants, and wines by the pH differential method: collaborative study, J. AOAC Int. 88 (5) (2005) 1269–1278.
12. C. Okoye, A. Chukwuneke, N. Ekere, J. Ihedioha, Simultaneous ultraviolet-visible (UVVIS) spectrophotometric quantitative determination of Pb, Hg, Cd, as and Ni ions in aqueous solutions using cyanidin as a chromogenic reagent, Int. J. Phys. Sci. 8 (3) (2013) 98–102.
13. G.T. Sigurdson, M.M. Giusti, Bathochromic and hyperchromic effects of aluminum salt complexation by anthocyanins from edible sources for blue color development, J. Agric. Food Chem. 62 (29) (2014) 6955–6965.
14. G.T. Sigurdson, R. Robbins, T. Collins, M. Giusti, Evaluating the role of metal ions in the bathochromic and hyperchromic responses of cyanidin derivatives in acidic and alkaline pH, Food Chem. 208 (2016) 26–34.

15. T. Fossen, L. Cabrita, O.M. Andersen, Colour and stability of pure anthocyanins influenced by pH including the alkaline region, Food Chem. 63 (4) (1998) 435–440.
16. F.A. Bernal, L.L. Orduz-Diaz, E. Coy-Barrera, Exploitation of the complexation reaction of ortho-dihydroxylated anthocyanins with aluminum (III) for their quantitative spectrophotometric determination in edible sources, Food Chem. 185 (2015) 84–89.
17. H.D. Schreiber, A.M. Swink, T.D. Godsey, The chemical mechanism for Al complexing with delphinidin: a model for the bluing of hydrangea sepals, J. Inorg. Biochem. 104 (7) (2010) 732–739.
18. C. Ancillotti, L. Ciofi, D. Pucci, E. Sagona, E. Giordani, S. Biricolti, M. Gori, W. A. Petrucci, F. Giardi, R. Bartoletti, Polyphenolic profiles and antioxidant and antiradical activity of Italian berries from Vaccinium myrtillus L. and Vaccinium uliginosum L. subsp. gaultherioides (Bigelow) SB Young, Food Chem. 204 (2016) 176–184.
19. L. Renai, C.V.A. Scordo, U. Chiuminatto, M. Ulaszewska, E. Giordani, W.A. Petrucci, F. Tozzi, S. Nin, M. Del Bubba, Liquid chromatographic quadrupole time-of-flight mass spectrometric untargeted profiling of (poly) phenolic compounds in Rubus idaeus L. And Rubus occidentalis L. Fruits and their comparative evaluation, Antioxidants 10 (5) (2021) 704.
20. M. Lettieri, R. Emanuele, S. Scarano, P. Palladino, M. Minunni, Melanochrome-based colorimetric assay for quantitative detection of levodopa in co-presence of carbidopa and its application to relevant anti-Parkinson drugs, Anal. Bioanal. Chem. (2021), https://doi.org/10.1007/s00216-021-03804-8.
21. G. Sigurdson, R. Robbins, T. Collins, M. Giusti, Spectral and colorimetric characteristics of metal chelates of acylated cyanidin derivatives, Food Chem. 221 (2017) 1088–1095.
22. K. Yoshida, M. Mori, T. Kondo, Blue flower color development by anthocyanins: from chemical structure to cell physiology, Nat. Prod. Rep. 26 (7) (2009) 884–915.
23. M. Buchweitz, J. Brauch, R. Carle, D. Kammerer, Application of ferric anthocyanin chelates as natural blue food colorants in polysaccharide and gelatin based gels, Food Res. Int. 51 (1) (2013) 274–282.
24. L. Estévez, M. Queiz´an, R.A. Mosquera, L. Guidi, E. Lo Piccolo, M. Landi, First characterization of the formation of anthocyanin–Ge and anthocyanin–B

complexes through UV–vis spectroscopy and density functional theory quantum chemical calculations, J. Agric. Food Chem. 69 (4) (2021) 1272–1282.

25. M. Buchweitz, J. Brauch, R. Carle, D. Kammerer, Colour and stability assessment of blue ferric anthocyanin chelates in liquid pectin-stabilised model systems, Food Chem. 138 (2–3) (2013) 2026–2035.
26. E. Bayer, H. Egeter, A. Fink, K. Nether, K. Wegmann, Complex formation and flower colors, Angew Chem. Int. Ed. Engl. 5 (9) (1966) 791–798.
27. T. Hondo, K. Yoshida, A. Nakagawa, T. Kawai, H. Tamura, T. Goto, Structural basis of blue-colour development in flower petals from Commelina communis, Nature 358 (6386) (1992) 515–518.
28. L. Jurd, S. Asen, The formation of metal and "co-pigment" complexes of cyanidin 3- glucoside, Phytochemistry 5 (6) (1966) 1263–1271.
29. K. Yoshida, S. Kitahara, D. Ito, T. Kondo, Ferric ions involved in the flower color development of the Himalayan blue poppy, Meconopsis Grandis Phytochem. 67 (10) (2006) 992–998.
30. J. Lee, C. Rennaker, R.E. Wrolstad, Correlation of two anthocyanin quantification methods: HPLC and spectrophotometric methods, Food Chem. 110 (3) (2008) 782–786.

PhD research activities – outline

Peer-reviewed publications

1) **Torrini F**, Palladino P, Brittoli A, Baldoneschi V, Minunni M, Scarano S. Characterization of troponin T binding aptamers for an innovative enzyme-linked oligonucleotide assay (ELONA). Anal. Bioanal. Chem. 411 (2019) 7709-16. https://doi.org/10.1007/s00216-019-02014-7
IF = 4.157 (2020)

2) Palladino P, **Torrini F**, Scarano S, Minunni M. Colorimetric analysis of the early oxidation of dopamine by hypochlorous acid as preliminary screening tool for chemical determinations of neuronal oxidative stress. J Pharm. Biomed. Anal. 179 (2020) 113016. https://doi.org/10.1016/j.jpba.2019.113016
IF = 3.935 (2020)

3) Palladino P, **Torrini F**, Scarano S, Minunni M. 3,3',5,5'-tetramethylbenzidine as multi-colorimetric indicator of chlorine in water in line with health guideline values. Anal. Bioanal. Chem. 412 (2020) 7861-69. https://doi.org/10.1007/s00216-020-02918-9
IF = 4.157 (2020)

4) **Torrini F**, Palladino P, Scarano S, Minunni M. Polydopamine-based quantitation of albuminuria for the assessment of kidney damage. Anal. Bioanal. Chem. 413 (2021) 2217-24. https://doi.org/10.1007/s00216-021-03192-z
IF = 4.157 (2020)

5) **Torrini F**, Palladino P, Baldoneschi S, Scarano S, Minunni M. Sensitive 'two-steps' competitive assay for gonadotropin-releasing hormone via

SPR biosensing and polynorepinephrine-based molecularly imprinted polymer. Anal. Chim. Acta. 1116 (2021) 338481. https://doi.org/10.1016/j.aca.2021.338481
IF = 6.558 (2020)

6) **Torrini F**, Caponi L, Bertolini A, Palladino P, Cipolli F, Saba A, Paolicchi A, Scarano S, Minunni M. A biomimetic enzyme-linked immunosorbent assay (BELISA) for the analysis of gonadorelin by using molecularly imprinted polymer-coated microplates. Anal. Bioanal. Chem. (2022), https://doi.org/10.1007/s00216-021-03867-7
IF = 4.157 (2020)

7) **Torrini F**, Renai L, Scarano S, Palladino P, Del Bubba M, Minunni M. Colorimetric selective quantification of anthocyanins with catechol/pyrogallol moiety in edible plants upon zinc complexation. Talanta 240 (2022) 123156.
https://doi.org/10.1016/j.talanta.2021.123156
IF = 6.057 (2020)

Proceedings:

8) **Torrini F**, Palladino P, Scarano S, Minunni M. Detection of small peptide hormones for anti-doping purpose via a molecularly imprinted polymer-based SPR Assay. The 1st International Electronic Conference on Biosensors (IECB 2020) Online Congress 2-17 November 2020. *Proceedings* **2020**, *60(1)*, 56. DOI: 10.3390/IECB2020-0743

Conference Contributions:

National Conferences (Presenting author is underlined)

1) **F. Torrini**, A. Brittoli, P. Palladino, M. Minunni, S. Scarano. ELONA-based approaches for the antibody-free detection of Troponin T, the key

biomarker of acute myocardial infarction. XXVII Congress of the Analytical Chemistry Division – Bologna (Italy), 16-20 September 2018. ISBN: 978-88-94952-04-9. (*Poster*).

2) **F. Torrini**. Characterization of Troponin T-binding aptamers for an innovative enzyme-linked oligonucleotide assay (ELONA), PhD-Day *University of Florence,* May 23, 2019. (*Poster*).

3) **F. Torrini**, P. Palladino, M. Minunni, S. Scarano. Novel approach for detection of peptide hormones in doping-control analysis. XXVIII Congress of the Analytical Chemistry Division - Bari (Italy), 22-26 September 2019. ISBN: 978-88-94952-10-0 (*Poster*).

4) P. Palladino, **F. Torrini**, V. Baldoneschi, S. Scarano, M. Minunni. Innovative uses of polydopamine (PDA) in the field of (bio)analytical chemistry. XXVIII Congress of the Analytical Chemistry Division - Bari (Italy), 22-26 September 2019. ISBN: 978-88-94952-10-0 (***Oral presentation***).

5) **F. Torrini**. Molecular imprinting as a new bioanalytical tool for small peptide hormones detection in the anti-doping field. Merck Young Chemists' Symposium 2019_Società Chimica Italiana Giovani - Rimini (Italy), 25-27 November 2019 (***Flash oral presentation 4 minutes + Poster***). ISBN: 978-88-94952-15-5.

6) **F. Torrini**. Enhancing sensitivity of a SPR molecularly imprinted biosensor to quantify low-molecular-weight peptides. School of Nanomedicine (Topics: nanodrugs, materials for nanomedicine, from bench to bed, nanodevices), Trieste (Italy) 11-13 December 2019 (*Poster*).

7) F. Torrini. A smart MIP-based sensing anti-doping platform for small peptides detection. PhD-Day *University of Florence,* Postponed (*Oral presentation*).

8) **F. Torrini**, P. Palladino, L. Caponi, F. Cipolli, A. Paolicchi, S. Scarano, M. Minunni. Development of a catecholamine-based molecularly imprinted polymer bioassay for gonadorelin detection in urine samples. Giornata Bioanalitica 2021 *online* July 13, 2021 (***Oral presentation***).

9) **F. Torrini**, P. Palladino, L. Caponi, F. Cipolli, A. Paolicchi, S. Scarano, M. Minunni. A competitive microplate bioassay to detect gonadorelin in urine samples via a polynorepinephrine-based molecular imprinted polymer. XXVII National Congress of the Italian Chemical Society – online, 14-23 September 2021 (***Oral presentation***).
Awarded with the grant for SCI 2021 virtual congress participation.

International Conferences (Presenting author is underlined)

10) S. Scarano, P. Palladino, A. Brittoli, E. Pascale, **F. Torrini**, V. Baldoneschi, M. Minunni. Polydopamine: a smart polymer for biosensing. 2nd European Biosensor Symposium (EBS 2019) – Florence (Italy), February 18-21, 2019 (***Oral presentation***).

11) **F. Torrini**, A. Brittoli, P. Palladino, M. Minunni, S. Scarano. ELONA-based approaches for the antibody-free detection of Troponin T, the key biomarker of acute myocardial infarction. 2nd European Biosensor Symposium (EBS 2019) – Florence (Italy), February 18-21, 2019 (*Poster*).

12) **F. Torrini**, P. Palladino, A. Brittoli, V. Baldoneschi, M. Minunni, S. Scarano. Development of a rapid detection strategy for cardiac Troponin

T based on an Enzyme-Linked OligoNucleotide Assay (ELONA). APTAMERS in Bordeaux – Bordeaux (France), June 28-29, 2019 (*Poster*).

13) **F. Torrini**, P. Palladino, S. Scarano, M. Minunni. Detection of small peptide hormones for anti-doping purpose via a molecularly imprinted polymer -based SPR assay. The 1st International Electronic Conference on Biosensors (IECB 2020) Online Congress 2-17 November, 2020. https://IECB2020.sciforum.net (*Poster*).

14) **F. Torrini**, P. Palladino, S. Scarano, M. Minunni. A polynorepinephrine-based molecular imprinting assay targeting a small peptide hormone in doping control analysis. 3rd European BioSensor Symposium Online (EBS 2021), 09-12 March, 2021. (***Oral presentation***).

15) **F. Torrini**, P. Palladino, S. Scarano, M. Minunni. An innovative biomimetic sensing platform as a promising nano-device for gonadorelin detection. Trends in Nano technology (TNT 2021) – Tirana (Albania). *Postponed to 4-8 October 2021* (*Poste*r).

16) S. Scarano, P. Palladino, V. Baldoneschi, **F. Torrini**, M.G. Lettieri, M. Banchini, M. Minunni. Affinity based sensing: trends and challenges. XXXVIII Reunion Biennal Real Societad Espagnola de Quimica (RSEQ) – Granada (Spain). 28 June – 1 July, 2022 (*Keynote invited*). https://bienal2021.com/index.php/en/speakers/invited-speakers.

17) S. Scarano, P. Palladino, V. Baldoneschi, **F. Torrini**, M.G. Lettieri, M. Banchini, M. Minunni. Advances in affinity-based sensing. Spanish Optoelectronics Meeting, OPTOEL 2021 Online, June 2021 (*Plenary invited*). https://bienal2021.com/index.php/en/speakers/invited-speakers.

Patents:

1) Kit for colorimetric determination of chlorine level in water used for recreational purposes. Inventors: P. Palladino, M. Minunni, F. Torrini, S. Scarano. Priority number: 102019000024778 (IT). Filed: December 19, 2014. Date of Patent: October 29, 2020. Assignee: University of Florence.